UNIVERSITEIT GENT

Sustainable Construction & Design

Proceedings of the Day of Research 2010

Laboratory Soete   –   2010

LABORATORY SOETE

Sustainable Construction & Design

Proceedings of the Day of Research 2010

Organizing Committee

Jan De Pauw
Stijn Hertelé
Wouter Ost
Yeczain Perez Delgado
Vanessa Rodriguez Fereira
Mohsen Safaei
Jeroen Van Wittenberghe
Matthias Verstraete
Prof. Patrick De Baets
Prof. Wim De Waele

Day of Research Proceedings 2010

The texts of the papers in this volume were set individually by the authors or under their supervision. Only minor corrections to the text may have been carried out by the publisher.

Preface

The first edition of the Day of Research in 2009 was organized to promote the research performed at the Laboratory Soete of Ghent University. In this ambitious second edition the scope is expanded to our associate partners of the HoGent and Howest and to the partner institutions of the Belgian Welding Institute, OCAS and the Szent Istvàn University in Gödöllö, Hungary in order to promote the scientific research performed in the field of mechanical engineering in these institutions.

Therefore this edition of Sustainable Construction & Design is dedicated to all contributions to the Day of Research 2010. Special attention is given to our master thesis students, which on this day will present the current status of their work. We hope that this day will enable them and all other attending students to get in touch with young, motivated researchers with whom they will have the opportunity to discuss during the breaks and that this leads to a positive input into their own research.

The presented program gives a good overview of current hot topics in mechanical engineering. Contributions are made from the field of biomechanical engineering, tribology, musicology, design, welding technology, numerical modelling and fatigue.

Finally, our thanks goes to our students, the authors, the presenters and the participants, we hope everybody enjoys this year's Day of Research.

Jeroen Van Wittenberghe

February 2010

Contents

Alphabetic list of principal authors

Morning Session 1

Chairman:

Jan De Pauw, Laboratory Soete, Ghent University, Belgium

INVITED LECTURE

DESIGN FOR [EVERY]^{ONE}: WHAT IF EVERYONE BECAME A POTENTIAL DESIGNER

Lieven De Couvreur[1]

[1] Hogeschool West-Vlaanderen (www.howest.be)

Design for [every]one is a Belgium based design and research project at the University College of West-Flanders (Howest). It aims to bridge the gap between contemporary design and assistive technology. User centered techniques are applied for an incremental personalization process involving design team members, patients and occupational therapists. The use of experience prototyping and rapid manufacturing techniques enable us to make products that are suited to specific end consumers and produced in small batches.

Basically, this approach works in two ways, personalized assistive products are fitted to the users and users become fitted to their products. Based on the Fablab philosophy the devices are produced that can be tailored to local or personal needs in ways that are not practical or economical using with mass production. By implementing active engagement with user experience prototypes and observational techniques, it is possible to reduce the stigmatization and augment the product affinity between patient and assistive tool.

For more information, see: **http://designforeveryone.howest.be/**.

INVITED LECTURE

WHERE TO GO WITH METALS RESEARCH IN FLANDERS: A SPLENDID OPPORTUNITY AT CAMPUS ARDOYEN

Sven Vandeputte[1]

[1] OCAS (www.ocas.be)

During the fall of 2009, the building of the Metal Structure Centre has started on the Campus Ardoyen. This new research centre will be operational by the end of 2010. The main goal is the development of sustainable metal constructions for the energy transport and delivery. The Metal Structure Centre is a unique cooperation between the academic and industrial research world. The founding partners are:

- **Laboratory Soete (http://www.tribology-fatigue.ugent.be)**: part of Ghent University and world leader in the development of safety criteria for and the testing of welded connections,

- **OCAS (http://www.ocas.be)**: responsible within Arcelor-Mittal for the development of pipelines for oil and gas transportation and thick plates for offshore constructions), and

- **BIL (http://www.bil-ibs.be)**: the Belgian Welding Institute, a Ghent University spin-off founded in 1972.

Besides, researchers from **Sirris**, **Clusta**, **CRM** and **Flamac** will also cooperate, which will result in a total of 220 scientist and engineers working in this new centre for innovation.

The focus of the new research centre will be on the development of specific knowledge enabling the development of sustainable metal constructions for energy transport, storage and generation. The final result of all research will be found in new wind turbines, power plants and high pressure pipelines.

In order to achieve these innovative developments, a wide range of material testing will be performed, ranging from nano scale to full scale. This means a full coverage of the material technology, starting from the numerical modeling to the integration and testing of the final construction.

One example on which the research will focus, is the development of a new welding procedure for high strength pipelines. Besides, the protection of pipelines against corrosion will be investigated, enabling them to withstand the influence of harsh environments and allowing the transport of sour gases.

PATELLOFEMORAL CONTACT DURING SQUAT SIMULATION ON CADAVERIC KNEES

A. Van Haver[1], J. Quintelier[2], P. Verdonk[3], F. Almqvist[3], M. De Beule[4], and P. De Baets[2]

[1] Ghent University College, Engineering Dept.,Belgium
[2] Ghent University, Dept. of Mechanical Construction and Production, Belgium
[3] Ghent University Hospital, Dept. of Orthopaedics, Belgium
[4] Ghent University, Dept. of Civil Engineering, bioMMeda – IBiTech, Belgium

Abstract   The Ghent Knee Rig was built in 2006 for studying the biomechanical behavior of post-mortem human knees. To validate this test rig the patellofemoral contact pressures and areas were investigated in 3 post-mortem knees tested under the same circumstances and compared to results in literature. To load the quadriceps, the vastus intermedius and rectus femoris were separated and clamped together. The pulling cable was aligned according to the shaft of the femur to keep the Q-angle at physiological values. A pressure film was inserted in the patellofemoral joint to measure the patellofemoral contact area and pressure. The results follow the general accepted trends of patellofemoral contact during knee flexion and extension; when the patella enters the trochlear groove at approximately 20 degrees of knee flexion, the intra articular contact pressure and area start to build up and the contact area on the patella shifts from distal to proximal. Though working with cadaveric specimens remains a simulation of in vivo situations with well known limitations, the test rig shows a good repeatability and reliability. The next stage of this research project is a comparison of normal with pathological knees.

Keywords   knee biomechanics, experimental, patellofemoral joint

1   INTRODUCTION

The purpose of this study is to validate the Ghent Knee Rig, developed in 2006 by the department of mechanical construction and production at Ghent University [1]. Our main interest is the patellofemoral contact area and pressure since increased patellofemoral pressures are often associated with anterior knee pain.

The patella plays an essential role in increasing the mechanical advantage of the quadriceps mechanism. The main biomechanical function of the patella consists of increasing the moment arm of the quadriceps by shifting the quadriceps tendon anteriorly [1] [3]. As a result the knee extension torque expands during extension. Due to the insertion of the patellar tendon on the tibial tuberosity, a great amount of force is necessary to displace the rather small weight of the foot, leading to high compressive forces in the patellofemoral joint. In closed kinetic chain movements, like squatting, the force of the quadriceps rises radically towards 90°, the contact area also increases but not in proportion, so the contact stress in the patellofemoral joint rises with deeper knee flexion. Research on patellofemoral biomechanics often focuses on patellar kinematics, extensor forces, and patellofemoral contact pressure and contact area.

In this study cadaveric knees were mounted in the Ghent Knee Rig to simulate a weight bearing squat. During this dynamic flexion-extension movement, the patellofemoral contact areas and pressures are continuously monitored.

2   MATERIALS AND METHOD

2.1   Specimens and specimen preparation

Since 2006, eighteen human post mortem knees were obtained from the anatomy lab of Ghent University and were tested in the Ghent Knee Rig. Three unpaired knees were selected for statistical analysis reported in this paper. The other knees showed variability in test conditions (e.g. movement speed, Q-angle, preparation method of the knees, flexion range), early failure of the specimen caused by low quality of the knee specimen, and dysfunction of the pressure-sensitive sensor. The three selected knees had a mean age of 90 years (± 7.4).

All knees were embalmed with a mixture of formol, phenol and thymol and were considered to be macroscopically intact, radiographic images didn't reveal any bony abnormalities. Each knee was amputated through the tibia and femur at approximately 20 cm from the apex of the patella. For mounting purposes, a complete dissection of all structures surrounding the bones was done at approximately 8 cm at the free end of the tibia, fibula and femur. The bones were placed in an aluminium cylinder and fixed with a polyester resin. At the knee joint care was taken to protect the retinacula, the medial and lateral collateral ligament and the tendon of quadriceps and patella from damage. The quadriceps were then further dissected into its 4 parts. The VI and RF were separated from the femur and their tendons were clamped together at approximately 5cm from the proximal pole of the patella. The clamping system, based on a polymer toothed rack, was designed especially for this purpose. (Figure 1)

Figure 1. The clamping system for the rectus femoris and vastus intermedius

By applying the definition given by Insall et al. [5] and Minkowitz et al. [5], the pulling cable was aligned according to the shaft of the femur. Doing so, the Q angle was kept at physiological values.

2.2 Test set-up

For the kinematic tests the department of mechanical construction and production developed a test rig, based on the Oxford Knee rig [6]. The set-up of the Ghent Knee Rig is shown in Figure 2.

A. Vertical Bars

B. Bridge Construction

C. Linear Motor

D. Mechanical Hip Joint

E. Clamped System

F. Steel Cable

G. Roller to guide the steel cable

H. Mechanical Ankle Joint

I. Pressure Sensitive Film + connection system
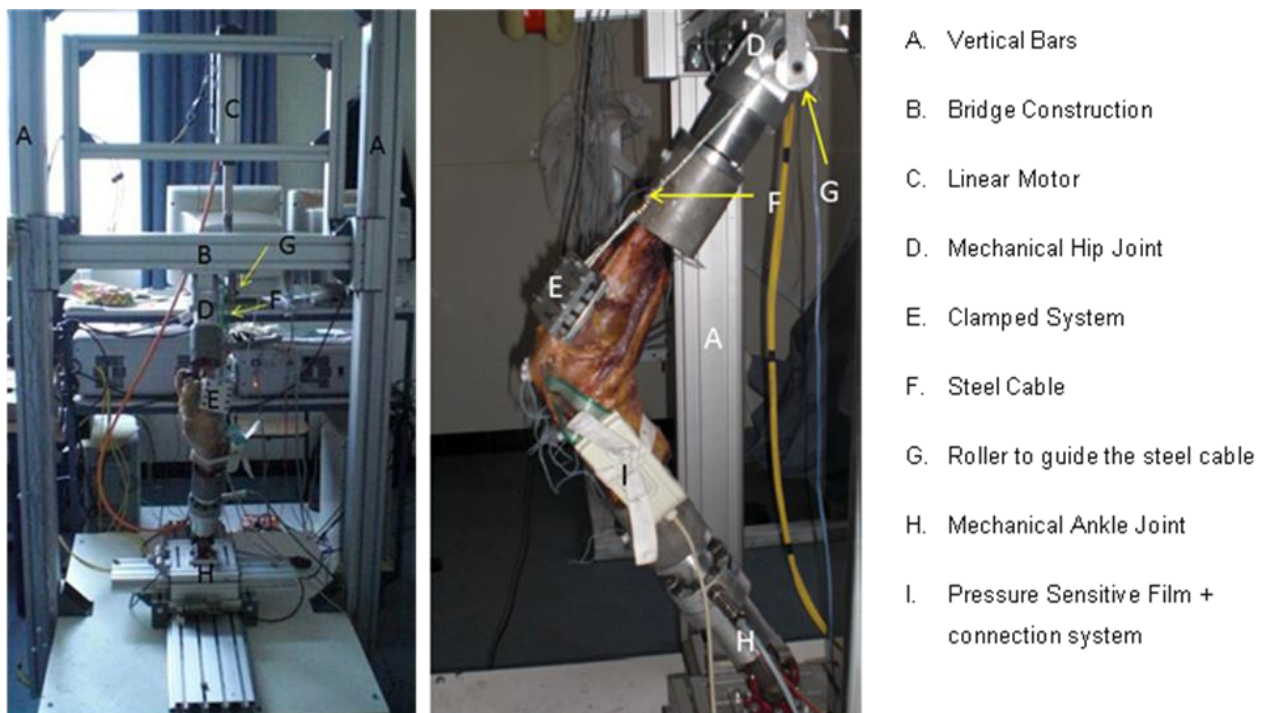
Figure 2. Experimental set up of the Ghent Knee Rig

Starting form a solid table, two vertical bars are responsible for the smooth gliding of a bridge construction, allowing the knee to flex and extend smoothly. The bridge construction rests on two mobile center points on the vertical sliding bars, which keep the knee flexion within its safety limits, taking the quality of the knee specimens into account. The total weight of the moveable part of the

construction is approximately 30 kg. This serves as a simulation of the body weight of a person during a squat movement.

The linear electrical motor unit is secured on the bridge construction and produces a maximum constant force of 1358 N and a maximal peak force of 3000 N. This force is transmitted to the quadriceps tendon through a steel cable and two pulleys. As a result the tension in the quadriceps tendon is being build up until the knee starts to extend.

The mechanical hip joint is also secured on the bridge construction and consists of an aluminum cylinder with two rotation axes which allow flexion-extension and internal-external rotation.

The mechanical ankle joint is fixed on two gliding platforms on the supporting table. These platforms allow simulating different positions of the ankle joint and consequently different positions of the knee. The aluminum cylinder is fixed with three screws on a cardan coupling unit, simulating the ankle joint. The unit has three rotational axes; flexion-extension, abduction-adduction and external-internal rotation of the tibia.

The knee flexion angle, the forces applied on the quadriceps tendon and the axial forces on the tibia are continuously measured together with the rotations of the tibia during flexion and extension. This test rig is built in such a way that it allows the six degrees of freedom of the knee joint.

In order to measure the contact area of the patellofemoral joint a 5051 I-scan pressure film (Tekscan Inc., South Boston, MA, USA), especially designed for intra articular measurements, is used with a pressure range of 8273 kPa (1200 model). The sensor is 0.1 mm thick and it has a 56 mm * 56 mm matrix consisting of 1936 sensing elements with a total contact area of 1600 mm^2. Sensors were calibrated before use in accordance with the manufacturers' guidelines. The pressure film was inserted in the patellofemoral joint through a lateral incision as described by Ostermeier et al. [7]. (Figure 3)

Figure 3. Positioning of the pressure film sensor.

The joint was opened with a lateral parapatellar incision. The pressure film was attached on the patella using a topical 2-octylcyanoacrylate tissue adhesive, Dermabond® (Ethicon NV, Johnson & Johnson, Somerville, New Jersey, USA). Prior to closing the incision with single stitches to restore physiological conditions, the margins of the retro-patellar facets were digitized by probing the I-scan sensor. The I-scan software was used to collect the contact area and pressure during testing.

3   RESULTS

For the three selected knees, all together 8 successful tests, each consisting out of 5 flexion – extension cycles were obtained.

In each test, the knees expressed a similar pattern of contact pressure distribution during the flexion and extension cycles. Pressure increased as the knee flexed and decreased as the knee extended.

The mean patellofemoral contact area measured in this study ranged from 68.8 (± 8) mm^2 at 20° to 336.5 (± 64.7) mm^2 at 60° knee flexion. The mean contact pressure ranged from 0.7 (±0.15) MPa at 20° flexion to 5.5 (± 1) MPa at 60°.

The contact areas on the patellar facets shifted from distal to proximal during knee flexion and from proximal to distal during extension, which is visualized in figure 4. Another remarkable observation is the difference between the flexion and extension phase (see figure 4).
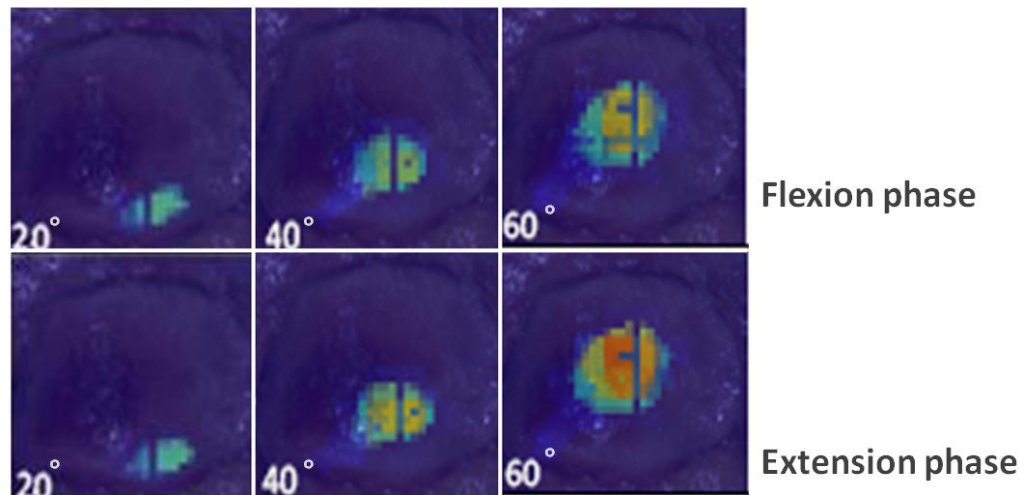
Figure 4. Patellofemoral contact area for 3 different knee angles (20°, 40°, 60°) during the flexion and extension phase

Statistical analysis of the contact area and pressure was done for knee flexion angles of 20°, 30°, 40°, 50° and 60° and for the flexion and extension phase separately. Out of the 5 x 2 conditions, 3 conditions did not have a normal distribution, so a Wilcoxon Signed Ranks Test was performed; a significant difference between the 2 movement phases for the contact area ($p < 0.001$, $z = -4.341$) as well as for the contact pressure ($p < 0.001$, $z = -4.627$) was found, with higher values for the extension phase compared to the flexion phase. This difference can be observed on figure 5.
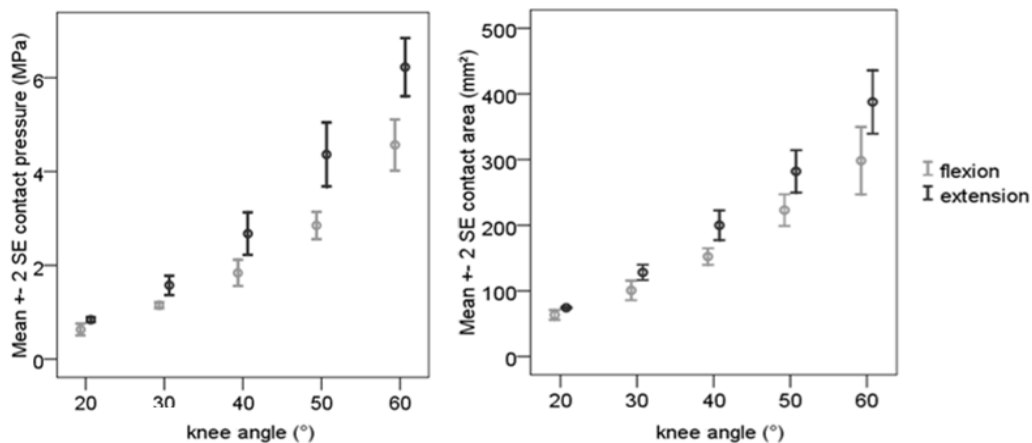
Figure 5. Mean patellofemoral contact area and contact pressure ± 2SE for 5 different knee angles

To reveal the predicting variables of the contact area and pressure, a linear regression was performed with the knee angle, flexion-extension phase and quadriceps force as independent variables. For the contact area as well as the contact pressure, the multiple regression models with these 3 independent variables show a very good correlation with the data, with respectively $R^2 = 0.88$ and $R^2 = 0.85$.
However, care should be taken in the interpretation of these results since the quadriceps force is highly correlating with the knee angle ($p < 0.001$) as well as the movement phase (flexion - extension) ($p < 0.001$). Mean values for the applied quadriceps force are reported in table 1.

Knee angle (°)	Mean quadriceps force ± SD (N)		
	Flexion phase	Extension phase	Total
20	281 ± 18	530 ± 51	419 ± 136
30	427 ± 40	800 ± 134	614 ± 215
40	589 ± 60	1091 ± 148	840 ± 281
50	851 ± 62	1438 ± 171	1145 ± 328
60	1093 ± 51	1714 ± 232	1404 ± 367
Total	639 ± 263	1095 ± 412	870 ± 414

Table 1. Mean quadriceps force for different knee angles and for the flexion – extension phase separately

This collinearity does not reduce the predictive power or reliability of the model as a whole; it only affects the reliability of the individual predictors. The model cannot provide valid results about any individual predictor, or about which predictors are redundant with others.

4   DISCUSSION

The experiments with the Ghent Knee Rig differ from previous experiments because the current knee rig simulates a dynamic weight bearing squat, which represents a high demanding exercise for the knee joint. Previous work on cadaver specimens either focused on dynamic measurements without simulation of a body weight or on static measurements with a certain load. In some studies, the sequences of static measurements are used as basic principle to represent kinematic data [8]. Reports have been published stating that the joint force in the patellofemoral joint during squatting can rise up to 7 times the body weight [12]. Due to its capabilities, the Ghent Knee Rig makes it possible to investigate the behavior of biomechanical characteristics during a simulation of such exercise. The assumption was made that a more complete image of pressure alterations could be obtained. Technical limitations however have lead to some restrictions. The RF and VI are the only two vasti loaded, this choice was based on a study performed by Elias et al. who performed EMG research on the quadriceps muscle and revealed that the forces necessary for knee extension are for 70% generated by the RF and the VI [13]. Nevertheless, this approach remains a simplified representation of the complex activity pattern of the quadriceps muscle. More and more authors tend to shift towards loading all four or even six parts of the quadriceps in order to obtain a more realistic representation of the quadriceps force. Besides the challenge of implementing very heavy extra linear motors on the bridge construction, it is not feasible to realistically simulate the physiological interactions between different muscles such as co-contraction, muscle activation sequence and the interaction between anta- and agonists in cadaver studies.

In order to measure the intra articular contact pressures and contact areas, an I-scan pressure sensitive film was inserted in the patellofemoral joint. This sensor is especially designed to determine pressure distribution in joints. Wilson and coworkers investigated the accuracy and repeatability of the I-scan pressure measuring system and the effect of cementing the sensors onto the retro patellar surface [14]. They conclude that the I-scan system is a valuable tool for assessing pressure and pressure distribution in the patellofemoral joint but that cementing reduces the sensors accuracy. As an alternative some authors have suggested to fixate the sensor by surrounding sutures [15]. In this study, the pressure film was fixated with a topical 2-octylcyanoacrylate tissue adhesive so that a complete inversion of the patella could be avoided.
Although the applicability of the I-scan system in the patellofemoral joint has been proven, careful interpretation is warranted. To insert the sensor, the knee joint was opened through a lateral incision, which might have an effect on the pressure distribution. Ostermeier and colleagues studied the effect of a lateral release on eight cadaver knees and no medialisation of the patella due to a lateral release was found and they observed no reduction of lateral instability of the patella, especially in extension. However, they state that there might be a relieving effect on the lateral patellar facet in knee flexion [15]. Therefore the influence of the sensor placement through lateral release on the measurements remains uncertain. Despite this potential influence on the knee joint, the results seem to follow the general accepted pattern of pressure distribution during knee flexion and extension.

When the patella engages in the femoral trochlear groove at approximately 20 degrees of knee flexion, the intra articular pressure and contact area start to build up, and increase further with

deeper knee bending. Early in-vitro studies by Hehne, Huberti et al. and Goodfellow et al. have reported on this phenomenon [9] [16] [17]. More recently, Luyckx et al. found that a maximum contact area is obtained at ninety degrees of knee flexion [18]. Besides the increase in contact area, a shift in contact area from distal to proximal on the patella was also observed during knee flexion. The results presented here show a similar pattern. As shown in figure 5, the contact area increases with the flexion angle. Furthermore, figure 4 nicely demonstrates that the contact area moves from distal to proximal during knee flexion.

Besides these well described patterns in literature, the present results also revealed a difference in contact area and intra articular pressure between the upward and downward squatting phase: lower contact pressures and smaller contact areas were observed during the downward phase. This difference needs to be further investigated; in the upward phase the linear motor systematically produces a greater force than in the downward phase, this difference in quadriceps force is correlated with the knee flexion angle, which makes it impossible to determine in which amount the difference in contact area and pressure between extension and flexion phase can be attributed to the knee angle, the quadriceps force and the direction of movement.

Some investigators have pointed out that the contact areas in the patellofemoral joint alter when the quadriceps tendon is loaded with different amount of forces [16] [19]. Most likely, these changes can be attributed to the greater amount of cartilage that comes in contact if the loads on the patellofemoral joint are augmented. Therefore the load on the quadriceps tendon should always be taken in mind when investigating the contact areas and pressures.

Comparing the results of contact pressures and areas of the present study with those found in literature, some similarities and some differences can be noticed. One possible explanation for the wide variation between all results is the difference in methods used to investigate the knee joint. These differences are demonstrated in table 2.

	Study conditions	Contact Area (mm²)			Contact Pressure (Mpa)
		30°	60°	90°	
Matthews et al. [19]	Experimental in-vitro Static	230	380	-	-
Huberti et al. [17]	Experimental in-vitro Static F_q: 125N tot 340N	260 (20°)	-	410	-
Csintalan et al. [20]	Experimental in-vitro	224	285	-	0,7 (60°)
Bohnsack et al. [21]	Experimental in-vitro Dynamic	75 (25°)	200	-	2 (60°)
Melegari et al. [22]	Experimental in-vitro Static F_q: 230N – 300N	272	-	479	1,2 (90°)
Ghent Knee Rig	Experimental in-vitro Dynamic F_q: up to 2000N	114	337	-	5,5 (60°)

Table 2. Overview of cadaver experiments

First of all, none of the other studies performed measurements in a weight bearing situation, and only in the study by Bohnsack et al. measurements were performed under dynamic conditions. Compatring the contact areas, it can be observed that the contact areas at 30° knee flexion in both our and Bohnsack's study are smaller. Maybe this can be explained by the test circumstances, a dynamic versus a static test setup. A wider variation can be seen in the intra articular patellofemoral pressure. The intra articular pressures found in current work seem to be greater than those found by other investigators. A possible explanation for this phenomenon are the substantially greater forces applied on the quadriceps tendon in the current study, which might result in larger intra articular pressures.

Due to different test setups, it remains difficult to compare different studies with each other. In addition, a limited number of knees are presented in this study and further work is necessary, however, the general trends that are found in biomechanical research of the patellofemoral joint by previous work, can be seen in the results of current work as well.

5   CONCLUSIONS

Analysis of these data shows that there is consistency of previous findings reported in the literature and our findings. It has also been proven that good quality cadaveric knees tested in the Ghent Knee Rig can provide us with reproducible results. It must be noted, however, that in the in-vivo patellofemoral joint, the investigated variables can't be considered as independent but should be seen as a complex related unit that interacts in a way that is still not fully understood.

Thanks to the repeatability and reliability of the designed test rig, it offers great potential for the research on pathological knees. Post-mortem knees can now be used on the Ghent Knee Rig to gain information about different kinds of morphological abnormalities of the knee and subsequently different kinds of treatments already used in surgery, but not yet fully understood. Final goal of this project is to better understand the biomechanical influence of knee abnormalities and their treatments, in order to provide an optimal and more objective approach in orthopedics.

6   REFERENCES

[1] J. Quintelier, F. Lobbestael, P. Verdonk, P. De Baets, F. Almqvist, *Patellofemoral contact pressures*, Acta of Bioengineering and Biomechanics, 10(2):23-28, 2008

[2] J. Bellemans, *Biomechanics of anterior knee pain*, Knee 10(2):123-126, 2003

[3] J.J. Mason, F. Leszko, T. Johnson, R.D. Komistek, *Patellofemoral joint forces*, Journal of Biomechanics, 41(11):2337-2348, 2008

[4] J. Insall, K.A. Falvo, D.W. Wise, *Chondromalacia Patellae. A prospective study*, Journal of Bone and Joint Surgery Am., 58(1):1-8, 1976

[5] R. Minkowitz, C. Inzerillo, O.H. Sherman, *Patella instability*, Bull NYU Hosp Jt Dis., 65(4):280-293, 2007

[6] A.B. Zavatsky, *A kinematic-freedom analysis of a flexed-knee-stance testing rig*, Journal of Biomech*anics, 30(3):277-280, 1997

[7] S. Ostermeier, M. Holst, C. Hurschler, H. Windhagen, C. Stukenborg-Colsman, *Dynamic measurement of patellofemoral kinematics and contact pressure after lateral retinacular release: an in vitro study*, Knee Surgery, Sports Traumatology, Arthroscopy,15(5):547-554, 2007

[8] A.A. Amis, W. Senavongse, A.M. Bull, *Patellofemoral kinematics during knee flexion-extension: an in vitro study*, Journal of Orthopaedic Research, 24(12):2201-2211, 2006

[9] H.H. Huberti, W.C. Hayes, *Patellofemoral contact pressures. The influence of q-angle and tendofemoral contact*, Journal of Bone and Joint Surgery Am., 66(5):715-724, 1984

[10] D.S. Hungerford, M. Barry, *Biomechanics of the patellofemoral joint*, Clinical Orthopaedic and Related Research, (144):9-15, 1979

[11] A.B. Zavatsky, A *kinematic-freedom analysis of a flexed-knee-stance testing rig*, Journal of Biomechanics, 30(3):277-280, 1997

[12] N.J. Dahlkvist, P. Mayo, B.B. Seedhom, *Forces during squatting and rising from a deep squat*, Eng Med. 1982;11(2):69-76.

[13] J.J. Elias, D.R. Bratton, D.M. Weinstein, A.J. Cosgarea, *Comparing two estimations of the quadriceps force distribution for use during patellofemoral simulation*, Journal of Biomechanics, 39(5):865-872, 2006

[14] D.R. Wilson, M.V. Apreleva, M.J. Eichler, F.R. Harrold, *Accuracy and repeatability of a pressure measurement system in the patellofemoral joint,* J Biomechanics, 36(12):1909-1915, 2003

[15] S. Ostermeier, M. Holst, C. Hurschler, H. Windhagen, C. Stukenborg-Colsman, *Dynamic measurement of patellofemoral kinematics and contact pressure after lateral retinacular release: an in vitro study,* Knee Surgery, Sports Traumatology, Arthroscopy 15(5):547-554, 2007

[16] H.J. Hehne, *Biomechanics of the patellofemoral joint and its clinical relevance,* Clinical Orthopaedics and Related Research, (258):73-85, 1990

[17] Goodfellow J, Hungerford DS, Zindel M., *Patello-femoral joint mechanics and pathology. 1. Functional anatomy of the patello-femoral joint*, Journal of Bone and Joint Surgery Br., 58(3):287-290, 1976

[18] T. Luyckx, K. Didden, H. Vandenneucker, L. Labey, B. Innocenti, J. Bellemans, *Is there a biomechanical explanation for anterior knee pain in patients with patella alta?: influence of patellar height on patellofemoral contact force, contact area and contact pressure*, Journal of Bone and Joint Surgery Br., 91(3):344-350, 2009

[19] L.S. Matthews, D.A. Sonstegard, J.A. Henke, *Load bearing characteristics of the patello-femoral joint,* Acta Orthopaedica Scandinavica, 48(5):511-516, 1977

[20] R.P. Csintalan, M.M. Schulz, J. Woo, P.J. McMahon, T.Q. Lee, *Gender differences in patellofemoral joint biomechanics*. Clinical Orthopaedics and Related Research, (402):260-269, 2002

[21] M. Bohnsack, P. Klages, C. Hurschler, A. Halcour , A. Wilharm, S. Ostermeier, O. Ruhmann, C.J. Wirth, *Influence of an infrapatellar fat pad edema on patellofemoral biomechanics and knee kinematics: a possible relation to the anterior knee pain syndrome*. Archives of Orthopaedic and Trauma Surgery, 129(8):1025-30, 2009.

[22] T.M. Melegari, B.G. Parks, L.S. Matthews, *Patellofemoral contact area and pressure after medial patellofemoral ligament reconstruction*. Am. Journal of Sports Medecine, 36(4):747-752, 2008

Morning Session 2

Chairman:
Stijn Hertelé, Laboratory Soete, Ghent University, Belgium

DYNAMIC SPINE SIMULATOR: DESIGN AND CONSTRUCTION

W. Allaert[1], J. Quintelier[2], A. Van Haver[1]

[1] Hogeschool Gent (HoGent)
[2] Ghent University, Laboratory Soete, Belgium

No paper was received for this contribution.

FRICTION WELDING OF CERAMICS TO METALS

D. Bonte[1], B. Derynck[1], P. De Baets[1], W. De Waele[1] and K. Faes[2]

[1] Ghent University, Laboratory Soete, Belgium
[2] Belgian Welding Institute, Belgium

Abstract This paper discusses the progress in a master thesis about friction welding of ceramics to metals. An existing friction welding machine has to be adapted for the experimental part of this research. The required capabilities of this machine are discussed in this paper. As an introduction, a general explanation about friction welding is given. The results of a literature survey on friction welding of ceramics to metals are discussed. The aim of this survey was to determine the process parameters required to obtain a good weld quality. It became clear that few literature exists on friction welding of these materials and that the cited values for the process parameters vary widely. Based hereon, a range of process parameter values was used to make certain design choices. Because a laboratory machine is aimed at, it has to be able to function at varying settings of the process parameters, including testing at higher rotational speeds. Finally, process windows illustrating sound combinations of friction pressure and specimen diameter are calculated. The design choices entail certain restrictions on the capabilities of the machine. These restrictions define the boundaries of the process windows.

Keywords friction welding, ceramics, metals, machine design

1   INTRODUCTION

The final goal of this research is joining ceramics to metals using the rotational friction welding process. Rotational friction welding is a forge welding process in which the necessary heat is generated as a result of the friction forces between two surfaces. These surfaces are rotated against each other under axial pressure. When sufficient heat is generated, the rotating part is stopped and a forge pressure is applied. In figure 1 the main parameters of the friction welding process are displayed as a function of time.
Friction welding is a process that can be easily automated. It can be used to join different materials that cannot be welded with conventional welding processes. Furthermore, friction welding also results in a smaller heat affected zone because of the smaller heat input.
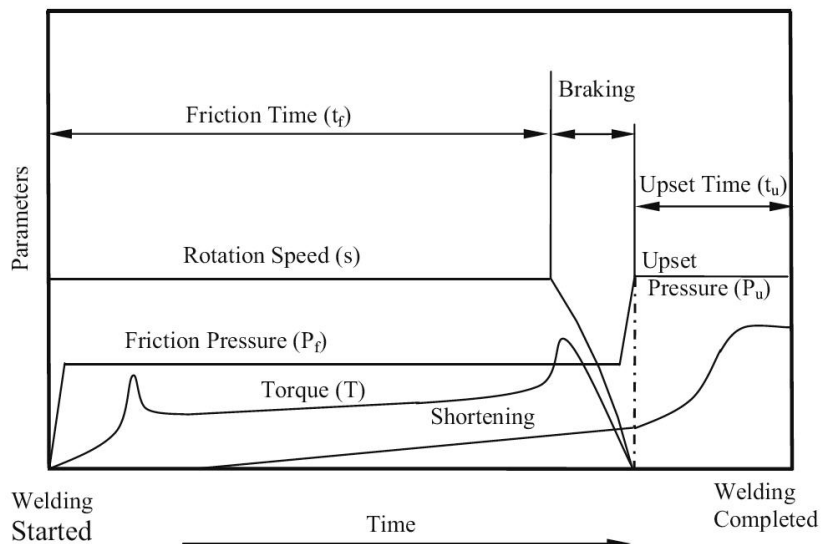
Figure 1: Friction welding process [1]

For this research, an existing friction welding machine has to be redesigned to meet the required settings of the process parameters. This work includes making some important design choices and developing process windows.

2 PROCESS PARAMETERS

2.1 Literature on friction welding parameters

In the last decades, quite a lot research effort has been made to tackle the different parameters that determine a good weld. However, this research mainly focused on the 'conventional' steel-steel shaft or tube connections. *The rotational speed, the axial force* during the friction and forging phases and the duration of the *friction and forging periods* are the major values that affect the behaviour during the weld cycle and the resulting weld quality. The speed is mostly represented by the circumferential speed at the outer diameter of the cylindrical specimen.

During a short literature survey, it was soon found that research on welding of ceramics to steel or copper by friction welding is very restricted. Based on the information from about twenty references [2-27], the following observations can be made:

1. Friction welding of ceramics to metals has not yet been addressed frequently.
2. The experiments that were conducted, were mainly performed with laboratory-scale samples (10 – 30 mm diameter).
3. A frequently used ceramic material is Al_2O_3 (can be considered the exemplary material to experiment with), sometimes with the use of an aluminium interface layer to facilitate the bonding process.
4. Circumferential speeds vary between 0,5 and 2,5 m/s, with a peak value of 7,55 m/s (for joining Al_2O_3 to aluminium).
5. The friction duration varies from 1 to 10 seconds, the forging duration is typically a bit longer.
6. Friction and forging (axial) pressures vary in a wide range. They are usually determinative to get an allowable weld quality for a specific situation.

The following general conclusions can be formulated:

1. With materials like Cu and Al, higher rotational speeds are required than with steel specimens [2]. This can be explained by the higher heat conduction in Cu and Al in comparison with steels. The temperature increase needed to achieve a weld, requires a faster heat input (same amount of energy in shorter time) to compensate the heat sink by conduction. Since the machine has to be as versatile as possible, this will be taken into account during the design.
2. Since friction and forging forces vary in the examined literature, it will be required to vary them and to investigate their relationship with the friction torque. These values need to be measured during the weld cycle.

2.2 The machine constraints

The Belgian Welding Institute acquired a friction welding machine in the late 1960's (Thompson Friction Welder 40 ton). The 40 ton refers to the axial force of 400 kN that can be delivered by the main cylinder. The machine was able to produce friction welds at 4 different speeds, between 500 and 2000 rpm. The friction welder had a 30 kW motor and was capable of welding rods up to 50 mm diameter and tubes up to 80 mm.

The machine has been adapted several times in order to make other test situations possible. The last upgrade was in 2000-2001, when a 160 kW electric motor with a frequency inverter was installed, to make medium-scale tube friction welds possible. In this configuration the machine was able to weld tubes up to 5'' (outer diameter 141 mm) at a speed of max. 300 rpm.

2.3 The friction welder in 2009-2010

In the machine upgrade for this master thesis, the achievable speed is a determining issue. A circumferential speed up to 8 m/s has to be achieved to get more insight in the influence of rotational speed on weld quality, especially in the case of welding copper or aluminium. After some calculations and comparisons, it was concluded that the rotational speed should be maximum 4000 rpm. This is an important requirement, making the use of some of the original components impossible. Furthermore, the 160 kW motor is to be used, because of the variable speeds that can be delivered by the frequency inverter. The axial hydraulic cylinder will be a minor issue; the original one is practically sufficient for all welding conditions. Further design considerations are explained later.

3 DESIGN CHOICES

To meet the process parameters discussed above, the existing friction welding machine has to be adjusted. In particular the combination of a high rotational speed, a high force and a low price is a challenging combination.

This entailed multiple design choices and several alternatives for the different functions were examined, see table 1.

Power Transmission	Timing belt	V-belt	Chain	Gearbox	Push belt
Speed Control	Frequency control	Continuously Variable Transmission			
Clamping	Hydraulic power chuck	Manual chuck	Clamping Bush		
Bearings	Tapered roller bearing	Spherical roller thrust bearing	Hydrodynamic bearing	Plain bearing	Hybrid bearing
Belt Tensioning	Gravity	Sideways tilting of motor	Slide rail	Tension idler	Lifting the motor
Torque Measuring	Torque sensor	Load cell			

Table 1: Design Choices

For the *power transmission* a timing belt was chosen. Strong advantages exist in comparison to the other alternatives. A timing belt is able to transmit the required torque and is more affordable than a gearbox. Chains have a lot of resonating frequencies leading to vibrations and noise, especially combined with a variable speed. A timing belt is also a slip free transmission which assures an accurate speed measurement.

For the *speed control,* the frequency inverter is used because this component was already available on the existing machine.

For the *clamping*, a manual chuck was chosen. The price is much lower than for a hydraulic chuck, and it has a lot more flexibility in possible clamping diameters than a clamping bush.

The *bearings* must be able to rotate at both low and high speeds (400 to 4000 rpm) and sustain a heavy axial load (400 kN). A combination of a spherical roller thrust bearing and a spherical roller bearing is chosen. Spherical roller thrust bearings can sustain a very high axial load, combined with a radial load. The spherical roller bearing will be mounted such that it is able to slide in the direction of the axial load. As a result it does not need to resist any of the friction and forging force, only the light pretension load.

For the *tensioning* of the timing belt, an idler wheel is selected. This induces additional bending of the belt but is the easiest way of tensioning, knowing that the electrical motor weighs too much to be used for tensioning.

For the *torque measurement,* a torque sensor is added, again because of design simplicity. A load cell would require a lever at the non-rotating side. Also the non-rotating clamping unit should then be able to rotate.

A more detailed overview of the advantages and drawbacks of each alternative can be found in appendix 1. By means of illustration, a 3D-view of the future machine is presented in figure 2.
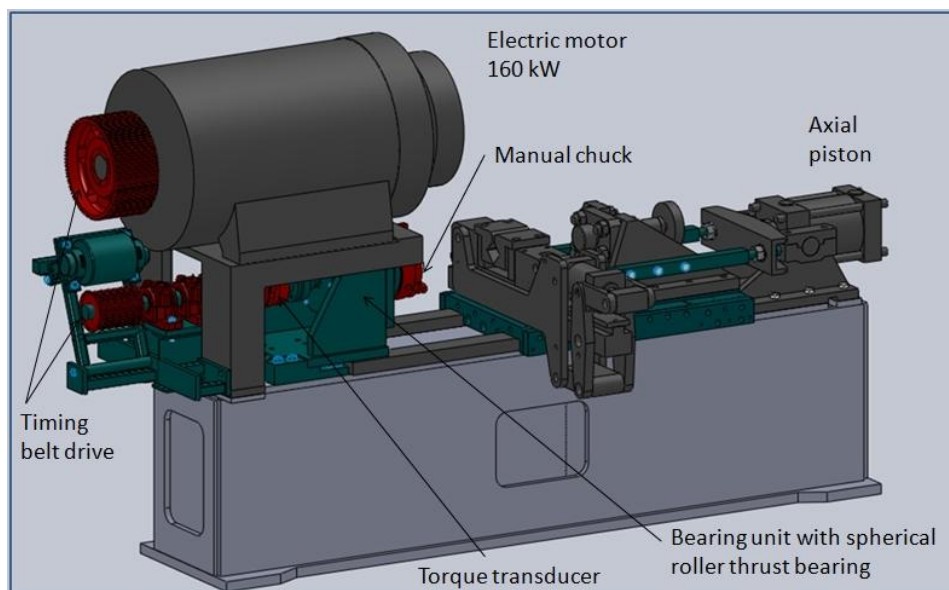
Figure 2: 3D view of the future adjustments of the friction welder

4 PROCESS WINDOW

As described above, machine components were selected to achieve a range of possible parameter settings. Also an overview of the machine capabilities was given. In an attempt to visualize these capabilities, a process window is constructed (see figures 3 and 4). By choosing a specimen geometry (rod or tube) and dimension (diameter), one can read from the graphs in what range the initial friction pressure can be varied.

In figure 3 the process window for a rod is shown. The green shaded area displays the allowable welding conditions for creating a weld. The sound area is bounded by 6 curves. The purpose of each one is described below.
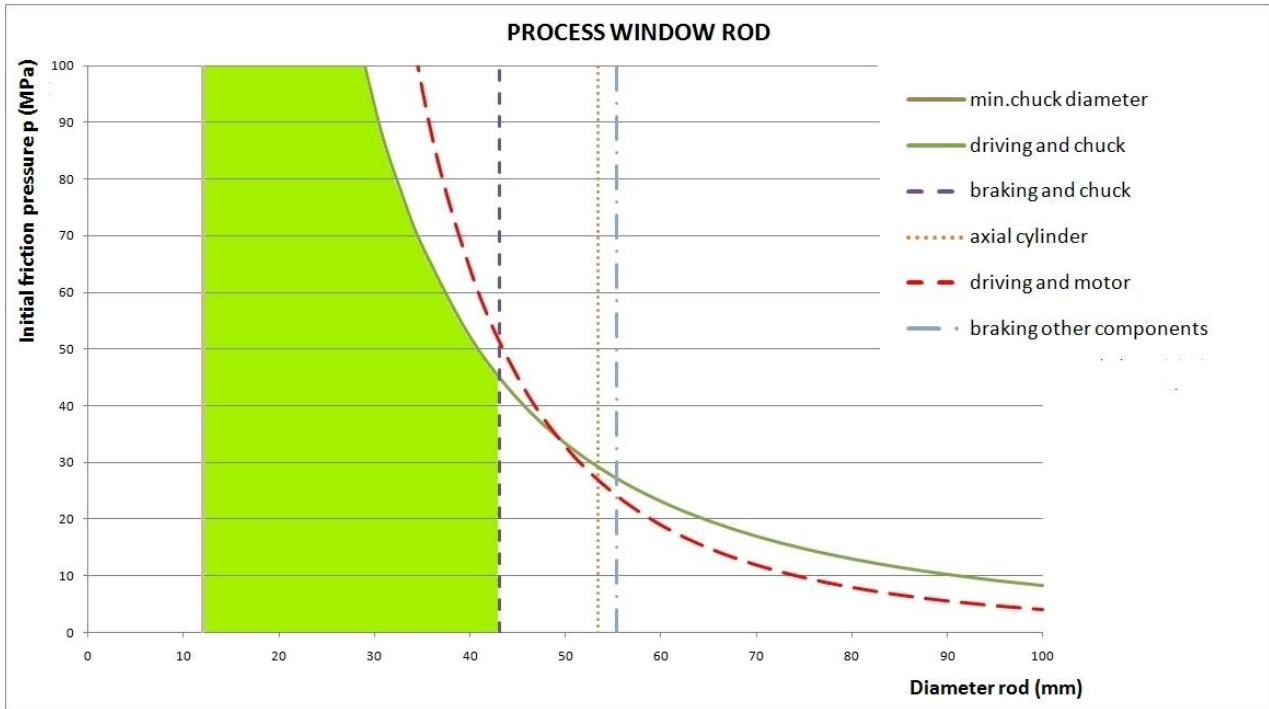
Figure 3: Process window for a rod

1. Minimum chuck diameter – *vertical solid line*
   The minimum component diameter to clamp in the selected chuck is 12 mm.

2. Driving and chuck – *hyperbolic solid line*
   It has to be prevented that the specimen slips in the chuck jaws during the friction phase. This condition can be expressed by a simple friction torque equation, and be solved as $p \sim 1/R^2$:

$$M_{chuck} = F_{chuck}\, \mu_{chuck}\, R = M_{friction\ weld} = \frac{2\pi}{3}\, \mu_{ini}\, p\, R^3 \qquad (1)$$

3. Braking and chuck – *vertical dashed line*
   Also while braking, the specimen is not allowed to slip in the chuck jaws. The same formula (1) applies, but now the contact pressure *p* is assumed to be 100 MPa. A specific value for the maximum outer radius is obtained, independent of the initial friction pressure.

4. Axial cylinder – *vertical dotted line*
   The maximum axial force produced by the hydraulic cylinder limits the maximum contact surface (and according diameter of the rod) that can be friction welded (A maximum friction pressure of 100 MPa is assumed to be reached in every weld at the end of the friction period).

$$p = \frac{F_{cylinder}}{A} \Rightarrow A_{max} = \frac{F_{cylinder}}{100\ MPa} \Rightarrow R_{max} \qquad (2)$$

5. Driving and motor – *hyperbolic dashed line*
   The electric motor can deliver a maximum torque of 1076 Nm to the weld (calculated after speed increase). This value is compared to the friction torque, and gives a relationship $p \sim 1/R^3$:

$$M_{motor,max} = 1076\ Nm = M_{friction\ weld} = \frac{2\pi}{3}\, \mu_{ini}\, p\, R^3 \qquad (3)$$

6. <u>Deceleration of other components</u> – *vertical dash-dot line*
Deceleration can be a dangerous situation for some other components as well. Normally, the motor is braking the weld. But the solidifying weld can cause a huge torque, which is able to exceed the motor braking torque. In that case the weld is braking the motor! If the weld braking torque would be excessive (when it exceeds 2000 Nm), other components like the belt and the torque transducer could be damaged. To prevent problems, either the diameter of the weld specimen has to be limited, or a safety device must be incorporated.

Similar curves can be calculated for tubular specimens. In figure 4 a process window for a tube is presented; here we assumed the tubes to have a wall thickness proportional to their outer radius.
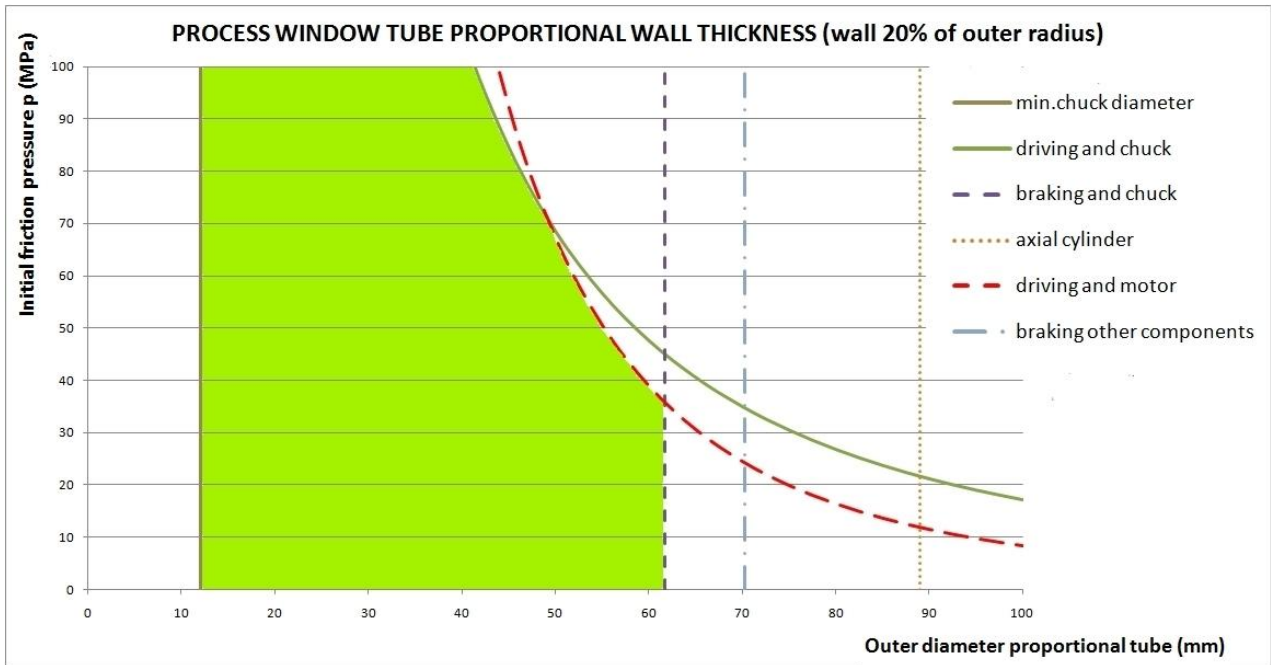
Figure 4: Process window for a tube (wall thickness proportional to outer radius)

5   CONCLUSIONS

This paper presents the progress of a master thesis about friction welding of ceramics to metals. Since an existing friction welding machine has to be redesigned and rebuild, the determination of the necessary capabilities of the future machine is an issue addressed in this paper.

A literature survey was conducted to find the determining process parameters and to obtain common ranges of values for them. Few literature on the subject of friction welding of ceramics to metals was found and the reported parameter settings showed a lot of variability.

Secondly, this range of process parameter settings was used to make certain design choices. Since a laboratory machine is aimed at, it has to be able to operate at both low and high speeds, with varying torques and axial loads. This leads to the design solution with a spherical roller thrust bearing, a timing belt drive and a torque transducer as the main new machine components.

Finally, process windows showing allowable combinations of friction pressure and specimen diameter were calculated. The design choices entail certain restrictions on the testing possibilities of the machine, which are represented by the boundaries of these process windows. These graphical representations allow to verify at a glimpse if a specimen can be welded.

6   NOMENCLATURE

M	torque	Nm	F	force	N
p	pressure	Pa	R	radius	m
A	surface	m^2	μ	Coefficient of friction	-

7   ACKNOWLEDGEMENTS

8   REFERENCES

[1] M. Sahin, *Joining of stainless-steel and aluminium materials by friction welding* The International Journal of Advanced Manufacturing Technology, 41 (5-6), 487-497, 2009.

[2] B. Humphreys, *A practical guide to friction welding*, Thompson Friction Welding Ltd., 1998.

[3] Ates, H., Turker, M., & Kurt, A.. Effect of friction pressure on the properties of friction welded MA956 iron-based superalloy. Materials and Design, 28 , pp. 948-953, 2007.

[4] Brogle, E., Staubli, M., Nazmy, M. Y., & Gausmann, D. Patent: Friction welding of γ-titanium-aluminide to steel body with nickel alloy connecting piece there between, 2006.

[5] Duffin, F., & Bahrani, A. *Friction welding of mild steel: the effects of varying the value of deceleration.* Metal Construction and British Welding Journal, pp. 125-132, 1973.

[6] Duffin, F., & Bahrani, A. *The deceleration phase in friction welding of mild steel.* Welding Research International, 6 (1), pp. 1-19, 1976.

[7] Fauzi, M. A., Uday, M., Zuhailawati, H., & Ismail, A. *Microstructure and mechanical properties of alumina- 6061 aluminium alloy joined by friction welding.* Materials and design, Accepted manuscript, 2009.

[8] Hascalik, A., & Orhan, N. Effect of particle size on the friction welding of Al2O3 reinforced 6160 Al alloy composite and SAE 1020 steel. Materials and Design 28, pp. 313-317, 2007.

[9] Inkson, B., & Threadgill, P. *Friction welding of FeAl40 Grade 3 ODS alloy.* Materials Science and Engineering A258, pp. 313-318, 1998.

[10] Kanayama, K., Tasaki, Y., Machida, M., Kume, S., & Aoki, S. *Joining of ceramics by friction welding.* Transactions of the Japan Welding Society, 16 (1), 95-96, 1985.

[11] Keat, Y. C., Jamaludin, S. B., & Ahmad, Z. A. The effect of varying process parameters on the microhardness and microstructure of Cu-steel and Al-Al203 friction joints. Jurnal Teknologi, University Teknologi Malaysia 41(A), pp. 85-95, 2004.

[12] Kobayashi, A., Machida, M., Matsuda, T., & Nishiwaki, N. *Study on the initial torque characteristics of friction welding.* IIW Database, Doc. No. III-1150-00, pp. 1-9, 2000.

[13] Li, Z., Maldonado, C., North, T., & Altshuller, B. *Mechanical and metallurgical properties of MMC friction welds.* Welding Research supplement, pp. 367s-373s, 1997.

[14] Lin, C., Mu, C., Wu, W., & Hung, C. The effect of joint design and volume fraction on friction welding properties of A360/SiC (p) composites. Welding Research supplement, pp. 100s-108s, 1999.

[15] Lindemann, Z., Skalski, K., Wlosinski, W., & Zimmerman, J. *Thermo-mechanical phenomena in the process of friction welding of corundum ceramics and aluminium.* Bulletin of the Polish Academy of Sciences; Technical Sciences 54-1, pp. 1-8, 2006.

[16] Midling, O., & Grong, O. *Continuous drive friction welding of SiC-particulate reinforced aluminum composites.* International Trends in Welding, Science and Technology, ASM International, (pp. 1147{1151), 1993.

[17] Mohamad, Z. N., Luay, B. H., & Zainal, A. A. *Alumina-mild steel friction welded at lower rotational speed.* Journal of materials processing technology 204, 279-283, 2008.

[18] Nakamura, K., & Nakahara, S. Study on friction welding - Torque in frictional process and optimum welding conditions for plain carbon steels. The Government Mechanical Laboratory of Japan, pp. 1-18, > 1965.

[19] Ochi, H., Yamamoto, Y., Kawai, G., & Suga, Y. *Tensile strength of friction welded joints of copper alloys to steels.* Proceedings of the Eighteenth (2008) International Offshore and Polar Engineering Conference, Vancouver (Canada), pp. 272-276, 2008.

[20] Ozdemir, N., Sarsilmaz, F., & Hascalik, A. Effect of rotational speed on the interface properties of friction-welded AISI 304L to 4340 steel. Materials and Design 28, pp. 301-307, 2007.

[21] Shin, H.-S., Jeong, Y.-Y., Choi, H.-Y., Kato, H., & Inoue, A. *Joining of Zr-based bulk metallic glasses using the friction welding method.* Journal of Alloys and Compounds 434-435, pp. 102-105, 2007.

[22] Sketchley, P. D., Threadgill, P., & Wright, I. *Rotary friction welding of an Fe$_3$Al based ODS alloy,* 2000. URL: http://www.twi.co.uk/j32k/protected/band_8/sppdsjuly2000.html

[23] Sketchley, P. D., Threadgill, P., & Wright, I. *Rotary friction welding of an Fe$_3$Al based ODS alloy.* Materials Science and Engineering, A329-331 , pp. 756-762, 2002.

[24] Voiculescu, I. The behaviour of aluminium matrix composites in welding processes, > 1997.

[25] Weiss, R. Residual stresses and strength of friction welded ceramic/metal joints. Welding research supplement, pp. 115s-122s, 1998.

[26] Yilbas, B. S., Sahin, A. Z., Kahraman, N., & Al-Garni, A. Z. *Friction welding of St-Al and Al-Cu materials.* Journal of Materials Processing Technology 49 , pp. 431-443, 1995.

[27] Zimmerman, J., Wlosinski, W., & Lindemann, Z. R. *Thermo-mechanical and diffusion modelling in the process of ceramic-metal friction welding.* Journal of Materials Processing Technology 209 , pp. 1644-1653, 2009.

9 APPENDIX: DESIGN TABLE

	TIMING BELT	V-BELT	CHAIN	GEARBOX	PUSH-BELT
A. Power Transmission	TIMING BELT +Slip free +Affordable -More Noise than V-belt -Less noise than chain	V-BELT +Less noise -Slip -Large number of belts	CHAIN -Resonating frequencies -Noise and vibrations	GEARBOX +High efficiency +Slip free -Expensive	PUSH-BELT Combined with CVT -Small power
B. Speed-control	FREQUENCY CONTROL +Already present +Large speed range -Field weakening	CVT Combined with push-belt			
C. Clamping	HYDRAULIC CHUCK +High clamping force +Less labor intensive +High flexibility in diameters -Expensive	MANUAL CHUCK +No push-bar (more compact) +High flexibility in diameters -Less clamping force then hydraulic	CLAMPING BUSH +Cheap -Labor intensive -Limited amount of diameters		
D. Bearings	TAPERED ROLLER + Less expensive then spherical -Short lifetime (high force)	SPHERICAL ROLLER THRUST +Large axial force allowable +Self aligning -Expensive -Restricted rotational speed	HYDRODYNAMIC +High rotational speed +Large axial force -Low rotational speed not possible	SLIDING BEARING -More friction -Low pv-limit	HYBRID BEARING +High rotational speed -Expensive
E. Belt tensioning	GRAVITY +Using weight of motor -Practical realisation	SIDEWAYS TILTING OF ENGINE +Alignment of belt -Weight of motor	SLIDE RAIL +Alignment of belt -Weight of motor	TENSION IDLER +Alignment of belt -Extra belt bending	LIFTING THE MOTOR -Alignment of belt -Weight of motor
F. Torque-measuring	TORQUE SENSOR +Easy to implement -Expensive	LOAD-CELL +Less expensive -Complex			

MAGNETIC PULSE WELDING

Jan Broeckhove[1], Len Willemsens[1], Koen Faes[2], Wim De Waele[1]

1 Ghent University, Laboratory Soete, Belgium
2 Belgian Welding Institute, Belgium

Abstract   The contemporary construction industry is evolving with a rapid pace and is pushing technological boundaries. Together with that progress new requirements on joints and joining techniques are imposed. This paper describes our research concerning an advanced joining technique, the Magnetic Pulse Welding process (MPW).
The first part of this article briefly describes the MPW process and summarizes the differences with respect to conservative welding techniques. Secondly an analytical model of the process will be investigated on accuracy. This model was developed by the manufacturer of the MPW machine used at the Belgian Welding Institute. Further a description is given of the methods which are used to investigate the experimental joints. After describing the recently performed experiments, finally an overview will be given depicting the work that will be carried out during the rest of this master thesis.

Keywords Magnetic Pulse Welding, MPW, analytical model, testing methods, experiments

1   INTRODUCTION

1.1   The principle

Magnetic Pulse Welding is a cold welding process which uses high velocity impact to join two parts. The process can be compared to explosion welding but using magnetic force to accelerate the object instead of explosives. Unlike conventional welding processes no melting is involved and thus no major changes in material properties take place. The working principle is based on the theory of the Lorentz force, dictating that an electrically charged particle, moving in a magnetic field, undergoes a force normal to the direction of the magnetic field and to the direction of movement:

$$F = q \, (\vec{v} \, x \, \vec{B}) \tag{1}$$

With: F is the force (in Newton), q is the electric charge (in coulombs), B is the magnetic field (in Tesla) and v the speed of the particle (in m/s). The force exerted by an electric field has been neglected since no significant electric field will be present in this application.
The main components of the welding machine can be schematically depicted as shown in Figure 1 .
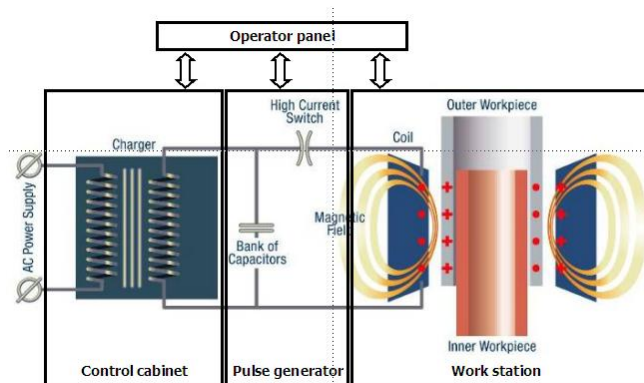
Figure 1: System schematic [1]

First a bank of capacitors is charged to an energy level chosen by the operator. Once the bank is fully charged the high current switch can be closed, sending a current through the coil. This current will induce a magnetic field in the coil. To concentrate the magnetic field in the desired region, a field shaper is placed inside the coil. The changing magnetic field will induce eddy currents in the outer work piece, also named the flyer tube. Further due to the shielding effect of an electrical conductor the flyer tube will prevent the

magnetic field of passing through. So considering the Lorentz Force, the magnetic field outside the flyer tube will exert a force on the flyer tube due to the eddy currents, thrusting the tube inward in radial direction. The high velocity of the inward motion and thus the high-energy impact between outer and inner work piece will result in a cold weld.

1.2   MPW versus conservative welding techniques

The main advantages of MPW can be summarized as follows: [1] [2]
- Since it is a cold welding process no heat affected zone, HAZ, is present. All original material properties reached by heat treatment or not, are maintained.
- It enables the possibility of joining dissimilar materials.
- No preparation of the parts is required. The parts do not have to be cleaned or degreased.
- No post weld finishing or cleaning has to be carried out.
- Possibility of a high degree of automation.

Its main disadvantages are:
- Only electrically conducting materials can be used as flyer material.
- The parts must overlap to generate the joint.

2   THEORETICAL CONSIDERATIONS

2.1   Analytical model

An analytical model is essential to gain insight in the parameters governing the MPW process, and to make a quick estimation of the required value of these parameters to obtain a successful weld. However it is not straightforward to develop an accurate set of equations that is able to accurately model the MPW process. The discharge current is a damped sinusoidal wave, which results in a time-dependent magnetic pressure. If a field shaper is used to increase the amplitude of the magnetic field, the pressure will theoretically be a function of axial and circumferential position, as well as time. Furthermore, complex deformation behaviour of the tubular work-pieces and high speed deformation both add to the problem of finding equations that have reasonable accuracy, as well as sufficient simplicity.

2.1.1   Pulsar model

We investigated an analytical model developed by the manufacturer of the welding machine (Pulsar), which should allow users to choose the process parameters needed to attain a good weld. The structure of this model is essentially correct. However, a multitude of simplifications result in decreased accuracy of the model.

The collision velocity, v_c, is first chosen depending on the materials. Considering the analogy between MPW and explosion welding, this data can be derived from experiments carried out with EW. [3] [4] An example is given in Figure 2: values for the impact velocity and collision angle should be chosen from a point in the shaded area to obtain a successful weld. The required acceleration can then be calculated, under the assumption that the velocity increases linearly from zero to v_c when travelling a distance equal to the stand-off distance, the distance between the flyer tube and the inner work piece.
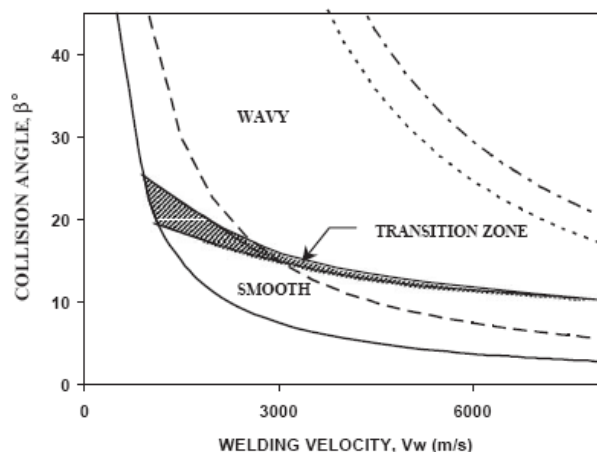
Figure 2: Example of a weldability window for EW (Al to Al joint) [3]

Next, the required pressure (exerted on the flyer tube) can be found as the sum of two components: the pressure to accelerate- and the pressure to deform the flyer tube. This pressure is exerted by the magnetic field, so a numerical value for this magnetic field can be obtained. Finally, through electrical circuit analysis, the required voltage stored by the capacitors is found.

Before further discussing the inaccuracies of the studied model, some analytical concepts are discussed.

2.1.2   RLC circuit

The electrical discharge circuit can be modelled as an RLC circuit. In this electrical circuit, *C* represents the total capacitance of the capacitor bank, *R* the equivalent resistance electrical circuit (circuit wires, coil and work piece) and *L* the equivalent inductance (circuit, coil, field shaper and work piece).
Circuit analysis shows that the discharge current is an exponentially damped sine wave (shown in Figure 3) represented by the following equation:

$$i(t) = \frac{V_0}{\omega_C L} \ e^{-\xi.t} \ \sin(\omega_C t) \tag{2}$$

In this equation, V_0 is the voltage to which the capacitor bank is charged, ω_c is the natural frequency of the circuit, *t* is the elapsed time and ξ is a damping factor. As ξ and ω_c are both functions of R, L and C, these three parameters *(R,L and C)* govern the entire circuit.
The value of *C* is a multitude of the capacitance of a single capacitor (the multitude equals the number of capacitors charged) [5] [6]. *R* and *L* are in reality *not* constant. Especially *L* shows a significant variation due to the field shaper and/or when the geometry of the work piece changes. For example an increase in the radial distance between the flyer tube and the field shaper will increase *L*, resulting in a lower amplitude of the discharge current. Consequently, the inductance is not constant during the welding process: compression of the flyer tube increases the radial distance and decreases *L*. These effects are neglected in order to keep the model simple enough to be applicable. [7] [8]

A current measurement as further described in **Error! Reference source not found.** can be used to determine the value of the resistance and the inductance. Given the measured current ω_c and ξ can be extracted. The equations defining ξ and ω_c then allow calculating *R* and *L*. When using a single MPW machine, an effective method would be to perform current measurements for a set of geometries and materials for each field shaper. Using curve fitting techniques, one or more functions could be extracted to model the influence of the above parameters on the value of the equivalent inductance *L*. Once such functions have been determined, a prediction of the current waveform can be made for each set of future experiments. [7]
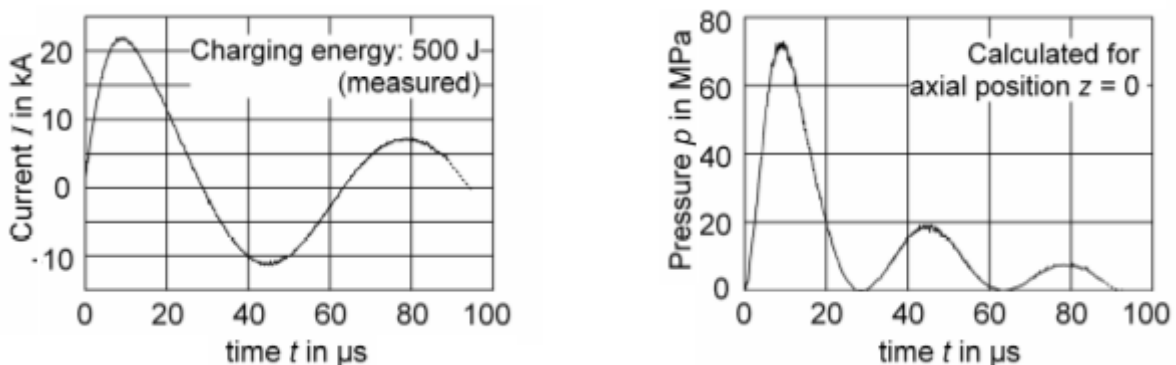
Figure 3: Discharge current and magnetic pressure [9]

2.1.3   Electromagnetic energy transfer

The damped oscillating current through the coil generates an axial transient magnetic field. According to Lenz's law, eddy currents in the work piece will be induced flowing in the opposite direction to its cause.
As a result, an electromagnetic force acts on the flyer tube, which is accelerated away from the coil and collides rapidly with the inner tube.

The magnetic pressure p exerted on the flyer tube is determined by the energy density of the magnetic field outside H_0 and inside H_i of the work piece and can be calculated on the basis of the (measured) coil current by equation 3 (where μ is the magnetic permeability) [9].

$$p = \frac{1}{2} \mu \, (H_0{}^2 - H_i{}^2) \qquad (3)$$

The pressure waveform is also shown in Figure 3. It should be noted that in this equation H is dependent of time, axial and radial position. The magnetic field between the coil and the flyer tube differs from that between the flyer tube and the inner tube, due to the shielding effect. Quantification of the skin depth δ, simplifies the expression for the magnetic pressure to the form of equation 4 [10].

$$p = \frac{1}{2\mu} B_0 (1 - e^{2T/\delta}) \quad \text{with } \delta = \sqrt{2/\omega\kappa\mu} \qquad (4)$$

These equations are valid for coils but do not take into account the effects of a field shaper, used to increase the amplitude of the magnetic field in a small region where welding will take place [11].

If it were not for the complex deformation behaviour, an analytical expression for the acceleration as a function of time could be established. Integration would then lead to a time function of velocity and radial displacement. As the stand-off distance is set in advance, a value for the time interval could be obtained and used to estimate the impact velocity consequently. [5]

2.1.4 Conclusions on the analytical modelling of the MPW process
The model proposed by Pulsar is (at this moment) the only analytical model available to describe the entire MPW process. However, after some research it is obvious that several simplifications and assumptions made in this model, limit the accuracy of its predictions.
First of all, the acceleration is assumed to be constant. This would require the magnetic pressure exerted on the flyer tube to be constant. However, this magnetic pressure originates from the damped sinusoidal current through the coil, and is consequently time-dependent.
Further the pressure required for deformation is determined in a simplified way. It is calculated as the pressure for which the yield strength is reached in a thin walled cylindrical tube subjected to radial compression. This formula can solely be used in case of linear elastic deformations and the simplification would suggest that the pressure compresses the entire tube with a radial displacement equal to the stand-off distance. In reality only one end of the tube is plastically compressed, and this at an extremely large deformation speed.

2.2 Numerical simulations

The discharge current and the magnetic field (and pressure) can be modeled analytically with acceptable accuracy. However, the effect of a field shaper (containing a radial slit where consequently B≈0) can only be quantified using finite element modeling techniques. In addition, the complex high speed deformation behavior of the flyer tube leads to complications when estimating the required deformation pressure. Consequently, the MPW process is increasingly being modeled using finite element (FE) methods. [12] [13] [14]

3 EXPERIMENTAL STUDY

Theoretically it is obvious that the simplifications in the analytical model proposed by Pulsar lead to significant inaccuracy. However, due to the absence of more accurate analytical models, there is no clear insight regarding the severity of these inaccuracies. Many corrections are found in literature, but most of them are being used in FE models of the MPW process, so they are essentially not applicable to increase the accuracy of the proposed model. For instance, the acceleration is time dependent and can be estimated using the RLC circuit. Nevertheless, no applicable analytical model can be proposed using these complex time equations. For these reasons, the MPW machine will be instrumented and process parameters measured during experiments to obtain more insight in the process.

3.1 Measurement of process parameters
Measurement of the discharge current is executed by means of a Rogowski coil and a digital oscilloscope. The current waveforms are primarily used to determine a maximum value for the voltage over the capacitor bank (for safety reasons) [15]. In future experiments, the measurements could be used to determine the parameters of the RLC circuit, as explained in section 2.1.2.

Additionally an instrument for measuring the magnetic field has been designed. Narrow tolerances and the fact that the center of the MPW machine is inaccessible during the process prohibit the use of measuring probes which are commercially available. The custom probe shown in Figure 4, had to be designed for the purpose of the magnetic field measurement.

Figure 4: Magnetic field measurement

The probe consists of a cylindrical tube (PVC) and is to be placed around the flyer tube, thus filling the gap between the flyer and the field shaper. The probe tube supports a single turn of copper wire, through which the axial magnetic flux lines will flow. The measurement principle is based on Lenz's Law: the transient magnetic field induces a voltage over the wire of the probe. The voltage can be measured by means of a digital oscilloscope, and the waveform of the magnetic field can be derived.

$$\Phi = B \cdot A \qquad (5)$$

$$V = 2\pi f \cdot \Phi \qquad (6)$$

The probe was calibrated using a Helmholtz coil, which generates a uniform magnetic field. The coil is connected to a current source which sends varying amplitudes of excitation current through the coil. The probe is placed in the center of the coil, and for each amplitude the induced voltage in the probe is measured. The relationship between excitation current and induced voltage, leads to the area of the copper winding (A) in equation 5.

3.2 Welding Experiments

The complicated nature of the MPW process makes it difficult to obtain an accurate analytical or numerical model. One of the objectives of this thesis is consequently to determine relationships between several process parameters and weld quality on an experimental basis. By varying material combinations, stand-off distance, overlap distance, flyer tube thickness, etc. during a large number of welds, the goal is to obtain empirical formulas and/or intervals for the optimal settings of the process parameters.

Up to now, a preliminary series of twenty copper (flyer tube) - aluminum weld tests was executed. In the experiments the flyer tube thickness was kept constant. The overlap length, stand-off distance and the voltage over the capacitor bank were varied. Based on the limited number of tests performed, no general conclusions could be drawn so far.

The welded tubes were first subjected to a leak test (section 3.3) and the apparently most successful welds were selected. These selected joints were then examined in more detail using microscopic evaluation. This is in fact a destructive testing method, because the tubes have to be cut through in the axial direction.
After cleaning both parts, they are embedded in epoxy resin and polished in several steps, to attain a clean and smooth surface. On copper-aluminum welds the polishing has to be carried out very carefully, as both metals are relatively soft and scratch easily (which affects the image quality).
The polished surface is then placed under a microscope, enabling visual inspection of the weld in levels up to micrometers. The images obtained will show whether the two materials are connected and/or whether metallurgical/physical changes have taken place. Expected phenomena include the formation of an intermetallic layer and a wave pattern.

An example of a microscopic image is shown in Figure 5. This image shows a connection that was properly welded. The two materials are joined together and an intermetallic layer was formed.
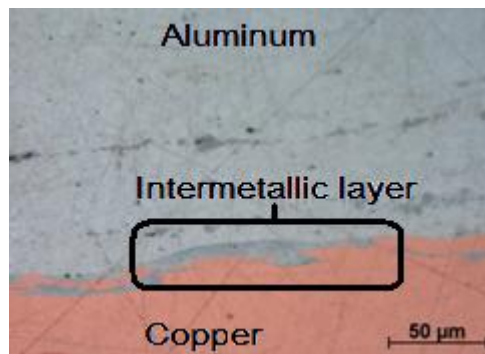
Figure 5: Microscopic image of a copper-aluminium MPW weld

3.3   Non Destructive Testing (NDT)

A simple leak test was developed in order to evaluate the welded tubes in a non-destructive manner. For several applications the most important requirement of the weld joining two tubes is that the connection does not leak. In this test the parts are connected to a source of pressurized air and are checked for leakage.

The welded tubes are connected to a pressurized air circuit, using a custom made connection, as shown in Figure 6, and the whole system is placed under water. A qualitative impression of the weld is obtained by inspecting the occurrence of air bubbles escaping from the joint. A more quantitative evaluation is possible by using a pressure gauge that measures the pressure in the circuit. If a pressure drop occurs, the welded connection is not leak free. The time necessary to obtain a certain pressure drop can be measured and used to describe the severity of the leak (and thus the quality of the weld).
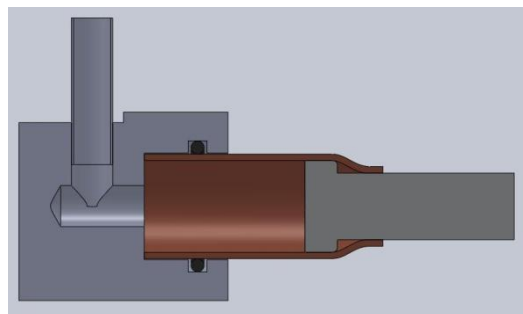
Figure 6: Leak test

4   FUTURE RESEARCH

The main objectives put forward at the start of our thesis are the evaluation of the analytical model and the development of welding windows based on extensive experimental research. Most attention thus far has gone to a general literature study and to the analytical modeling of the MPW process. In addition, a leak test setup and a magnetic field measurement probe were developed. The leak test setup will be further refined (accurate measurement of pressure changes) in the next stage of our research. The magnetic field measurement probe has been designed, constructed and calibrated, but has not yet been used in welding tests. Performing tests using the probe, will be the object of future experiments. Hopefully, the results will provide a more thorough understanding of the accuracy and applicability of the analytical model.

As mentioned before, we aim to determine relationships between welding parameters and weld quality on an experimental basis. By varying material combinations, stand-off distance, overlap distance, flyer tube thickness, etc. during a large number of welds, the goal is to obtain empirical formulas and/or intervals for the aforementioned parameters which result in a successful weld. In order for these relationships to be established, a large number of experimental weld tests will be performed. In addition to microscopic inspection, other non-destructive techniques such as ultrasonic testing [16] [17] and computer tomography [18] [19], will be applied to provide us with a better understanding of the MPW process. A last objective of our thesis is to develop a test method for the determination of weld strength.

5   CONCLUSIONS

Further research is imperative for the development of an accurate understanding and analytical description of the magnetic pulse welding process. The magnetic field measurement will hopefully lead to some valuable conclusions regarding the effect of the field shaper. Perhaps an analytical formula for a correction factor on the amplitude of the magnetic field (in the presence of a field shaper) could be obtained. On the other hand further experimental testing will provide deeper insight into relationships between different welding parameters. Multiple series of experiments will be performed and weld quality evaluated based on both destructive and non-destructive methods. The final objective of our thesis is to define *weldability windows*, which allow a simple determination of optimal process parameters.

6   NOMENCLATURE

EW   Explosive Welding

FE   Finite Elements

HAZ   Heat affected zone

MPW Magnetic Pulse Welding

NDT   Non-destructive testing

7   ACKNOWLEDGEMENTS

The authors would like to acknowledge the support of the technical staff of the Laboratory Soete and the Belgian Welding Institute. Further they would also like to thank the technical staff of the laboratory EELAB, a department of the University of Ghent, for their support on the development of the magnetic field measurement probe.

8   REFERENCES

[1] Shribman, V. *Magnetic Pulse Welding,* Pulsar ltd. Magnetic Pulse Solutions, 2007
[2] Peihui Zhang, M.S. *Joining enabled by High velocity deformation*, Phd. Thesis, University of Ohio, 2003
[3] F. Gringon, D. Benson, K.S. Vecchio, M.A. Meyers, *Explosive welding of aluminium to aluminium: analysis computation and experiments*, USA, 2004
[4] P.V. Vaidyanathan, AR. Ramanathan, *Design for quality welding*, Journal of Materials Processing Technology, 32, 2007
[5] Manish Kamal, M.S. *A Uniform Pressure Electromagnetic Actuator For Forming Flat Sheets*, Phd. Thesis, University Of Ohio, 2005
[6] Kleiner, M. *High Speed Forming 2004*, Proceedings of the 1st international conference, Germany, 2004
[7] Wei Xu, Hongyuan Fang, Wenli Xu, *Analysis of the variation regularity of the parameters of the discharge circuit with the distance between workpiece and inductor for electromagnetic forming process,* Journal of materials processing technology, 2008 pp 216-220
[8] M.Kleiner, C. Beerwald, W. Homberg, *Analysis of process parameters and forming mechanisms within the electromagnetic forming process,* Germany.
[9] P. Barreiro, V. Schulze, D. Löhe, M.Marré, C. Beerwald, W. Homberg, M.Kleiner, *Strength of Tubular Joints Made by Electromagnetic Compression at Quasi-static and Cyclic Loading*, High Speed Forming, pp. 107-116, 2006
[10] Kashani, Tomokatsu Aizawa and Mehrdad. *Magnetic Pulse Welding (MPW) Method for Dissimilar Sheet Metal Joints.* Tokyo Metropolitan college of Technology
[11] Daehn, Glenn S. *High Velocity Metal Forming* ASM International, Volume 14B, 2006, pp. 405-418
[12] Mamalis, A.G., *Electromagnetic Forming Tools and Processing Conditions: Numerical Simulation.,* Materials and Manufacturing Processes, 21, 2006, pp.411 – 423
[13] M.A. Bahmani, K. Niayesh, A. Karimi, *3D Simulation of magnetic field distribution in electromagnetic forming systems with field shaper,* Journal of Materials Processing Technology,209,2009, pp.2295-2301
[14] Goes, Patrick and Martínez Valle, Álvaro. *Research Report: Modelling of the Magnetic Pulse Forming Process.* Ghent : ArcelorMittal Research and Development Industry, 2009.
[15] Broeckaert, Filip and De Ketele, Michael. *An exploratory study into the feasibility of magnetic pulse forming,* thesis, University Ghent : Belgium, 2009.

[16] http://www.ndt-ed.org/EducationResources/CommunityCollege/Ultrasonics/cc_ut_index.htm, 2008
[17] Robert E. Shaw Jr., P.E., M. ASCE., *Ultrasonic Testing Procedures, Technician Skills and Qualifications*, 2002
[18] V.V. Koshovyi, O.E.Levyts'kyi, I.M. Romanyshyn and R.V. Sharamaha., *Evaluation of the homogeneity of the metal of welded joints by ultrasonic computed tomography*, Materials Science, Vol 43, 2007
[19] Uwe Ewert, Bernhard Redmer, Jürgen Müller, *Mechanized weld inspection for detection of planar defects and depth measurements by tomosynthesis and planartomography,* Germany, 2000

Afternoon Session 1

Chairman:

Jeroen Van Wittenberghe, Laboratory Soete, Ghent University, Belgium

FINITE ELEMENT MODELLING OF SEVERAL PHYSICAL ENGINEERING PROBLEMS

M. Abdel Wahab
Professor of Applied Mechanics
Ghent University, Laboratory Soete, Belgium

Abstract: This paper presents the application of the Finite Element Method (FEM) to a wide range of physical engineering problems and analysis types. It summarises some of the research works carried out by the author using FEM. The types of analysis, which are coved in this paper, include linear and non-linear stress analysis, heat transfer analysis, diffusion analysis, coupled thermal-stress and coupled diffusion-stress analysis, fracture mechanics analysis and modelling of macro-cracks, fatigue damage initiation and crack propagation analysis, modal analysis, transient dynamics analysis and traffic flow analysis.

Keywords Finite Element Analysis, stress analysis, heat transfer, diffusion of moisture, coupled field analysis, fracture mechanics, fatigue, modal analysis, transient dynamics, traffic flow.

1   INTRODUCTION

The Finite Element Method (FEM), also known as Finite Element Analysis (FEA), is a numerical technique that can be used to solve partial differential equations and integral equations. The concept is simply based on replacing the partial differential equations by a system of simultaneous algebraic equations for steady state problems and a system of ordinary differential equations for time dependent problems. This can be done in two essential steps; a) writing the variational equivalent or weak form of the partial differential equation and b) replacing the infinite dimensional problem by a finite dimensional one through discretisation of the space. The resulting system of simultaneous equations can then be easily solved using a digital computer. One of the widely used techniques to convert the partial differential equations to algebraic equations is the variational formulation, also known as weighted residual formulation. For example, for a simple bar element, the governing differential equation for static analysis is given by:

$$EA\frac{\partial^2 u}{\partial x^2} - f = 0 \tag{1}$$

Where *EA* is the axial stiffness, *u* is the displacement and *f* is the applied distributed axial load. Both *u* and *f* are functions of the coordinate *x*. The variational equivalent or weak form of Equation (1) is given by:

$$\int \phi(x)\left(EA\frac{\partial^2 u}{\partial x^2} - f \right) = 0 \tag{2}$$

Where $\phi(x)$ is a weigh function vector. Discretisation of the space is usually done by writing the displacement function in terms of the nodal displacements $[U]$ using interpolation functions or shape functions [N], which varies from 0 to 1, so that:

$$u = [N]^T [U] \tag{3}$$

Substituting Equation (3) into Equation (2), using $\phi(x) = [N]$ as in the Galerkin Finite Element approach and solving by integration by parts, yields the well known FE equation:

$$[K][U] = [F] \tag{4}$$

Where $[K]$ is the stiffness matrix ($[K] = EA\int_0^1 \frac{\partial [N]}{\partial x}\frac{\partial [N]^T}{\partial x}\, dx$), $[U]$ is the displacement vector or degree-of-freedom vector and $[F]$ is the force vector containing both the axial distributed load components and boundary conditions. FEM is originally developed in 1941 for stress analysis problems. Nowadays, it is applicable to many other physical engineering problems. Many textbooks on FEA and its applications are available in the literature, e.g. [1, 3].

2   STRESS ANALYSIS

In stress analysis, the degrees of freedom are translations as in case of bar elements, plane elements and 3-D solid elements, and/or rotations as in case of beam elements, plate elements and shell elements. For linear elastic analysis, Equations (4) is solved for the degree-of-freedom vector for a given stiffness matrix and force vector. After obtained, the degrees of freedom, the strain components are calculated from the compatibility equation, i.e. the relationship between strains and the displacements or rotations, as follows:

$$[\varepsilon]=[B][U] \tag{5}$$

Where $[B]$ is the strain-displacement or compatibility matrix. The stresses are then calculated from the strains using the constitutive equation or stress/strain relationship, i.e.

$$[\sigma]=[D][\varepsilon] \tag{6}$$

Where $[D]$ is the constitutive matrix. An example for linear elastic stress analysis for a hydraulic Manifold due to in-service system pressure is shown in Figure 1, where von Mises stress contour is plotted [4]. Due to symmetry, only half of the manifold was modelled using 3-D solid elements. The manifold was made of steel and the maximum applied pressure was 68 MPa.

In case of geometric non-linearity (large deformation) or material non-linearity (elastic-plastic), the stiffness matrix becomes function of the unknown degrees of freedom so that Equation (4) becomes:

$$[K(U)][U]=[F]$$

The solution cannot be obtained in one step and an iterative solution is required. Furthermore, due to the non-linear force-displacement or stress-strain behaviour, an incremental solution is necessary. Thus, the incremental solution for non-linear stress analysis problems becomes:

$$\Delta\psi=[K(\Delta U)][\Delta U]-[\Delta F] \tag{7}$$

Where ΔU is the incremental displacement vector, ΔF is the incremental force vector and $\Delta\psi$ is the incremental residual force vector, which should be equal to zero for a converged solution. The iterative solution is usually solved using Newton-Raphson method. An example for a large deformation analysis is shown in Figure 2, where the deformation of a road sweeping brush is plotted [5]. The brush was made of steel tines and modelled using beam elements. The deformed shape in Figure 2 is for a flat flicking brush, which is in contact with the ground and has a penetration of 50 mm.
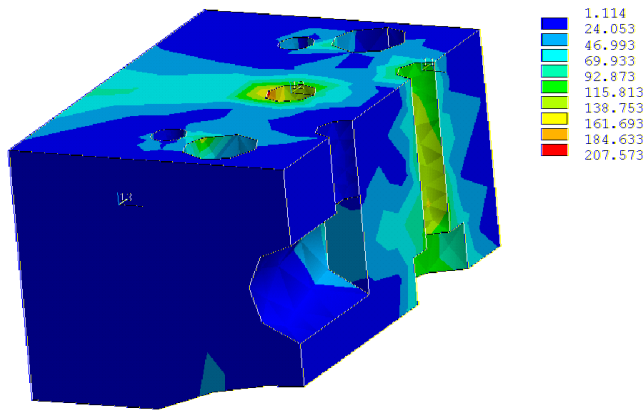
Figure 1. Linear elastic analysis of a Hydraulic Manifold – von Mises stress (MPa)
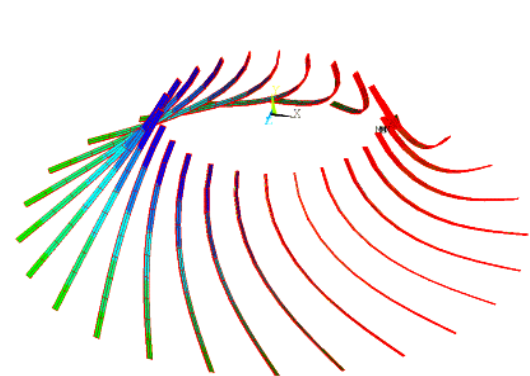
Figure 2. Large deformation analysis of a road sweeping brush – deformed shape

An example of material non-linearity finite element modelling is a thick walled tube subjected to autofrettage process [6], which is usually used in manufacturing barrels of handguns, rifles, artillery, and cannons mounted on military aircrafts. Autofrettage is carried out by means of an oversized mandrel or swage that is forced through the bore creating a region of plastic deformation. The mandrel is then withdrawn so that the elastic material surrounding the plastic zone attempts to return to its undeformed state. The material that is permanently deformed partially prevents this response. Hence a compressive residual hoop stress field is created at the inner surface of the tube. Figure 3 shows a plot of the residual hoop stress in a 2-D axsymmetric model of the thick walled tube. An elastic perfectly plastic material model was used and the autofrettage process was simulated through the application of an overstrain (overstrain is defined as $\delta=R_m-R_i$, where R_m is the mandrel radius and R_i is the inner radius of the tube). The overstrain has been applied to the tube by prescribing the corresponding interference at the inner wall side as initial

boundary condition. The prescribed interference was applied gradually until it reaches its maximum value; then it was removed gradually in order to simulate the unloading process. The FE results are also compared to the analytical solution in Figure 3, for three different overstrain values, namely Φ = 25, 60 and 100 % ($\phi = \dfrac{R_m - R_i}{R_i} \times 100\%$).
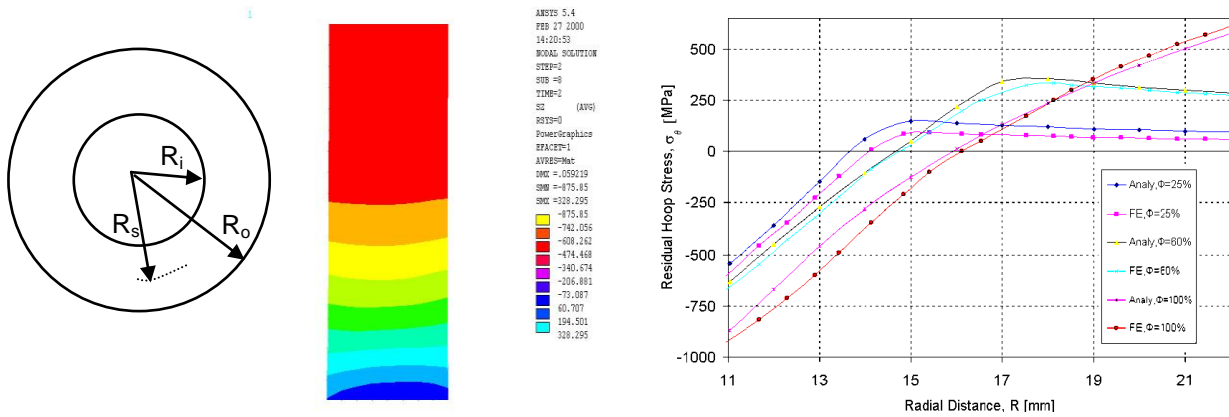
Figure 3. Residual hoop stress in an autofrettaged tube (MPa)

3   HEAT TRANSFER ANALYSIS

In heat transfer analysis, the degree of freedom is usually temperature. In general, there are two types of analysis, namely steady state analysis and transient analysis. In steady state analysis, the temperature distribution and related quantities are determined under steady state condition, i.e. variation over time is ignored. Whereas in transient analysis, the temperature distribution and related quantities are determined at different time intervals. The governing differential equation for isotropic heat transfer in 3-D space, also known as the heat equation, is given by:

$$\frac{\partial T}{\partial t} = \frac{K}{c_p \rho} \left(\frac{\partial^2 T}{\partial x^2} + \frac{\partial^2 T}{\partial y^2} + \frac{\partial^2 T}{\partial z^2} \right) \tag{8}$$

Where t is time, K is thermal conductivity (J/m.s.^{o}C or W/m.^{o}C), ρ is mass density (kg/m^3), c_p is specific heat capacity (J/kg.^{o}C) and T is temperature, which is function of space and time. Applying the variational formulation or weighted residual formulation to Equation (8), the FE conduction heat transfer equation is obtained as:

$$[C]\left[\frac{\partial T}{\partial t}\right] + [K][T] = [q] \tag{9}$$

Where $[K]$ is the conductivity matrix, $[C]$ is the specific heat matrix, $[T]$ is the temperature vector, $\left[\dfrac{\partial T}{\partial t}\right]$ is the rate of change of temperature vector over time and $[q]$ is the heat flux vector. Equation (9) is solved using numerical integration, usually Euler integration scheme, in which the derivative of temperature with respect to time is approximated as $\dfrac{\partial T}{\partial t} = \dfrac{T(t + \Delta t) - T(t)}{\Delta t}$, where $T(t + \Delta t)$ is the temperature at time step $t + \Delta t$ and $T(t)$ is the temperature at time step t. For steady state analysis, the problem is independent of time, thus the term concerned with time in Equation (9) is eliminated, and the FE equation is reduced to:

$$[K][T] = [q] \tag{10}$$

An example of steady state conductivity heat transfer FEA is a Railko Marine Bearing [7]. The bearing consists of two layers, namely a backing and a liner. The backing has a thermal conductivity of 0.35 W/m.^{o}C and a thickness of 28 mm, while the liner has a thermal conductivity of 0.22 W/m.^{o}C and a thickness of 21 mm. The average inner diameter is 740 mm and the outer diameter is 838 mm. 2-D plane heat transfer elements were used to model the two layers with mesh refinement near sharp corners and at interface. The inside temperature was 100°C, whereas the outside temperature was 30°C. Figure 4 shows the steady state temperature distribution in the bearing.
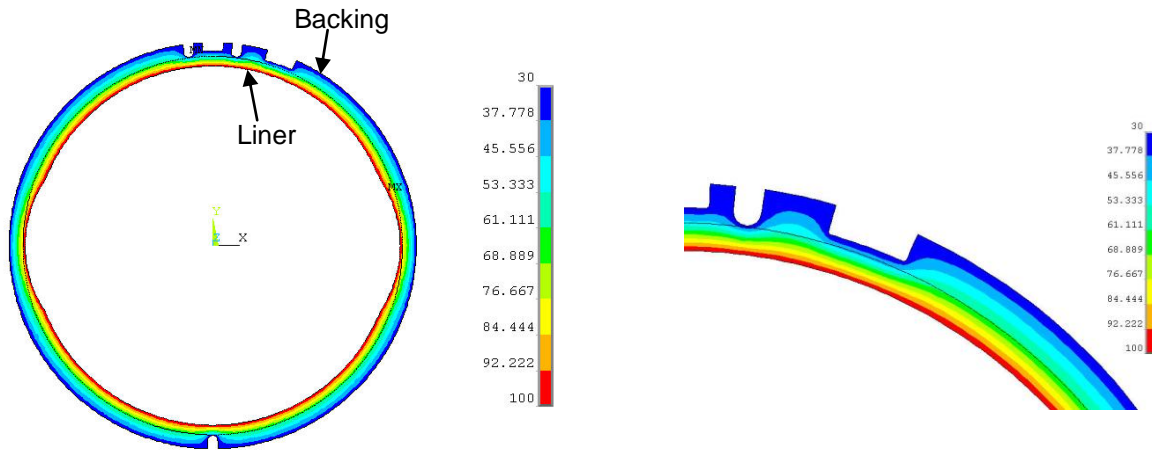
Figure 4. Steady state heat transfer analysis - Temperature (^{o}C) distribution in Railko bearing

4   DIFFUSION ANALYSIS

In diffusion FE analysis, the degree of freedom is moisture concentration. The general form of the governing differential equation for isotropic diffusion in 3-D space can be expressed as:

$$\frac{\partial c}{\partial t} = D\left(\frac{\partial^2 c}{\partial x^2} + \frac{\partial^2 c}{\partial y^2} + \frac{\partial^2 c}{\partial z^2}\right) \tag{11}$$

Where D is the diffusion coefficient (m^2/s) and c is the moisture concentration, which is a function of time and space. The moisture concentration c (also denoted as C/C_∞) is a dimensionless quantity and varies between 0 and 1 with a value of 0 indicating dry condition, and a value of 1 indicating fully saturated condition. We can easily notice the similarity between Equation (11) for diffusion analysis and Equation (8) for heat transfer. If we substitute by $c_p \rho = 1$, $K=D$ and $T=c$ in Equation (8), it becomes identical to Equation (11). Therefore, the heat transfer FE equations for steady state analysis (Equation (10)) and for transient analysis (Equation (9)) are applicable to diffusion analysis. Furthermore, in commercial FE packages, a diffusion analysis can be performed using heat transfer element with different interpretation of the physical meaning of the degree of freedom and its related quantities. An example of a transient diffusion analysis is a lap strap joint [8] shown in Figure 5. The lap strap joint consists of two substrates made of carbon fibre reinforced polymer (CFRP) composite materials bonded together using adhesives. The adhesive layer has a rectangular fillet at the edge of the joint. The diffusion coefficient used in the analysis presented in Figure 5 for adhesive was 9.3×10^{-13} m^2/s and for the composite material was 3.6×10^{-13} m^2/s. The transient diffusion analysis was performed in the commercial software ANSYS using heat transfer elements. As initial and boundary conditions, all edges including composites, adhesive and fillet are assumed to be saturated (i.e. all edges are exposed). The distribution of moisture concentration along the centre of the adhesive layer is plotted in Figure 5 after three different exposure times, 10, 20 and 30 days.
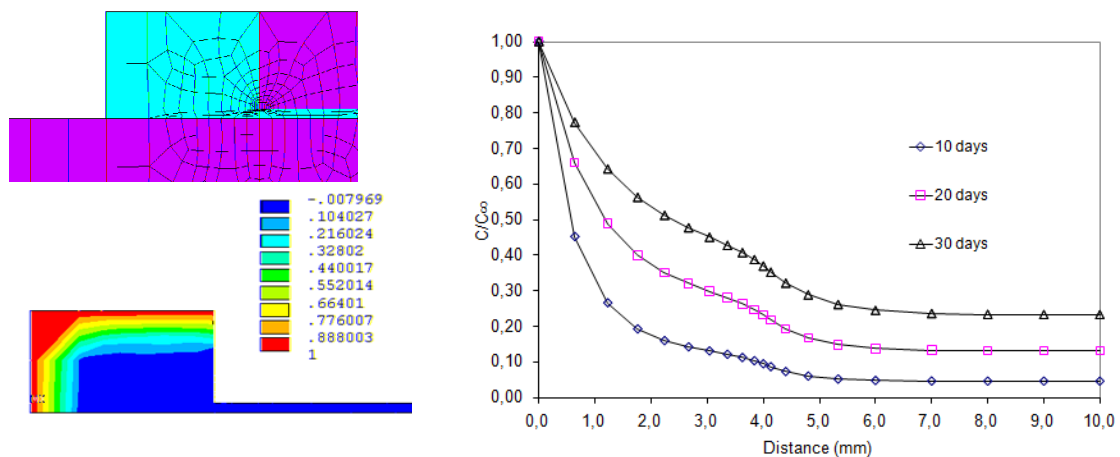
Figure 5. Transient diffusion FE analysis for a lap strap adhesive joint

5 COUPLED-FIELD ANALYSIS

A coupled-field analysis, also known as multi-physics analysis, is a combination of two or more dependent analyses from different physics field. The output of one analysis would be the input for the next analysis. For example, after performing heat transfer analysis, the temperature distribution would generate thermal strains, which can be applied to a subsequent stress analysis. We present herein two examples of coupled field analysis, namely thermal-stress analysis and diffusion-stress analysis. The steps that are involved in performing the coupled field analyses are summarised in Figure 6(a). The same finite element mesh should be used for both heat transfer and stress analyses. However, the element type should be switched from heat transfer element to structural element. If the mechanical properties are thermal or moisture dependent, they have to be defined for each element according to its temperature or moisture concentration. The thermal strains ($\varepsilon_t = \alpha \times \Delta T$, where α is the coefficient of thermal expansion and $\Delta T = T - T_{ref}$ with T the calculated temperature and T_{ref} a reference or strain free temperature) or swelling strains ($\varepsilon_d = \alpha_s \times c$, where α_s is the coefficient of swelling and c is the moisture concentration) are calculated for each element. The mechanical loads, if any, are applied and the stress analysis is solved. The first example is the thermal-stress analysis of the Railko bearing [7] presented in section 3. The mechanical properties of the backing were Elastic modulus E = 37 GPa and Poisson's ratio=0.3 and for the liner: Elastic modulii E_x=19 GPa, E_y=39 GPa, E_z=20 GPa and Poisson's ratio=0.3, where x is the radial direction, y is the hoop direction and z is the axial direction. A contour of the hoop stress due to only thermal strains is shown in Figure 6(b). The second example is the diffusion-stress analysis of the lap strap joint [9] presented in section 4. The mechanical properties for the adhesive were dependent on the moisture concentration. Therefore, the stress-strain response for each adhesive element was defined on the basis of the moisture concentration in the element. For CFRP composite substrates, the moisture didn't affect the mechanical properties. A mechanical load of 5 kN was applied to the joint. A plot of the peel stress in the adhesive layer along the adhesive/substrate interface is shown in Figure 6(c). The joints were aged in hot/wet environment, 90°C/97%RH up to saturation (denoted as 90 wet in Figure 6(c)) and tested in dry at 90°C (denoted as /dry) and wet 97%RH at 90°C (denoted as /wet) conditions.

Heat transfer or diffusion analysis	Switch element type from heat transfer to structural element	Define thermal or moisture dependent mechanical properties	Apply thermal strains or swelling strains and mechanical loads	Solve stress analysis

(a)

(b)

(c)
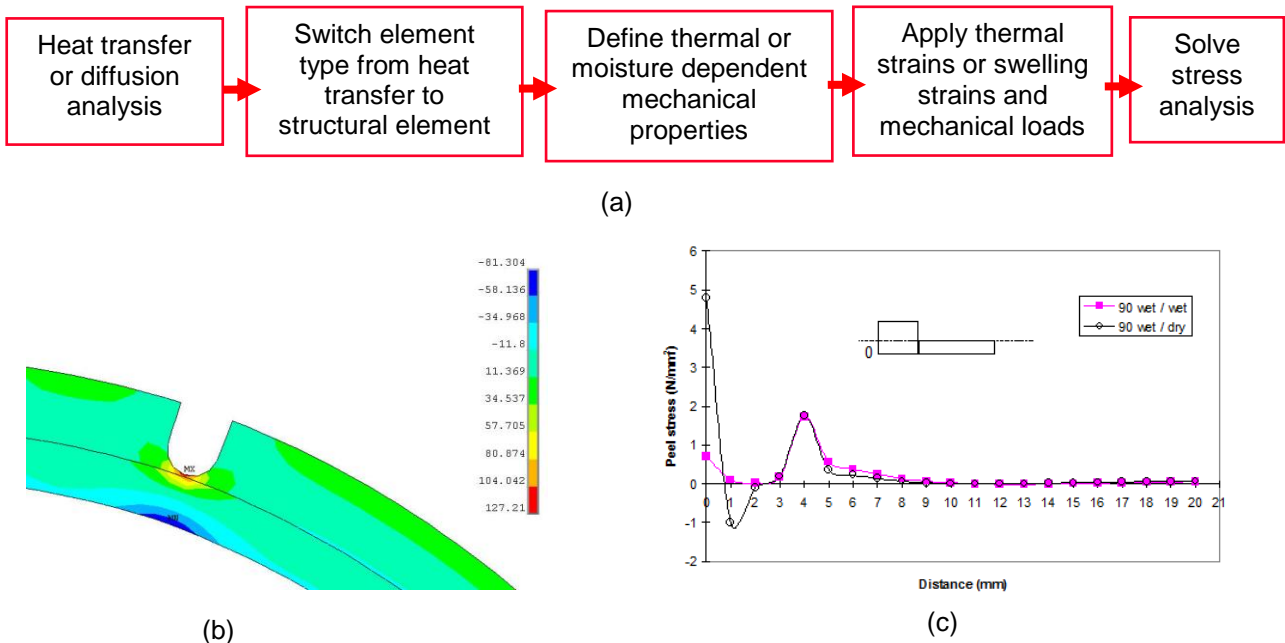
Figure 6. Coupled-field analysis: (a) Procedures, (b) Thermal-stress analysis of Railko bearing and (c) Diffusion- stress analysis of lap strap joint.

6 FRACTURE MECHANICS ANALYSIS

Fracture mechanics analysis using FEA involves two main steps, namely; a) modelling of macro-crack and b) extracting fracture mechanics parameters from stress analysis results. When modelling the crack in FEA, the crack faces should coincident but not connected together. The elements around the crack tip should be quadratic to capture the high stress and stain gradient near the crack tip, as shown in Figure 7(a). In Linear Elastic Fracture Mechanics (LEFM), the displacement variation near the crack tip is proportional to the square root of the distance from the crack tip ($u \propto \sqrt{r}$) and the stress and strain singularity is of the square

root type ($\sigma \propto \frac{1}{\sqrt{r}}$ & $\varepsilon \propto \frac{1}{\sqrt{r}}$). In such a case, the quarter point singularity elements [10], in which the mid-side nodes at the crack tip are shifted to the quarter position in order to produce square-root stress singularity, as show in Figure 7(b). In Elastic-Plastic Fracture Mechanics (EPFM), the stress singularity is not of the square root type and has an order of $\frac{1}{m+1}$, where m is the power law constant in the Ramberg–Osgood equation [11] ($\sigma \propto \frac{1}{r^{1/m+1}}$) and the strain singularity has an order of $\frac{m}{m+1}$ ($\varepsilon \propto \frac{1}{r^{m/m+1}}$). Also, in composite materials when cracks terminate at an interface, the order of the singularity is no more of the square root type and has a general order λ ($u \propto r^\lambda$ & $\varepsilon \propto r^{\lambda-1}$), which can be a real number $0 \le \lambda \le 1$, or a complex number, depending on the geometry of the problem and material properties. To approximate the general power type singularity in FEA, special crack tip elements as the one shown in Figure 7(c) have been developed [12, 13]. After obtaining the FE results, fracture mechanics parameters such as stress intensity factor, strain energy release rate and J-integral can be calculated. There are many computational techniques to extract fracture mechanics parameters from FE results. We present herein two simple techniques to calculate the stress intensity factor and the strain energy release rate using the nodal displacements behind the crack tip and the nodal forces ahead of it. Consider the arrangement of nodes in a quarter point element as shown in Figure 7(b), a two-point formula for calculating the stress intensity factor for a symmetric cark is given by [14]:

$$K_I = \frac{E}{4}\sqrt{\frac{2\pi}{L}}(4u_{y_{i-1}} - u_{y_{i-2}}) \tag{12}$$

Where E is the Elastic modulus and $u_{y_{i-1}}$ and $u_{y_{i-2}}$ are the crack opening displacements of nodes i-1 and i-2, respectively. For the same arrangement of nodes shown in Figure 7(b), the strain energy release rates for mode I and mode II, derived from a virtual crack closure approach, are given by [15]:

$$G_I = \frac{2u_{y_{i-1}}}{L}(F_{y_{i+1}} + (1.5\pi - 4)F_{y_i}) \tag{13}$$

$$G_{II} = \frac{2u_{x_{i-1}}}{L}(F_{x_{i+1}} + (1.5\pi - 4)F_{x_i}) \tag{14}$$

Where F_x and F_y are the crack closure nodal forces in the x and y directions, respectively, and u_x and u_y are the crack sliding and opening displacements, respectively. Deformation near an interface crack in a lap strap joint [16] is shown in Figure 7(d).
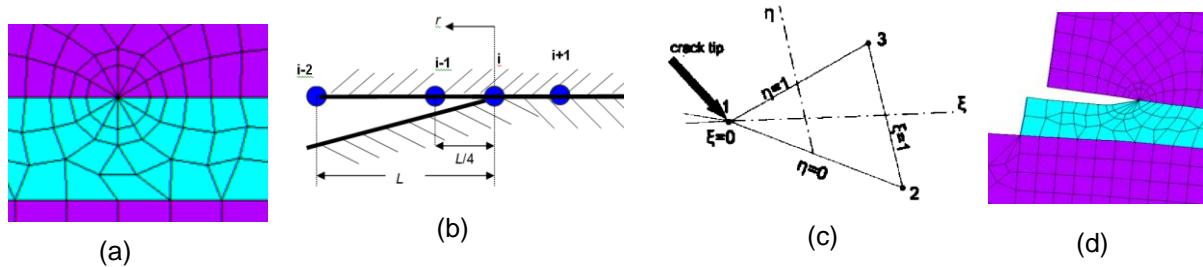
Figure 7. Fracture mechanics analysis: (a) FE mesh at a crack tip, (b) Quarter point, (c) General power singularity element and (d) Deformation near a crack tip.

7   FATIGUE ANALYSIS

Fatigue analysis combines stress analysis with either continuum damage mechanics for fatigue crack initiation analysis or fracture mechanics for fatigue crack propagation analysis. In continuum damage mechanics, the fatigue damage accumulation is represented by a damage variable D, which is equal to zero for a virgin material and 1 for a fully damaged material. The damage variable can be calculated from FE stress analysis results, providing that some damage material parameters are given. For low cycle fatigue, the damage variable (D) is expressed as [17]:

$$D = 1 - \left[1 - A(\beta + m + 1)(\Delta\sigma_{eq})^{\beta+m}R_V^{\beta/2}N\right]^{\frac{1}{\beta+m+1}} \tag{15}$$

Where N is the number of cycles, $\Delta\sigma_{eq}$ is the range of von-Mises stress, R_V is the triaxiality function, m is the power constant in Ramberg-Osgood equation, and A and β are damage parameters, which can be determined experimentally. For given N, m, A and β, the range of von-Mises stress $\Delta\sigma_{eq}$ and triaxiality function R_V can be determined from stress analysis results, and therefore D can be calculated using Equation (15). An example of the evolution of D in an adhesive layer with fillet used for a scarf joint [18] is shown in Figure 8.

$N = 1$
$D_{max} = 0.002$

$N = 15$
$D_{max} = 0.038$

$N = 28$
$D_{max} = 0.204$
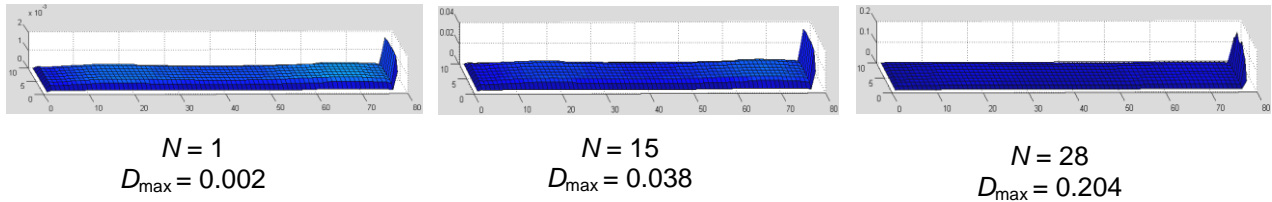
Figure 8. Fatigue damage evolution in adhesive layer

In fatigue crack propagation analysis, a crack growth equation (e.g. Paris law) is numerically integrated within a FE stress analysis. A modified Paris law that includes the threshold and accelerating crack growth regions is given by [19]:

$$\frac{da}{dN} = DG_{max}^n \left[\frac{1 - \left(\dfrac{G_{th}}{G_{max}}\right)^{n_1}}{1 - \left(\dfrac{G_{max}}{G_c}\right)^{n_2}} \right]$$

(16)

Where da/dN is the crack growth rate, G_{max} is the maximum strain energy release rate at a specific stress ratio, G_{th} is the fatigue threshold, G_c is the fracture toughness, and n, n_1 and n_2 are constants. A procedure that is used to numerically integrate the crack growth law in FE analysis is shown in Figure 9. This procedure has been implemented in the FE package ANSYS. The application of the crack propagation procedure to a single lap joint is shown in Figure 10 [19]. Only half of the joint was modelled with rotational symmetric boundary conditions in the mid-plane. The number of cycles to failure were calculated twice for each load value; a) using the total strain energy release rate (G_{max} or G_T) and b) using the mode I strain energy release rate (G_I).
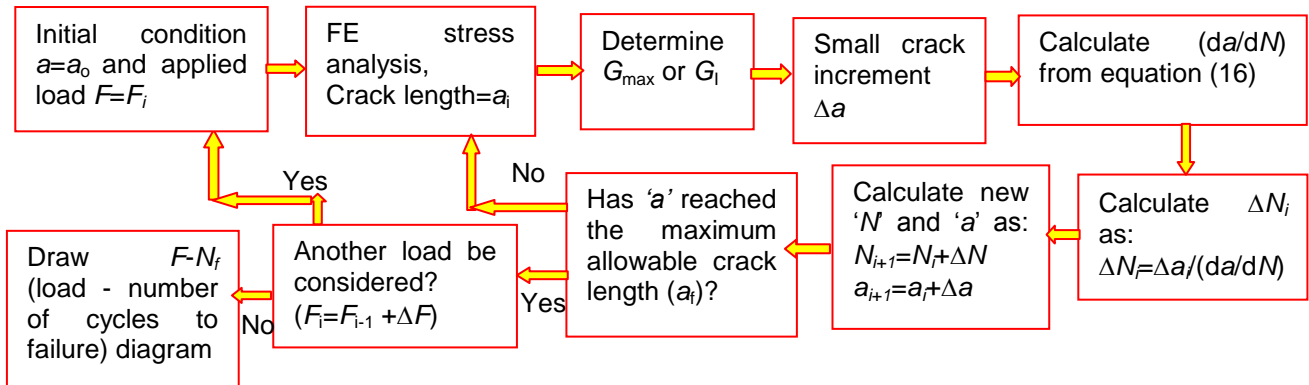
Figure 9. Fatigue crack propagation procedure
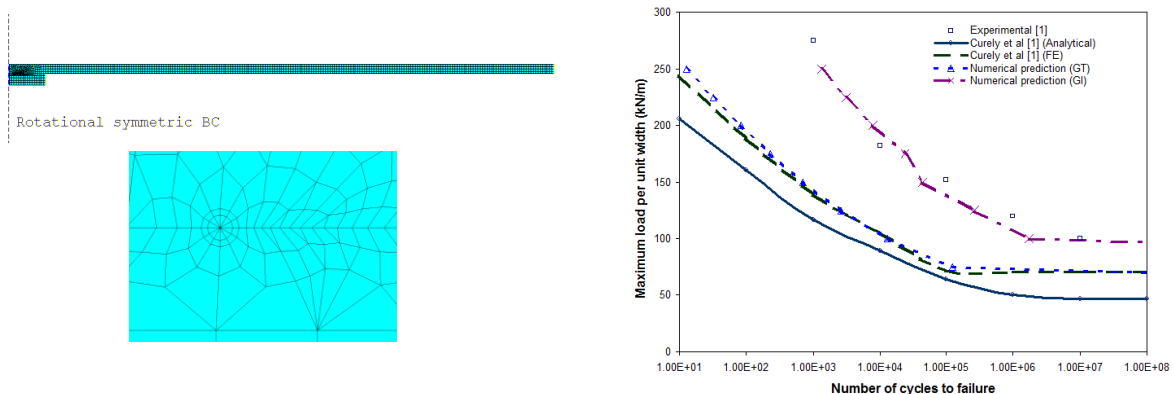
Figure 10. Fatigue crack propagation in a single lap joint

36

8   MODAL ANALYSIS

FE Modal analysis is performed to determine the natural frequencies and the mode shapes of a structure in free vibration. The FE equation that should be solved in modal analysis is derived from the generalised equation of motion, which is given by:

$$[M][\ddot{U}]+[C][\dot{U}]+[K][U]=[F] \tag{17}$$

Where $[K]$ is the stiffness matrix, $[U]$ is the displacement vector, $[C]$ is the damping matrix, $[\dot{U}]$ is the first derivative of the displacement vector with respect to time (velocity vector), $[M]$ is the mass matrix, $[\ddot{U}]$ is the second derivative of the displacement vector with respect to time (acceleration vector) and $[F]$ is the force vector. For un-damped free vibration, both damping matrix and force vector are equal to zero and Equation (17) becomes:

$$[M][\ddot{U}]+[K][U]=0 \tag{18}$$

The displacement time response solution of this differential Equation is $[U]=[U_m]\sin(\omega_n t+\psi)$, where the vector $[U_m]$ contains the maximum amplitude for each degree of freedom, ω_n is the angular frequency and ψ is the phase angle. Differentiating the displacement twice with respect to time and substituting in Equation (18), yields:

$$([K]-\omega_n^2[M])[U_m]=0 \tag{19}$$

Equation (19) is an eigenvalue problem, which has 'n' number of eigenvalues (angular frequencies) and eigenvectors (mode shapes). The eigenvalue problem is solved using iterative numerical solution such as inverse iteration method, and tridiagonalisation and QR algorithm. An example of FE modal analysis is the free vibration of a pre-stressed concrete bridge, B14 [20]. The B14 bridge, built in 1971, is located between the two villages Peutie and Melsbroek and crosses the highway E19 between Brussels and Antwerp in Belgium. It has an overall length of 89 m, a width of 13 m and two traffic lanes. The bridge has three spans and is supported by two piers and two abutments. A 3-D finite element model was constructed using solid elements and modal analysis was performed. Due to symmetry, only one-quarter of the bridge was modeled with appropriate symmetric or anti-symmetric boundary conditions in order to determine all symmetric and anti-symmetric modes of vibration. The FE mesh consists of 3321 brick elements and 4938 nodes. Figure 11 shows the first three mode shapes of the bridges B14.

Mode 1 – 2.35 Hz   Mode 2 – 3.28 Hz   Mode 3 – 4.40 Hz
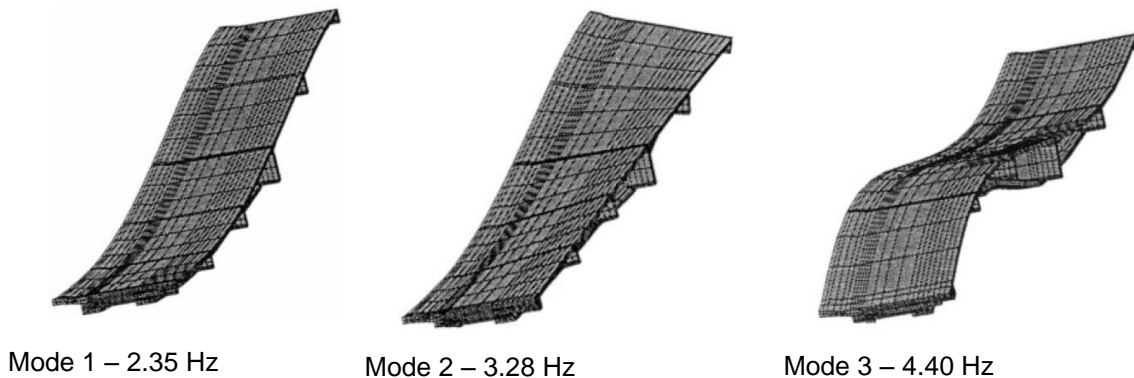
Figurer 11. FE Modal analysis of bridge B14

9   TRANSIENT DYNAMICS ANALYSIS

Transient dynamics analysis, also known as time-history analysis, is concerned with the determination of the time response of a structure, i.e. displacements, strains, stresses as functions of time under the action of time dependent loads. The FE equation that should be solved in transient dynamics analysis is Equation (17), the generalised equation of motion. Because of the time dependent, Equation (17) is solved in time steps using numerical integration such as Euler integration scheme. In the explicit direct numerical integration scheme, the velocity and acceleration vectors at time step t are approximated as:

$$[\dot{U}(t)]=\frac{1}{2\Delta t}[U(t+\Delta t)-U(t-\Delta t)] \tag{20}$$

$$[\ddot{U}(t)]=\frac{1}{\Delta t^2}[U(t+\Delta t)-2U(t)+U(t-\Delta t)] \tag{21}$$

With appropriate initial conditions at t=0, solution of $[U]$ at different time steps can be found, using Equations (17), (20) and (21). As the time step becomes smaller, the numerical solution converges to the exact solution. An example of a FE transient dynamics analysis is shown in Figure 12, where a footbridge, Wilcott bridge, is excited using a walking pedestrian [21]. The Wilcott footbridge is a newly constructed FRP composite footbridge crossing the new A5 Nesscliffe Bypass near Shrewsbury, UK. Wilcott footbridge is a suspension bridge, has a single span of 50.24 m and provides a footway of 2.3 m wide. The finite element package ANSYS was used to simulate the transient dynamics response of the footbridge. 3-D beam elements (Figure 12(a)) were used to model all the structural members including; cross beams, deck, posts, cables and hangers. Mass elements were used to model handrails, ballast in the cells, and deck finishing. A time history analysis is performed to calculate the dynamic response of the footbridge under the action of a walking pedestrian at a frequency close to the second vertical natural frequency of the bridge (1.6 Hz). Humans walking pacing rate normally lies in the range 1.6-2.4Hz. The vertical dynamic load induced on the footbridge by a pedestrian taken from BS5400 is a pulsating moving load of: F(t)=180sin(ω.t) N. The displacement time response in the mid-span of the bridge is shown in Figure 12(b).

(a)

(b)
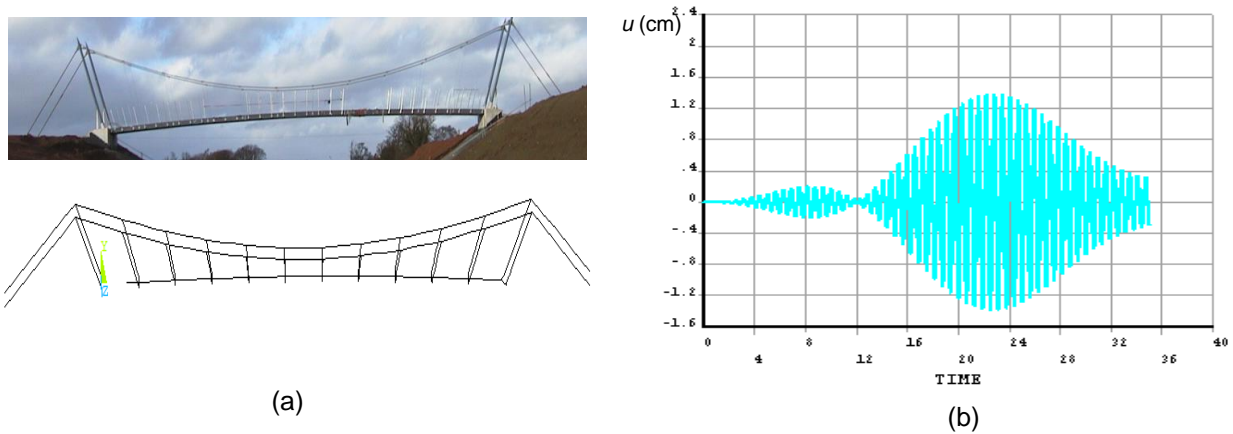
Figurer 12. Wilcott bridge: (a) FE model and (b) Mid-span response due to a walking pedestrian

10 TRAFFIC FLOW ANALYSIS

In traffic flow analysis, the degree of freedom is the traffic density. The governing partial differential equation of traffic flow is known by LWR (Lighthill, Witham and Richards) model. For one dimensional constant speed traffic flow, LWR equation is given by [22]:

$$\frac{\partial k}{\partial t} + u_o \frac{\partial k}{\partial x} = 0 \tag{22}$$

Where k is the traffic density (vehicle/m), which is a function of time and space, and u_o is the traffic speed (m/s). Applying variational formulation or Galerkin method to Equation (22), the FE equation in matrix form is obtained as:

$$[A]\left[\frac{\partial k}{\partial t}\right] + [B][k] = 0 \tag{23}$$

Again, the solution of Equation (23) is obtained in different time steps using numerical integration. An example of traffic flow analysis is a simulation of a 5 km road [22], where the boundary conditions at the beginning of the road (x=0) are as shown in Figure 13(a). The convergence of traffic flow density at a distance of 2 km is plotted in Figure 13(b) by considering different element sizes (Δx).

(a)

(b)
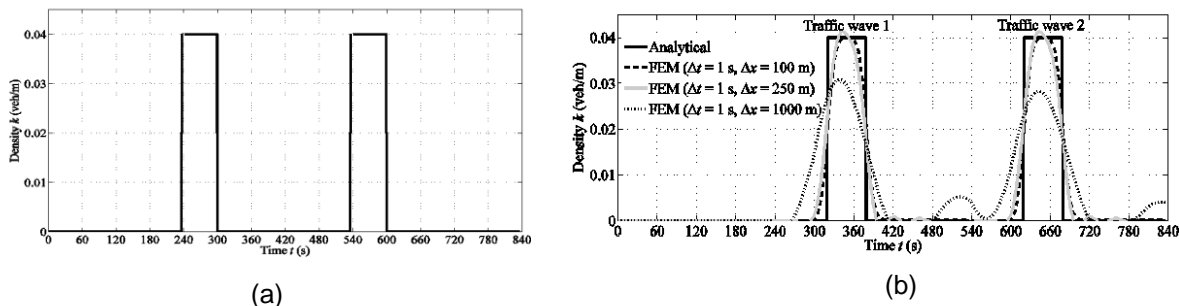
Figurer 13. FE traffic flow analysis: (a) Boundary conditions at the beginning of the road x=0 and (b) Convergence of density at x= 2 km as function of Δx

11 CONCLUSIONS

The Finite Element Method is a generic technique that can be used in several disciplines and can be applied to many physical engineering problems. Although many disciplines and applications have been covered in this paper, there are still other disciplines, which have not been considered, such as electro-magnetic, acoustics and fluid mechanics, where FEM can provide very useful numerical solutions. Nowadays, FEA is well established numerical technique and many commercial software's are available for educational purposes and industrial uses. However, research and development into FEM is still going on in order to improve accuracy, facilitate the user interaction with the software and further implementation of specific applications.

12 REFERENCES

[1] R.D. Cook, D.S. Malkus and M.E. Plesha, *Concept and applications of finite element analysis*, John Wiley & Sons, USA, Third edition, 1989.

[2] T.R. Chandrupatla and A.D. Belegundu, *Introduction to finite elements in engineering*, Pearson Education, USA, Third edition, 2002.

[3] S. Moaveni, *Finite element analysis: theory and application with ANSYS*, Pearson Education, USA, Second edition, 2003.

[4] M. M. Abdel Wahab, *Stress analysis of a Manifold for Heypac pumps*, Heypac Ltd, Internal Report, University of Surrey, December, 2000.

[5] M.M. Abdel Wahab, G.A.Parker and C.Wang, *Modelling Rotary Sweeping Brushes and Analyzing Brush Characteristic using Finite Element Method*, Finite Element in Analysis and Design, 43, 521-532, 2007.

[6] M. M. Abdel Wahab, S. A. Kandil, M. S. Abdel-kader and M. Moustafa, *Stress intensity factor calculation for autofrettaged tube test-specimens using finite element method*, 9th International Conference on Aerospace Sciences & Aviation Technology, *ASAT- 9,*Cairo, Egypt, May 8-10, 2001.

[7] A. W. E. Henham and M. M. Abdel Wahab, *Railko Marine Integrated Bearings*, Railko Ltd, Internal Report, University of Surrey, UK, June, 2001.

[8] M. M. Abdel Wahab, I. A. Ashcroft, A. D. Crocombe and S. J. Shaw, *Diffusion of moisture in adhesively bonded joints*, Journal of Adhesion, 77, 43-80, 2001.

[9] I. A. Ashcroft, M.M. Abdel Wahab and A.D. Crocombe, *Predicting degradation in bonded composite joints using a semi-coupled FEA finite element method*, Mechanics of Advanced Materials and Structures, 10, 227-248, 2003.

[10] R.S. Barsoum, *On the use of isoparametric finite elements in linear elastic fracture mechanics*, Inter. J. Numer. Meth. Engng, 10, 25-37, 1976.

[11] W. Ramberg and W.R. Osgood, *Description of stress-strain curves by three parameters*, Technical Note No. 902, National Advisory Committee For Aeronautics, Washington DC, 1943.

[12] M. M. Abdel Wahab and G. De Roeck, *A 3-D six-noded finite element containing a λ singularity*, International Journal of Fracture, 70, 347-356, 1995.

[13] M. M. Abdel Wahab and G. De Roeck, *A 2-D five noded finite element to model power singularity*, International Journal of Fracture, 74, 89-97, 1995.

[14] J. Martinez and J. Dominguez, *Short Communication on the Use of Quarter-Point Boundary Elements for Stress Intensity Factor Computations*, Int. J. Num. Meth. Engn., 20, 1941-1950, 1984.

[15] M. M. Abdel Wahab, On the use of fracture mechanics in designing a single lap adhesive joint, Journal of Adhesion Science and Technology (ISSN 0169-4243), Vol. 14, No. 6, pp. 851-866, 2000.

[16] M. M. Abdel Wahab, I. A. Ashcroft, A. D. Crocombe, D. J. Hughes and S. J. Shaw, *The effect of environment on the fatigue of composite joints: Part 2 fatigue threshold prediction*, Composites part A, 32(1), 59-69, 2001.

[17] M. M. Abdel Wahab, I. A. Ashcroft, A. D. Crocombe and S. J. Shaw, *Prediction of fatigue threshold in adhesively bonded joints using damage mechanics and fracture mechanics*, Journal of Adhesion Science and Technology, 15(7), 763-782, 2001.

[18] M. M. Abdel Wahab, I. Hilmy, I.A. Ashcroft and A.D. Crocombe, *Damage parameters of adhesive joints with general triaxiality: Part 2 scarf joint analysis*, J. of Adhesion Science and Technology, to appear, 2010.

[19] M.M. Abdel Wahab, I.A. Ashcroft, A.D. Crocombe and P.A. Smith, *Numerical prediction of fatigue crack propagation lifetime in adhesively bonded structures*, International Journal of Fatigue, 24(6), 705-709, 2002.

[20] M. M. Abdel Wahab and G. De Roeck, *Dynamic testing of prestressed concrete bridges and numerical verification*, American Society of Civil Engineers, Journal of Bridge Engineering, 3(4), 159-169, 1998.

[21] R.A. Votsis, M. M. Abdel Wahab and M.K. Chryssanthopoulos, *Simulation of damage scenarios in an FRP composite suspension footbridge*, Key Engineering Materials, 293-294, 599-606, 2005.

[22] W. Ceulemans, M. M. Abdel Wahab, K. De Proft and G. Wets, *Modelling traffic flow with constant speed using the Galerkin finite element method*, World Congress on Engineering, The Proceedings of The International Conference of Applied and Engineering Mathematics, 993-999, London,1-3 July, 2009.

INTERPRETATION OF STRESS-STRAIN CURVE IN PIPELINE RESEARCH

J.-B.Wellekens[1], W. De Waele[2], R. Denys[2], S. Hertelé[2] and M. Verstraete[2]

[1] Ghent University, Belgium
[2] Ghent University, Laboratory Soete, Belgium

Abstract

For the design of on-shore pipelines installed in areas that are susceptible to ground movements and off-shore pipelines, axial stresses above yield must be considered. In such so-called strain-based design, knowledge of the stress-strain behaviour of the pipeline steel and girth welds is highly important. These behaviours are influenced by many factors, including: welding parameters, operation temperature, tensile test specimen geometry and orientation, and microstructure of the steel. This paper focuses on the influence of the tensile test specimen geometry and orientation, for the case of UOE formed pipes. As regards the geometry, it is concluded that the stress-strain diagram is most representative for a flat full-thickness test specimen. As regards the orientation, the yield stress is higher for transversal test specimens, as compared to longitudinally oriented test specimens.

Keywords pipeline steels, strain-based design, stress-strain curve, UOE, microstructure, anisotropy

1   INTRODUCTION

The mechanical properties of pipeline steels change during plate production and subsequent pipe forming. First, the rolling process is a source of anisotropy, producing differences in stress-strain behaviour between the directions parallel and perpendicular to the rolling direction. Second, pipes can be produced from flat plates in different ways. This paper focuses on the UOE process, illustrated in Figure 1. It is performed by three press processes (edge crimping press, U-ing press, O-ing press), followed by seam welding and a circumferential expansion [1]. Obviously, this cold forming process produces changes in the mechanical properties of the used steel.
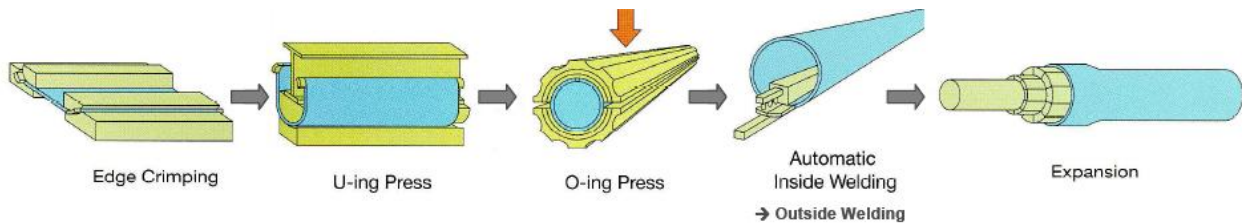
Fig. 1: Schematic illustration of production of UOE pipe.

The stress-strain behaviour of a steel is generally characterized by a tensile test. This paper discusses, for the specific case of UOE-formed pipes, the influence of test specimen geometry and orientation on the measured stress-strain behaviour.

2   GEOMETRY OF THE TENSILE TEST SPECIMEN

As regards common geometries of tensile test specimens in the pipeline industry, a distinction can be made between a *round bar* and a *flat strap* (full thickness) specimen.

Looking at a round bar specimen, the measured yield stress (YS) depends on the specimen diameter. This diameter is usually much smaller than the plate thickness, and thereby merely produces a measurement of local properties. This effect is pronounced for round bar specimens of girth welds, since these welds show a large degree of heterogeneity. Indeed, a weldment mostly consists of several weld runs, producing a mixture of coarse and fine microstructures. This results in heterogeneity in the thickness direction (Figure 2, above, [2]) and in the circumferential ('o' clock) direction (Figure 2, below, [3]). In the base metal, the microstructure also varies in the thickness direction. This phenomenon is due to the inhomogeneous cooling during plate production after rolling.
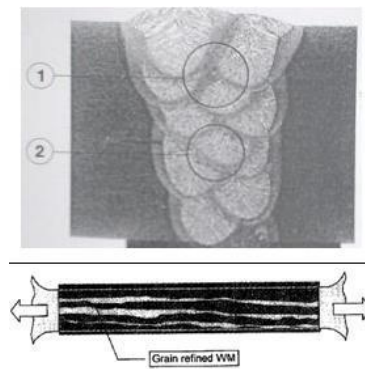
Fig. 2: Variations in the microstructure of a round bar tensile specimen, taken from a pipeline girth weld. Above: thickness direction [2], Below: circumferential ('o' clock) direction [3].

Considering the abovementioned, round bar specimens may produce stress-strain curves with limited representativeness in terms of the global structural behaviour. Therefore, to obtain an average value of strength properties throughout the entire thickness of the pipe, flat strap specimens of full pipe thickness are advised. This conclusion should, however, be nuanced for transversally oriented test specimens, since full thickness specimens have to be flattened in that case (see section 3.1).

3 ORIENTATION OF THE TENSILE TEST SPECIMEN

Several investigations reveal that the mechanical properties of pipeline steels are highly dependent on the orientation of the tensile test specimens, relative to the pipe axis. A distinction can be made between *transversally* (perpendicular to the pipe axis) and *longitudinally* (parallel to the pipe axis) oriented specimens. This observed heterogeneity is due to the steel rolling process, as well as the UOE pipe forming process. Asahi et al. [4] found that both yield stress and ultimate tensile stress in transversal and longitudinal direction are higher than their respective values of the original flat plate (Fig. 3). Differences between the transversally and the longitudinally oriented specimens are further discussed below.
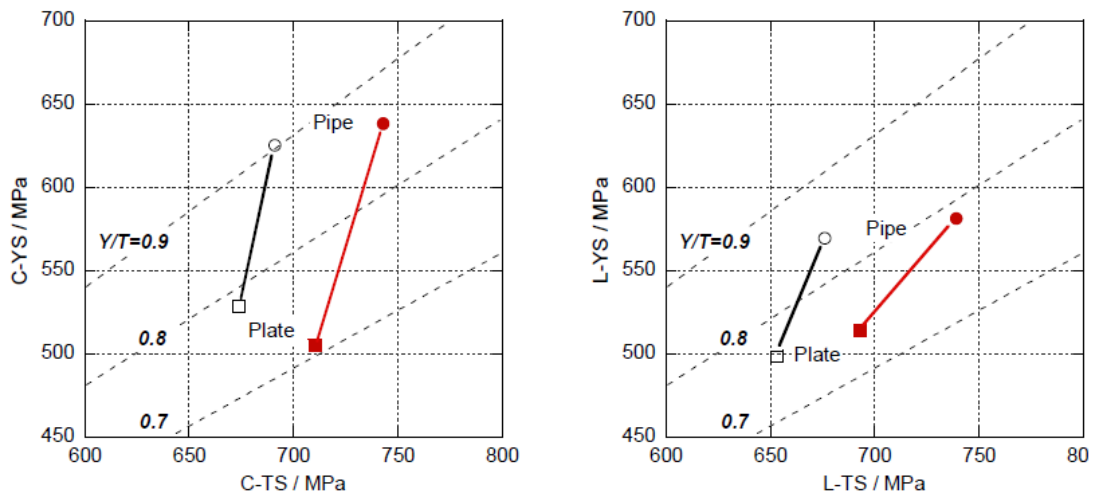
Fig. 3: Both yield stress and ultimate tensile stress increase due to UOE pipe forming [4]. Left: circumferential direction; right: longitudinal direction.

3.1 Transversally oriented specimen specimen

For the determination of the tensile properties of pipeline steels in the transversal direction, three methods can be applied: round bar specimens, flat strip specimens, and the ring expansion method. The flat strip specimen is in this case flattened, since a pipe is curved in the transversal direction. In the ring expansion method, a ring is taken from the pipeline and subjected to a radial expansion.

Several studies have shown that the flat strip specimens produce lower yield strengths than the round bar and ring expansion specimens [5-11] (Fig. 4 [10]). This effect can be assigned to the Bauschinger effect that occurs during the flattening of the strip specimen, as explained below.
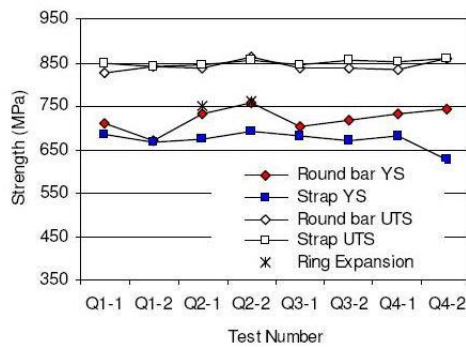
Fig. 4: A comparison of round bar, flat strip (strap) and ring expansion tensile test results [10].

During the cold forming of steel plate to its pipe configuration, the mechanical properties change at every point, due to a location-specific deformation cycle. A part of the plate undergoes a tensile load (A → B in Fig. 5). Then, in case of a flattened strip specimen, a second deformation cycle is imposed due to flattening. The material that saw a tensile cycle during pipe forming, is now subjected to a compression (B → D). If, eventually, the test specimen is subjected to a tensile test (D → C'), it can be seen that the yield strength has decreased from A (original plate) to A' (flattened strip specimen). [12-15].
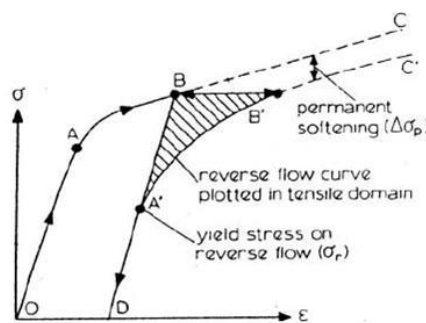
Fig. 5: Illustration of the Bauschinger effect.

Fig. 4 indicates that the yield stresses of a round bar test are similar to those of a ring expansion test. These values are, for transversally oriented specimens, considered the most representative. Preference is given to the round bar specimen, since this method imposes less practical issues than the ring expansion method.

3.2 Longitudinally oriented specimen

In order to determine the strength-properties in the longitudinal direction, two specimens are commonly used: the round-bar specimen and rectangular bar covering the full wall thickness. From Fig. 6 [10] it can be noted that the kind of test specimen has an influence on the measured yield and tensile strength. This variation originates from the microstructure tested. Using a rectangular bar, the testing is performed on a section containing both the coarse and fine grained microstructure which is found in the through thickness direction. On the other hand, the use of a round-bar specimen results in the testing of a section less than the wall thickness. This means it is susceptible to the local properties, depending on the position of the round bar specimen, another microstructure will be tested. Testing a fine grained section will unambiguous result in a higher measured yield and tensile strength, whilst a coarse microstructure will lead to a deterioration of the measured properties [6,8,9,11,16].

Therefore it is recommended to use a rectangular test specimen covering the full wall thickness. This will result in more representative measured data compared to the full pipe behavior. Besides, the preparation of a round-bar specimen requires a higher work load than the preparation of a rectangular bar.
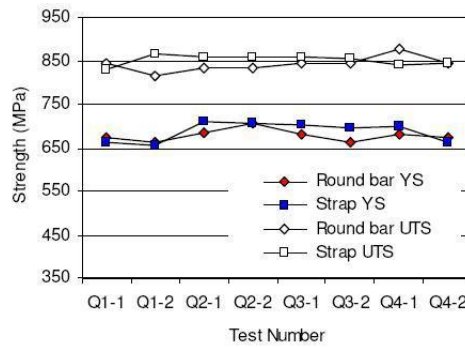
Fig. 6: Results of tensile tests on longitudinally oriented specimens [10].

The presence of anisotropy is also worth mentioning. From Fig. 7 a clear difference can be seen between the measured yield strength of a longitudinal and transversal round bar specimen. On the other hand, the tensile strength is comparable for both directions. This difference has most probably originated from the different amount of cold work in these two directions. Due to the pipe forming process, the yield strength of the material might increase [4, 16-30]. Another sort of anisotropy is noted in the right part of Fig. 7. From the elliptical shape of the fractured area it can be seen that the post-yield behavior in the thickness direction differs from the behavior in the testing direction.
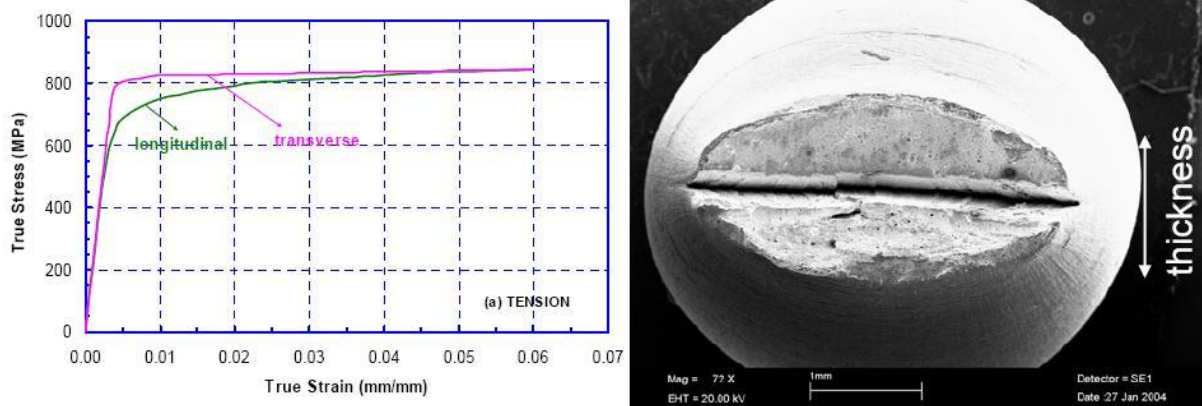
Fig. 7: Stress-strain behaviour of an X100 pipeline steel [17].

4   CONCLUSIONS

Defining the mechanical properties of pipeline steels is not straight forward. An overall picture cannot easily be provided since many factors affect the final tensile properties of pipeline steels. Therefore the testing conditions may never be neglected when the results are discussed.

From the literature review, it can be concluded that the use of a full thickness test specimen is more representative and less susceptible to scatter than a round-bar specimen, which only covers part of the wall thickness. Furthermore, the test specimen should not be subjected to any unnecessary plastic deformation during the testing phase, in order to keep the measured strength properties as close as possible to the full pipe behavior.

5   NOMENCLATURE

YS   yield strengh

UTS   Ultimate Tensile Strength

Y/T   Yield to Tensile ratio

WM   Weld Material

BM   Base Material

6   REFERENCES

[1]   K. Nagai, Y. Shinohara, S. Sakamoto, E. Tsuru, H. Asahi, T. Hara, *Anistropic Strain Aging Behavior of High Strength UOE Linepipe,* Proceedings of the Nineteenth International Offshore and Polar Engineering Conference, 56-60, Osaka, Japan, June 21-26, 2009.

[2]   R. Denys, *Testing for weld metal yield strength,* Mis-Matching of Welds, ESIS17 (Edited by K.-H. Schwalbe and M.Koçak), Mechanical Engineering Publications, 777-787, London, UK, 1994.

[3]   R. Denys, *Weld Metal Strength Mismatch: Past, Present, and Future,* Osaka, May 16, jaartal

[4]   H. Asahi, T. Hara, E. Tsuru, H. Morimoto, *Development and commercialization of high-strength linepipe,* Procdings of the Pipeline Technology Conference, Ostend, Belgium, October 12-14, 2009.

[5]   M. Hamada, S. Okaguchi, H. Shitamoto, Y. Komizo, *Tensile properties and deformation behaviour at the weld position of X100 line pipe steel,* Proceedings of the Pipe Dreamer's Conference, Pacifico Yokohama, Japan, November 7-8, 2002.

[6]   H. Asahi, T. Hara, E. Tsuru, H. Morimoto, et al., *Development and Properties of Ultra-High Strength UOE Linepipe,* Proceedings of the International Pipeline Conference, Calgary, Canada, October 4-8, 2004.

[7]   H. Asahi, T. Hara, E. Tsuru, H. Morimoto, et al., *X120 UOE Linepipe With Improved Properties and Varied Sizes,* Proceedings of the International Pipeline Conference, Calgary, Canada, September 25-29, 2006.

[8]   Z. Xiaoli, Z. Chuanjing, J. Lingkang, F. Yaorong, Z. Wenzhen, H. Chunyong, Z. Xinwei, G. Shaotao, *The micro structural characteristic parameters of high grade pipeline steel and its mechanical properties,* Proceedings of the International Pipeline Conference, Calgary, Canada, September 25-29, 2006.

[9]   H. Hillenbrand, A. Liessem, F. Grimpe, V. Schwinn, *Manufacturing of X100 Pipes for the TAP project,* Proceedings of the International Pipeline Conference, Calgary, Canada, September 25-29, 2006.

[10]   R. Klein, L. Collins, F. Hamad, X. Chen, D. Bai, *Determination of Mechanical Properties of High Strength Linepipe,* Proceedings of the International Pipeline Conference, Calgary, Canada, September 29 – October 3, 2008.

[11]   J. Johnson, M. Hudson, N. Takahashi, M. Nagase, A. Yamamoto, *Specification and Manufacturing of Pipes for the X100 Operational Trial,* Proceedings of the International Pipeline Conference, Calgary, Canada, September 29 – October 3, 2008.

[12]   P. Verleysen, *Modellering van Mechanisch Materiaalgedrag Partim: Plasticiteit en Visco-elasticiteit,* Ghent, Belgium, 2008.

[13]   J.B. Winkel, M. Rieder, H. Henein, T. Schulz, *Effect of Material Characteristics on the Properties of a Steel Pipe,* Proceedings of the 4th International Pipeline Conference, Calgary, Canada, September 29 – October 3, 2002.

[14]   J.B. Winkel, M. Rieder, H. Henein, *Evolution of the Bauschinger Effect During Fabrication of Micro-Alloyed Pipeline Steels,* Proceedings of the International Pipeline Conference, Calgary, Canada, October 4-8, 2004.

[15]   P. Thibaux, D. Van Hoecke, G. De Vos, *Influence of Forming and Flattening on the Measured Tensile Properties of Linepipe,* Proceedings of the International Pipeline Conference, Calgary, Canada, September 25-29, 2006.

[16]   H. Chen, L. Ji, Y. Feng, W. Xie, *Strain Aging Effect on Mechanical Properties of X80 High Strength Line Pipe,* Procdings of the Pipeline Technology Conference, Ostend, Belgium, October 12-14, 2009.

[17]   Y.-Y. Wang, M. Liu, *The Role of Anisotropy, Toughness Transferability, and Weld Misalignment in the Strain Based Design of Pipelines*, Proceedings of the Seventeenth International Offshore and Polar Engineering Conference, Lisbon, Portugal, July 1-6, 2007.

[18]   L. Ji, X. Li, H. Chen, C. Y. Huo, S. Gong, X. Zhao, *On the Relationship between Yield Ratio, uniform Elongation, and Strain Hardening Exponent of High Grade Pipeline Steels,* Proceedings of

the Seventeenth International Offshore and Polar Engineering Conference, Lisbon, Portugal, July 1-6, 2007.

[19]   Y.-Y. Wang, M. Liu, D. Rudland, D. Horsley, *Strain Based Design of High Strength Pipelines,* Proceedings of the Seventeenth International Offshore and Polar Engineering Conference, Lisbon, Portugal, July 1-6, 2007.

[20]   J.M. Treinen, W.E. Luecke, J.D. McColskey, P.P. Darcis, Y.-Y. Wang, *Anisotropic Behavior of X100 Pipeline Steel,* Proceedings of the Eighteenth (2008) International Offshore and Polar Engineering Conference, Vancouver, BC, Canada, July 6-11, 2008.

[21]   D.-H. Seo, J.-Y. Yoo, W.-H. Song, K.-B. Kang, *Development of X100 Linepipe Steel with High Deformation Capacity,* Proceedings of the 7th International Pipeline Conference, Calgary, Canada, September 29-October 3, 2008.

[22]   D.-M. Duan, J. Zhou, B. Rothwell, D. Horsley, N. Pussegoda, *Strain Aging Effects in High Strength Line Pipe Materials,* Proceedings of the 7th International Pipeline Conference, Calgary, Canada, September 29-October 3, 2008.

[23]   N. Ishikawa, M. Okatsu, S. Endo, J. Kondo, J. Zhou, D. Taylor, *Mass Production and Installation of X100 Linepipe for Strain-Based Design Application,* Proceedings of the 7th International Pipeline Conference, Calgary, Canada, September 29-October 3, 2008.

[24]   I. Takeuchi, *Property of X80 Grade SAW Pipes For Resistance to Ground Movement,* Proceedings of the 7th International Pipeline Conference, Calgary, Canada, September 29-October 3, 2008.

[25]   A. Liessem, G. Knauf J. Schröder, S. Zimmermann, M. Pant, C. Stallybrass, et al., *Investigation of the Stress-Strain Behaviour of Large-Diameter X100 Linepipe in View of Strain-Based Design Requirements,* Proceedings of the 7th International Pipeline Conference, Calgary, Canada, September 29-October 3, 2008.

[26]   T. Yoshida, T. Terasava, T. Hara, A. Tsuru, H. Morimoto, *Establishment of Commercial Production for High Strength UOE Linepipe up to X120,* Proceedings of the Nineteenth International Offshore and Polar Engineering Conference, Osaka, Japan, June 21-26, 2009.

[27]   H.-G. Hillenbrand, C. Kalwa, J. Schroeder, *Meeting Highest Requirements for the Challenge of the Nord Stream Project,* Procedings of the Pipeline Technology Conference, Ostend, Belgium, October 12-14, 2009.

[28]   A. Liessem, R. Rueter, M. Pant, V. Schwinn, *Production and Development Update of X100 for Strain-Based Design Application,* Procedings of the Pipeline Technology Conference, Ostend, Belgium, October 12-14, 2009.

[29]   E.Tsuru, Y. Shinohara, J. Agata,H. Asahi, *Dominant Factors for Buckling Resistance of UOE Linepipe Used in Strain-Based Design,* Procedings of the Pipeline Technology Conference, Ostend, Belgium, October 12-14, 2009.

[30]   H. Shitamoto, M. Hamada, S. Okaguchi, N. Takahashi, N. Yamamoto, I. Takeuchi, S. Fujita, *Effect of Thermal Aging on Deformability of X80<SAW Pipes,* Procedings of the Pipeline Technology Conference, Ostend, Belgium, October 12-14, 2009.

WEAR INVESTIGATION OF WET CLUTCH FRICTION MATERIAL

B. Genbrugge[1], P. De Baets[2], W. Ost[2]

[1] Ghent University, Belgium
[2] Ghent University, Laboratory Soete, Belgium

Abstract Wear of friction plates for wet clutch applications can result in a decreasing transmittable torque and the occurrence of vibrations throughout the entire drive chain causing loss of performance and discomfort. The need for a simple wear model exists to predict the lifetime of the clutch and to give an insight in the combined influence of the operational parameters such as pressure and speed. In this paper wear of paper-based friction material is investigated on a simplified SAE#2 test-rig using only one friction plate and one spacer plate. During engagement torque, applied pressure and sliding velocity are continuously monitored. After a set number of engagement cycles the thickness change of the friction plate is measured and surface topography of the spacer plate is registered. Based on Archard's wear law a specific wear rate is derived.

Keywords wet clutch, wear, specific wear rate

1   INTRODUCTION

Wet friction clutches consist of a pack of alternating friction- and separator plates anchored to the in- and outgoing axle by in- and external teeth. A normal force applied to the clutch pack by a piston, enables the clutch to transmit a friction torque between both axles. Wet clutches are commonly used as shift clutches in automatic transmissions for passenger cars and heavy duty off-road vehicles. As the number of engagement cycles increases during the lifetime of the clutch, the friction material wears out which results into a change in thickness of the plate and alteration of the friction surface. This over time will lead to a drop of the maximal transmittable torque and the end of life of the clutch.

Paper-based friction plates for wet clutches are produced by inbedding cellulose fibres into a resin. Wear of such materials is known to be depending on a large number of parameters. These parameters include the operational conditions of the wet clutch as well as the material properties of the friction plate itself. Experimental results show that elastic friction material is able to make a more uniform contact with the opposing separator. This uniform contact leads to a better heat distribution and reduced wear of the surface [1]. By decreasing the E-modulus, the occurrence of so called hot-spots, places of increased surface temperature on the separator, is reduced [2]. In the same way as the E-modulus, non-flatness of the separator results in increased wear-rates due to temperature differences [1]. These uneven temperature distributions may lead to failure of the clutch by coning [3].

Although performance of the clutch is improved by appropriate material selection during design and careful manufacturing of the friction plates, wear of the clutch during its lifetime greatly depends on the conditions of use, such as relative velocity at the start of engagement, and operational parameters. The latter include the inertia of the drive line and the preset applied normal force. No strict conclusions can be drawn concerning the influence of pressure. On one hand increasing pressure leads to a shorter stop time thereby reducing sliding distance and probably wear. On the other hand shorter stop times lead to an increased power input enhancing elevated surface temperatures and possible additional wear. What can be concluded is that combining high power load with high energy load always results in extreme wear [3]. It is remarkable to notice that wear of paper-based friction material seems to be more sensitive to changes in energy input due to inertia, rather than change in energy load due to velocity [3].

Noticing that sliding distance is the product of instant velocity and time, both pressure and velocity are combined in Archard's wear law. This wear law predicts steady state thickness change using a specific wear rate coefficient. Here the wear behaviour of a paper-based friction plate was studied based on Archard's law and under fixed conditions. Knowledge on the combined influence of operational parameters and the presence of a predictive wear model can lead to an optimized maintenance scheme and could make contributions to the development of new friction materials and to wet clutch design.

2   TEST RIG
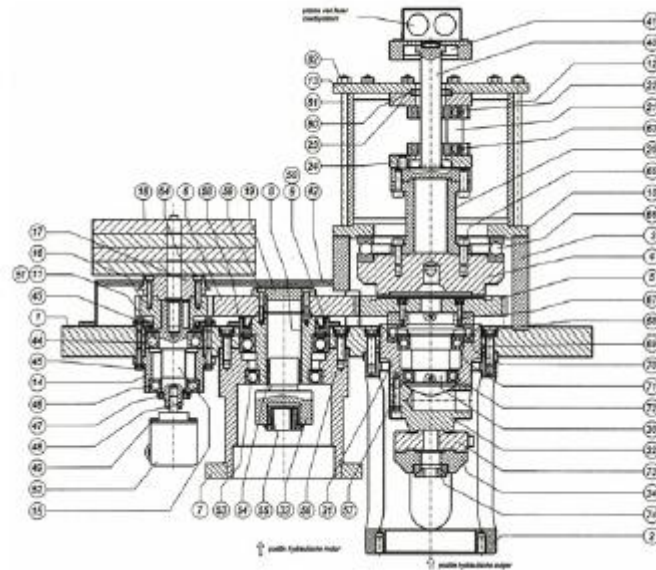
Fig 1: View of the test rig.

A test rig, similar to the apparatus described by Holgerson [4], is used with only one friction plate and one spacer plate. An overview is given in figure 1. Gears connect the inertia plates (18) to the test plate allowing for a 2:1 reduction. A hydraulic motor is connected to the middle gearwheel (6) through a one way clutch. A steel plate separator with inner diameter of 98 mm and outer diameter of 133 mm is mounted on the third gearwheel (5) and rotates at motor speed.

Two Rexroth-Bosch HACD-1 Digital Control Cards are programmed to accelerate the motor up to 700 rpm and to control linear movement of the hydraulic piston. Once the preset rotational speed is reached the motor stops. During one second the 0.1475 kgm^2 rotating inertia is allowed to spin freely as a result of the unidirectional coupling between the motor and middle gearwheel. After this small pause the hydraulic piston is send out to press the separator against the static friction plate. During engagement F_a is held constant at 11.5 kN until the kinetic energy of the rotating inertia is dissipated in the clutch and the inertia is stopped. After a pause of 5 sec this engagement cycle is repeated.

Automatic transmission fluid, Texametic 7045, is used at a rate of 0.85 l/min. No external cooling of the oil sump was used and inlet oil temperature never reached more than 35 °C.

2.1   Measurements

Two pairs of friction and separator material were submitted to approximately 4000 resp.3250 engagement cycles. Measurements were performed during and after the tests.

2.1.1   online measurements

During engagement normal force, torque, axial displacement of the piston, rotation speed of the inertia and inlet oil temperature were continuously monitored during the 1st minute of every 15 minutes. Signals were sampled at a rate of 600 Hz resp. 1000 Hz and processed with LabView 8.0.

2.1.2   offline measurements

To investigate wear of the friction plate, thickness measurements were performed at four points 90 degrees apart before, during and after completion of the test program. A digital micrometer was used with an accuracy of 0.01 mm.

For the second test specimen surface topography of the separator was inspected. Surface parameters R_t, R_{max}, R_z, R_a, R_{sk} and R_{ku} were acquired at six different positions (see figure 4) using a Hommel Tester T1000 Surface Scanner.

3 RESULTS

3.1.1 wear of paper-based friction material
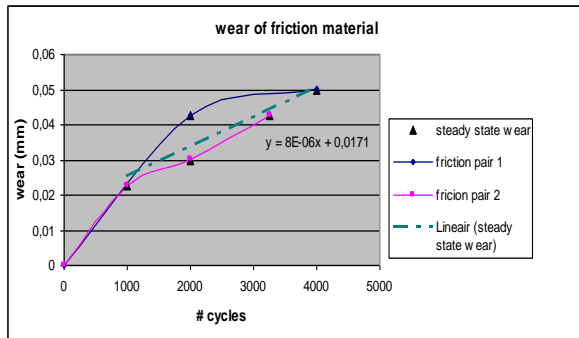
Fig 2: Wear of friction material with trendline.
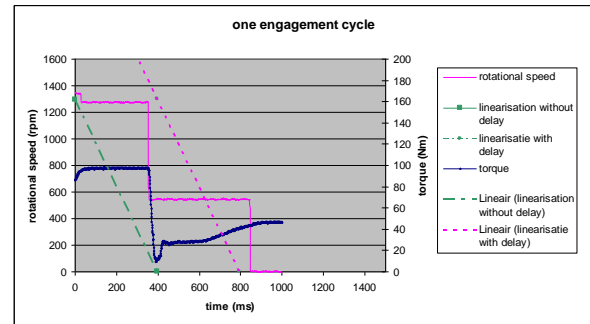
Fig 3: Rotational speed of inertia and torque curve during one engagement.

An average was calculated of the four measured thickness changes on the friction plate. Although wear of the paper-based friction material is very small, a drop in wear-rate can be seen approximatly halfway the testprogram. This suggest a running-in period of 2000 engagement cycles. Based on the wear results of the two test specimens and using Archard´s wear law (1), an estimation of the specific wear rate can be made for the subsequent steady state wear cycles.

$$\Delta h = K \cdot p \cdot s \qquad (1)$$

Sliding distance can be calculated by integrating instant sliding velocity over engagement time. As seen in figure 3, integration of the velocity data would be inaccurate as steps in the velocity curve occur. These steps are probably due to delay in signal processing before these signals reached the data acquisition. Because of the short stop time of 0,397 s it is a reasonable to suggest that velocity decreases linear with time. Sliding distance per cycle can be estimated as 780 mm. For a total of 4000 resp. 3250 cycles that makes approximately 3121 m resp 2535 m.

Calculation of the specific wear rate based on a steady state wear rate of $8 \cdot 10^{-3}$ mm/1000 cycles (see figure 2) results in $5{,}661 \cdot 10^{-15}$ m^2/N.

3.1.2 surface inspection of the separator

pair 2	# cycles	Rt	Rmax	Rz	Ra	Rsk	Rku
position 1	0	1.72	1.62	1.21	0.13	-1.386	7.774
	1000	2.38	2.38	1.34	0.13	-2.658	21.733
	2000	3.3	3.3	1.64	0.15	-2.153	19.393
	3250	2.66	2.66	1.3	0.13	-2.898	23.435

pair 2	# cycles	Rt	Rmax	Rz	Ra	Rsk	Rku
position 4	0	2.32	2.3	1.51	0.19	-1.953	10.371
	1000	1.95	1.92	1.38	0.15	-1.999	10.237
	2000	1.61	1.54	1.23	0.15	-1.623	7.218
	3250	1.3	1.26	1.08	0.14	-1.504	6.453
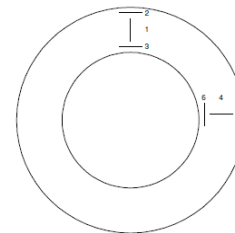
Fig 4: Positions of roughness measurement.

Table 1: Roughness measurement on position 1 and 4 of the second friction pair.

Based on experiments conducted on the same test rig under similar test conditions [5], it was expected that roughness parameter R$_a$ would increase when measured perpendicular to the direction of sliding i.e. positions one and four. This could be explained by the presence of wear debris between friction plate and separator making wear grooves in the sliding direction. Although grooves appeared after testing, no such trends could be noticed in the results presented here. This is probably due to the short period of testing.

4   CONCLUSIONS

1. Under the specified test conditions the running-in period for the tested paper-based friction plate and steel plate separator takes approximately 2000 engagement cycles.
2. Experimental results have shown a steady state specific wear rate for the paper-based friction material of $5{,}661 \ 10^{-15} \ \text{m}^2/\text{N}$. Better estimations might be achieved by improving accuracy of the velocity measurements and extending test duration.

5   NOMENCLATURE

Δh	thickness change	m
F_a	axial force	N
K	specific wear rate	m^2/N
p	contact pressure	Pa
s	sliding distance	m

6   ACKNOWLEDGEMENTS

7   REFERENCES

[1] Barker K., The effect of separator flatness on the performance and durability of wet friction clutches, International Congress and Exposition, Detroit, March 1993
[2] Zagrodzki P., Truncone S.A., Generation of hot spots in a wet multidisk clutch during short-term engagement, Wear 257 (2003)
[3] Lloyd A.F., Anderson J.N., Bowles L.S., Effects of operating conditions on performance of wet friction materials: a guide to material selection, SAE Technical Paper 881280, International Off-higway and Powerplant Congress and Exposition, Milwaukee, september 1988
[4] Holgerson M., Apparatus for measurement of engagement characteristics of a wet clutch, Wear 213 (1997), 140-147
[5] Dekeyser K., Slijtagegedrag van frictiematerialen voor oliegesmeerde lammellenkoppelingen, masterthesis, Universiteit Gent, 2007

FATIGUE BEHAVIOUR OF THREADED COUPLINGS - EXPERIMENTAL RESEARCH

Bruno Meertens[1], Patrick De Baets[2], Wim De Waele[2], Jeroen Van Wittenberghe[2]

[1] Ghent University, Belgium
[2] Ghent University, Laboratory Soete, Belgium

Abstract In this article the fatigue behaviour of threaded connections is studied, as used in oil country tubular goods (OCTG). Some manufacturers have designed their own couplings (so called 'premium connections') and they claim having an improved fatigue life or better sealability. This study will compare different coupling designs with the standard API connection. The methods used to compare the different designs are based on two-dimensional finite element analyses. Experimental research is conducted to validate the results of the FEA. The experimental research consists of a 4-point bending fatigue test, which will result in a SN-curve for the threaded connection. Based on numerical and experimental results a performance factor is deduced for the particular connection design. This factor will be used to find the best design of threaded couplings. As eventual goal of this study, with the insights gained, a threaded connection with optimized fatigue life and sealability will be designed.

Keywords threaded connections, fatigue, experimental, finite element model

1   INTRODUCTION

Threaded connections are used to couple tubular members together. The coupling consists of a male member, also known as the *pin*, which is made up into a female part, also known as the *box*. Threaded connections are commonly used to connect pipe strings where it is not possible to connect them by welding because the pipes should be frequently coupled and uncoupled. This is especially the case for drill strings and offshore production risers.

In offshore applications, those connections are subjected to cyclic loads due to currents, the tide, movement of the oil platform... For drill strings the most common (between 65% and 75% [1-3]) failure modes of threaded connections are caused by fatigue. Failure of the connection is a costly problem in the oil and gas industry and it has a serious impact on the environment. Fatigue cracks in threads commonly occurs at the root of the last engaged thread (LET, Figure 1) [4, 5]

Threaded connections can be divided in two main categories, standard connections and premium connections. Standard connections are defined by the API 5B and API 5L specifications [6, 7]. Premium connections are designed to have a better resistance to fatigue and/or optimised sealing properties.

The objective of this research is to define a performance factor. This performance factor can then be used to compare different threaded connection designs. The parameters in the performance factor should be found in numerical studies of the designs. After that, the numerical studies are validated by experiments.

The final goal of this study is to design a threaded connection with an optimised fatigue life and sealability.

2   NUMERICAL RESEARCH

2.1   2D axisymmetric model

The performance analyses of threaded connections using finite element models are nowadays replacing the use of full-scale tests in the design phase. The model is a two dimensional axisymmetric model. The main advantage to use a 2D axisymmetric model compared to a full 3D model is the reduced calculation time and it is easier to change subtle details to the geometry. The disadvantage of the 2D axisymmetric model is that it does not take into account the thread helix and the thread runout region. Zhong A. [8] calculated the Von Mises stresses by means of a 3D FEA of a threaded connection and he showed that the stresses are approximately axisymmetric. Zhao et al. [9] showed that the threads can be modelled as an axisymmetric ring when the lead angle of the thread is small enough. Thus, the results of a 2D model are in good agreement with full 3D models.

2.1.1   Geometry
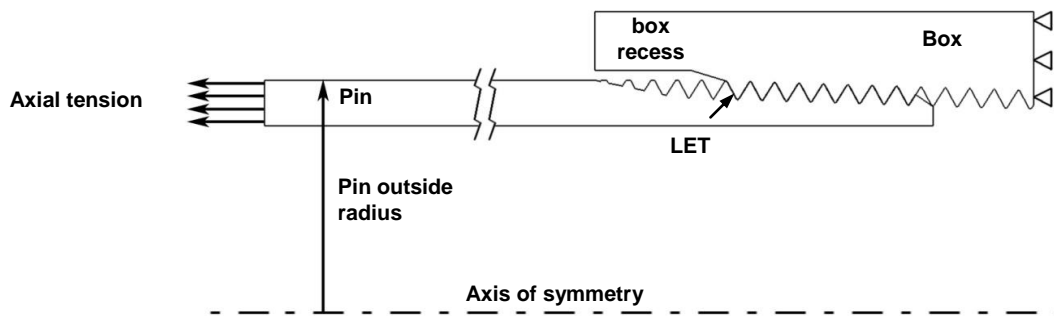
Figure 1: 2D axisymmetric model of the standard API Line Pipe connection

Figure 1 shows the 2D axisymmetric model of the standard API Line Pipe connection. The finite element analyses are carried out using the commercial FEA software package ABAQUS® 6.8-1. The nominal size of the connection is 1 inch according to the API 5B specifications [6].

2.1.2   Boundary conditions and loads

Because the connection is symmetric, only a half connection is modelled. On the right side of Figure 1 the boundary conditions are defined in such a way that the model cannot move parallel to the axial direction, hence introducing a plane of symmetry.

To maintain a sealed and secured connection while being subjected to external loads, the connections are commonly preloaded. With conical connections (like the API line pipe connection) this can be done by tightening the pin and the box with a specified torque, the "*make-up*" torque. In a 2D axisymmetric connection make-up is modelled by an overlap on the threads of pin and box, corresponding to the specified number of make-up turns.

On the left side of Figure 1 the load is applied. The load is modelled as an axial surface stress. It is applied in 2 stages. First a load of 100 MPa is applied, in a second stage the load increase to 150 MPa. Typical in-service values of stresses ranging from 30 to 150 MPa [10].

2.1.3   Material properties

The material of the threaded connections is API Grade B steel with yield strength of 299.8 MPa, an ultimate tensile strength of 575 MPa. The corresponding elongation is 23%. The model uses a Young's modulus of 208 GPa and a poisson coefficient of 0.3. The material properties match to the properties specified by API 5L [7] (Table 1).

Table 1: material properties specified by API 5L

Material	Yield Strength, minimum [MPa]	Yield Strength, maximum [MPa]	Ultimate Tensile Strength, minimum [MPa]	Ultimate Tensile Strength, maximum [MPa]
Grade B	241	448	414	758

2.2   Analyses of the standard API Line pipe and modified Line pipe connections

2.2.1   Standard connection

The results from the FEA simulation are shown in the figures below. Figure 4 shows the relative distribution of the force over the thread of the connection. It can be seen that the LET take the greatest part of the load. Fatigue cracks nucleate at the root of the LET, because there the stresses are the highest (Figure 2). On Figure 5 the opening between the thread can be seen. This is defined as the perpendicular distance between the thread profile of the pin and the profile of the box. The threads are numbered as in Figure 3. These results will be used to compare modified designs to the standard connection.
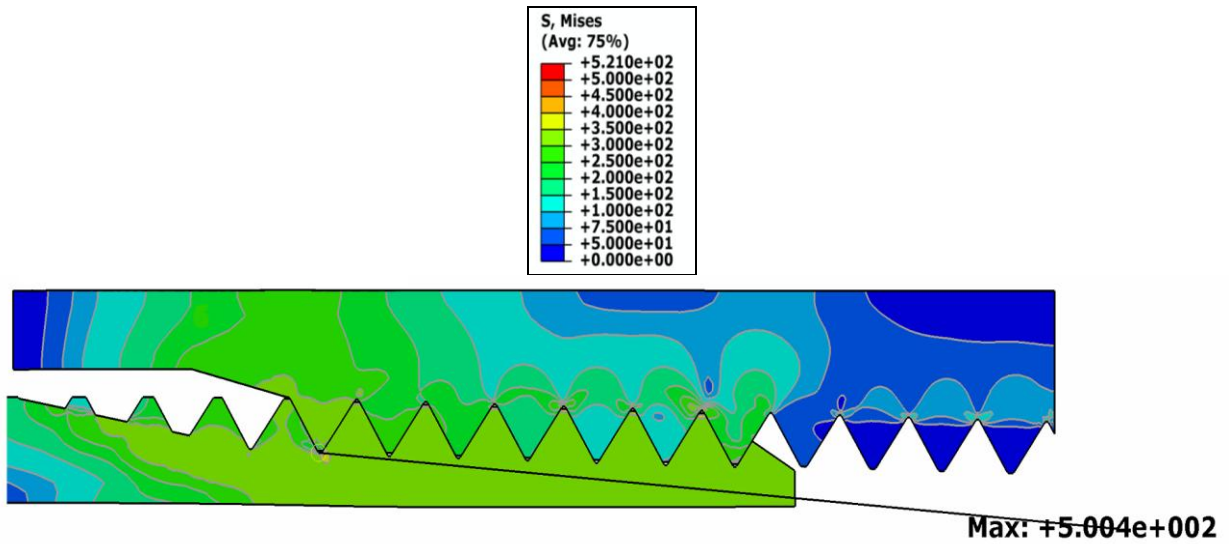
Figure 2: stress distribution with a load of 100 MPa
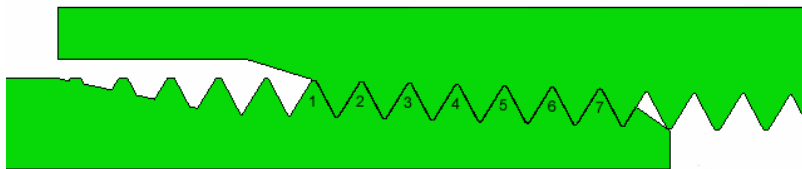
Figure 3: thread numbers
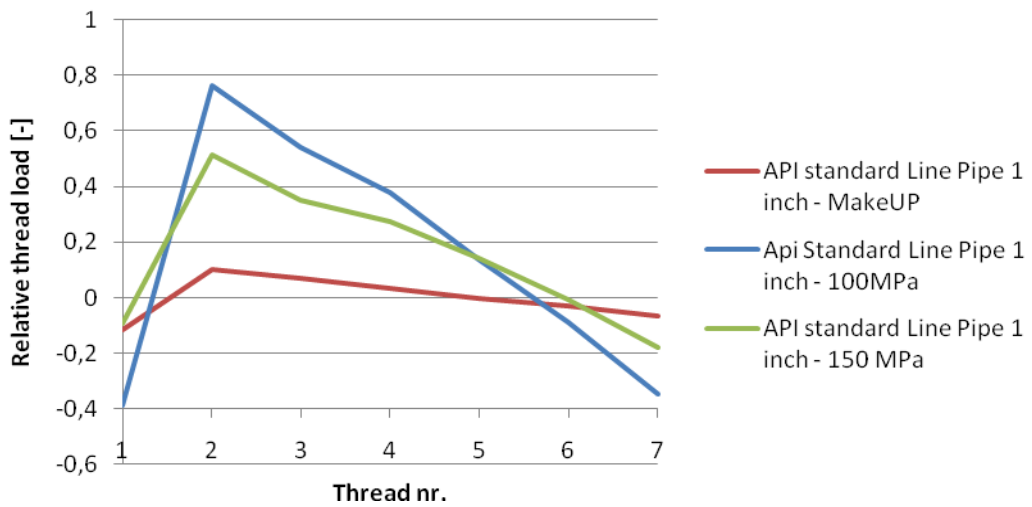
Figure 4: Thread load for the standard API line pipe connection

opening 1 inch norm
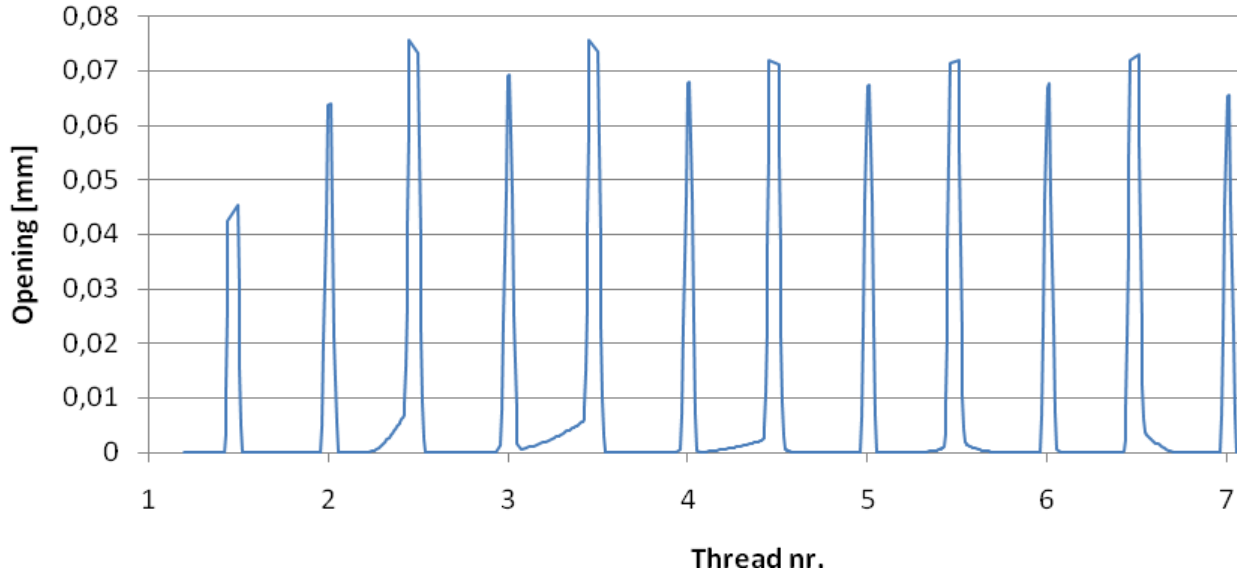
Figure 5: opening for the standard API line pipe connection

To compare the different coupling designs, the surface below the curve (Figure 5) will be used as a measure for the opening between the threads of the connection. For the standard 1" API Line Pipe connection, this surface is 0.1250 mm².
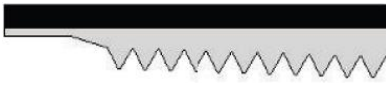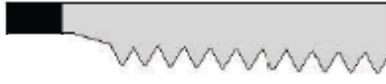
2.2.2 Modified connections
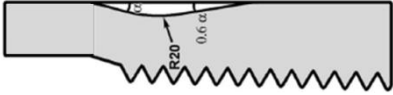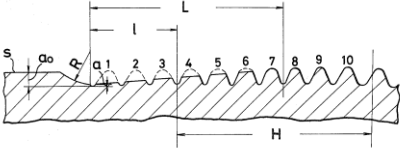
To distribute the forces more evenly over all the threads the stiffness of the box is reduced. Due to the stiffness reduction, the box will deform a little more and the connection force will be better rearranged over the threads of the connection. This will reduce the stresses in the root of the LET and hence increasing the fatigue life of the connection. The principles of modified connections a-d (see Table 2) are based on stiffness reduction of the box.

The modified connections e-f use the principle that a reduced height of the LET will diminish the threadforce taken by the LET and thus reducing the stresses at the root of the LET.

Connection g uses the principle of a stress relief groove to have a better flow for the stress and thus reducing the stress intensity factor in the root of the threads.

Table 2: Modified connections

Modified Connections
a) Reduction of wall thickness of the box.
b) Reduction of box recess
c) Stiffness gradient according to DeLange and Evans [11]

d) Waisted groove according to Verdillon [12]
e) Crest cut-off threads according to Sinichi Nisida [13]
f) Redesign LET according to Tsukano [14]   Tsukano proposes to redesign the last engaged thread (LET) of the pin by reducing its height of about 70-percent.
g) Relief groove pin according to Weiner [15]   The optimum relief groove should have a diameter which has a cross-sectional amount of inertia of about 30 percent of the cross-sectional moment of inertia of the drill collar.

2.2.3   Comparison between different connections

The different designs will be compared when subjected to a load of 100 MPa, because with this load the FEA model is still mostly elastic.

Figure 6: Load distribution over the threads (100MPa)

The ideal connection should have the load distributed equally over all the threads. This is in practical condition never achieved, but the design that spread his load most evenly is the one where the wall thickness is reduced with 2mm. This connection has an optimised fatigue life, which will be validated with experimental tests.

54

Table 3: Opening between threads

Name connection	Surface below opening curve [mm²]
norm	0.1250
Wall Thickness-1	0.1353
Wall Thickness -2	0.1409
recess-1	0.1390
recess -2	0.1388
recess -3	0.1385
recess -4	0.1380
recess -5	0.1373
Stiffness gradient 2°	0.1390
Stiffness gradient 4°	0.1388
Stiffness gradient 6°	0.1386
Stiffness gradient 8°	0.1383
Stiffness gradient 10°	0.1380
Stiffness gradient 12°	0.1376
Patent 6752436	0.1016
Patent 4189975A	0.2582
Redesign LET	1.12254
Relief Groove Pin	0.1110

A minimal value in Table 3 is desired to have an optimal seal capacity. The design with the smallest value is the design according to Verdillon [12]. Most of the connection designs are situated in a small range between [0.10 mm² – 0.14 mm²].

3 EXPERIMENTAL RESEARCH

3.1 Description of the test setup

A four-point bending fatigue setup will be used to validate the results of the numerical simulations. The test specimens are the same as those in the numerical simulations. They consist of two threaded pipe segments connected by a 1" API Line Pipe coupling or a modified coupling. The four-point bending setup gives a constant bending moment in the section comprising the coupling. This setup will measure the number of cycles which the coupling can sustain at a specified stress. To detect a failure, the connection is put under pressure. If a pressure reduction is observed, it means that there is a leak in the coupling and thus the connection has failed. The experimental program is part of the future work of this study.

3.2 Comparison of SN-curves from different premium connections

To assess the fatigue life of a structure, SN-curves are commonly used. Figure 7 shows SN-curves of different premium connection found in literature. The curves found by the 4-point bending fatigue test will be compared with the Wöhler-curves of the premium connection. The main objective of this research is to find a design with an optimal fatigue life.
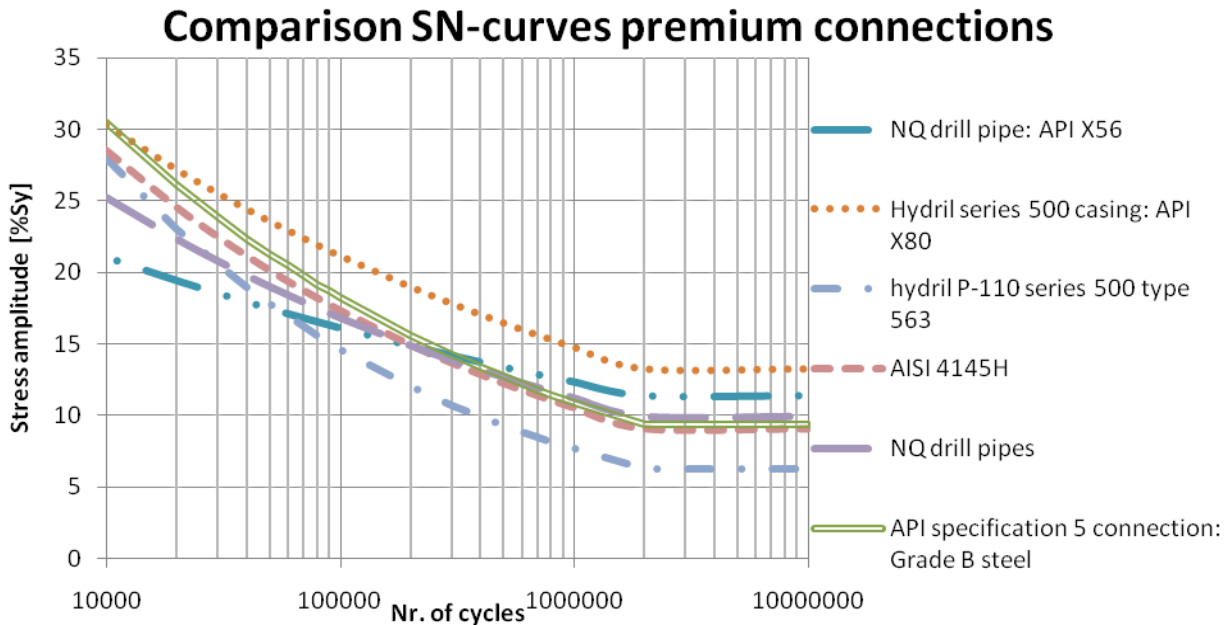
Figure 7: SN-curves premium connection

4   PERFORMANCE FACTOR P

A connection that has an excellent fatigue life but no sealing capacities is not usable in the oil and gas industry. This is why a performance factor is introduced. This is a factor in function of the thread opening (*o*) and the distribution of the thread forces (*F*) of the threaded connection. The thread forces are a measure for the fatigue life of the connection like mentioned above. To assess the sealing capacity of a connection, the opening between the thread of the coupling will be used.

$$P(F, o) = \frac{\alpha * \frac{1}{F}}{\beta * o} \tag{1}$$

5   NOMENCLATURE

LET   last engaged threads

Pin   male part of the connection

Box   female part of the connection

F   force   N

o   opening   mm

6   ACKNOWLEDGEMENTS

7   REFERENCES

[1]   M. J. Knight*, et al.*, "Controlled failure design of drillstring threaded connections," *Fatigue & Fracture of Engineering Materials & Structures,* vol. 26, pp. 1081-1090, Nov 2003.
[2]   J. C. R. Plàcido*, et al.*, "Fatigue Analysis of Aluminum Drill Pipes," *Materials Research,* vol. 8, pp. 409-415, 2005.
[3]   G. F. Miscow*, et al.*, "Techniques to characterize fatigue behaviour of full size drill pipes and small scale samples," *International Journal of Fatigue,* vol. 26, pp. 575-584, Jun 2004.

[4]   K. A. Macdonald and J. V. Bjune, "Failure analysis of drillstrings," *Engineering Failure Analysis,* vol. 14, pp. 1641-1666, 2007.
[5]   L. Bertini*, et al.*, "Fatigue on drill string conical threaded connections, test results and simulations," in *International fatigue congress*, Atlanta, Georgia, 2006.
[6]   API, "API specification 5B," in *Specification for threading, gauging and thread inspection of casing, tubing and line pipe threads (U.S. Customary Units)*, ed, 1996.
[7]   API, "API specification 5L," in *Specification for Line Pipe*, ed, 2000.
[8]   A. Zhong, "Thread Connection Response to Critical Pressures," *Abaqus Users' Conference,* pp. 690-706, Paris, France, May 2007.
[9]   H. Zhao*, et al.*, "Stress-intensity factor for a semi-elliptical surface crack at the thread root of a screwed-pipe joint," *Computers & Structures,* vol. 59, pp. 419-424, May 1996.
[10]   M. J. Knight and F. P. Brennan, "Fatigue life improvement of drill collars through control of bore eccentricity," *Engineering Failure Analysis,* vol. 6, pp. 301-319, Oct 1999.
[11]   R. W. DeLange and M. E. Evans, "Threaded and coupled connection for improved fatigue resistance," US 6,609,735 B1, 2003.
[12]   L. Verdillon, "Fatigue-resistant threaded bevelled tubular element," France Patent US 6,752,436 B1, 2004.
[13]   S. Nisida*, et al.*, "Screwed connection having improved fatigue strength," US 4,189,975, 1980.
[14]   O. Vaisberg*, et al.*, "Fatigue of drillstring: State of the art," *Oil & Gas Science and Technology-Revue De L Institut Francais Du Petrole,* vol. 57, pp. 7-37, Jan-Feb 2002.
[15]   P. D. Weiner, "A means of increasing drill collor connection life," *Journal of engineering for industry, ASME,* vol. 95, pp. 243-246, 1973.

Afternoon Session 2

Chairman:
Matthias Verstraete, Laboratory Soete, Ghent University, Belgium

TRACTION AND WEAR MECHANISMS DURING ROLL-SLIP CONTACT

J. De Pauw[1], J. Van Wittenberghe[1], P. De Baets[1]

[1] Ghent University, Laboratory Soete, Belgium

Abstract In the transportation industry every vehicle that makes contact with the road and propels itself, is subjected to roll-slip in the wheel-road interface. Therefore a good understanding of this phenomenon is important. This article describes roll-slip contacts in general, with extra attention for the wheel-rail contact which is commonly used. Firstly the contact area and the pressure distribution that occur when a normal load is applied between two bodies is discussed. On this base, the traction mechanisms for static and rolling configurations are shown. Lastly, wear mechanisms and two different wear maps are shown which are very useful and commonly used in wear mapping of roll-slip contacts. A good agreement with field measurements can be obtained.

Keywords Roll-slip contact, wear, traction, friction

1   INTRODUCTION

The contact mechanics in rolling and roll-slip problems have been investigated for a long time, in particular in transport engineering, where the oldest frequently cited paper dates from 1926 [1]. In this sector traction is needed for the propulsion of trains, cars and other vehicles. A high traction coefficient is required for fast acceleration and braking. To optimize this traction, a theoretical description is needed. This optimization is not only beneficial for faster accelerating and braking, a higher traction coefficient can also lead to vehicles that are able to drive on steeper slopes.

Roll-slip contact also occurs in gears, bearings and transmission belts, where the traction coefficient is a disadvantage and a source of energy loss.
In a gear the entire interacting tooth flanks roll and slip simultaneously over each other except at the pitch diameter, where the contact is only obtained by pure rolling. Traction between the tooth flanks is undesirable because it causes an opposing torque, generates heat, and encourages rolling contact fatigue which can lead to surface fatigue [2].

Research in roll-slip problems results in a better understanding of the mechanisms, and lead to more accurate theories. These theories can be used to develop higher traction coefficients and a better wear control, which is beneficial for traction applications.

In this article we will focus on roll-slip problems in general, with special attention to wheel-rail contact which are often used in the railway industry.
The contact area and corresponding pressure distribution will be discussed for simple contact geometries and more complex wheel-rail contact geometries.
Consecutive, traction modeling in the contact area is discussed. This modeling is necessary for traction applications.
Finally, we highlight wear mechanisms and wear regimes in roll-slip contacts, since they affect the previously discussed points, and since wear is an important economical factor. Again the wheel-rail problem will be used as example.

2   CONTACT MODELING

The contact between two surfaces gives rise to an area of contact, and a pressure distribution over this contact area. If the surfaces have a simple geometry, the contact theory of Hertz (1881) can be used for calculating the contact area and the pressure distribution. For contacting surfaces that have a more complex shape, there is in most cases no closed form analytical solution. Boundary- and finite element programs [3, 4] can calculate the contact area and the associated pressure distribution.

2.1 Hertz contact

As previously stated the Hertz contact theory can only be used if the contacting bodies have a simple geometry. A geometry is simple if the curvature of the body is constant, and has at most two different curvatures in perpendicular direction, like a smooth sphere, smooth cylinders or flat plane. The Hertz contact theory can be used for all combinations of the three previous states bodies, accept the plane-plane contact.

Beside the geometry condition, two other conditions should by fulfilled. The deformation has to be fully elastic and the surfaces are supposed to be frictionless.

If two bodies touch each other in the absence of a normal load, there will be a point or line contact, depending on the contacting surfaces. An initial point contact will grow with increasing load to a circular or an elliptical contact area, while a line contact will develop to an elongated elliptic contact.

In the case of a sphere with a radius R_1 loaded against a flat plane with a force F, the radius a of the contact area will be:

$$a = \sqrt[3]{\frac{3}{2} \frac{F \cdot R_1}{E'}} \tag{1}$$

Where E' is the effective modulus of elasticity, defined by:

$$\frac{1}{E'} = \frac{1 - v_1^2}{2E_1} + \frac{1 - v_2^2}{2E_2} \tag{2}$$

The pressure distribution is parabolic over the contact area, with the maximum pressure p_{max} occurring in the centre of the contact area.

$$p_{max} = \frac{3 \cdot P}{2 \cdot \pi \cdot a^2} \tag{3}$$
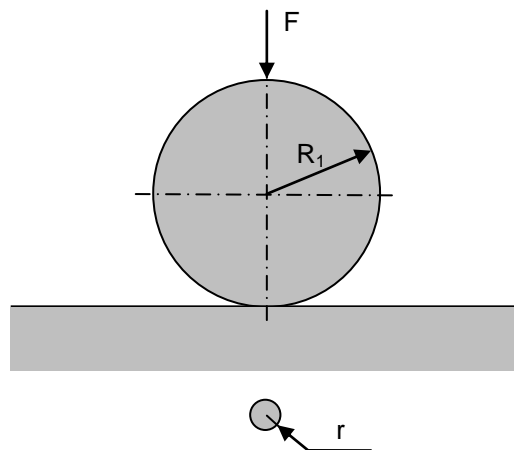
Figure 1. Contact area in a sphere-plane contact

The contact theory of Hertz assumes smooth surfaces, so no surface roughness is taken into account. However, every engineering surface has a certain surface roughness. The simplest model to take surface roughness into account is that of Archard [5], where the surface of the sphere with radius R_1 is covered with an evenly distribution of identical spherical protuberances of radius R_2, where $R_1 >> R_2$. A mathematical solution for the contact area is available.

More recent experimental research about the influence of surface roughness specific in roll-slip contact is given by L. Xiao et al. [6]. Where it is found that rough surfaces have a higher friction coefficient than smooth surfaces, and the friction coefficient is function of the slip S.

2.2   Non Hertz contact

If the interacting surfaces have a more complex shape, boundary - and finite element programs can be used to calculate the contact area and the corresponding pressure distribution. In contrast to the Hertz contact model, it is not necessary that the behavior is fully elastic; rough surfaces and strain hardening can be included in the model.

Roll-slip contact between complex shapes can be found in particular in the railway industry, where steel wheels running on steel rails provide the necessary traction for propulsion. The contact area and the pressure distribution can by calculated by general finite element programs like Abaqus® or Ansys®. Wheel/rail contact simulations can also be performed by dedicated programs, each with their specific algorithm, like *Contact* [7], *Fastsim* [7] or *Non-Hertz* [8].
The first two algorithms are given by Kalker, who uses a half-space assumption that is not restricted to elliptic contact. The *Contact* program divides the contact area in small rectangular elements in which the traction is constant, the adjacent elements interact with each other using an influence function approach.
The weakness of this program is the numerical integration that is required, so online calculations for transient vehicle simulations are impossible. The *Fastsim* algorithm uses the Kalker's simplified theory, in which a constant stress gradient is assumed until the limiting traction force is reached. The traction bound is defined as the normal force multiplied by the coefficient of friction.

Figure 2 shows a S1002 wheel profile and a UIC60 rail profile. Depending on their relative position to each other, the position and shape of the contact area vary, as clearly shown in Figure 3. Also the pressure distribution will be affected.
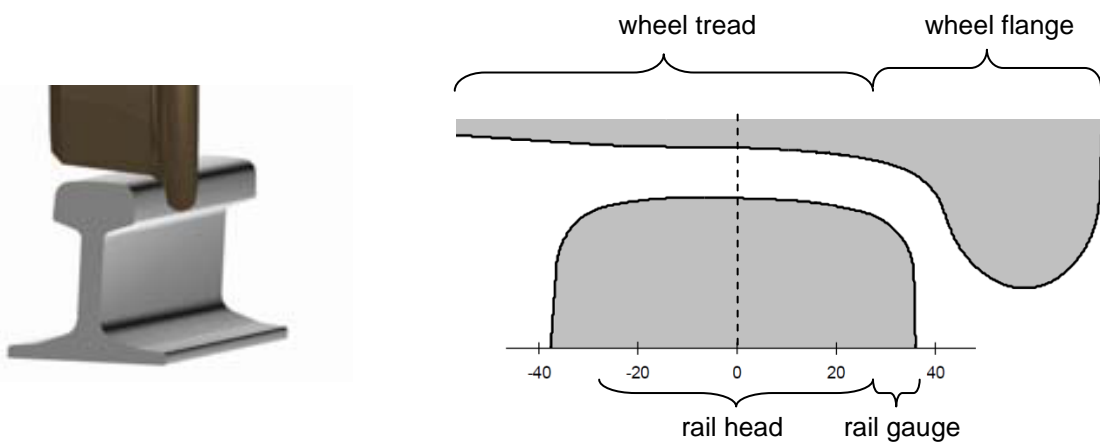
Figure 2: left: general view, right: surface detail with wheel profile S1002 and rail profile UIC60
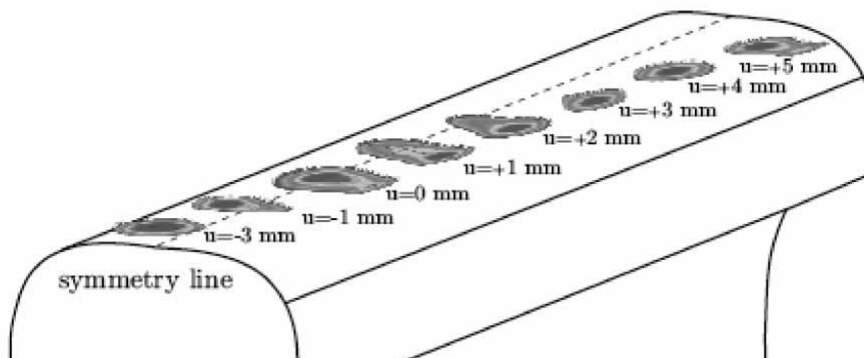
Figure 3. Comparison of the position and the shape of the contact area, depending on the variation of the lateral shift *u* (positive towards the gauge face) [9]

If the lateral displacement *u* increases extraordinary, there will be contact between the wheel flange and the rail gauge. This additional contact disturbs the common contact area between the rail head and the wheel tread, leading to a contact area that is characterized by two pressure peaks, as shown in Figure 4.
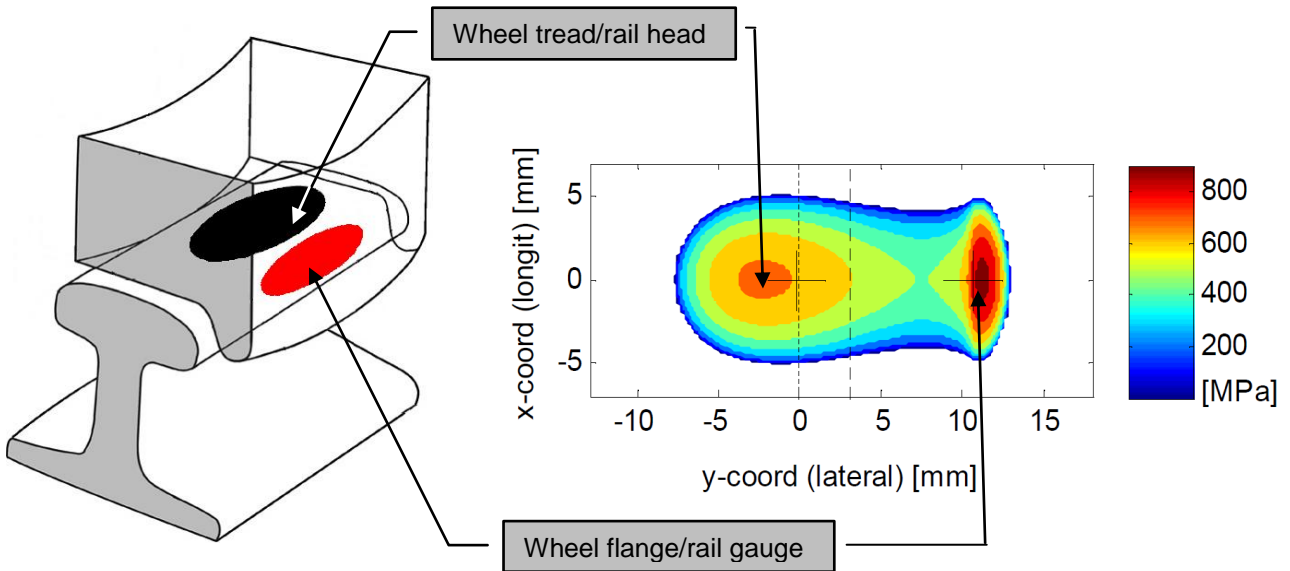
Figure 4: Wheel flange/rail gauge contact, left: overview, right: pressure distribution

3   TRACTION MODELLING

Traction is required between two bodies if propulsion or braking takes place. This phenomenon has to be well understood and controlled for accurate function of trams or trains.

When a vehicle accelerates, no excessive macroscopic slip may take place, otherwise the vehicle will hardly depart, and significant wear will occur on the wheels and the rails.

In the case of braking, too much macroscopic slip is also unacceptable because of the high wear rate. A slip ratio of 100% is totally undesirable for the reason that a flat spot will occur on the wheel, this flat spot affects the roundness of the wheel which leads to vibrations in the rail vehicle, thus decreasing ride comfort.

Traction is often considered as a black box, where only the experimental relation between the traction coefficient and the slip is known (Figure 5). The slip S is defined as the ratio between the sliding velocity and the mean velocity.

$$S = 2 \cdot \frac{v_1 - v_2}{v_1 + v_2} \qquad (4)$$
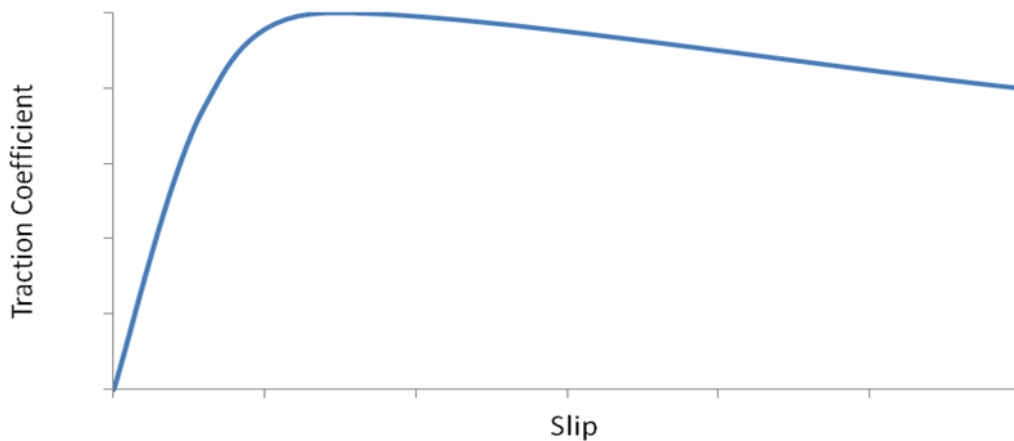
Figure 5: General curve of traction coefficient in function of slip

Pure rolling takes place in the contact area when the surface velocity of the two bodies is equal. In the case of two equal cylinders in contact, they must have the same rotational speed. If the circumference velocity are unequal, the rolling motion is accomplished with sliding.

If two contacting bodies experience a tangential force Q, a shear stress will arise in the contact area. No macroscopic sliding takes place if the tangential force is smaller than the limiting friction force μF. From the

microscopic point of view, a shear stress q occurs in the contact area. The distribution of the shear stress is not predictable in advance and has to be found by trial and error, until all the specific boundary conditions are fulfilled.

The effect of a tangential force in a static Hertz contact (Figure 1) has been studied by Mindlin [10]. If no relative sliding between the two surfaces takes place, a shear stress q is proposed as shown in Figure 6. At the edge of the contact the shear stress becomes infinite, which is physically impossible. Mindlin supposed that local slip will occur where the shear stress is bigger than the limiting friction stress μp. The contact area is divided in two sections, a stick zone where no relative motion between the surfaces takes place, and a slip zone, where the shear stress is the limiting friction stress.
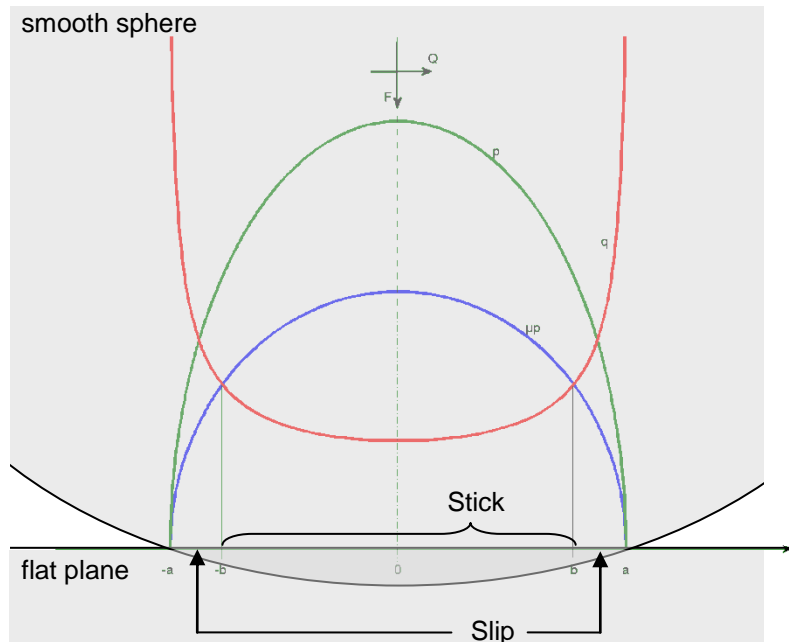
Figure 6: pressure (p) and shear (q) distribution in a static contact area

In pure rolling or roll-slip contacts, the contact area is divided in a stick (pure rolling) and slip region [11]. However the boundary conditions differ from those in the static case, as previously described. In the stick area, no slip may occur (5) and the shear stress must be lower than the limiting friction stress (6)

$$S = 0 \tag{5}$$

$$|q(x,y)| < \mu \cdot p(x,y) \tag{6}$$

In the slip area the shear stress equals the limiting friction stress (7), and the direction of slip must oppose the tangential force (8)

$$|q(x,y)| = \mu \cdot p(x,y) \tag{7}$$

$$\frac{q(x,y)}{|q(x,y)|} = -\frac{S(x,y)}{|S(x,y)|} \tag{8}$$

Any configuration of stick and slip zone that respects the four boundary conditions is a solution of this problem. For tractive rolling of elastic cylinders which have an elongated elliptical contact area, Carter [1] presented a shear stress distribution q with associated stick and slip area as shown in Figure 7.
If the slip S increases a little, the slip area will be enlarged which leads to a higher amount of shear stress in the contact area. The integral of this shear stress over the contact are is the tractive force, which also enlarges with increasing slip. This relation can be seen on an experimental traction curve (Figure 5) as the rising slope of the curve.

For pure elliptic or circular contact areas a similar solution can be found. The position of the stick area is located at the trailing edge to respect boundary condition (7), the contour of this area is commonly assumed to be 'pear' or lemon' shaped [11].
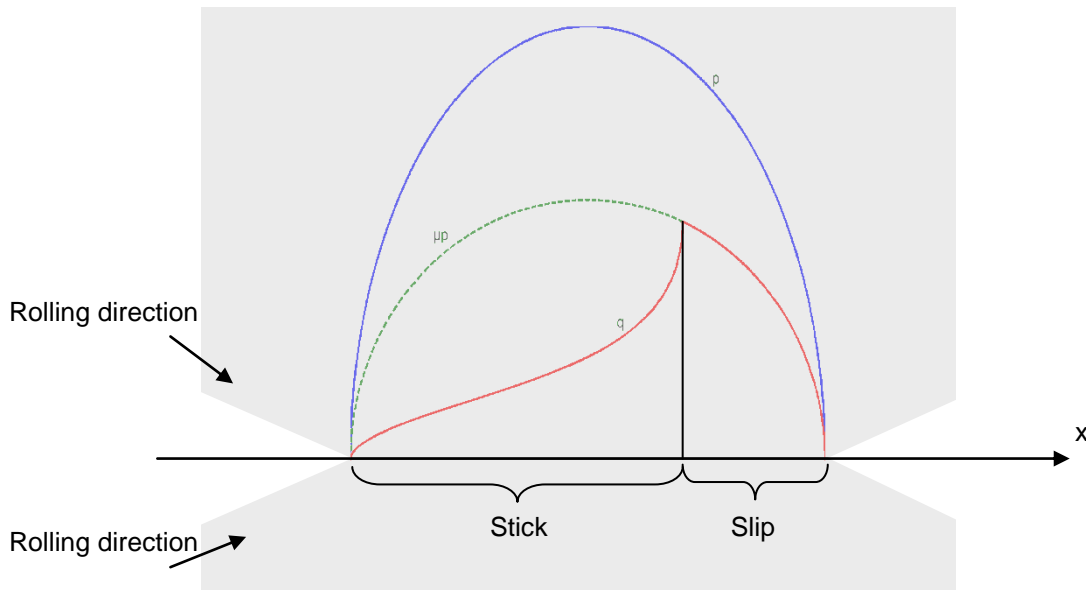
Figure 7: pressure (p) and shear (q) distribution in tractive rolling cylinders

4   WEAR MODELLING

In pure sliding problems, the most commonly used wear model is that of Archard [12], where the wear volume (V) is proportional with normal force (F), sliding distance (s) and hardness (H) of the material:

$$V = K \cdot \frac{F \cdot s}{H} \qquad (9)$$

K is the dimensionless wear coefficient.

In roll-slip contacts two regions can be distinguished. In the stick area no relative motions between the two bodies occur; in the slip area sliding takes place. Equation (9) can be used for modeling wear in roll-slip contacts, where s is the sliding distance in the slip area, or the total macroscopic sliding distance.

In dry or poorly lubricated contact conditions, it is known that the wear coefficient is function of a number of parameters, like normal load, sliding velocity or surface temperature. A sudden change in the wear coefficient indicates a transition in wear mechanisms. The simplest wear classification distinguishes two types of wear: mild and severe wear.
Mild wear results in a surface that is often more smooth than the original surface, with minimal oxide wear debris and plastic deformation. Severe wear is characterized by a rough surface, which is usually rougher than the original surface. In this case a significant amount of plastic deformation, and flake-like wear debris is seen.

The transition between wear regimes is clearly shown in wear maps. In the study area of wear mapping in roll-slip contacts two graphs are frequently used.
In wheel-rail problems the wear mapping of Bolton and Clayton [13] is frequently used, see Figure 8. The wear rate in µg/m$_{rolled}$/mm²$_{contact\ area}$ is plotted against TS/A, where T is the limiting traction force (normal force multiplied by the coefficient of friction), S the slip and A the contact area.
A more general view of wear mapping in roll-slip is given by a 3D plot or contour plot that expresses wear volume or wear coefficient in function of normal force and sliding velocity [14-17]. In Figure 9 three boundaries separate the four presented wear regimes: mild, severe, severe-catastrophic transition and catastrophic wear.
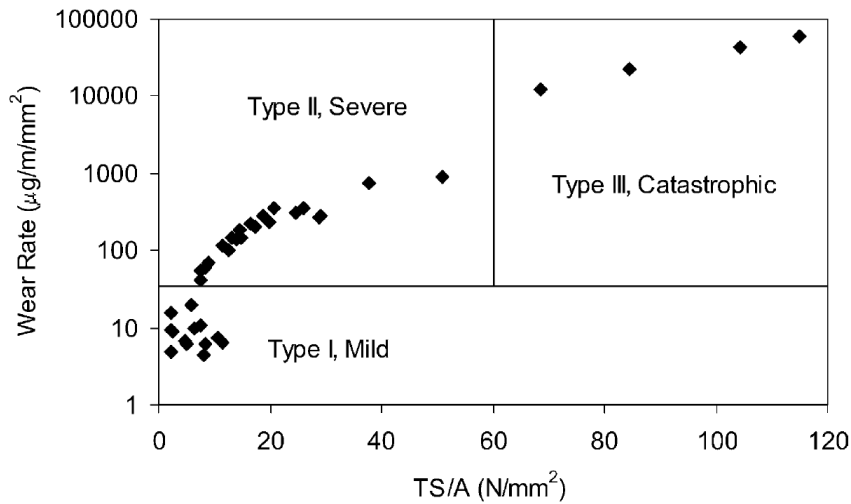
Figure 8: Wear regimes during twin disc testing of BS11 rail material vs. Class D tyre material [13]
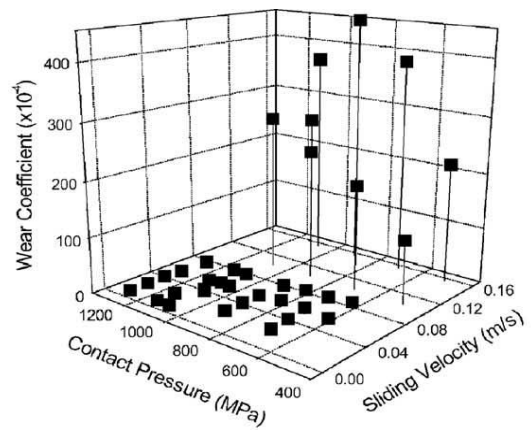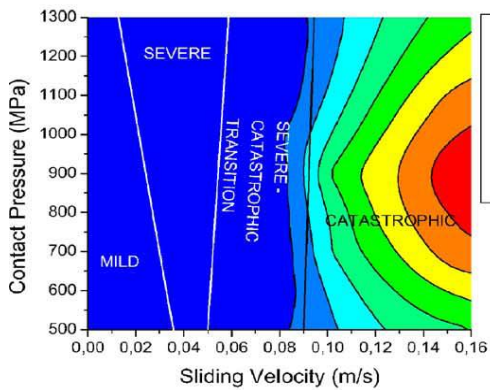
Figure 9: Wear coefficient maps for standard carbon steel. left: contour plot, right: 3D plot [17]

To locate the different wear regimes in wheel-rail contacts, the wear map and the wheel-rail contact conditions map are plotted together on one graph, as shown in Figure 10. This shows that the rail head/wheel tread contact is in the mild to severe wear range while the rail gauge/wheel flange will experience severe to catastrophic wear.

This theory is in good agreement with field measurements of worn rails and wheels [14]. Figure 11 shows the profile of a new rail and a worn rail, these measurements were performed on a straight track. It is clear that the rail gauge/wheel flange contact area is more worn than the rail head/wheel tread contact area.
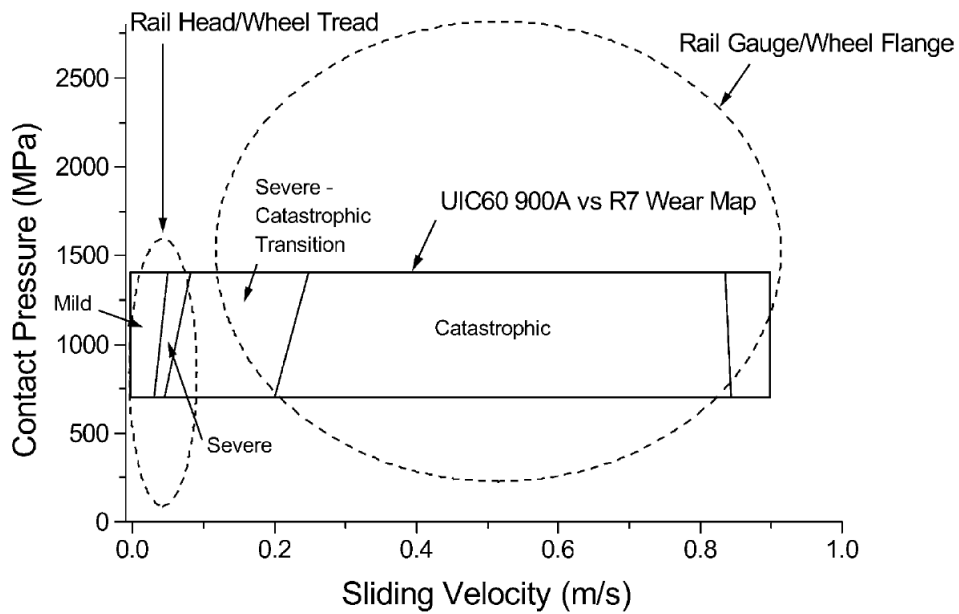
Figure 10: UIC60 900A rail steel wear map over wheel-rail contact conditions [15]
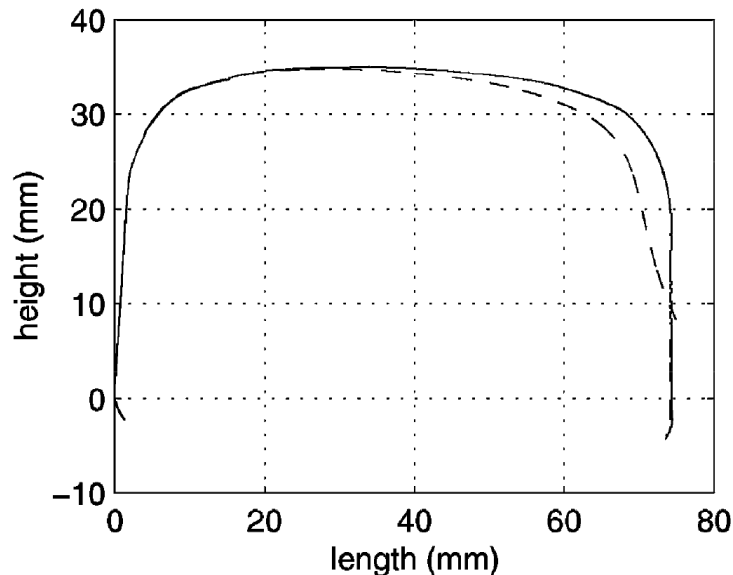
Figure 11: New high rail profiles (——) compared with profiles after 16 months of traffic (- -)

5   CONCLUSION

Traction and wear are two important issues in roll-slip contact, particular in the transportation industry where the driving force of vehicles is obtained by this phenomenon.

The formation of an contact area and pressure distribution is briefly discussed for contacting bodies, with special attention for a sphere-plane contact and wheel-rail contact.

Traction is often considered as a black box, where only the relation between the slip and traction coefficient is known. However this article discusses the formation of traction in the contact area, firstly for static contacts and subsequently for roll-slip contacts.

Wear modeling of roll-slip contacts is based on the theory that the contact area is divided into two regions, a stick and slip region. In the stick area only pure rolling occurs and no wear will arise. In the slip area, the Archard wear model for pure sliding is used. Leading to a wear model for the entire roll-slip contact.

Two types of wear mapping are presented. For the rail industry a wear map based on experimental coupon tests is plotted together with theoretical calculations about the wheel-rail contact. This graph can be used to clarify the location and amount of wear that is observed in field measurements.

6 NOMENCLATURE

A	contact area	mm²
a	radius of contact area	mm
E	modulus of elasticity	GPa
E'	effective modulus of elasticity	GPa
F	Normal force	N
H	Harness	MPa
K	wear coefficient	-
Q	tangential force	N
R_1	radius sphere	mm
s	sliding distance	mm
S	slip	-
T	traction force	N
u	lateral shift between wheel and rail	mm
V	wear volume	mm³
µ	coefficient of friction	-
v	poisson coefficient	-
σ	stress	MPa

7 ACKNOWLEDGEMENTS

8 REFERENCES

[1] F.W.Carter, *On the action of a locomotive driving wheel.* Proc. Roy. Soc.: p. 151-157.1926
[2] A.VanBeek, *Advanced engineering design.* 2006, Delft.
[3] Segond, D. and A. Tafreshi, *Stress analysis of three-dimensional contact problems using the boundary element method.* Engineering Analysis with Boundary Elements. **22**(3): p. 199-214.1998
[4] Wiest, M., et al., *Assessment of methods for calculating contact pressure in wheel-rail/switch contact.* Wear. **265**(9-10): p. 1439-1445.2008
[5] J.F.Archard, Proc. R. Soc. **A 243**.1957
[6] Xiao, L., S. Bjorklund, and B.G. Rosen, *The influence of surface roughness and the contact pressure distribution on friction in rolling/sliding contacts.* Tribology International. **40**(4): p. 694-698.2007
[7] Kalker, J.J., *Rolling contact phenomena - linear elasticity.* CISM International Centre for Mechanical Sciences. Vol. 411. 2001: Springer.
[8] S.Cretu, *The influence of roughness on pressure distribution and stress state of concentrated contacts subjected to normal loads.* Constructii de masini: p. 1-12.2007
[9] Enblom, R., *Deterioration mechanisms in the wheel/rail interface with focus on wear prediction: a literature review.* Vehicle System Dynamics: International Journal of Vehicle Mechanics and Mobility. **47**(6): p. 661 - 700.2009
[10] Mindlin, R.D., *Compliance of elastic bodies in contact.* Journal of Applied Mechanics. **16**.1949
[11] K.L.Johnson, *Contact Mechanics.* 1985, Cambridge Cambridge University Press.
[12] J.F.Archard, *Contact and rubbing of flat surfaces.* J. Appl. Phys. **24**: p. 981-988.1953
[13] Bolton, P.J. and P. Clayton, *ROLLING SLIDING WEAR DAMAGE IN RAIL AND TYRE STEELS.* Wear. **93**(2): p. 145-165.1984
[14] Olfsson, U. and I. Telliskivi, *Wear, plastic deformation and friction of two rail steels-a full-scale test and a laboratory study.* Wear. **254**(1-2): p. 80-93.2003
[15] Lewis R. and O. U., *Mapping rail wear regimes and transitions.* Wear. **257**(7-8): p. 721-729.2004
[16] Lim, S.C., *Recent developments in wear-mechanism maps.* Tribology International. **31**(1-3): p. 87-97.1998
[17] Danks, D. and P. Clayton, *COMPARISON OF THE WEAR PROCESS FOR EUTECTOID RAIL STEELS - FIELD AND LABORATORY TESTS.* Wear. **120**(2): p. 233-250.1987

TRIBOLOGICAL BEHAVIOR OF WIRE-EDM'ED ZrO$_2$-COMPOSITES AND CEMENTED CARBIDES

Y. Perez Delgado[1], K. Bonny[1], O. Malek[2,3], P. De Baets[1], W. Ost[1], J. Vleugels[2], B. Lauwers[3]

[1] Ghent University, Laboratory Soete, Belgium
[2] Catholic University of Leuven, Metallurgy and Materials Engineering Department, Belgium
[3] Catholic University of Leuven, Mechanical Engineering Department , Belgium

Abstract

Five ZrO$_2$-based composites (ZrO$_2$-WC, ZrO$_2$-TiCN and ZrO$_2$-TiN grades) and five WC-Co cemented carbide grades were machined by wire-EDM and tested on a linearly reciprocating sliding pin-on-flat tribometer PLINT TE77 in dry conditions against WC-6wt%Co pins. Measurement of friction coefficient and penetration depth due to wear was performed continuously. The results revealed a strong influence of the secondary phase, surface finish, chemical and mechanical properties on the tribological characteristics of the ZrO$_2$-based composites and cemented carbides. WC10Co(Cr/V) displayed superior wear resistance compared to the other grades. The lowest coefficient of friction was encountered with ZrO$_2$-WC.

Keywords Friction, Wear, Electrical Discharge Machining, ZrO$_2$-composite, WC-Co

1   INTRODUCTION

Nowadays, there is an industrial need for materials to be applied under heavy tribological conditions and preferably without lubrication and high temperatures as for example for tools (chisels, cutting tools, dies, punches, etc.) and various machine parts (brakes, bearings, gears, sealings, etc.). To date hardened steels or hardmetals are often used for these applications. Some technical ceramic materials are used as well, in bulk or as a surface coating. The main purpose of these materials is to extend the lifetime of existing devices and components by decreasing their wear rate. A significant disadvantage of these materials is their relatively high coefficient of friction in dry contact conditions (heat development and energy loss). Moreover, their high hardness makes them intrinsically difficult to shape and to finish using conventional manufacturing methods. Usually the only suitable cutting technique is grinding by diamond or boron nitride tools, which restricts however seriously the possibilities in geometries that can be accomplished. Electro-discharge machining (EDM) allows a production of complex shapes in materials, irrespective of their mechanical properties, provided they are sufficiently electrically conductive.

Some research has already been performed on the effects of wire-EDM on friction and wear behavior of WC-Co cemented carbides [1, 2] and ZrO$_2$-based composites [3]. This paper compares tribological characteristics of these materials in dry reciprocating sliding wear tests with the goal to improve the fundamental insight into the tribology of these materials and to further extend the scientific perception of the influence of wire-EDM on tribological performance. Correlations between surface finishing conditions, testing parameters, material properties and friction coefficient and wear resistance are elucidated.

2   METHODOLOGY

2.1   Materials

The manufacturing process for ceramics is similar to powder metallurgy, where the end characteristics of components are largely dictated by powder characteristics (purity), "green densification" in forming, and finally the sintering process [4]. The present zirconia based composites were obtained by hot pressing Yttri-stabilised ZrO$_2$ powder mixtures with 40% vol.% WC, TiC$_{0.5}$N$_{0.5}$ or TiN. Starting powders were used in nanometric and micrometric sizes, the two corresponding grain sizes in the secondary phases are referred to as "fine" and "coarse" throughout the text. More information on processing and characterisation has been published in [5-7]. Physical and mechanical properties are listed in Table 1 as a function of secondary phases, microstructural properties for ZrO$_2$-WC, ZrO$_2$-TiCN and ZrO$_2$-TiN grades and five WC-Co cemented carbides grades.

Table1. Physical and mechanical properties for ZrO_2–based composites and WC-Co cemented carbides

Grade	Composition	Crystal size[i] [nm]	E [Gpa]	HV_{10} [kg/mm2]	$K_{IC, 10Kg}$ [Mpa.m$^{1/2}$]	Density [g/cm^3]	Average grain size, d_{av} (μm)	Grain size, d_{50} (μm)	Grain size, d_{90} (μm)
A	ZrO_2-WC	20-40	382±2	1691±8	8.5±0.4	9.8	0.25	0.11	0.54
B	ZrO_2-WC	800-1000	340±6	1502±9	8.5±0.2	9.79	0.3	0.17	0.17
C	ZrO_2-TiCN	<100	307±2	1629±8	3.9±0.1	5.59	0.15	0.12	0.33
D	ZrO_2-TiCN	1600	284±2	1422±10	7.0±0.2	5.76	0.37	0.22	0.84
E	ZrO_2-TiN	800-1200	274±1	1370±7	5.6±0.1	5.81	0.39	0.25	0.86
F	WC10Co	-	578±6	1149±10	>14.9±0.1	14.33	2.2	1.8	4.2
G	WC12Co(*V*)	-	563±2	1286±8	>14.9±0.1	14.08	0.9	0.7	1.5
H	WC12Co(*Cr*)	-	546±2	1306±5	>14.9±0.1	14.01	0.9	0.8	1.7
I	WC10Co(*Cr/V*)	-	541±4	1685±38	11.0±0.6	14.23	0.3	0.3	0.6
J	WC6Co(*Cr/V*)	-	609±4	1913±13	8.4±.02	14.62	0.6	0.5	1

[i] crystal size of the secondary phase starting powders;

2.2 Surface finish

The finest wire-EDM regime F4 and E23 was selected for sliding tests in dry conditions in order to compare the frictional response of fine and coarse ZrO_2-based composites and WC-Co cemented carbides respectively. Additional information of machining for the composites mentioned above is given in [2, 8]. The corresponding wire-EDM settings are listed in Table 2.

Table 2. Parameters and device settings for finer cutting EDM regimes

EDM regime	F4	E23
Open voltage (V)	120	140
Pulse duration, t_e (μs)	0.4	1
Pulse interval, t_o (μs)	4	4
Reference servo voltage Aj (v)	0	0
Pulse ignition height IAL (A)	5	2.5
Flushing pressure (bar)	0	0
Wire tension (N)	12	10
Wire winding speed (m/min)	8	4.8

2.3 Wear Testing

The dry sliding friction and wear behaviour of ZrO_2 and cemented carbide composites are investigated using a Plint TE77 tribometer according to ASTM G133 in ambient air, for instance, 23 ± 1 °C and 60 ±1 % relative humidity, WC-6wt%Co cemented carbide pins (length l = 22mm and diameter d ≈ 8mm) was rubbed in oscillating movement against flat specimens (width w = 38 mm x length l = 58 mm x thickness t = 4 mm) with a constant frequency of 10Hz, a stroke length of 15 mm and an average sliding velocity of 0.3 m/s. Three normal contact forces were imposed, i.e., 15, 25 and 35 N. Schematic illustration of linearly reciprocating pin-on-flat sliding wear system geometry is outlined in Figure 1.
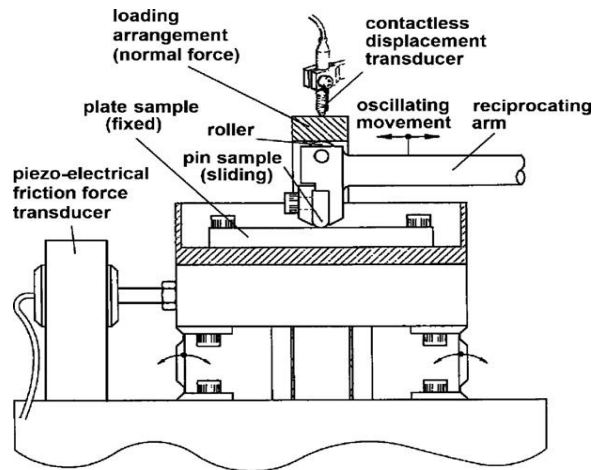
Figure 1. Schematic view of Plint TE 77 reciprocating pin-on-plate tribometer [9].

3 RESULTS AND DISCUSSION

3.1 COEFFICIENT OF FRICTION (μ)

A continuous registration of the imposed normal contact force (F_N) and the tangential friction force (F_T) of pin-on-flat sliding pairs was carried out using a load cell, parallel with the lever of the loading frame, and a piezo-electric transducer respectively. The coefficient of friction (μ) is calculated from the F_T / F_N ratio. In addition, the measured friction force can be differentiated in a static and a dynamic component:

$$F_{T,stat} = \frac{\left|F_{T,\min}\right| + \left|F_{T,\max}\right|}{2} \tag{1}$$

$$F_{T,dyn} = \sqrt{\frac{1}{T}\int_{0}^{T}(F_T(t))^2\,dt} \tag{2}$$

The data obtained from online monitoring are provided in table 4, in which friction coefficient and penetration depth at different sliding distance (running in and steady state) are compared for cemented carbides and ZrO_2 composites. The static and dynamic friction coefficients of the tested tribopairs are in the range of 0.55 – 0.86 and 0.39 – 0.68, respectively. Within whole data range it can be clearly seen that cemented carbides showed lower friction coefficient, however, the lowest friction level was recorded for the ZrO_2-WC Course, whereas the ZrO_2-TiN achieved the highest coefficient of friction. On the one hand, the effect of secondary phases and grain size is very important in ZrO_2-composites, the friction coefficient for course composites is lower than fine composites and even the penetration depth for coarse are shallow. On the other hand, the secondary phases were not much relevant for cemented carbides because those composites showed similar friction coefficients. As can be seen in Table 3 in the full sliding distance range with contact load of 35N the lowest wear depth was recorded for WC10Co(Cr/V), whereas wear testing of ZrO_2-TiN (Grade E) yields the highest penetration depth.

Table 3. Friction coefficient (static and dynamic) and penetration depth as function of sliding distance (s) for wire-EDM'ed ZrO$_2$-based composites and WC-Co cemented carbides against WC-6wt%Co (F$_N$=35N).

Grade	Surface finish	μ_{stat}				μ_{dyn}				Δd_p(mm)			
	s(km)	0.015	1	4	10	0.015	1	4	10	0.015	1	4	10
A	F4	0.80	0.77	0.78	0.75	0.53	0.51	0.52	0.51	6.4	22.2	40.0	55.6
B	F4	0.56	0.55	0.56	0.56	0.39	0.40	0.41	0.40	2.1	8.7	20.6	30.8
C	F4	0.83	0.86	0.86	0.84	0.64	0.65	0.65	0.63	11.0	161.5	197.8	274.8
D	F4	0.75	0.79	0.80	0.81	0.59	0.60	0.61	0.60	3.0	36.8	45.4	63.1
E	F4	0.79	0.81	0.82	0.82	0.61	0.65	0.68	0.68	9.9	99.6	200.5	362.7
F	E23	0.66	0.64	0.64	0.64	0.43	0.42	0.42	0.42	2.6	6.8	7.6	11.1
G	E23	0.64	0.63	0.63	0.62	0.43	0.42	0.42	0.41	2.1	5.9	6.6	8.2
H	E23	0.68	0.64	0.63	0.61	0.44	0.42	0.42	0.41	1.9	5.5	7.1	8.1
I	E23	0.64	0.62	0.64	0.61	0.41	0.41	0.41	0.40	2.3	4.8	6.0	7.5
J	E23	0.64	0.63	0.62	0.60	0.41	0.41	0.41	0.40	4.1	5.8	6.7	8.0

After the full sliding distance of 10 km the wear track was quantified for ZrO$_2$-composites, evidencing how it can be affected by the secondary phase, surface finish and the applied normal contact force (Figure 2). ZrO$_2$-WC course (grade B) showed the highest wear resistance, whereas the lowest wear resistance is found for ZrO$_2$-TiN (Grade E). Analogously, the highest wear is found with EDM'ed surfaces compared to equivalent ground ZrO$_2$-based composites. Moreover, it can be seen that the largest volume wear was encountered when the heaviest normal force was imposed.
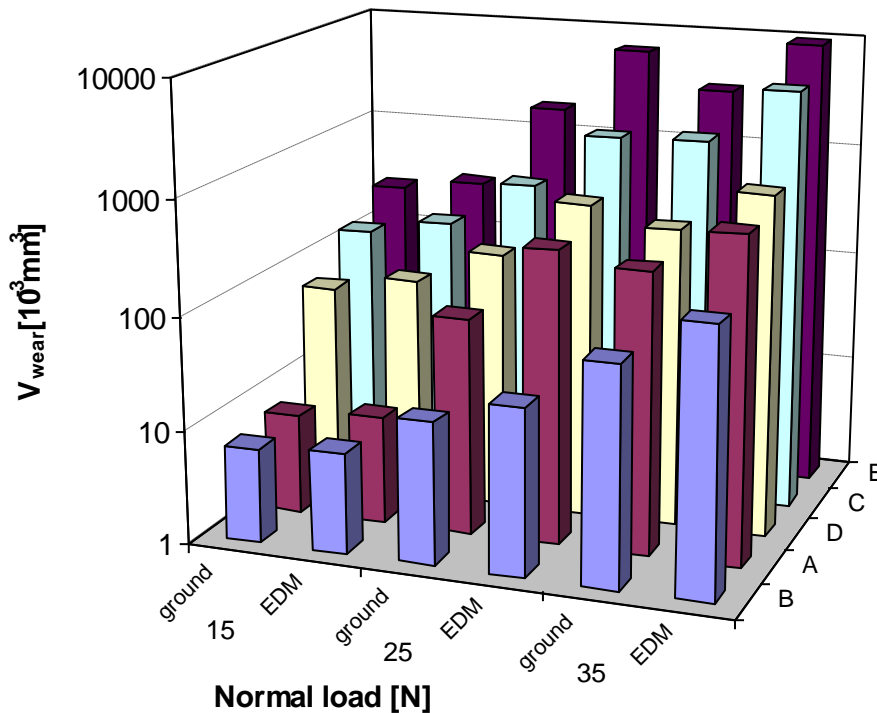
Figure 2. Volumetric wear of ZrO$_2$-based composite grades as function of surface finish at 15, 25 and 35N. (Sliding distance 10km, v = 0.3m/s)

4   CONCLUSIONS

Dry sliding pin-on-flat experiments on reciprocating movements of wire EDM'ed ZrO_2 composites and cemented carbides plates against WC-6%wtCo pins under normal contact loads of 15, 25 and 35 N revealed that the tribological properties are intimately affected by surface finishing, physical and chemical characteristics of the secondary phase and the imposed normal contact force. The lowest friction coefficient was encountered with ZrO_2-WC Coarse (grade B), whereas ZrO_2-TiCN Fine (grade C), displayed the highest friction at the normal force of 35N. Furthermore, the lowest wear was encountered with WC10Co(Cr/V) (grade I), while ZrO_2-TiN (grade E) showed the highest wear.

5   NOMENCLATURE

μ	Coefficient of friction	-
F_N	Normal contact force	N
F_T	Tangential friction force	N
μ_{stat}	Coefficient of friction static component	-
μ_{dyn}	Coefficient of friction dynamic component	-
V_{wear}	Wear volume	mm^3

6   ACKNOWLEDGEMENTS

7   REFERENCES

[1]   Bonny, K., et al., Influence of electrical discharge machining on the reciprocating sliding friction and wear response of WC-Co cemented carbides. International Journal of Refractory Metals & Hard Materials, 2009. 27(2): p. 350-359.

[2   Bonny, K., et al., Influence of electrical discharge machining on the reciprocating sliding wear response of WC-Co cemented carbides. Wear, 2009. 266(1-2): p. 84-95.

[3]   Bonny, K., et al., Influence of electrical discharge machining on tribological behavior of ZrO2-TiN composites. Wear, 2008. 265(11-12): p. 1884-1892.

[4]   Beitz, W. and K.-H. Küttner, Handbook of Mechanical Engineering. 1994, London: Springer-Verlag.

[5]   Salehi, S., O. Van der Biest, and J. Vleugels, Electrically conductive ZrO2-TiN composites. Journal of the European Ceramic Society, 2006. 26(15): p. 3173-3179.

[6]   Anné, G., et al., Hard, tough and strong ZrO2-WC composites from nanosized powders. Journal of the European Ceramic Society, 2005. 25(1): p. 55-63.

[7]   Vleugels, J. and O. Biest, Development and Characterization of Y_2O_3-Stabilized ZrO_2 (Y-TZP) Composites with TiB_2, TiN, TiC, and $TiC_{0.5}N_{0.5}$. Journal of the American Ceramic Society, 1999. 82(10): p. 2717-2720.

[8]   Bonny, K., et al., EDM machinability and frictional behavior of ZrO2-WC composites. International Journal of Advanced Manufacturing Technology, 2009. 41(11-12): p. 1085-1093.

[9]   Bonny, K., et al., Impact of Cr3C2/VC addition on the dry sliding friction and wear response of WC-Co cemented carbides. Wear, 2009. 267(9-10): p. 1642-1652.

FRICTION STIR OVERLAP WELDING OF 2124 ALUMINIUM PLATE

W. Van Haver[1], A. Geurten[2], B. de Meester[3] and J. Defrancq[4]

[1] Belgian Welding Institute, Belgium
[2] CEWAC, Belgium
[3] UCL-PRM, Belgium
[4] Ghent University, Belgium

Abstract In this ongoing investigation, experimental results of friction stir welding (FSW) applied to high-thickness 2124 aerospace aluminium alloy are discussed. Flanges of 30 mm high are produced onto a 44 mm thick plate by two consecutive overlap welds in this non-fusion weldable material, followed by a final milling step. This approach results in significant material savings compared to the conventional production route, which consists of milling out the entire part starting from a high-thickness plate. Furthermore, the flanges built up by FSW consist fully of fine-grained material. Due to the nature of the processing route, the nugget zone of the first weld pass is partially reheated by the second weld pass. The influence of parent material temper (i.e., T851 or T4) on friction stir welding characteristics is studied; it is noted that in T4 temper, a significant increase in welding speed can be obtained compared to T851. The softer T4 temper also causes less danger of tool fracture, which allows incorporating more features to the pin and shoulder of the tool. During this investigation, the emphasis is put on microstructural characterisation and microhardness testing of various zones in the weld.

Keywords Friction stir welding; Light metals; Aluminium alloys; High thickness; Lap joints; Microstructure; Weld defects; Hardness; Aerospace

1   INTRODUCTION

1.1   Background

It is well established that aluminium alloys have a large potential in many industrial sectors (automotive, aerospace, construction, general engineering, packaging) due to their interesting properties, e.g. low density, good mechanical properties, good corrosion resistance and high thermal/electrical conductivity. However, the industrial use of certain aluminium alloys was somewhat inhibited, since these are considered difficult to join with conventional fusion welding techniques.

In the case of the high-strength Al-Cu (2xxx series) and Al-ZnMgCu alloys (certain 7xxx series alloys, such as 7075), the high tendency to hot cracking is problematic when conventional fusion welding processes causing shrinkage and stresses in the welded zone are applied. Successfully welding these alloys with MIG or TIG would require the use of filler material with a lower melting range than the parent material, combined with a sufficiently high strength. Filler materials that meet both requirements are not commercially available (with the exception of 2319 for welding of alloy 2219 [1]).

Because of this, highly hot crack sensitive alloys are generally joined in a purely mechanical manner (such as bolting and riveting), or parts are produced by milling the entire structure from a high-thickness plate. For these alloys in particular, "Friction Stir Welding" (FSW), a fully mechanical solid phase welding process, provides a solution. This technique was invented and patented in the early nineties by The Welding Institute (TWI, UK) [2].

The basic principle of this process is to soften the material by frictional heat generated between the material surfaces and a rotating tool. In the classic butt joint set-up, the components to be joined are rigidly clamped on a backing plate. A rotating tool, consisting of a profiled pin and a shoulder, is forced down into the material until the shoulder meets the surface of the workpieces. The material in the close surrounding of the tool is thereby frictionally heated to temperatures where it is easily plasticized. As the tool moves forward, material is stirred from the leading to the trailing edge of the pin. Behind the pin, the joint is formed – see Figure 1 on the left. A distinction is made between the advancing side of the weld (side where the tool rotation direction is the same as the welding direction), and the retreating side (side where the tool rotation direction is opposite to the welding direction), as also indicated on Figure 1 on the left.
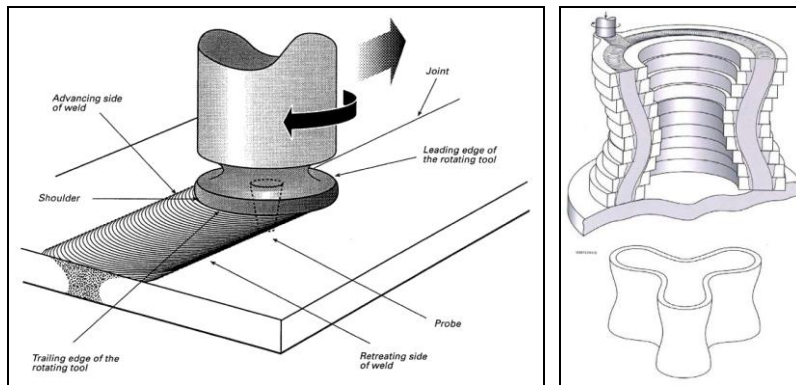
Figure 1. Schematic representation of (left) friction stir butt welding process [3], and (right) Pro-Stir™ technique [4]

By all means, an analogous approach as in friction stir butt welding can be used for the realization of lap joints. Pro-Stir™ is a near-net shape manufacturing technique using friction stir overlap joints, developed by The Welding Institute. It concerns the build-up of a structure by repeated lap welding of sheets or plates, followed by machining (Figure 1 on the right). This technique allows:

- the build-up of structures which would otherwise necessitate, using other techniques (fusion welding, machining, forging), a great degree of material loss in order to produce the desired structure;
- the manufacturing of complex structures which are difficult/impossible to produce with conventional techniques.

Only very little practical examples could be identified so far in literature, e.g. build up of flanges in Ti-6Al-4V alloy [5], and complex-finned aluminium heat exchangers, created by a combination of abrasive waterjet cutting, friction stir lap welding and CNC machining [6].

1.2 Application

The application envisaged for the current study concerns the production of complex aerospace wing elements, which are currently produced as deeply machined parts – see Figure 2.
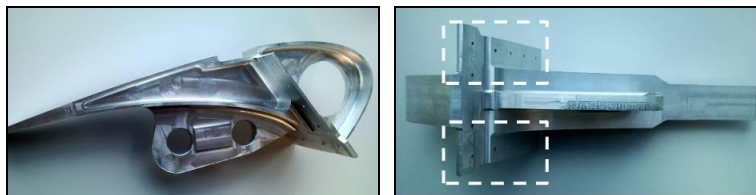
Figure 2. Photographs of the deeply machined aerospace part. Left: side view; right: top view (note the vertical flanges, indicated by the white rectangles)

In this investigation, the build-up of the 30 mm high flanges (Figure 2 on the right) is produced by FSW. Given the fact that overlap welding 30 mm 2124 material in one welding pass is not possible with the FSW equipment available at CEWAC (see §2.1), the flanges are built up by friction stir overlap welding two 17 mm thick 2124 material plates onto a 44 mm thick base plate (in order to make abstraction of the rest of the piece), as follows:

- the first 17 mm thick "flange plate" is overlap welded onto the base plate (Figure 3 – A);
- after welding, the top 2 mm of the weld is removed by milling;
- one week after realization of the first weld pass, a second 17 mm thick flange plate is overlap welded onto the previous weld pass (Figure 3 – B).

In actual production, machining would be carried out in order to obtain the final desired dimensions of the part (Figure 3 – C and D). This way, the flange will consist, after milling, fully of recrystallised material – see also weld *T8-2-0* in Figure 7.
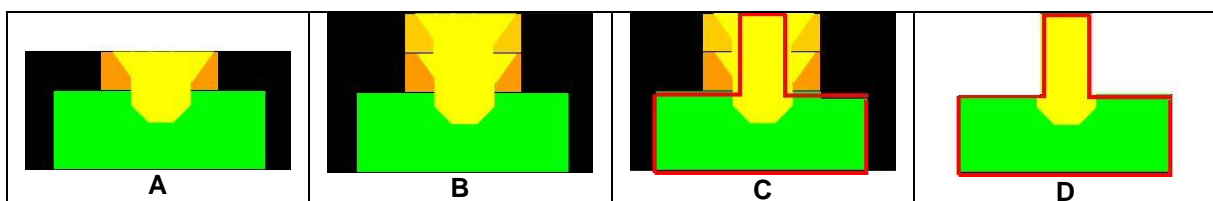
Figure 3. Schematic processing route for the production of flanges in 2124 material

It is clear that this production route can be considered an application of Pro-Stir™. The main potential advantages of the new processing route that can be recognized for this case are:

- Very significant material savings compared to the current production route (estimated to 40-50%);
- Time savings (hence economical benefits);
- Economic alternative for casting, forging or linear friction welding;
- No available alternative in fusion welding processes such as MIG, TIG, (hybrid) laser welding or electron beam welding given the aforementioned high proneness to hot cracking of 2124 alloy.

1.3   Parent material

EN AW-2124 aluminium alloy is in the EN 573-3 standard also indicated by means of chemical symbols as EN AW-Al Cu4Mg1(A). It is a heat treatable wrought alloy, with Al_2CuMg as the main precipitation hardening component. 2124 alloy was delivered as large rolled plates with a thickness of 44 mm (used as base plate) and 26 mm (used for the build-up of flanges), in the T851 temper according to EN 515. In Table 1, the chemical composition of the parent materials is given.

	Si	**Fe**	**Cu**	**Mn**	**Mg**	**Cr**	**Zn**	**Ti**	**Other**
EN 573-3	0.20 max.	0.30 max.	3.8 – 4.9	0.30 – 0.9	1.2 – 1.8	0.10 max.	0.25 max.	0.15 max.	0.15 max.
Certificate 26 mm	0.03	0.07	4.00	0.56	1.28	0.00	0.01	0.02	0.02
Certificate 44 mm	0.03	0.07	4.11	0.61	1.28	0.00	0.02	0.03	0.02

Table 1. Chemical composition of 26 and 44 mm 2124 material compared to EN 573-3

T851-temper is the state in which the 2124 alloy was originally supplied. This temper designation applies to material which has been solution heat treated, stress relieved by stretching to a controlled amount (permanent set 1.5 to 3% for plate) and then artificially aged. Products receive no further straightening after stretching. 2124 alloy is mostly used in this temper, as it then possesses good toughness and strength and optimum machinability.

Within the investigation, part of the 2124-T851 material was subjected to a T4 heat treatment, which corresponds to solution heat treating and water quenching (performed in accordance with the specifications in AMS 2772C), followed by natural ageing during at least 1 month. Tensile properties of both base plate and flange plate material in T851 and T4 material (executed according to EN 485-2) are given in Table 2. Clearly, the T4 heat treatment has a large influence in terms of yield strength and elongation after fracture; the tensile strength on the other hand is only marginally affected.

Material	**Yield strength $R_{p0.2}$ [MPa]**	**Tensile strength R_m [MPa]**	**Elongation A_{50} [%]**
2124-T851 (26 mm, certificate)	449 ± 6	486 ± 5	11.2 ± 0.3
2124-T851 (26 mm, BWI)	454 ± 2	495 ± 1	12.8 ± 0.8
2124-T851 (44 mm, certificate)	448 ± 1	491 ± 1	10.8 ± 0.2
2124-T851 (44 mm, BWI)	450 ± 1	494 ± 2	10.6 ± 1.0
2124-T4 (26 mm, BWI)	291 ± 1	450 ± 1	28.5 ± 0.9
2124-T4 (44 mm, BWI)	306 ± 2	473 ± 2	24.5 ± 0.3

Table 2. Tensile test results of 2124-T851 and 2124-T4 parent material

The plates were sawn to appropriate dimensions, followed by milling down to the correct thickness. The final dimensions for welding are:

- for the base plate: 400 mm long (parallel with rolling direction), 155 mm wide and 44 mm thick;
- for the flange plates: 400 mm long (parallel with rolling direction), 65 mm wide and 17 mm thick.

2   FSW JOINT REALISATION

2.1   FSW equipment

The friction stir welding experiments were executed by CEWAC on an ESAB SuperStir™ FSW 53 STL machine. This equipment, capable of carrying out FSW both in position control or in force control, is suited for linear welding only. It allows to weld conventional (e.g. 6xxx series) aluminium alloys in thickness from 2 mm up to 30 mm. The clamping system which was used for the processing route (described in §1.2) is shown in Figure 4: the base plate (1) is bolted directly to the machine table with the clamping system (A), which assures a good clamping between the flange plate (2) and the base plate (1). After realization of the first weld pass and machining off the top 2 mm from the first flange plate, clamping system (A) is replaced by clamping system (B) for welding the second flange plate. In order to avoid generation of excessive heat in the parts, a water cooled clamping system was used. Furthermore, the tool holder was cooled with a mixture of 65% water and 35% glycol, with a maximum flow rate of 5.5 l/min.
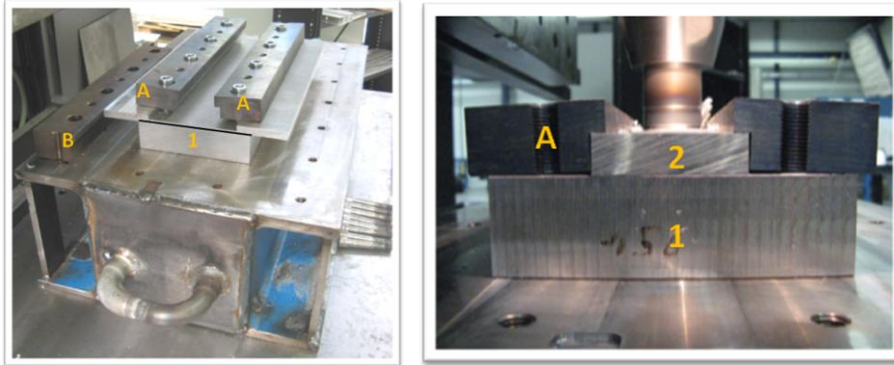
Figure 4. Experimental setup of the backing plate and clamping equipment

2.2   FSW parameters

Weld lengths of 320 mm were realized on the workpieces with dimensions already specified in §1.3. The welding parameters (in force control) used for this investigation are summarized in Table 3. Note that the first two digits of the designations indicate the temper of the parent material, the second digit mentions the number of weld passes, and finally the third digit gives the "tool number".

Designation	Temper	# passes	Tool geometry (*)	Welding speed [mm/min]	Rotation speed [rev/min]	Plunge force [kN]	Tilt angle [°]
T8-1-0	T851	1	St. 1 (tool 0)	5	200	30-31	1.5
T8-2-0	T851	2	St. 1 (tool 0)	5	200	26	1.5
T4-2-08	T4	2	St. 1 (tool 0)	5	200	32.5-30	1.5
T4-1-0	T4	1	St. 1 (tool 0)	60	300	62.5	1.5
T4-2-0	T4	2	St. 1 (tool 0)	60	300	55-62.5	1.5
T4-2-1	T4	2	St. 2 (tool 1)	55	300	55-65 40-65	1.5
T4-2-2	T4	2	Triflat™ (tool 2)	55	300	55-65 40-55	0
T4-2-3	T4	2	Triflute™ (tool 3)	55	300	52.5-65 55-52.5	0

Table 3. Welding parameters of the current investigation; (*) see Table 4

All tools were made from "QRO 90 Supreme" Cr-Mo-V alloyed hot-work tool steel [7], hardened to HRC 55. Further data about the tool geometry are included in Table 4.

In 2124-T851 material, it was very hard to achieve welds without tool fracture (occurring at the base of the pin, near the shoulder). For that reason, the welding speed could not be increased above 5 mm/min. Moreover, it was not possible to include more tool features than an unprofiled concave tool shoulder and a conical threaded pin: other features such as shoulder spirals or pin flutes made the tool weaker, and fracture became more likely to occur.

Intentionally, one weld in 2124-T4 material (designated *T4-2-08*, with the "8" at the end indicating that the same welding parameters as for 2124-T851 were used) was performed with comparable parameters as those used for 2124-T851. In 2124-T4 parent material, the welding speed could be increased significantly

without tool fracture (by a factor of more than 10: e.g. compare *T4-2-0* with *T8-2-0*). This led to believe that it would become possible to use more advanced shoulder and pin geometries.
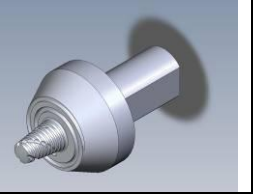
	"Standard" tools		Triflat™ tool	Triflute™ tool
	Tool 0	*Tool 1*	*Tool 2*	*Tool 3*
Drawing				
Ø shoulder [mm]	35			
Tool shoulder angle [°]	*St. 1:* 1.5 *(concave)*	*St. 2:* 1.5 *(concave)*	0	0
Shoulder features	/		spiral machined with Ø 2.5 mm ball-shaped tool	spiral machined with Ø 2.5 mm ball-shaped tool
Ø pin [mm]	15 *(shoulder)* 10 *(extremity)*			
Pitch of thread [mm]	1.5	2	2	2
Pin features	/		3 flats @ 120° 0.75 mm below pin surface	3 threads with 35 mm pitch
Pin length [mm]	20			

Table 4. FSW tool geometry data

It should be noted that for the welds *T4-2-1*, *T4-2-2* and *T4-2-3* the welding speed and rotation speed were intentionally kept the same, in order to allow for a comparison between three different tool geometries.

Welds *T8-1-0* and *T4-1-0* were performed for comparison with *T8-2-0* and *T4-2-0*, respectively – this was done in order to check whether the realization of a second weld pass had an influence on the base plate characteristics (more precisely: on the microhardness). For all double-pass welds, the second weld pass was realized at least one week after performing the first weld pass.

3   PARENT MATERIAL AND JOINT CHARACTERISATION

3.1   Methods of characterisation

All parent materials and welds were subjected to metallography and microhardness testing. No test specimens were extracted from the first or the last 50 mm of weld length, in accordance with ISO/DIS 25239-4. Two metallographic samples were extracted from each weld, which were examined microscopically after etching with Keller's modified (consisting of 1 ml 38-40% HF, 1.5 ml 37% HCl, 10 ml 70% HNO_3 and 100 ml water) etchant using a Zeiss-Axioskop 2 optical microscope, equipped with an AxioCam Mrc5 digital colour camera and the AxioVision image processing programme. The metallographic samples were 65 mm wide – the width of the flange plates – and 61 mm or 76 mm high, which corresponds with the thickness of the base plate and 1 or 2 weld passes, respectively. It should be noted here that etching was very difficult for the welds *T8-1-0*, *T8-2-0* and *T4-2-08* (all executed with a very high input): a strong attack of the parent material occurred, whereas the weld nugget was hardly affected. For that reason, the nugget area was embedded separately and re-etched, which did make grain boundaries visible. HV0.2 microhardness profiles were performed on all metallographic samples, using a Struers Duramin A300-D automatic hardness indenter, with a 27 s indentation time and 0.3 mm spacing between individual indentations. A horizontal microhardness profile was made 1.5 mm below the base plate upper surface (see path *H* in *T4-2-0* in Figure 7), while a vertical microhardness profile was carried out through the weld middle (path *V* in *T4-2-0* in Figure 7). The hardness profile extended through the entire metallographic sample, in order to measure unaffected parent material hardness as well.

In all weld macro- and micrographs as well as in all microhardness profiles, the advancing side (AS) is displayed on the left, and the retreating side (RS) on the right.

3.2 Parent material observations

The result of optical microscopy on the 2124-T851 and 2124-T4 parent materials, as well as microhardness values, are shown in Figure 5. The displayed microhardness values are based on at least 20 individual microhardness measurements performed throughout the thickness of each parent material sample. The standard deviation is also mentioned. It can be derived that the T4 heat treatment has only a minor effect on the microhardness when compared to the original T851 temper, which indicates that the microhardness follows the same tendency as the tensile strength of the parent materials (Table 2). Furthermore, the base plate material and the flange plate material of the same temper have the same microhardness.
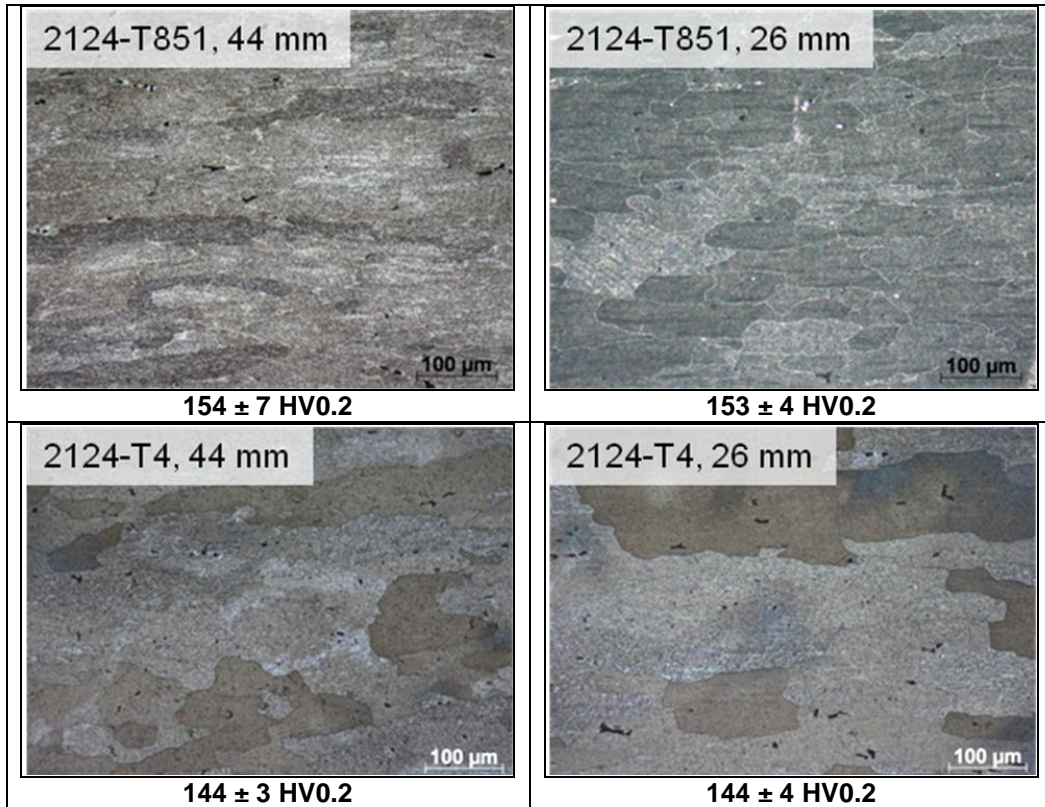
Figure 5. 2124 parent materials microstructure and HV0.2 microhardness

3.3 Weld microstructure observations

Macrographs of the various welds included in this investigation (see Table 3) are shown in Figure 7. No voids (tunnel defects or other) were found in the two welds in 2124-T851. In weld *T4-2-08* on the other hand, small voids were visible on the advancing side near the face of the second pass – this is the region where defects, assuming that they are present, tend to appear. An example of these voids – which are sometimes surface-breaking near the start of the weld – is shown in Figure 6.
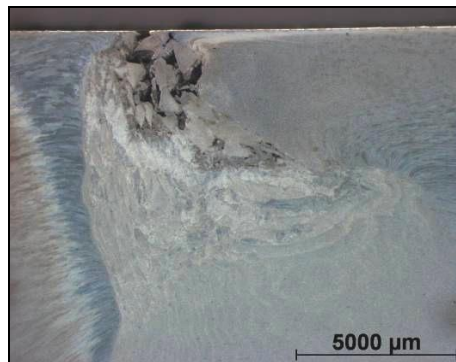
Figure 6. Macrograph of voids on AS of second pass in weld *T4-2-0* (as an example)

The only weld in 2124-T4 where these voids were not observed in either of the two metallographic samples extracted from each was *T4-2-2* (in other words: the weld realised with the Triflat™ tool). Furthermore, the nugget shape of that weld is somewhat different: it has a more of a "chalice"-like shape with relatively straight edges, whereas the nugget shape of the other welds is more rounded-off.
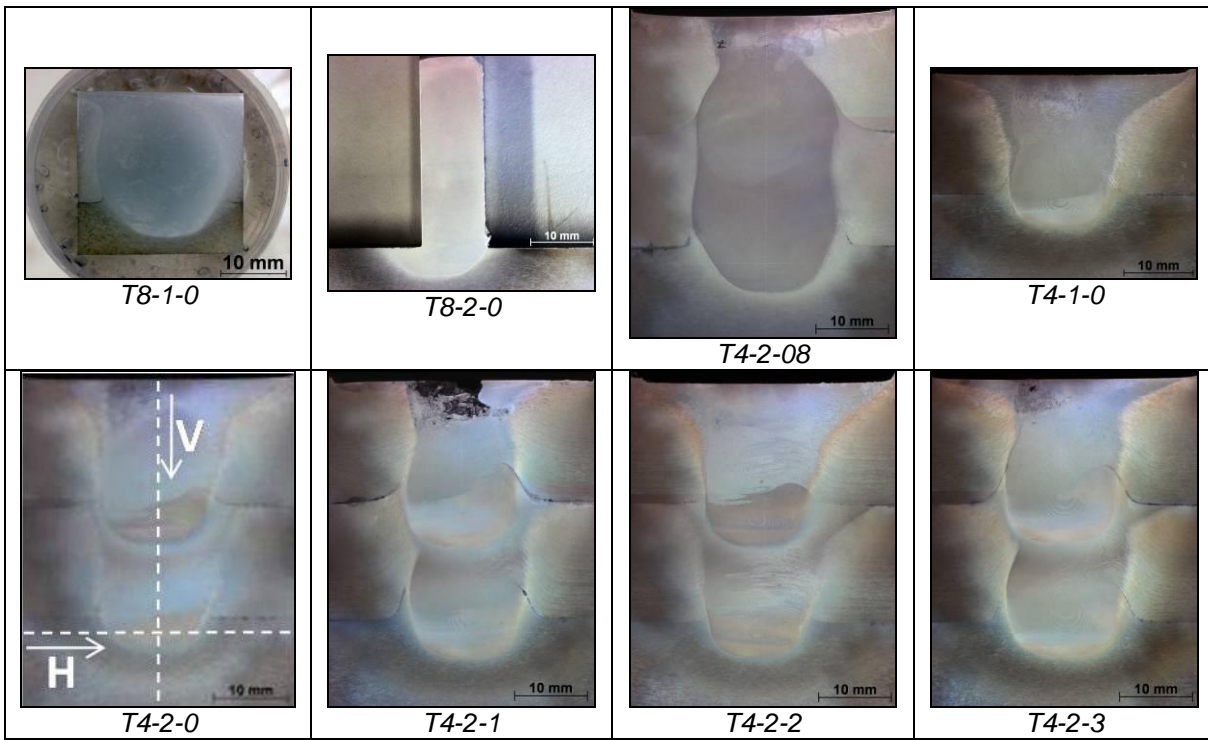
Figure 7. Etched macrographs of the joints included in this investigation

Furthermore, the metallographic samples were subjected to microstructural investigation. Some details are shown in Figure 8. Despite large differences in welding speed, hence heat input (*T8-2-0* and *T4-2-08* compared to e.g. *T4-2-2*), the nugget grain size is very fine compared to the parent material grain size (see Figure 5) and of the same order of magnitude in all cases, namely around 2-5 μm (see Figure 8). Due to the heat treatment that the first weld pass has undergone during the realisation of the second weld pass, grain boundaries become hard to distinguish. However, no significant coarsening seems to have taken place in the nugget of the first weld pass.
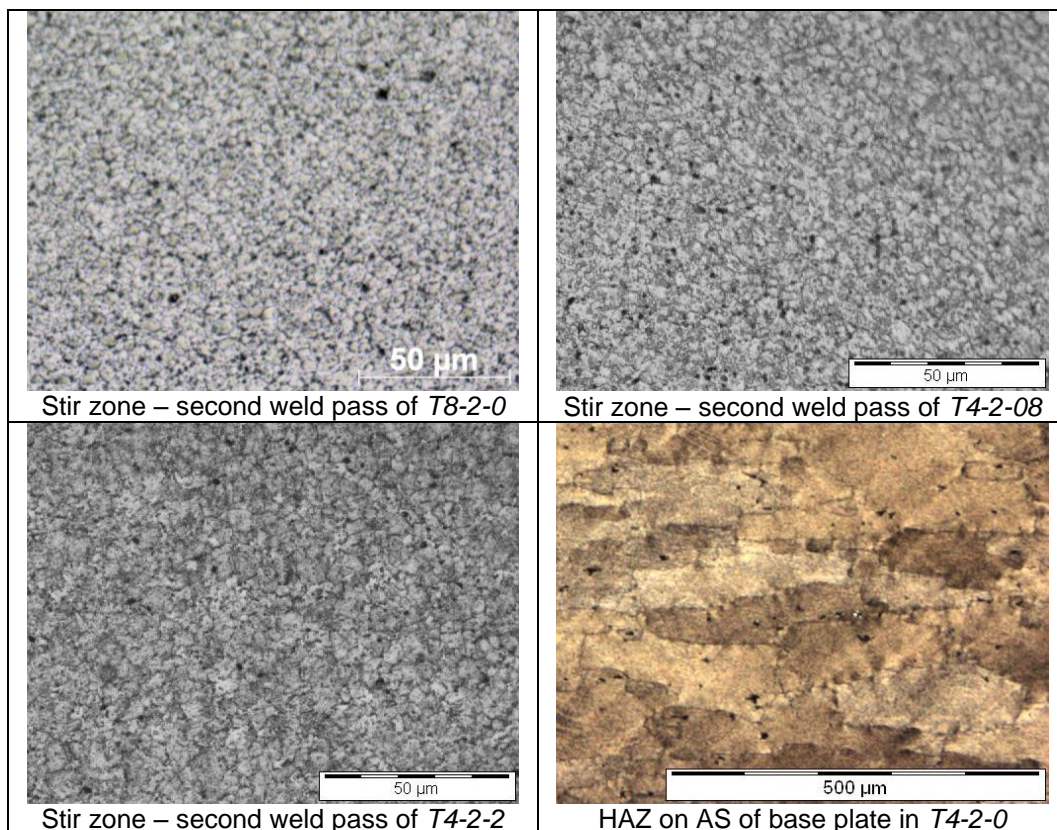
Figure 8. Selected etched microscopic details

3.4 Microhardness results

3.4.1 Microhardness results: welding with very high heat input

Figure 9 gives the horizontal and vertical hardness traverses (refer to *H* and *V* in Figure 7, sample *T4-2-0*) for the 2 two-pass welds carried out with a very low welding speed.

| Horizontal profiles | Vertical profiles |
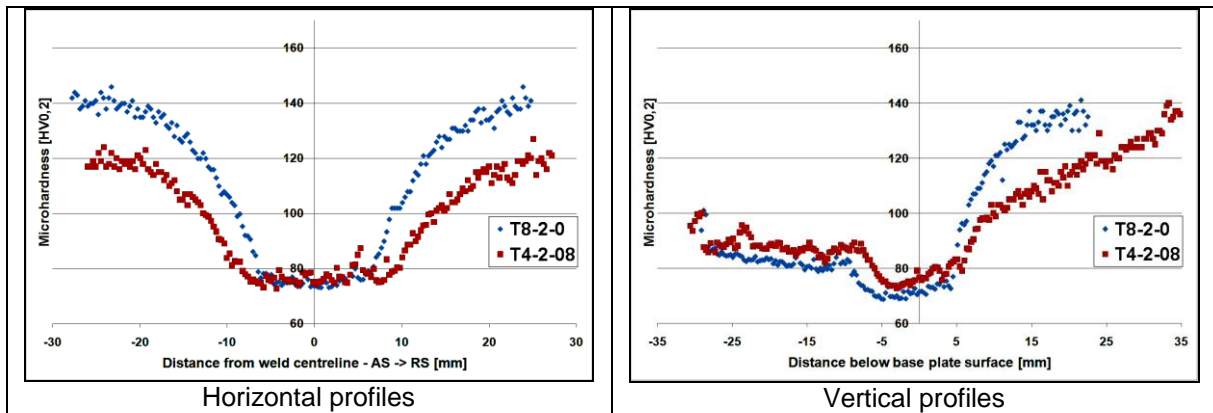
Figure 9. HV0.2 microhardness profiles for welds *T8-2-0* and *T4-2-08*

The following general tendencies are noted:

- Horizontal profiles:
  - For both welds, the nugget hardness in the base plate is more or less comparable, namely around 75 to 80 HV0.2. This could signify that, due to the very high heat input, the nugget material is put in more or less the same metallurgical state in terms of precipitation; moreover it was already indicated in §3.3 that the nugget grain size is more or less comparable.
  - In *T8-2-0*, the minimum is reached in the stir zone (located between -7 mm and +7 mm from the weld centreline). Moving out of the stir zone, towards the HAZ goes along with a hardness increase. The 2124-T851 parent material hardness (around 154 HV0.2) is still not reached at 30 mm from the weld centreline.
  - In *T4-2-08* on the other hand, the width of the hardness minimum is wider than the nugget width, indicating that the hardness of the HAZ immediately next to the nugget is comparable to that of the nugget itself. At 30 mm away from the weld centreline, the hardness is still significantly lower than that of 2124-T4 parent material (which was equal to 144 HV0.2). The hardness increase in the HAZ moving away from the nugget of *T4-2-08* is slower than in *T8-2-0*.
  - Some asymmetry can be noticed in both cases: the hardness increase moving away from the nugget is somewhat steeper on the advancing side than on the retreating side of the joint.
- Vertical profiles:
  - The nugget hardness of weld *T4-2-08* is consistently some 5-10 HV0.2 higher than that of weld *T8-2-0*. In both cases, the absolute hardness minimum occurs in the first weld pass, namely in the HAZ of the second weld pass (which lies in the first weld pass). In both cases, the nugget hardness in the second weld pass increases slightly towards the face of the weld.
  - As in the horizontal hardness profile, the hardness increase in the HAZ moving away from the nugget of *T4-2-08* is slower than in *T8-2-0*.

3.4.2 Microhardness results: influence of tool geometry in 2124-T4

In Figure 10, the hardness profiles are given of all four double-pass friction stir welds in 2124-T4, executed with more or less the same welding speed and rotation speed but with different tool designs.
The following can be noted:

- Horizontal profiles:
  - First of all, the attention should already be drawn to the significantly different shape of the horizontal hardness profiles. In the current case, the nugget hardness (between 115 and 125 HV0.2) lies between the minimum hardness, noted in the HAZ close to the nugget (of which a micrograph is shown in Figure 8 on the lower right) with a value around 95-100 HV0.2 for the different profiles, and that of the parent material with values between 140 and 160 HV0.2.
  - Only small, possibly insignificant differences can be noted for the different tool in terms of nugget hardness (within the order of 10 HV0.2), with sometimes a rather high scatter.
  - The width of the HAZ is more or less the same for all four welding tools: the parent material hardness is reached at some 20 mm away from the weld centreline.

| Horizontal profiles | Vertical profiles |
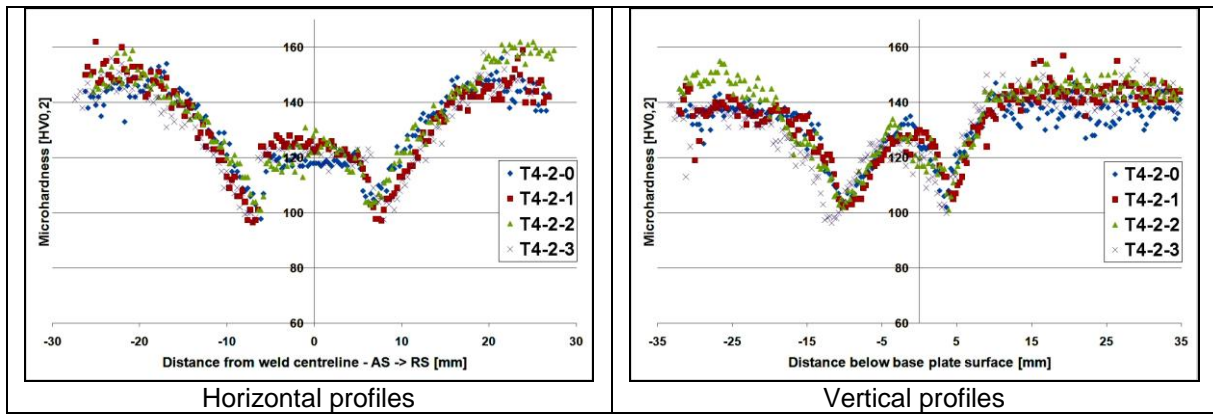
Figure 10. HV0.2 microhardness profiles for the four different FSW tools on 2124-T4

- Vertical profiles:
  - The steep hardness drops near the weld face (around -30 mm in the graph) can be explained by the fact that in three of the four welds, areas with voids occurred, as shown in Figure 6 – this was only not the case for weld *T4-2-2*. In the latter weld, high nugget hardness values of the same order as 2124-T4 parent material are found near the weld face.
  - Starting from 20 mm above the base place and moving "inward", the four profiles share the same tendencies: a significant hardness drop occurs in the HAZ of the second weld pass, which is also more or less comparable as the hardness drop occurring in the HAZ of the first weld pass – i.e., in the base plate. This minimum hardness is around 100 HV0.2 which is 25 HV0.2 higher than the minimum value found in *T4-2-08* (Figure 9). Between the HAZ hardness minima, a local maximum occurs in the nugget of the first weld pass which corresponds to a hardness value between 130 to 135 HV0.2. A hardness value of 140 HV0.2 is already reached at some 10 mm below the base plate surface.

3.4.3   Microhardness results: influence of second weld pass

It was found interesting to check the influence of the realisation of the second weld pass on the hardness of the first weld pass, and also to see whether the realisation of the second weld pass had an influence on the base plate hardness evolution. For that cause, Figure 11 gives the horizontal and vertical hardness traverses of *T8-1-0*, *T8-2-0*, *T4-1-0* and *T4-2-0*. As shown in Table 3, these welds were performed using a tool with the same geometry, but with significantly different welding parameters and a different parent material temper. The influence of these significantly different welding parameters on the hardness evolution in the joint has already been mentioned in §3.4.2, and the same observations can be made in the present paragraph.

| Horizontal profiles | Vertical profiles |
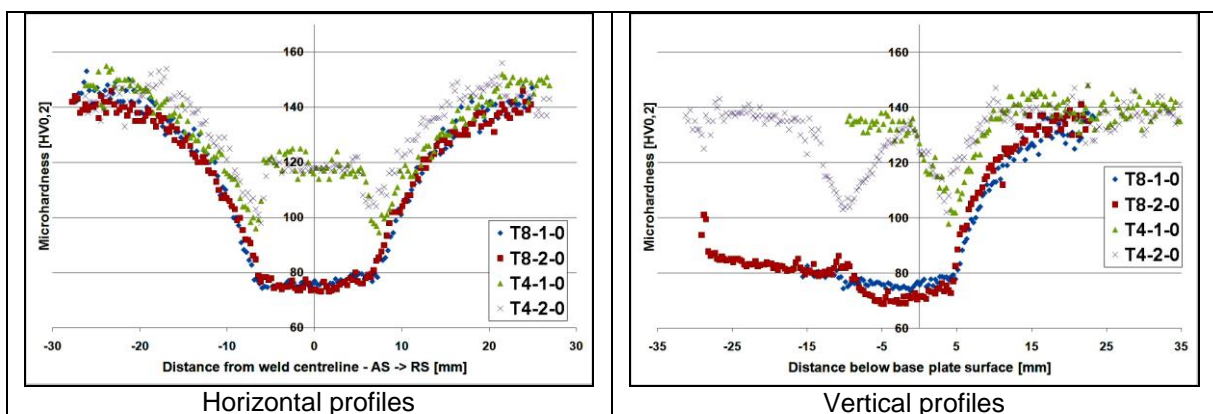
Figure 11. HV0.2 microhardness profiles: influence of second weld pass

The main observations that can be made by comparing *T8-1-0* with *T8-2-0* on the one hand, and *T4-1-0* with *T4-2-0* on the other hand are the following:
- Horizontal profiles:
  - In the 2124-T851 welds, the hardness profiles are very comparable. For that reason, it can be stated that the realisation of the second weld pass has no notable influence on the hardness evolution in the base plate.
  - The same reasoning seems valid for the 2124-T4 welds in the nugget region; however, the base material hardness is more readily reached in the two-pass weld compared to the single-pass weld.

This might indicate that in the HAZ of the base plate, there is still a potential for artificial ageing during the short thermal cycle due to the realisation of the second weld pass.

- Vertical profiles:
  - o In the 2124-T851 welds, the realisation of the second weld pass seems to soften even more the part of the first weld pass nugget which lies in the HAZ of the second weld pass: the minimum hardness decreases from 75 HV 0.2 to 70 HV0.2 due to the realisation of the second weld pass. It can be noted that the nugget hardness of the second weld pass in *T8-2-0* is higher than the nugget hardness of the first weld pass in *T8-1-0*. The HAZ hardness in the base plate evolves more or less in the same way for the two welds.
  - o For the 2124-T4 welds, the nugget hardness in the first weld pass of *T4-1-0* is more or less comparable to the 2124-T4 parent material. The realisation of a second weld pass (*T4-2-0*) creates a HAZ with comparable hardness development (i.e. rate of hardness decrease, value of hardness minimum and rate of hardness increase) as that already created in the base plate. The nugget hardness of the second pass in *T4-2-0* is very comparable to that of first pass in *T4-1-0*.

    The same tendency in terms of HAZ hardness development in the base plate (i.e. the somewhat faster attainment of the parent material hardness in *T4-2-0* compared to *T4-1-0*) can be noted as for the horizontal hardness profiles in these welds.

3.5   Interface properties and depth of penetration as a function of tool geometry

Specifically for the friction stir welds in 2124-T4, the depth of penetration as well as the dimensional "interface properties" were measured, based on the macrographs – see Figure 12. The way these distances were measured is indicated in the top left figure of Figure 12. All data indicated in the graphs are based on measurements of two separate metallographic samples. The following observations were made:
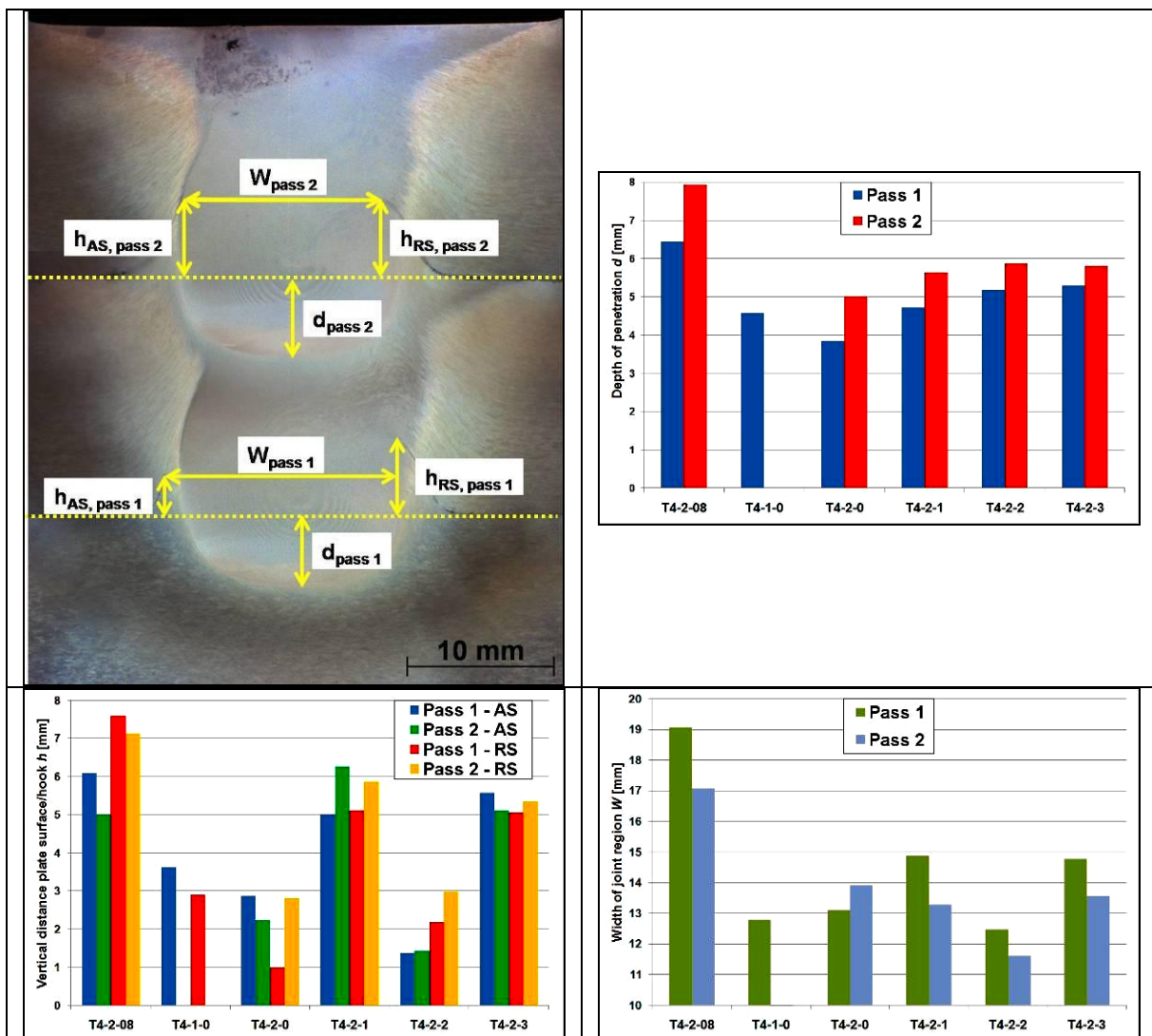
Figure 12. Depth of penetration and interface properties in 2124-T4 welds

- *d* (maximum depth under the surface of the underlying plate where recrystallised material is found)
  - The penetration depth is clearly the highest for the weld realised with the lowest welding speed (*T4-2-08*), which is most likely due to the much higher heat generation, causing easier penetration.
  - More or less comparable penetration depths are found for the welds performed with the four different tool geometries and comparable welding parameters.
  - In all cases, the penetration depth of the first weld pass is lower than that of the second weld pass. Most probably, this is due to the fact that the heat can escape much more easily in the massive base plate during the realisation of the first pass, while during the second weld pass the heat will mainly escape through the lower thickness flange plates. Additionally, the base plate possesses a higher hardness during the realisation of the first weld pass than the first flange plate during the realisation of the second weld pass.
- *h* (distance that the hook extends in the flange material in vertical direction)
  - The highest *h*-values are found for *T4-2-08*, which must be related to the much lower welding speed. This assumption is justified when comparing these with *T4-2-0*, executed with the same tool geometry but at a 12 times higher welding speed.
  - For the welds executed with different tool geometries but comparable welding parameters, the the h-value is the lowest for both tool 0 (standard tool 1) and tool 2 (Triflat™), and the highest for both tool 1 (standard tool 2) and tool 3 (Triflute™).
  - No consistent tendencies could be found in terms of *h*-value for the first and second weld pass, nor for the advancing or retreating side.
- *W* (width of the joint region)
  - The highest heat input condition resulted in the largest joint width.
  - The narrowest joint width is found for weld *T4-2-2*; this is due to the fact that in this Triflat™ weld, hooking on the retreating side extends quite deeply in the horizontal direction.
  - With the exception of weld *T4-2-0*, the largest joint width is noticed in the first weld pass.
  - In all conditions, the joint width is higher than 10 mm, which means that a flange of 10 mm can easily be machined out of the structure without exposing cracks to the surrounding.

4 CONCLUSIONS

By the present work, which is part of an ongoing investigation, the authors have indicated the possibilities for the realisation of flanges in high thickness EN AW-2124 aerospace aluminium alloy by means of consecutive friction stir overlap welds. At this stage of the investigation, especially the importance of parent material temper becomes clear: the use of an appropriate "welding temper" allows a higher productivity on the one hand, and the use of more advanced tool geometries without risking tool pin fracture on the other hand. These more advanced tool geometries might lead to a further increase in productivity, but they have especially an influence in the generation (or avoidance) of joining defects. An optimum tool geometry at this point seems to be the Triflat™ tool: this tool allows to achieve sound welds in this material without the creation of voids. For the current application, the disadvantage of significant hooking on the retreating side in the horizontal direction encountered with this tool is of less significance, as a flange of 10 mm can still easily be machined out of the structure without exposure of this hooking to the surrounding.
In this ongoing investigation, future attention will go out to post-weld heat treatments, corrosion properties, microtensile tests and fracture mechanical testing of flanges.

5 ACKNOWLEDGEMENTS

6 REFERENCES

[1] G. Mathers, The welding of aluminium and its alloys, Woodhead Publishing ISBN 1 85573 567 9, September 2002, 248 pages
[2] W.M. Thomas et al., Friction Stir Butt Welding, International Patent Application PCT/GB92/02203, GB Patent Application 9125978.8, 6 Dec. 1991
[3] W. M. Thomas et al., Friction stir welding for the transportation industries, Materials & Design 1997, Vol. 18, Nos. 4 6, pp. 269-273
[4] W.M. Thomas et al., Developments in Friction Stir Welding, ASM Materials Solutions 2003 Conference & Exposition, 13-15 October 2003 Pittsburgh, Pennsylvania, USA

[5] C. Wiesner et al., Joining and Near-Net Shape Manufacturing processes, presentation at www.specialmetalsforum.com/doc/download/7

[6] http://lyle.smu.edu/rcam/rcamweb/fswrp.htm

[7] http://www.uddeholm.be/french/files/Uddeholm_QRO_90_Supreme_E2.pdf

[8]

Poster Session

HIGH CONDUCTIVE GRAPHITE ADDITIVES FOR MAGNESIUM CATALYZED CAST PA6 POLYMER MATRIX

Mátyás ANDÓ, Gábor KALÁCSKA
Institute for Mechanical Engeneering Technology,
Szent István University, H-2100. Gödöllő, Pater K. út 1.

Tibor CZIGÁNY
Department of Polymer Engeneering,
Budapest University of Technology and Economics,
H-1111. Budapest, Műegyetem rkp. 3

Abstract At this article we give a brief review about the additives effects for cast polyamide 6 engineering plastics. The natural grade Magnesium catalyzed polyamide 6 has unique mechanical properties. Our target is to keep the mechanical and tribological properties with the development of antistatic and ESD composite version. High conductive very effective to improve the electrical conductivity of magnezium catalized cast PA 6. Only few amount, 0,5% can result good antistatic property for the base matrix. Over 3% of additive the surface resistance of the material – performing 10^7 Ω - can reach the ESD (Electrostatic Dissipative) category.

Key words Polyamide 6, surface resistivity, antistatic behaviour, high conductive graphite additive

1. INTRODUCTION

The spread of plastics in electronic use was quite fast as its insulating characteristics had an invaluable count. By now, with more wide use of plastics a demand rose for such special compounds, which have lower resistance or are antistatic. Plastics considered like conventional ones (insulating plastics) are not able to conduct the charge, therefore they get charged. There are more disadvantages of electrically charged plastics: their surface can get contaminated easily, they can adhere (foils), charges can be taken away by humans that can be observed as a „strike". Sparks can emerge, which can cause - in special surroundings - explosion or burn. In agricultural point of view this latest effect is not negligible as several times the ambient condition is critical (seeds powder mixed with air, pneumatic transport) in which a spark is enough for explosion (powder explosion). In such fields it is beneficial to use antistatic engineering plastics.

2. ANTISTATIC BEHAVIOUR AND ITS EXAMINATION

To classify the antistatic behaviour the surface resistance and half-period of materials are commonly used. These values are not independent from each other, the relation between them is the discharging process of condensators, which can be characterized with an exponential equation (in more details: [1]). Based on surface resistivity the following categories are used in engineering practice (Table 1) [2, 3, 4] (Kalácska 2007).
Meaning of surface resistance was standardized log time ago. Now the second edition of „IEC 60093 Methods of Test for Volume Resistivity and Surface Resistivity of Solid Electrical Insulating Materials" is valid since 1980 (Figure 1.). For our research the measuring instrument was set with 100V potential for 10^5 - $2 \cdot 10^{11}$ Ω surface resistivity range. That is the investigated range of the cast polyamide 6 versions. The accuracy in this range is ±5 % according to the manufacturer's data that were controlled, as well.

Table 1. *Classification of materials by surface resistance*

Surface resistance (Ω)	Group
$<10^{-3}$	Electrically conductive range of metals
10^{-2}-10^{0}	Conductive range of natural coal
10^{1}-10^{2}	Electrically shading polymers
10^{3}-10^{5}	Electrically conductive polymers
10^{6}-10^{9}	Continuously conduct the electrical charges (beside little resistance), ESD materials
10^{10}-10^{12}	Polymers having antistatic characteristics (beside high resistance)
$>10^{13}$	Insulating polymers

Fig. 1. *Measuring layout of surface resistivity*

3. SPECIMEN MATERIALS AND PREPARATION

In Germany PA6 was first produced in 1938. This is a polycondensational procedure [3]. Natrium-catalyzed cast PA6 was developed only later, but it did not fulfil the requirements. It was not appropriate for fiber production but it was excellent for block casting. The industrial-scale production technology of magnesium catalysed cast PA6 was worked out by Hungarian researchers in the 1990s. The use of the magnesium catalyzator did not solve the problem of the fiber production, it only modified the characteristics of cast PA6 (better toughness and abrasion resistance). Nowadays the Quattroplast Ltd. produces magnesium catalyzed cast PA6 with a unique production technology in the world. It takes the advantage of ring opening polymerisation [5]. The surface resistance of natural PA6 is 10^{13} Ω (produced with the Hungarian technology).

In plastic industry several additives are used for increasing the volumetric conduction characteristics of the matrix. These materials are [3]: black carbon, graphite, carbon fibre, metal coated graphite, glass fibres, metal coated glassballs. Characteristics change can only be reached by using more additives than a specific concentration. With this, they are able to compose a continual frame in the material. Conventianally more than 30% additive is given to the base matrix to reach electrical conductivity.

One of the additives of material development was high conductive graphite. Graphite is also widely used to decrease surface resistivity [6-9], but the literature is somewhat poor in respect of polyamides. In the case of other polymers (e.g. epoxy resins) surface resistivities in the order of 10^{9} Ω can be achieved. In the case of polyamides graphite additives are also used to improve wear resistance [10-11] and flame resistance [12].

For measuring the surface resistance, the specimen should be prepared, as polyamides are able to absorb humidity, and the absorbed water makes fake the measured results. Casting of test samples took several weeks, so the first samples have time enough to absorb more humidity. To exclude the effect of humidity from measurement, 2 mm of the materials were machined from the surface. The remove the upper 2 mm is sufficient for polyamides because the absorption is in accordance with the law of diffusion (the diffusion speed slows from the surface to the depth of the materials). Beside the measurements in dry conditions, we also made humid condition and standard condition measurements to investigate the potentially best surface conductivity, as well. The humid condition specimens were pre-soaked for 24 hours in 20°C water before the wet measurements. Then we let them dry for 5 minutes on 20°C air before the test. The standard condition specimens were pre-soaked at 20 ºC under 50% relative humidity (RH).

4.   RESULTS

Figure 2 shows the effects of high conductive graphite content on surface resistance.
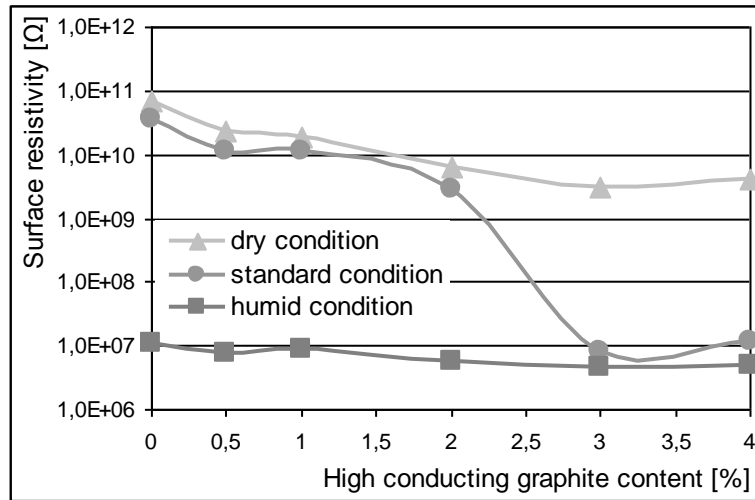
Fig. 2. Effects of high conductive graphite content on surface resistivity

5.   EVALUATION

Four important circumstances should be taken into consideration when evaluating the results:
1. The producer delivers semi-finished products (blocks), which is machined by the enduser or customer according to their needs. Therefore the use of coating-like antistatics makes no sense (e.g. by milling the removal of the surface results no antistatic behaviour later).
2. The agricultural circumstances does not mean stable environmental conditions, so the surface resistance of machine parts independently of environmental effect (in worse case despite of it) should stay below 10^9 Ω (the quality limit of the antistatics determined as a target.)
3. During the evaluation it is enough to examine only the surface resistance of specimen: in the agriculture the environment may change, the surface resistance of the cast PA probably follows it with change of magnitudes.
4. The primary (basic) value is the surface resistance measured under dry conditions, as during the use, this is the value which can be provided by the material in the worst environmental circumstances, too (under wet conditions the antistatic characteristics are always better).

In dry condition, with the increasing of the high conductive graphite content, the value of the surface resistance is decreasing, which is in harmony with the literature. It can be stated that in this system, the antistatic effect can be reached also with less additives, there is no need for eg. more than 20% of additive content, as in case of PUR and EP. Only 0,5% additive can decrease the originally electrical insulating base material's surface resistance to antistatic region. At 2% of high conductive graphite content the 10^9 Ω magnitudes can be reached, which means a good antistatic behaviour. After treating the material samples in normal surroundings (50%RH, 23ºC) it can be stated that between 2 - 3% additive content a transition point can be reached, where the distance of additive particles in the matrix decreases to a critical value resulting enhanced transport of electrical charges. Due to that phenomenon over 3% additive (50%RH, 23ºC) the new composite samples perform ESD (Electrostatic dissipative) properties. This means much better behaviour that it was preliminary expected. It can be seen that for the humid conditions the surface resistance of specimen decreases to 10^7 Ω. On the basis of tendency, the sample reaches this magnitude under standard conditions with 3% of high conductive graphite content, so there is no significant difference between the standard and the humid value. These materials are less independent from the environmental effects in case of electrical characteristics. However it should be noticed that the high conductive graphite content rise over a certain limit does not have notable surface resistance change. In case of such surface resistance decrease, the 3-4% graphite content means an ESD polymer compared with the originally insulating PA6.

6. CONCLUSION

High conductive graphite efficiently develops the electrical characteristics in case of magnesium catalyzed cast polyamide 6. Despite of other researchers' earlier experiences, in this system 0,5% of additive was enough for the development of antistatic characteristics (at least 10^{10} magnitude). Only 2% additive material can result good antistatic composite version. PA6 with more than 3% of additives decreases surface resistance in standard condition to 10^7 Ω. This result is better than the expected one reaching the ESD category. The surface resistance values measured under wet conditions are in 10^7 Ω magnitude. With this characteristics they are able to conduct the charges well under standard and wet conditions, too. On the basis of these it can be stated that antistatic and ESD characteristics were managed to reach by magnesium catalyzed polyamide 6 with effective additives.

7. REFERENCES

[1] Gächter R., Müller H.: Plastics Additives. Hanser Publishers, Munich, 749-766 (1990).
[2] Bruyne D.: ERTA Engineering Plastics. 3P Engineering Workshop. Seminar booklet. Tielt, Belgium (1998).
[3] Kalácska G.: Engineering polymers and composites in the mechanical engineering practice (in Hungarian) 3C-Grafika Kft., Gödöllő (2007).
[4] Varis, J.: Static dissipative compounds: solutions for static control. Plastics Additives & Compounding, 3, 16–19 (2001).
[5] Macskási L.: Chemical and procedural basics of polymer manufacturing (in Hungarian). Abigél Bt., Budapest (1996).
[6] Markarian F.: New developments in antistatic and conductive additives. Plastics Additives & Compounding 10, 22-25 (2008).
[7] Novák I., Krupa I.: Electro-conductive resins filled with graphite for casting applications. European Polymer Journal, 40 1417-1422 (2004).
[8] Li J. H., Feng L. L., Jia Z. X.: Preparation of expanded graphite with 160 μm mesh of fine flake graphite. Materials Letters, 60 746-749 (2005).
[9] Zheng W., Lu X. H., Wong S. C.: Electrical and mechanical properties of expanded graphite-reinforced high-density polyethylene. Journal of Applied Polymer Science, 91 2781-2788 (2004).
[10] Chang L., Zhang Z., Zhang H., Schlarb A.: On the sliding wear of nanoparticle filled polyamide 66 composites. Composites Science and Technology 66, 3188–3198 (2006).
[11] Arjula S., Harsha A.: Study of erosion efficiency of polymers and polymer composites. Polymer Testing 25, 188–196 (2006).
[12] Dasari A., Yu Z., Mai Y., Cai G., Song H.: Roles of graphite oxide, clay and POSS during the combustion of polyamide 6. Polymer 50, 1577–1587 (2009).

DESIGN TO CONNECT

T. Bleuzé[1,2], P. De Baets[2] and J. Detand[1]

[1] University College of West-Flanders, Industrial Design Center, Belgium
[2] Ghent University, Laboratory Soete, Belgium

Abstract

Design to Connect is a cooperation between Howest University, Industrial Design Center and Ghent University, Laboratory Soete. The aim of the research is to create a methodology to support (industrial) designers to design mechanical connections and joining methods considering mechanical and user centred factors in the total product life. This paper gives a short overview of the most important existing methods, guidelines and tools to design and select mechanical connections. It also situate the research project and its potential added value for product designers to the existing methods. Finally a basic framework for developing the new methodology is created: Design to Connect (D2C).

Keywords mechanical connections, product life cycle, DFX, process selection

1   INTRODUCTION

The most daily used products contains more than one part. Connections and joints play therefore a key role in product design. Joining components influence the individual component complexity [1], the movement between components, the accessibility of components and functional requirements like electrical and thermal conduction. Historically, joining methods are sector and material oriented. In the past products were made with mono materials, like wood or steel. Every material has his own well known joining methods. Welding and mechanical fasteners to join metal parts, wood joinery... Today, more and more products are made with different materials [2], multi materials, hybrid materials and composite materials to fulfil the more and more requiring product needs. Product disassembly and recycling plays a major role by the increasing materials shortage and environmental aspects. In most cases the design and selection of connections and joining methods during the design process happens through the experience of the designer. In that way designers fall back on known joining solutions and there is no place for innovation. Since the degree of complexity is growing, it's also important for designers to consider joining aspects already in the first stage of the design process [3].

2   PRODUCT LIFE CYCLE

A connection can influence the production and assembly, the use of the product and the disassembly of the components to recycle. In that way it's important for a designer to consider the total 'product life' during the design of the product. Pahl and Beitz define the 'Product Life Cycle' (PLC): *"This cycle is triggered by a market need or a new idea. It starts with product planning and ends—when the product's useful life is over—with recycling or environmentally safe disposal. This cycle represents a process of converting raw materials into economic products of high added value."* [4] The PLC described by Pahl and Beitz can be simplified into six steps: Design of the product, manufacturing, distribution, trading, use or consuming of the product and finally dispose the product for recycling. These six steps are shown in figure 1. This PLC should not be confused with the 'Product Life Cycle' from marketing where the life phases of a product are defined in the market.

PRODUCT LIFE /
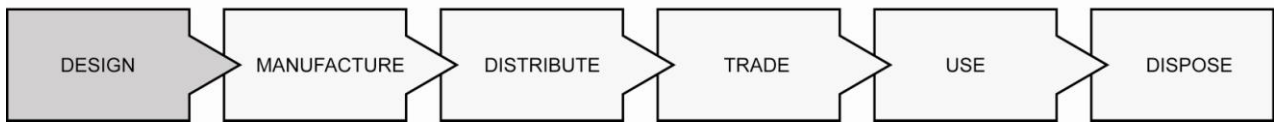
Figure 1. Product Life Cycle (PLC)

3   DESIGN FOR X GUIDELINES

To help designers select and design connections, people have already developed several methods and selection tools. Ashby and Esawi define two techniques that contribute cost-effective assembly: *"That of design to minimise part count and easy mating (Design for Assembly) and that of selecting the joining process that best suits the joint during life."* [5] The first technique, Design for Assembly (DFA), fits together with other guidelines like Design for Disassembly under the label Design for X (DFX) [6]. The most important DFX guidelines that consider joining aspects are mentioned in this paper. Design for Manufacturing and Assembly (DFMA) is developed by Dr. Boothroyd and Dr. Dewhurst. The DFMA methodology simplify the assembly and manufacturing of your designs [7]. In that way it's possible to reduce the manufacture and assembly cost of the product. Design for Recycling (DFR) are guidelines to reuse raw materials in order to move towards more sustainable development [4]. A variant is Design for Disassembly (DFD), that involves designing a product for easy disassembling. In that way it's easier to maintain, repair, and reuse product components and materials. A new evolution in DFD is Active Disassembly (AD) developed by Dr. Joseph Chiodo: *"AD technology is a method of disassembling products into their separate components using specifically engineered and/or Smart materials, adhesives to allows for a clean, nondestructive, quick & efficient method of component separation."* [8] All of these DFX guidelines are focused on one phase in the PLC: manufacturing or disposal (recycling, disassemble). There is no holistic technique or methodology that considers all the aspects of a connection in the total product life. An overview of the DFX guidelines discussed in this paper is shown in figure 2.

PRODUCT LIFE /
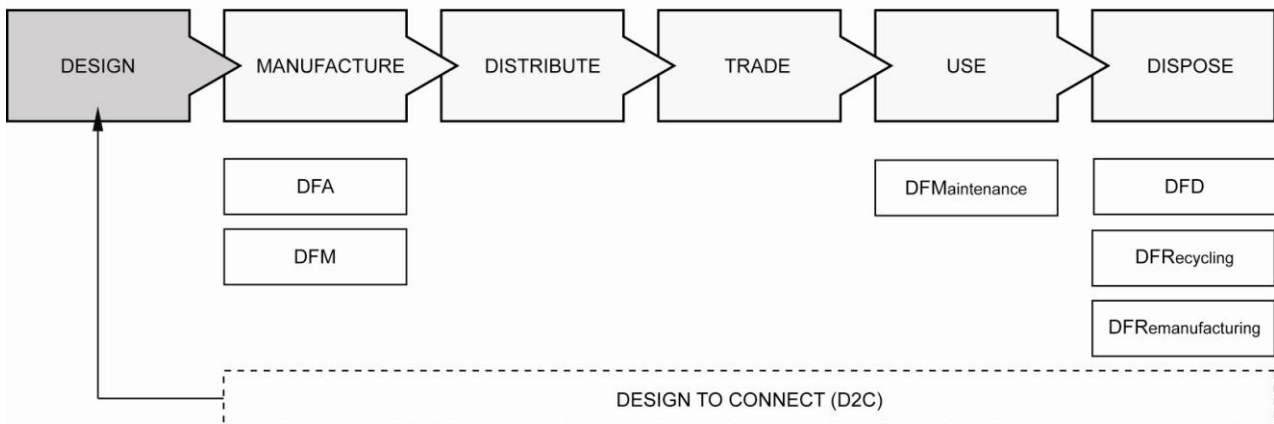
Figure 2. DFX guidelines through the life of a product

4   PROCESS SELECTION IN MECHANICAL DESIGN

The second group of techniques are the (joining) process selection methods. These tools help the designer choose the best suited joining process. Lovatt and Shercliff define three categories of (joining) process selection: *"Following an idea proposed by Ishii, process selection may be considered to fall into three broad categories: preliminary, functional and task-based. Each of these categories considers the selection of a manufacturing process at an increasing level of detail in the design process."* [3] Some research projects involved the development of a joining selection tool implemented in a software environment [9]. Several joining process selection methods/tools are already developed. 'Granta CES selector' is a powerful selection method and software tool for the selection of materials and processes developed by the University of Cambridge [10]. Some free online tools are available to select joining processes.'

Archetype joint' [11] is an online database that helps designers to select fastening and joining methods that meet their specific joint requirements. 'Dunne-plaat online' [12] is an information website with a tool that helps designers to select methods for joining sheetmetal parts. All these tools are developed for Mechanical Design problems, engineering materials and joining processes. Mechanical design considerations [13] are based on 'shape', 'material', 'function' and 'manufacturing process'. User centred aspects like 'use' and 'product personality' aren't taken into consideration in Mechanical Design. Materials like wood and textiles and connections like a zipper or 'hook and loop' aren't always involved in the selection process. In that way the designer is limited by the processes and materials that are involved in the selection database.

5   USER CENTERED CONSIDERATIONS

In Product Design the user and the interaction with the product plays an important role. Ilse Van Kesteren developed a consideration model that showed the relations between 'use', 'product personality', 'function', 'material', 'shape' and 'manufacturing process' [14]. A comparison of the mechanical design considerations and the user centered design considerations from Van Kesteren is shown in figure 3.
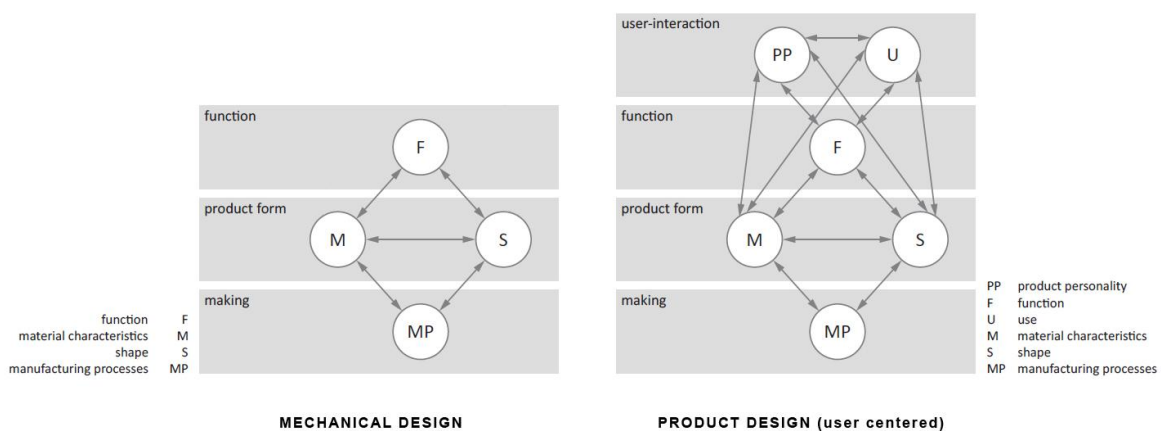
Figure 3. Mechanical Design considerations model [1] and Product Design considerations model [14]

In material selection are, beside technical information, aesthetics and tactile aspects also important. There are already some material selection tools that considered user – centered and esthetic aspects. An example is Skin [15], developed by Daniel Saakes. It's a tool that projects graphics on prototypes and objects to quickly review the aesthetics from materials. In that way it is possible to select the materials in an early stage of the design process. During the use and consumption of products, connections and joints can also play an important role for the user. Think of opening a remote control to change the batteries, change vacuum cleaner tools in a fast and easy way, personalize your cell phone cover, … In the book Materials and Design, Ashby and Johnson describe that joints can be used as a mode of expression in product design: "*Joining, too, can be used expressively. It reaches an art form in bookbinding, in the dovetailing of woods, and in the decorative* seaming *of garments. In product design, too, joints can be used as a mode of expression.*" [16] To help industrial designers design and select joining methods, there is a need to develop a method that consider beside the mechanical aspects also user – centered aspects. For example the usability of a removable connection and the aesthetics or product personality of a joint.

6   DESIGN TO CONNECT

D2C wants to create a methodology that helps product designers and students to design connections in a product. The methodology must consider beside the mechanical requirements also user – centered aspects of the connection and the total life of the product (PLC). The methodology may not be material (ex. plastics) or sector (ex. machine design) oriented but a holistic approach to different defined joining problems. The methodology may not restrict the designer in here/his creative process and can be used in the first stages of the design process. Using the methodology the designer must be able to explore many possible solutions in a structured, effective and creative way and select one solution. At the end of the process the designer must be able to evaluate the founded solution with the predefined requirements. A basic framework to setup the D2C methodology is shown in figure 4.
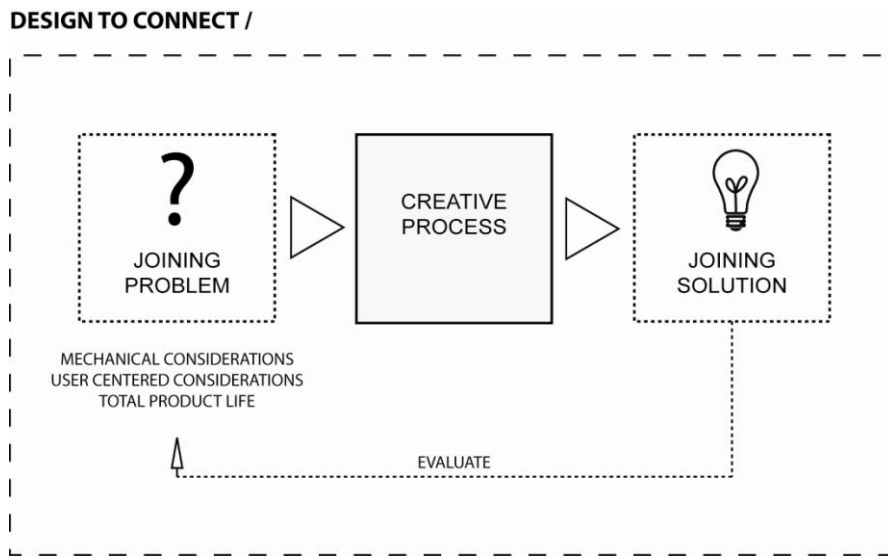
Figure 4. Basic framework to setup the D2C methodology.

7   REFERENCES

[1]   C. LeBacq, *et al.*, "Selection of joining methods in mechanical design," *Materials & Design,* vol. 23, pp. 405-416, Jun 2002.

[2]   C. Lefteri. (2007) Material Timeline. *Ingredients*. 2.

[3]   A. M. Lovatt and H. R. Shercliff, "Manufacturing process selection in engineering design. Part 1: the role of process selection," *Materials and Design,* vol. 19, pp. 205-215, 1998.

[4]   G. Pahl and W. Beitz, "Engineering Design: A systematic approach," J. Feldhusen and K. H. Grote, Eds., 3th ed. London: Springer, 2007.

[5]   A. M. K. Esawi and M. F. Ashby, "Computer-based selection of joining processes: Methods, software and case studies," *Materials & Design,* vol. 25, pp. 555-564, 2004.

[6]   *Design for X*. Available: http://en.wikipedia.org/wiki/Design_for_X

[7]   I. Boothroyd Dewhust. *Design for manufacture and assembly*. Available: http://www.dfma.com/

[8]   *Active Disassembly*. Available: http://www.activedisassembly.com/

[9]   T. L'Eglise, *et al.*, "A Multicriteria Decision-Aid System for Joining Process Selection," in *IEEE International Symposium on Assembly and Task Planning (ISATP 2001)*, Fukuoka, Japan, 2001.

[10]   *Granta Design CES selector*. Available: http://www.grantadesign.com/

[11]   *Archetype joint*. Available: www.archetypejoint.com

[12]   *Dunne plaat online*. Available: http://www.dunneplaat-online.nl

[13]   M. F. Ashby and MyiLibrary. (2005). *Materials selection in mechanical design (3rd ed.)*.

[14]   I. V. Kesteren, "Selecting materials in product design," phd, Faculty of Industrial Design Engineering, Delft University of Technology,, Delft, 2008.

[15]   *Skin*. Available: http://www.studiolab.nl/skin/

[16]   M. F. Ashby, *et al.* (2002). *Materials and design the art and science of material selection in product design*. Available: http://www.myilibrary.com?id=75444

WELDABILITY OF MICRO-ALLOYED HIGH-STRENGTH PIPELINE STEELS USING A NEW FRICTION WELDING VARIANT

K. Faes [1], P. De Baets [2], A. Dhooge [1,2], W. De Waele [2], R. Denys [2],
E. Van Der Donckt [3] and D. Delbaere [3]

[1] Belgian Welding Institute, Belgium
[2] Ghent University, Laboratory Soete, Belgium
[3] DENYS NV, Belgium

Abstract : An innovative welding method for fully automatic joining of pipelines has been developed. The proposed welding procedure is a variant of the conventional friction welding process. A rotating intermediate ring is used to generate heat necessary to realise the weld. The working principles of the welding process are described. The weldability of the micro-alloyed high-strength pipeline steel API-5L X65 is experimentally investigated. It was found that the new welding process is suitable for joining this material. When welding with a sufficiently low heat input, a high weld quality is obtained. Under these circumstances the weld strength, ductility and impact toughness are high and fulfil the requirements of the commonly used standard EN 12732 for joining pipes.

Keywords : friction welding, pipelines, micro-alloyed high-strength pipeline steels

1   INTRODUCTION

Unprecedented demand growth for natural gas and petroleum is fuelling an enormous global need for pipeline construction in the coming years. According to pipeline industry analysts [1], up to 237.000 km of new pipeline construction is announced worldwide. Based on reasonable assumptions, this figure implies not less than 15 to 20 million welds to be made. Obviously this prospect is representing a robust growth-opportunity for companies involved in pipeline construction (construction contractors, welding subcontractors, engineering offices, welding equipment manufacturers, etc.). But at the same time it is putting an unseen challenge in terms of productivity, quality assurance, employee safety and environmental impact for welding operations.

Traditional manual welding techniques have several limitations in relation to the above mentioned challenges. An increasing end-user driven demand for high-strength steels for pipeline applications is observed. These steel grades typically are more difficult to weld with the conventional technology. The quality requirements are increasingly stringent and there is a need to guarantee a constant, reproducible quality. Moreover, it is difficult to find skilled welders and it is foreseen that the shortage will increase in the coming years.

2   PRINCIPLE OF THE NEW VARIANT OF THE FRICTION WELDING PROCESS

In order to cope with the challenges, several automatic welding processes have been developed [2-7]. Friction welding [8] is one of the processes which has been investigated for pipeline girth welding. Friction welding is a forge welding process in which the heat is generated as a result of the friction between two surfaces rubbing against each other under controlled axial pressure. Conventional friction welding is however not suitable for joining long components, such as pipelines, since these parts cannot be rotated for practical reasons.

To enable pipelines to be welded using friction welding, a new variant of the conventional process has been developed, which is called "FRIEX". The major difference of the new variant with conventional friction welding is that a "filler material" in the form of a solid ring is used. The welding ring is placed in between the pipes, and rotating the ring under an axial pressure generates the required friction and associated heat [9-13].

After the pipes are brought into contact with the welding ring, the friction between the rotating ring and the pipes increases the temperature in the contact area, until the forge temperature is reached. At that moment, the rotation of the ring is rapidly stopped, and the axial force is increased to the final forge force. After welding, the remaining welding ring material and welding flashes are removed using automated turning and milling mechanisms.
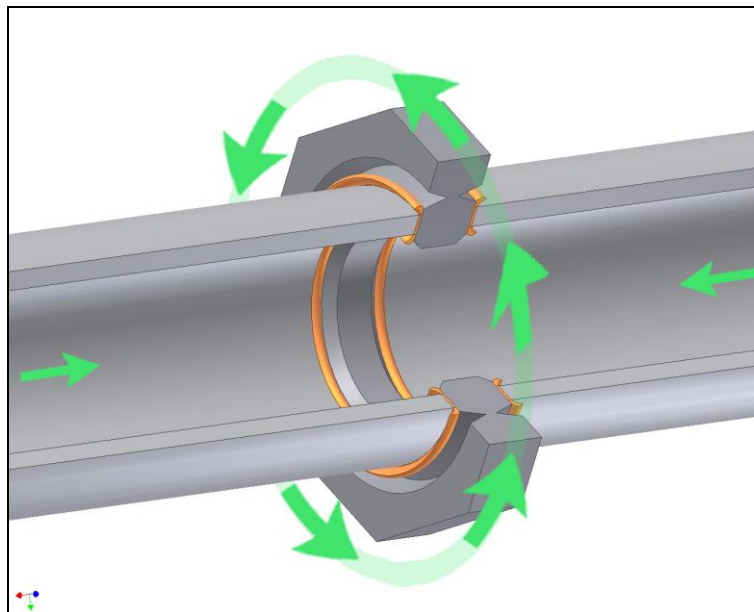
Figure 1. Principe of the welding process

3 EXPERIMENTAL RESEARCH

The feasibility of the new variant of the friction welding process for joining pipes has been successfully proven for welding pipes in conventional rolled pipeline steels API-5L X42 and X52, with a ferritic-pearlitic microstructure. The welding trials have been performed with pipes with an outer diameter of resp. 88,9 and 114,3 mm, using a small-scale test set-up [9-13].

For these pipeline steels the influence of the welding parameters on the weld properties was investigated. A work program was established to examine experimentally the factors affecting the toughness properties of welded pipes. The general aim was to study the influence of the process parameters in order to be able to select the appropriate process parameters for ensuring high-quality welds.

After parameter optimisation high-quality welds could be realised, which fulfilled the requirements of the often used standard EN 12732; "Gas supply systems - Welding steel pipework - Functional requirements". This frequently used standard contains the production and testing requirements of weld joints for installation of onshore steel pipelines and pipework used in gas supply systems. Also the welding ring material, shape and dimensions were optimised. Welding rings with a compatible microstructure, strength and toughness were used.

The ever increasing demand for energy world wide requires the construction of high pressure gas transmission lines with the greatest possible transport efficiency, in order to minimise the cost of pipeline construction and gas transportation. This is particularly the case when large distances have to be covered. Nowadays the trend is therefore using pipelines of larger diameter and/or increasing the operation pressure of the pipeline. This necessitates the use of higher-strength steel grades to avoid a large pipe wall thickness. In consideration of the future acceptance, the welding process was validated for joining high-strength micro-alloyed pipeline steels, such as API-5L X65, X70 and X80.

4 LARGE SCALE EXPERIMENTAL TEST SET-UP

A large full-scale test set-up was designed and built for welding pipes up to a diameter of 504 mm (see Figure 2). The axial friction and forge force is exercised by two large hydraulic cylinders. The maximum available force equals 3000 kN.

The rotation of the welding ring is realised by using 6 hydraulic motors, each connected to a planetary gear system (gear ratio 1:3,25), which are in their turn mounted on a central placed large gear transmission with a gear ratio of 1:4. The total gear ratio thus equals 1:13. The welding ring is mounted in the large hollow gear wheel of the gear system, in a rigid clamping device able to transmit the drive power and torque. The maximum rotation speed of the welding ring is 250 rpm. The available effective drive power and torque equals 600 kW and 100.000 Nm respectively.
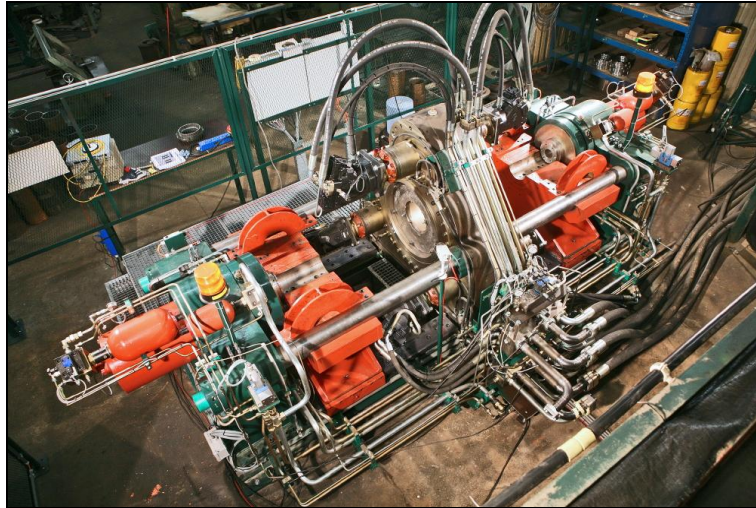
Figure 2. Large scale test set-up

The rotational speed, the axial friction and forge force and the friction time are the principle variables that are controlled in order to provide the necessary combination of temperature and pressure to form the weld. The heating time is controlled by measuring the axial shortening during the weld cycle. Sufficient material must be consumed to assure adequate heating prior to forging. When the predetermined shortening of the pipe ends is attained, the welding ring is decelerated and the axial force is increased to the forge force to cause additional shortening.
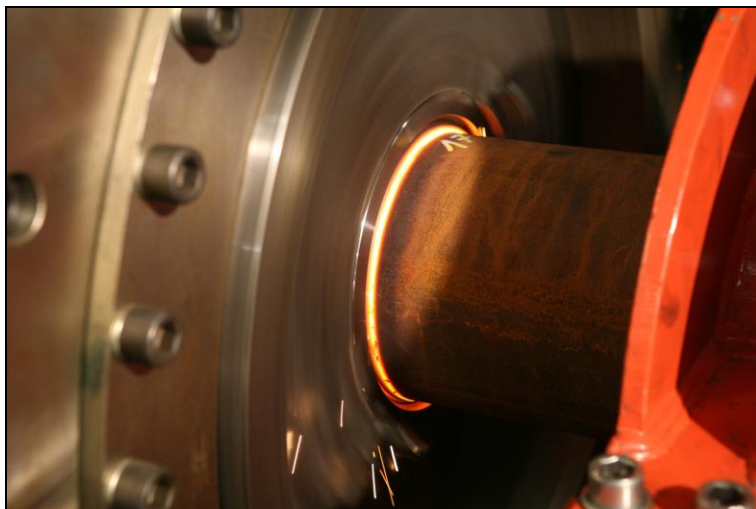
Figure 3. Welding experiment

5   WELDING EXPERIMENTS WITH API-5L X65 PIPELINE STEEL

5.1   Materials

For investigating the feasibility of the use of the new welding process for joining high-strength micro-alloyed pipeline steels, exploratory welding trials were performed with the quenched and tempered micro-alloyed high-strength pipeline steel API-5L X65. The yield stress, tensile strength, impact toughness and hardness were equal to respectively 487-534 MPa, 533-608 MPa, 260 J (at -20°C) and 193 HV1. For the welding ring the high-strength thermomechanically rolled steel with accelerated cooling EN 10225 S460G2+M was used. The yield stress, tensile strength, impact toughness and hardness were equal to respectively 495 MPa, 630 MPa, 342 J (at -20°C) and 196 HV1.The chemical composition of these materials is specified in Table 1.

The utilised pipes have a diameter and a wall thickness of respectively 219,1 and 8,2 mm. The thickness of the welding ring was equal to 15 mm.

Chemical composition of API-5L X65										
C	Si	Mn	S	P	Al	Cr	Ni	Mo	Cu	V
0,092	0,235	1,30	0,0015	0,009	0,026	0,044	0,149	0,160	0,168	0,005
As	Sn	Ti	Nb/Cb	N	Pb	B	Ca	Bi	Ceq	
0,0030	0,0050	0,002	0,031	0,0079	0,001	0,0001	0,0022	0,0009	0,37	
Chemical composition of S460G2+M										
C	Si	Mn	S	P	Cr	Ni	Mo	Cu	V	Al
0,039	0,340	1,650	0,0010	0,010	0,170	0,017	0,001	0,014	0,002	0,038
Ti	N	B	Nb	Ceq						
0,014	0,0042	0,0002	0,038	0,35						

Table 1. Chemical composition of the materials used (in wt%)

5.2   Process parameters

After the pipe ends are brought into initial contact with the welding ring, the latter is accelerated and a stepped pressure cycle is applied [9-13]. At the beginning of the friction phase the pipes are in contact under an initial low axial contact pressure p_0, which is used to achieve some pre-heating and to reduce the coefficient of friction before the contact pressure is increased. During this phase, considerable power is required to rotate the welding ring, since the friction torque can be quite high during this stage of the process. A low contact pressure is therefore used in order to prevent stalling of the drive motor or to limit the required drive power. The initial stage continues for a predetermined time t_0. Subsequently the axial pressure is increased proportionally, and after the time duration t_1, the pressure is increased to the second friction pressure p_2.

During the second friction phase, the pipe ends and welding ring deform plastically and the characteristic flashes are formed. The displacement of material (usually called "burn-off") ensures that contaminants are removed from the weld interface. When the pre-set shortening per pipe end (Δl_{set}) is reached, the welding ring is decelerated in a duration t_{dec}. After the delay time t_d, the second friction phase ends and the contact pressure is increased to the forge pressure p_f. Forging can take place when the rotation of the welding ring has completely stopped ($t_d > t_{dec}$), or while the welding ring is still in motion, dependant on the parameter settings of t_d and t_{dec}. The shortening during the pressure increase from p_2 to p_f is equal to $\Delta l_{f,p}$. When using a long deceleration an additional shortening $\Delta l_{f,d}$ takes place during the forge phase. The total shortening during forging equals Δl_f (see Figure 4).
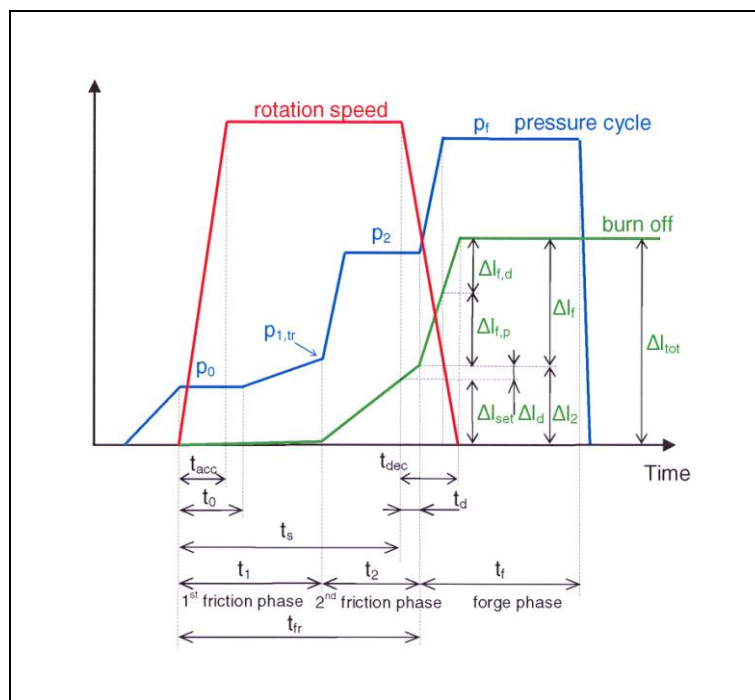
Figure 4. Process parameters of the process

After performing preliminary welding trials, 3 welds were selected for further evaluation. The three welds were performed with the same contact pressure during the weld cycle (first stage friction pressure: 5,5 MPa; second stage friction pressure: 55,2 MPa; forge pressure: 107,7 MPa). The allowable shortening during the friction phase and the rotation speed of the welding ring was varied. The variation of these parameters resulted in a different duration of the friction phase (t_{fr}) and heat input. A smaller allowable shortening and a lower rotation speed results in a smaller friction time and heat input:
- Weld 1: n_{wr} = 130 rpm; Δl_{set} = 5,5 mm resulted in a friction time t_{fr} of 15,0 sec,
- Weld 2: n_{wr} = 180 rpm; Δl_{set} = 4,0 mm resulted in a friction time t_{fr} of 13,8 sec,
- Weld 3: n_{wr} = 130 rpm; Δl_{set} = 4,0 mm resulted in a friction time t_{fr} of 12,0 sec.

5.3   Visual examination of the welds

All welds were visually examined. No weld defects or misalignment were observed. Figure 5 shows weld 2 in the as-welded condition.

Figure 5. Visual examination of weld 2

5.4   Weld quality assessment

The weld quality was assessed based on metallographic examinations, tensile, bending and Charpy impact testing. The tensile test specimens were prepared according to EN 895. The test specimens made from the 3 welds fractured in the pipe base material, at a tensile strength equal to the pipe base material tensile strength. Face and root bending tests were performed according to EN 910. All test specimens could be bent to an angle of 180° without fracture.

Charpy impact tests were performed in accordance with EN 875. For each weld 3 sets of at least 6 impact tests were carried out. Three types of test specimens were used, based on the position of the notch. The specimens were taken out axially and the notch was always located through the thickness, either in the middle of the welding ring, or at the left or at the right weld interface. The tests were performed with subsized specimens with a thickness of 5 mm. The measured energy was converted proportionally to the impact energy of standard specimens. In EN 12732 an average impact energy of 40 J is required, with the individual values not lower than 30 J for steel grades with a specified minimum yield stress higher than 360 MPa. The testing temperature is equal to the minimum design temperature (in Belgium: -20°C).

The impact toughness of the 3 investigated welds is shown in Figure 6 as a function of the total heat input. The heat input was calculated based on the measurement of the friction torque, the rotation speed and the friction duration. At the weld interface, the highest impact toughness is obtained for the lowest heat input. The impact toughness decreases for a higher heat input. The impact toughness measured in the middle of the welding ring is always high and not dependent on the heat input.
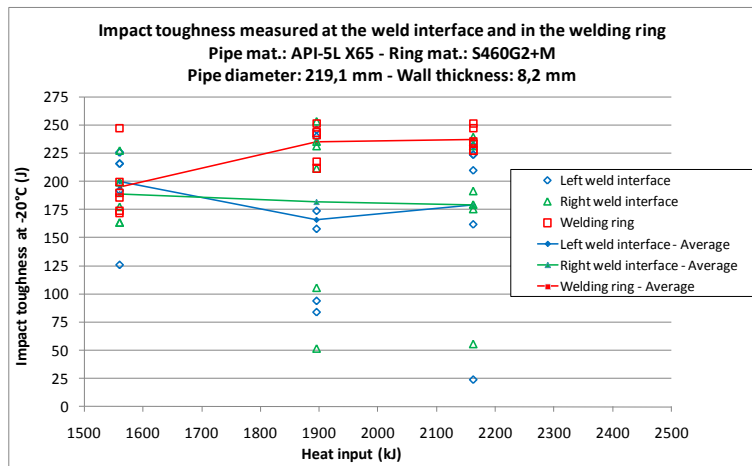
Figure 6. Charpy impact toughness as function of the heat input

The microstructure at the weld interface of weld 1 and 3 is shown in Figure 7. In the pipe heat affected zone (HAZ) the microstructure consists of ferrite with aligned second phase [14]. In the welding ring HAZ a similar microstructure is observed, but with a smaller amount of aligned second phase. The finest microstructure and the smallest HAZ is observed in weld 3, realised with the lowest heat input. In the middle of the welding ring of all welds, a microstructure similar to the base material microstructure is observed.
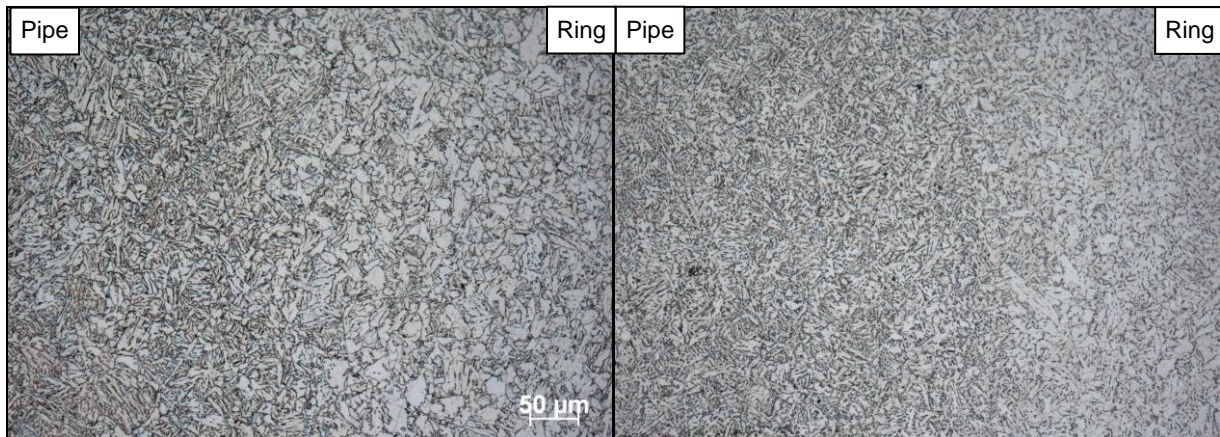
Figure 7. Microstructure at the weld interface of weld 1 (left) and 3 (right)

The hardness profile of the welds is shown in Figure 8. In the pipe HAZ of all welds, the hardness decreases below the base material hardness value (193 HV1), at 2 to 6 mm from the weld interface. Also in the welding ring HAZ softening is observed (hardness ring base material: 196 HV1). The width of the softened zone decreases for a lower heat input. Weld 3, executed with the lowest heat input, contains the smallest softened zone. Also the hardness decrease is minimal for this weld.
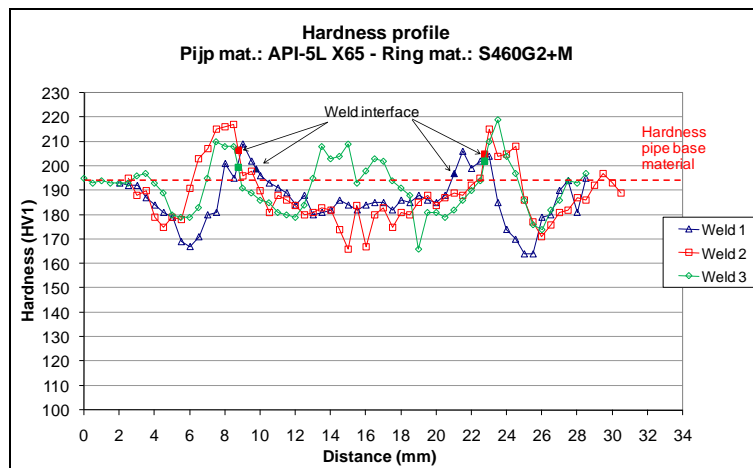
Figure 8. Hardness profile of the investigated welds

6   CONCLUSIONS

A new friction welding process was developed for automatic joining of pipelines. After investigating the weldability of normalised pipeline steels, welding trials were performed to study the weldability of the micro-alloyed high-strength pipeline steels. The investigation was performed with the quenched and tempered steel API-5L X65.

The parameter settings for obtaining a good weld quality were defined. When welding this material using a sufficient low heat input (corresponding welding time: 12 sec), good mechanical properties were obtained. An appropriate welding ring material was determined (the TMCP-steel EN 10225 S460G2+M). Under these conditions the HAZ microstructure is fine grained and consists of ferrite with aligned second phase. Softening in the pipe and welding ring material was observed, but was in none of the welds problematic, since the tensile test specimens always broke in the pipe base material. The impact toughness decreases for a higher heat input. When welding with a heat input of 1550 kJ a high impact toughness was obtained (± 200 J at -20°C), as well as at the weld interface as in the welding ring.

The finest microstructure was observed in the weld realised with the lowest heat input. The HAZ hardness decreased and the width of the softened zone increased for a higher heat input. In the weld realised with the lowest heat input the hardness decreased from 193 HV1 (pipe base material) to 175-180 HV1.

7   ACKNOWLEDGEMENTS

8   REFERENCES

[1]: SIMDEX Future Pipeline Projects Worldwide Guide – Update May 2008 (http://www.simdex.com)

[2]: S.A. Blackman, D.V. Dorling, *Advanced welding processes for transmission pipelines,* Proceedings of the 3rd International Pipeline Technology Conference, Brugge, Belgium, May 21-24, 2000, 371-387.

[3]: D. Yapp, S.A. Blackman, *Recent developments in high productivity pipeline welding*, IIW Doc. No. XII-1786-2004.

[4]: Y. Gainand, J.P. Mas, J.P. Jansen, J.C. Coiffier, J.C. Dupont, C. Vauthier, *Laser orbital applied to offshore pipe line construction*, Proceedings of the 3rd International Pipeline Technology Conference, Brugge, Belgium, May 21-24, 2000, 327-342.

[5]: Y. Hara, M. Toyoda, M. Ushio, H. Irie, H. Masuda, T. Yamakawa, *Development of electron beam welding for girth welding of gas transmission pipelines*, Proceedings of the 3rd International Pipeline Technology Conference, Brugge, Belgium, May 21-24, 2000, Vol. II, 343-357.

[6]: S.I. Kuchuk-Yatsenko, A.S. Nikitin, *Flash butt welding of pipes from stainless steels*, Stainless Steel World, Sept. 1999, 43-49.

[7]: L. Fletcher, C. Stubbs, G. Stecher, *Developments in the application of MIAB welding of pipelines*, Proceedings of the 4th International Pipeline Technology Conference, Ostend, Belgium, May 9-13, 2004. Vol I, 315-323.

[8]: Welding Handbook, 8th Edition, Vol. 2, Chapter 23 - American Welding Society, 1991, p 739 – 763.

[9]: K. Faes, A. Dhooge, O. Jaspart, L. D'Alvise, P. Afschrift, P. De Baets, *New friction welding process for pipeline girth welds: parameter optimization*, Proceedings of the Institution of Mechanical Engineers. Part B. Journal of engineering manufacture, vol. 221, no 5, 2007, 897-907.

[10]: K. Faes, A. Dhooge, P. De Baets, E. Van Der Donckt, W. De Waele, *Parameter optimisation for automatic pipeline girth welding using a new friction welding method*, Materials and Design 30, 2009, 581-589.

[11]: K. Faes, W. Vermeirsch, P De Baets, R. Denys, E. Van Der Donckt, *Influence of forge pressure on properties of friction welded pipelines using intermediate ring*, Science and Technology of Welding & Joining, Vol. 13, No. 5, July 2008, 445-451 (7).

[12]: K. Faes, A. Dhooge, P. De Baets, P. Afschrift, *New friction welding process for pipeline girth welds - welding time optimization*, The International Journal of Advanced Manufacturing Technology, Vol 43, No. 9-10, August, 2009, 982-992. DOI 10.1007/s00170-008-1775-z

[13]: K. Faes, A. Dhooge, P. De Baets, P. Afschrift, *Influence of deceleration phase on properties of friction welded pipelines using intermediate ring*, Science and Technology of Welding & Joining, Vol. 13, No. 2, Febr. 2008 , 136-145 (10).

[14]: Guide to the light microscope examination of ferritic steel weld metals. Welding in the World, 1991; 29 (7/8), 160 - 176. (IIW Doc.No.IX-1533-88, June 1988).

THE EFFECT OF THE DIFFERENT CUTTING TOOLS ON THE MICRO-GEOMETRICAL SURFACE OF ENGINEERING PLASTICS

Gabriella Farkas[**]

[**]Bánki Donát Faculty of Mechanical and Safety Engineering,
Institute of Material Science and Manufacturing Engineering, Universitas Budensis

Gábor Kalácska[*]

[*]Institute for Mechanical Engineering Technology,
Faculty of Mechanical Engineering, Szent István University

Abstract We would like to present in this article the results of the microgeometrical study of the engineering polymer surfaces and the applied cutting tools. We compare the effects of different technological parameters (cutting speed, cutting feed, depth of cut) having on the microgeometrical characteristics (R_a, R_z) and we summarise the results and conclusions from the practical engineering life.

Keywords Engineering plastics, parameters of cutting, cutting tools, parameters of the surfaces roughness.

1. INTRODUCTION

In the machining circumstances and data should be chosen in the cutting process so that the work piece machined is in accordance with the accuracy to gage, geometrical trueness and surface quality given by design engineer. Several researchers dealt with the cutting of metals and the study of effect of cutting features [1]. The aim of my research work is mainly the analysis of the roughness parameters of cutting surfaces in case of different circumstances. Other important task is the elaboration of surface planning criterions in accordance with the expected functional behaviour. The most important aspect was that the results of tests would be useful for the technical practice. That's why we chose several thermoplastic polymers which are important in the technical practice but their behaviour isn't known in case of cutting.

2. EXPERIMENT OF CUTTING

The technical literature provides cutting parameters generally [2,3,4,5]. Cutting speed can be average and high rate between 200 and 600 m/min. Feed rate can be low and average rate is between 0,05 and 0,4 mm. The optimal cutting parameters are not exactly determined for certain polymers with regard to surface roughness. We performed the cutting tests in the machine shop of the Institute by NCT EUROTURN 12B CNC controlled HSC lathe. We fixed the work pieces into the chuck. The turning was made with 80 mm length and 40 mm diameter. We chose several polymers in accordance with technical application: PA6, POMC, PET, PEEK.

We cut the work pieces always without cooling with different parameters given below:

- cutting speed, v_c [m/min]: 200–250–315–400

- cutting feed, f [mm/rev.]: 0,05–0,08–0,12–0,16–0,2–0,25– 0,315–0,4

- depth of cut, a [mm]: 0,5

- parameters of workpieses: ø40x80 mm,

- we don't used cooling.

We used three different tools for experiment. Figure 1. contains the parameters of tools.

parameters	A tool	B tool
κ_r	93 °	93 °
ε_r	35 °	55 °
α_0	5 °	7 °
λ_s	0 °	0 °
r_ε	0.4 mm	0.4 mm
r_n	14,1 ± 5,6 µm	6,75 ± 0,96 µm
R_a (tool)	1,29 ± 0,15 µm	0,58 ± 0,03 µm
R_z (tool)	6,43 ± 0,62 µm	2,66 ± 0,18 µm

Figure 1. Edge-geometry of"A", "B" tools

Before cutting I measured the edge radius (r_n) and the edge of roughness (r_ε) of the tools as well as the arithmetic mean deviation of the roughness profile (R_a) and the maximum height of roughness profile (R_z) of tools. In case of "A" tool the value of r_n has got large standard deviation and roughness parameters differed differing. It was typical of "B" tool the small edge radius (r_n) and the little surface roughness (R_a, R_z) with small standard deviation in this way it was the better quality tool.

3. STUDY OF MICROGEOMETRY

During machining typical microgeometrical unevenness is arousing on the surface which depends on applied technological parameters, geometrical features of tool and machinig circumstances.

Regarding micro-geometric characteristics, the roughness and waviness parameters are applied which have been worked out for decades and are still subject of research at present, and provide information about divergences and characteristics of the surface. Several measuring processes have evolved for the examination of surface texture by today.

2D Stylus instruments are generally used for measuring and evaluation; however, there is an increasing demand for 3D topographic scanning in order to learn more about the characteristics of surface texture (random, periodical, isotropic, anisotropic, etc.) and its stereoscopic position [6,7].

The examinations were performed on surfaces with Perthometer-Concept type stylus scanning instruments. The surfaces were evaluated on an evaluation length (LM=4 mm) complying with the ISO standard with the standard filter (LC=0.8 mm) and a one grade smaller filter (LC=0.25 mm). Considering the possibilities of measuring techniques during the tests, the following data were taken: unfiltered profile (P), filtered roughness profiles (R), as well as 8 roughness (R), 4 waviness (W) and 5 unfiltered (P) parameters. 2 figures were included in the precise comparison, which are also generally used in industrial practice: parameters of height (R_a, P_a, R_t, P_t), one spacing parameter (R_{sm}, P_{sm}), and two characteristics of shape (R_{sk}, P_{sk}, R_{dq}, P_{dq}).
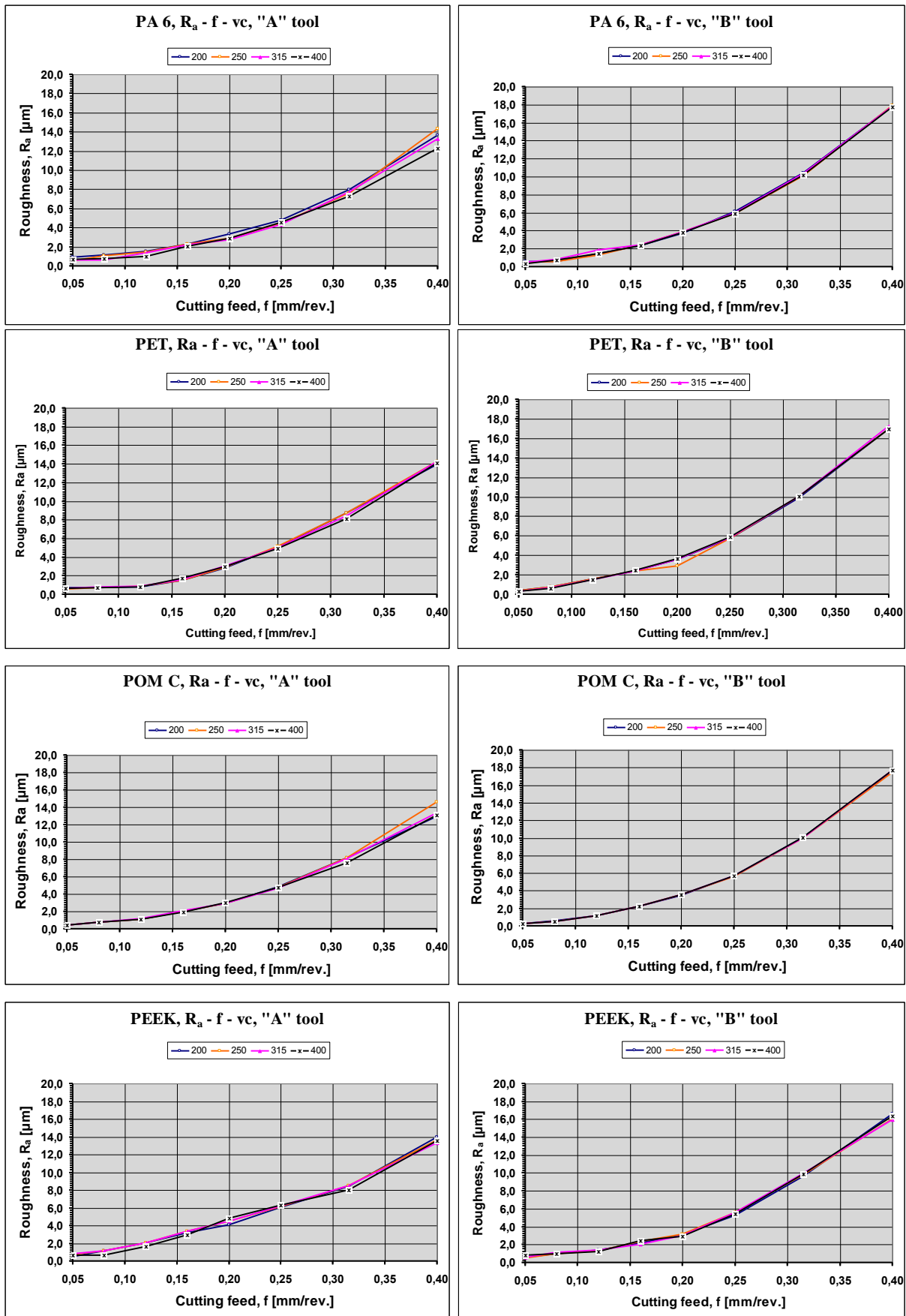
Figure 2. The results of R_a in case of "A", "B" tools

The results of measurements represent the graphs were include the Figure 2. in case of polyamide 6 (PA 6). It can be see that the results of R_a is more different in case of "A" tool like the other two tools. The behaviour of the polymer studied by different cutting speed and by the same cutting feed is stable the value of arithmetical mean deviation of the assessed profile is about constant. The results of Ra is better in case of „B" tool, so it has larger angle of tool (ε_r=55°). This is true the all studied polymers (PET, POM C, PEEK) as well.

3. STUDY OF THE THEORETICAL ROUGHNESS (R_E) WITH DOE (DESIGN OF EXPERIMENTS)

I have planned and carried out the tests with method of the Design of Experiments. I have modelled R_a and R_z values measured with power functions.

The parameters in the factorial test plan were:

- R_a (arithmetical mean deviation of the assessed profile) [µm]

- R_z (maximum height of profile) [µm]

The factors:

- v_c (cutting speed) [m/min]

- f (cutting feed) [mm/rev.]

The two parameters of surface roughness and the cutting data factors set can be given with the following function:

$$R = C_R \cdot v_c^{x_1} \cdot f^{x_2} \text{ [µm]}$$

I carried it out with Minitab14 statistical software the regression function examination. I have decided with the help of program the coefficient of individual models and exponents (C_R, x_1, x_2), the values of the standard deviation (s) and the correlation (R).

3.1 STUDY OF THE CUTTING TOOL "A"

We executed the cutting tests with "A" tool at first.

The functions write down the measuring results with small standard deviation (s= 0,054-0,16) and relatively large correlation (R= 0,877-0,983). It's exponents of variables significant in case of "A" tool. Increasing cutting speed causes decreasing of the roughness in the domain examined. Speed is having effect on the surface roughness (x_1= from -0,003 to -0,316). The cutting feed has almost linear connection with R_a, R_z values (x_2= 1,2 - 1,68), it has a smaller effect on the measuring results as the Baurer-formula shows that. This experience is reverse with the measurement outcomes, which at his steels fashioning by machine tool our well versed in our try efforts.

Polyamide 6 (PA6)						
A tool			B tool			
Model	s	R	Model	s	R	
$R_a = 191 \cdot v_c^{-0,292} \cdot f^{1,46}$	0,111	0,94	$R_a = 93 \cdot v_c^{-0,036} \cdot f^{1,8}$	0,093	0,971	
$R_z = 631 \cdot v_c^{-0,316} \cdot f^{1,2}$	**0,106**	0,921	$R_z = 240 \cdot v_c^{-0,017} \cdot f^{1,58}$	0,105	0,953	
Poly(etylen-tereftalat) (PET)						
A tool			B tool			
Model	s	R	Model	s	R	
$R_a = 46 \cdot v_c^{-0,008} \cdot f^{1,6}$	0,1606	0,899	$R_a = 120 \cdot v_c^{-0,067} \cdot f^{1,88}$	0,052	0,992	
$R_z = 117 \cdot v_c^{-0,026} \cdot f^{1,37}$	**0,154**	0,877	$R_z = 490 \cdot v_c^{-0,105} \cdot f^{1,75}$	0,074	0,98	
Poly(oxi-metylen) (POMC)						
A tool			B tool			
Model	s	R	Model	s	R	
$R_a = 50 \cdot v_c^{0,003} \cdot f^{1,68}$	0,077	0,977	$R_a = 110 \cdot v_c^{-0,002} \cdot f^{2,1}$	0,035	0,997	
$R_z = 234 \cdot v_c^{-0,062} \cdot f^{1,54}$	**0,076**	0,974	$R_z = 288 \cdot v_c^{0,0319} \cdot f^{1,95}$	0,060	0,99	

Poly(eter-eterketon) PEEK					
A tool			B tool		
Model	s	R	Model	s	R
$R_a = 63 \cdot v_c^{-0,048} \cdot f^{1,48}$	0,067	0,978	$R_a = 42 \cdot v_c^{0,04} \cdot f^{1,6}$	0,110	0,95
$R_z = 275 \cdot v_c^{-0,089} \cdot f^{1,36}$	**0,054**	0,983	$R_z = 135 \cdot v_c^{0,062} \cdot f^{1,47}$	0,128	0,923

Figure 3. Results of DoE in case of polymers studied

3.2 STUDY OF THE CUTTING TOOL "B"

We carried out the cutting tests with "B" tool for the second time. The exponents of variables are not significant in case of "B" tool because the effect of the cutting speed less than standard deviation of values measured. The values of standard are between (s= 0,035-0,128) and the correlation is larger than in case of "A" tool (R= 0,923-0,997).

Cutting speed is shows almost much smaller effect of the "B" tool (x_1= from -0,002 to 0,062), the cutting feed has a quadratic connection with the roughness (x_2= 1,47 – 2,1), so better this suits better to the theoretical formula used at turning with regular egde-geometrical tool.

According to results found in the microgeometrical study the line of the theoretical roughness (R_e) follows the line of the roughness measured (R_z maximum height of profile) in the domain studied.

4. SUMMARY OF RESULTS

The behaviour of the polymer studied by different cutting speed and by the same cutting feed is stable. That is different from what we have experienced with steel. The result of R_a (arithmetical mean deviation of the assessed profile) is under 2 µm by low cutting feed and by the cutting speed used [8,9].

Overall the effect on the roughness characteristics of the cutting speed examined at plastics can be observed.

This experience is contradictory with those measuring results, which we have experienced in our tests at cutting steels.

REFERENCES

[1] dr. Palásti K., B. - Czifra, Á.: Forgácsolt felületek mikrogeometriája és mikrotopográfiája. Gyártóeszközök, szerszámok, szerszámgépek, 2002/2. p. 67-71.

[2] dr. Kalácska Gábor: Műszaki műanyagok gépészeti alapjai, M-Sop. Sopron, 1997. 62. old.

[3] dr. Füzes László, dr. Kelemen Andorné: Műszaki műanyagok zsebkönyve. Műszaki Könyvkiadó. Budapest, 1989. 182-362. old.

[4] Mehmet Sagdic, Friedrich Dubbert: Spanende Bearbeitung von Kunststoffen. Bildschirmpresentation, LBK, FSM-02, 2002.

[5] George Southard: High Performance Thermoplastics. Materials, properties and applications. The IAPD Education Committee (Module 5), 2001

[6] *Kovács K., Palásti Kovács B.*: Műszaki felületek mikrotopográfiájának jellemzése háromdimenziós paraméterekkel. I. A háromdimenziós topográfiai paraméterek áttekintése. Gépgyártástechnológia, 1999/8. 19-24. p.

[7] *K.J. Stout, P.J. Sullivan, W.P. Dong, E. Mainsah, N. Luo, T. Mathia, H. Zahouaro*: The Development of Methods for the Characterisation of Roughness in Three Dimensions, Commission of the European Communities, 1994.

[8] Farkas, G. – Palásti, K. B.: Forgácsolt műszaki műanyagok felületi simasága, Gépgyártás, XLVI évfolyam, 2006. 5. szám, p. 6-10. HU ISSN 0016-8580

[9] Farkas, G.: A megmunkálási körülmények hatása a felületi mikrogeometriára műszaki műanyagok esztergálásakor, Gyártóeszközök, szerszámok, szerszámgépek, XII. évfolyam, 2007-1. szám, p. 9-12. ISSN 1587-6853, ISSN 1587-9267

BIOMECHANICAL RESEARCH OF SZENT ISTVÁN UNIVERSITY

B. Csizmadia[1], G. Fekete[1]

[1] Szent István University, Institute of Mechanics and Machinery, Hungary

Abstract This paper represents a short summary of the human knee joint modeling. The Biomechanical Team of the Szent István University investigates the motion of the human knee in the case of squatting. In the analysis of the previously mentioned motion the emphasis is laid on the kinematical properties, which is approximated by experimental and numerical ways. Primarily the sliding and rolling properties of the human condyles are examined, especially I in those domains where pure rolling, rolling and sliding jointly, and pure sliding may occur. Since only the two extremities are well known in the theoretical and applied mechanics, this paper wishes to furnish further information to the subject. On the other hand, in order to determine special additional features the global experimental investigations of the knee are also crucial. These results can be essential for further investigations of the phenomena of the combination of rolling and sliding and to show a new path of creating prosthesis.

Keywords knee joint, experimental, computational model, kinematics

1   INTRODUCTION

The aim of the Biomechanics Team of Szent István University is to reach a deeper understanding of the human knee joint, by carrying out both experimental and theoretical investigations. Different tasks are being explored such as the determination of the axis of revolution by Bíró [1], the governing angles of motion of knee by Csizmadia [2], the global determination of the acting forces or the local motions by Fekete [3]. The team has carried out significant work in this area, and has already presented experimental results. The final aim of the project is to develop a new kind of prosthesis which surface and topography is designed according to the data of multiple cadaver experiments. The steps to successfully carry out this project are the followings:

- Creating a mechanical model to provide initial and boundary conditions,
- Carrying out experimental results in order to determine the acting forces and the governing angles in the knee joint and its surroundings. The results can be useful to verify and even to correct the mechanical model,
- Creating a computational model to ease the calculations and to take into consideration (if necessary) complex geometry. According to the large number of simulations the results can be extended to the level of creating an averaged condyle topology of the human knee.

Worthy of note, there are two governing hypothesizes in the research of the human knee. The first one attributes the importance of the human knee motion properties to the connecting surfaces of the bones (the contact points of the femur and tibia on the condyles), while the function of ligaments remains as a kind of control of the kinematical trajectory of the knee joint. The second one claims the opposite and hereby it must be mentioned that the SZIE Biomechanical Team follows the first hypothesis. Thus, beside many others, the precise mapping of the condyles geometry is an important issue in our research.

2   ANALYTICAL GLOBAL MECHANICAL MODEL

In the 1st phase, the SZIE Biomechanical Team started using both cadaver and intact living knees in their experimental researches. In order to carry out the experiments a special apparatus was needed which was proper to clutch a cadaver knee, and load the joint as well, in the case of squatting (*Figure 1.*).
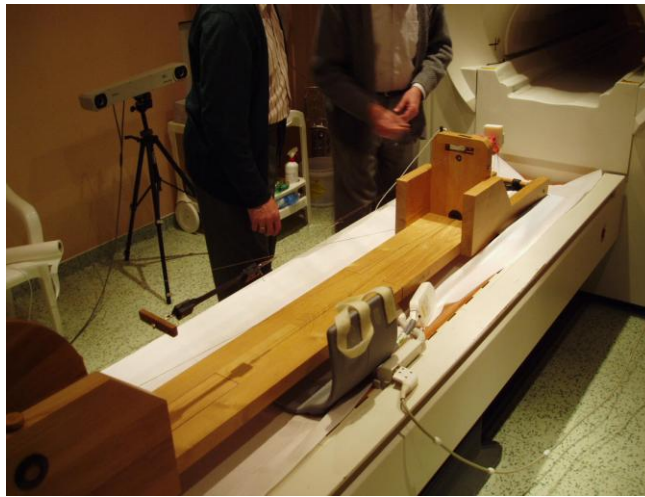
Figure 1.

During the load of the test rig, the governing angles are being recorded by the POLARIS system, which can simultaneously determine the tracks of many isolated points while they are in the move. Besides the test rig, the Team created a 2D, global mechanical model [4] to determine the forces in the muscles of the human knee joint (*Figure 2. and Figure 3.*).
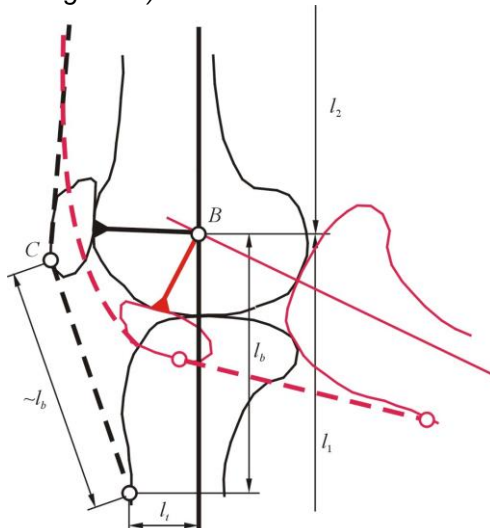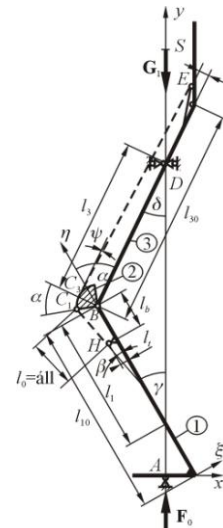
Figure 2.	Figure 3.

The model provides the evaluation of the forces of the connecting ligaments in the function of an arbitrarily α angle, in the ratio of the load desribed by Csizmadia [4]. The main problem of the model was the lack of initial and boundary conditions which are represented as missing functions and constants. These are the following parameters:

- λ_1 (l_1 / l_{10}): Active proportional length of tibia.
- λ_3 (l_3 / l_{30}): Active proportional length of femur.
- λ_b (l_b / l_{10}): Proportional length of ligmentum patellae.
- λ_f (l_f / l_{30}): Proportional thickness of thigh.
- λ_t (l_t / l_{10}): Proportional thickness of shin.
- β: The angle of the ligamentum patellae compared to the tibia.
- ψ (γ / α): The proportional angle of the γ.

Among the parameters, the λ_1, λ_3, ψ, β are the functions of α, while the λ_t, λ_f, λ_b are proportional constants.

3   EXPERIMENTAL METHODS, RESULTS, AND VALIDATION

3.1   Method

In order to obtain these parameters, experiments were carried out on fourteen human persons. The experimental persons were between in the age of 21 to 27, nine male, and five female in normal physical condition. The aim of the experiment was to measure the center of gravity, and to construct the so-called bone-axes (namely the femur and tibia) so the demanded proportional values could be measured as well.

For the experiment, a SPIDER-8 data acquisition system was used, controlled by the Catman Express 3.0 program. Three KALIBER type dynamometers were connected to the SPIDER-8. Before the measurement, certain boundary conditions were given to the experimental persons, such as:

- stretched arms
- straight spine
- heel adapted to the apparatus
- 3 second steady-state in each experimental setting.

The experiments were carried out by having each person stand on to the board shown on the *Figure 4*,

Figure 4.

while the 'x' and 'y' components of center of gravity were measured in seven static positions. The average value and its standard deviation were also determined with the statistical error, calculated by the Student criteria. Since the prospective values were available, the bone-axes could be constructed. Markers were put on to the end of the bones, so if they are connected with a line, the theoretical axes will be given in each status. This method was correct in the first status of the squatting, so the axes were constructed, but in the other statuses, the connective tissue was shifted, so the marker did not represent the real position of the end of the bone. The solution of the problem was given by the functional anatomy. In case of squatting, the posterior muscles of the thigh are in a totally laxed condition, while the same statement is valid to the front muscles of the shin [5]. This fact can be expended as follows: during the motion of squatting the muscles do not act, or the action is not significant in the above mentioned accentuated areas thus the gradient of the volume is zero. So these areas can be modeled as rigid bodies. In the view of this conclusion, two more auxiliary vertices can be taken, and now, with the use of basic construction methods, the demanded vertices can be easily allocated.

3.2 Results

When the axes of the bones are constructed in each status, the prospective values of the center of gravity can be plotted as a line, and by the intersections, the unknown values can be appointed. Due to the applied methods, the following results can be reported. All of the constant proportional values have been estimated with their deviation.

$$\lambda_t = 0,10 \pm 0,037 \qquad \lambda_b = 0,158 \pm 0,087 \qquad \lambda_f = 0,164 \pm 0,057$$

In addition, all the proportional functions are given as well [6]. In the case of β function, another result is put in the diagram, given by the Marcus-Wimmer-Adriacchi formula [7]. Unequivocally, it is the segment of the determined domain. Eventually, the results in diagrams are the followings (*Figure 5.*).
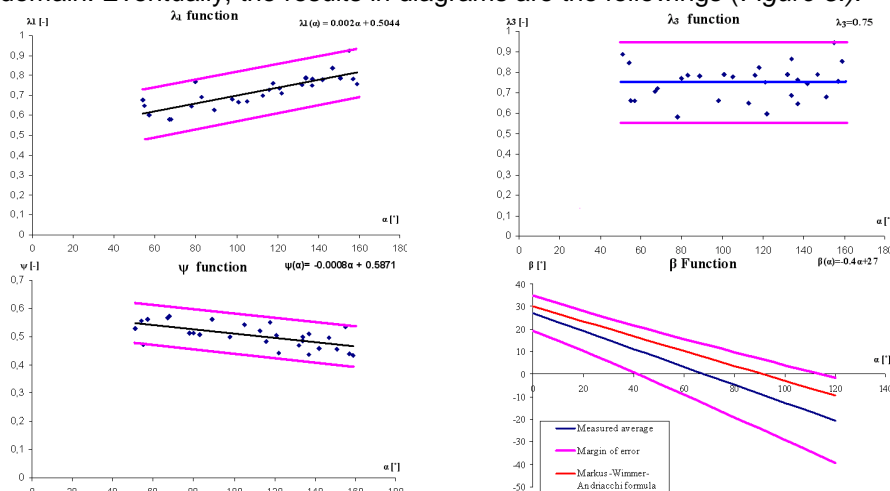
Figure 5.

With the introduction of these constants and functions, the mechanical model turned to be ready to execute. The solution of the proportional quadriceps force function with the average values of the proportional parameters during flexion is shown on the *Figure 6*.
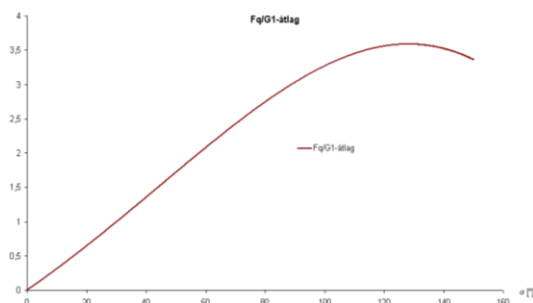
Figure 6.
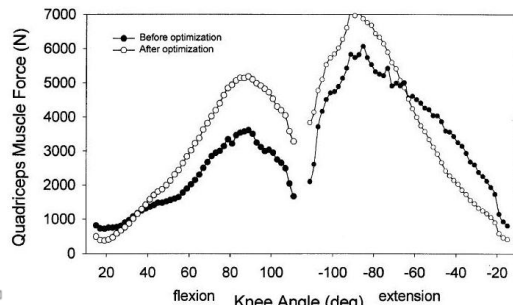
Figure 7.

Approximately, the function is linear to 80˚, and besides the theoretical result of the SZIE mechanical model, an experimental result is shown carried out by Zheng [8] (*Figure 7.*). Apparently, the character of the model and the experimental result is very similar in the case of flexion.

3.3   Comparison of results

Since results derived by pure theoretic models can show great differences between model and reality, in association with the Ghent University verification tests were done on a totally different test rig. The Ghent University set-up is capable to measure the force in the quadriceps, but the proportional parameters can not be adjusted, so the given results are not an entirely appropriate model of the human squatting.

The *Figure 8.* represents the result of the artificial knee according to the mechanical model, which is only segment to 55˚.
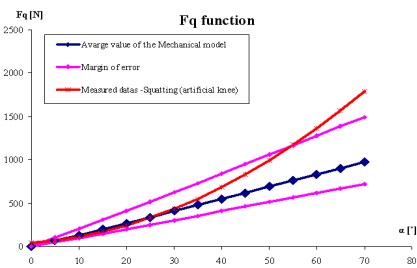
Figure 8.
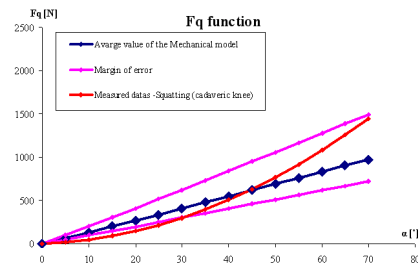
Figure 9.

With the cadaver knee, the given results are better; the segment goes to 70˚ (*Figure 9.*). This way the demanded parameters have been estimated with their statistical error, and in the case of the β function, compared with the reference formula. Using the obtained parameters, the solution of the quadriceps force function correlates with the experimental results of the reference. For further use, the functions of the mechanical model can be applied in the computation knee joint model as more realistic and validated boundary conditions, according to the former 'constant loaded' conditions [9, 10]. The applicability of the test rigs is also determined with these calculations and experiments.

4   EXPERIMENTAL METHODS, RESULTS, AND VALIDATION

4.1   Internal motions and their background

Since different results about the human knee joint are available, the internal motions and special addition features such as the combination of sliding and rolling must be examined. Two kinds of motions occur inside of the human knee joint during action, which are namely sliding and rolling. Their gradient and proportion is currently unknown. Zuppinger was the first among the medical researchers who claimed according to X-ray images that the relation between the tibia and femur was basically rolling until 20° of flexion and beyond that point, sliding and rolling jointly occurred. Making a decision about the proportion of movements and the behavior of the phenomena by using only X-ray images is simply impossible. This is the reason why the other aim of the team is to found a new and applicable method to correctly investigate and determined the phenomena of *sliding-roll*. To do so, a special proportional value will be introduced.

4.2   Model creation

In order to correct these hypothesizes and to make further steps in the research the MSC.ADAMS program system was used to carry out computational examination and to build a complex knee model. MR images were taken and a model was mapped from them. With basic CAD methods a geometric model was generated and imported into the ADAMS (*Figure 10.*).
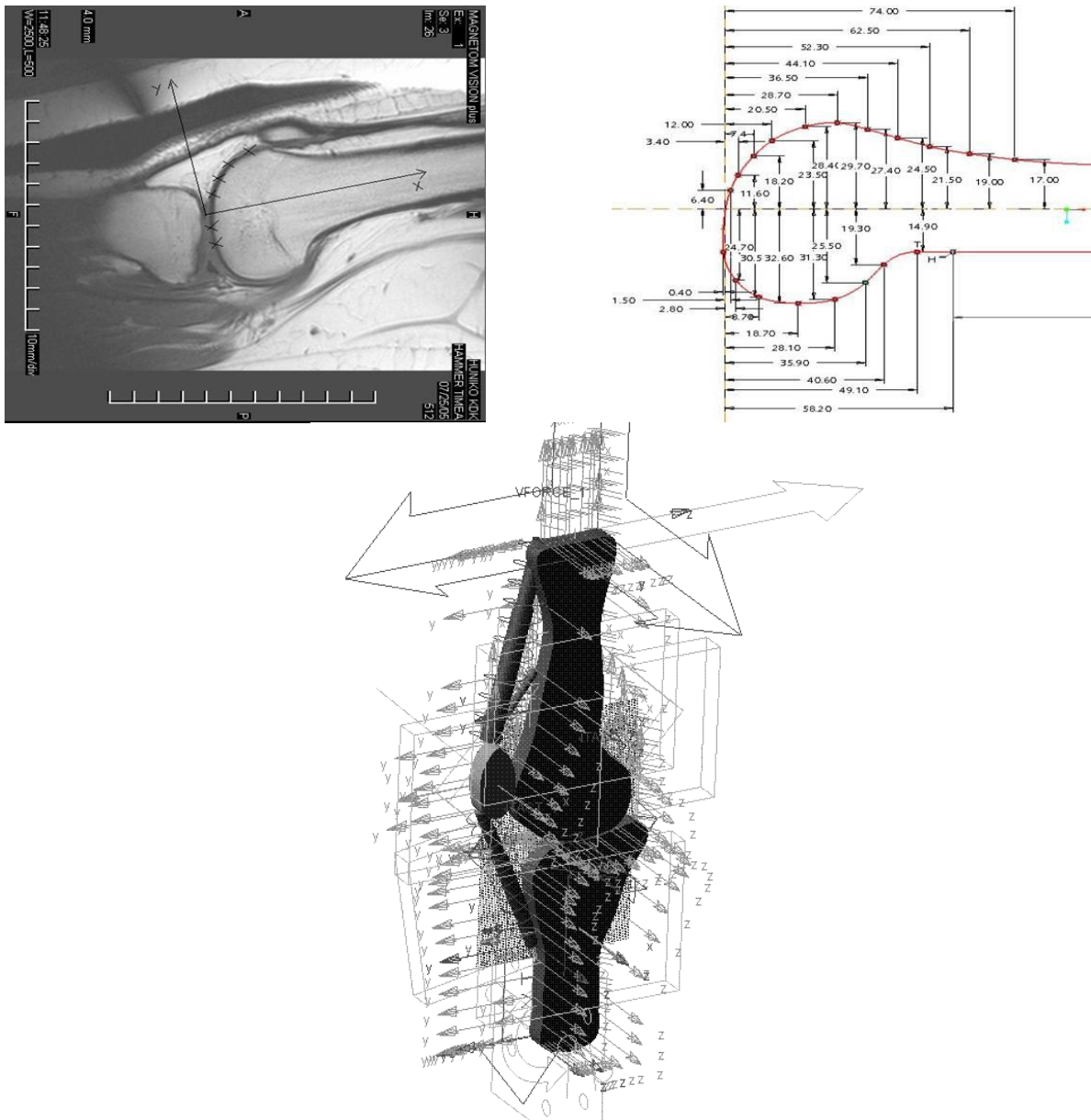
Figure 10. The geometrical model

The following simplifications were applied:

- 2.5D model (it involves a third finite extent)
- Bones are considered to be rigid bodies
- The damping and mechanical properties of the meniscuses are neglected but their lubricating behavior is taken into consideration

In the interest of to carry out squatting motion, kinematical constraints must be set to the model elements. The elements such as the femur, tibia and patella must be fixed to each other and to the environment. The following constraints and boundary conditions were applied in the program:

- Tibia, femur and patella can only perform planar motion (PLANAR JOINT),
- The top of the femur is attached to the hip-bone, thus deflection in the 'x' direction is not possible (MOTION JOINT),
- Bodies are attached to each other by springs (SPRING), therefore the muscle model is introduced,
- The tibia is attached to the environment by a hinge, thus the rotation around the 'z' axis is permitted (HINGE),
- The static friction coefficient is 0.11, while according to Wang [8] the dynamic friction coefficient is 0.008,
- One force in the 'y' direction is acting on the femur with a magnitude of 60 N.

4.3 Calculation method

Let a new specific value be introduced, which shall be titled as *sliding-rolling coefficient*, and denoted with χ. Let χ defined as:

$$\chi = \frac{\Delta s_{2i} - \Delta s_{3i}}{\Delta s_{2i}} \tag{1}$$

- $\Delta s_{2i} = s_{2i} - s_{2K}$: Difference of the ith arc length extracted the initiative K arc length of the 2nd body,

- $\Delta s_{3i} = s_{3i} - s_{3K}$: Difference of the ith arc length extracted the initiative K arc length of the 3rd body.

The above-mentioned quantity shows the proportion of the connecting arc lengths in percentages, thus exact conclusions can be drawn to the sliding and rolling feature of the motion. If the value of χ equals to 1, then it is pure sliding, and if it equals to 0, then it is pure rolling.

To carry out this calculation, the arc lengths must be determined. The following kinematic quantities can be calculated by the MSC.ADAMS during the simulation of the motion:

- $\bar{r}_K(t)$ vector-scalar function, which determines the instantaneous position of the connecting points of the two bodies (*Figure 11.*),
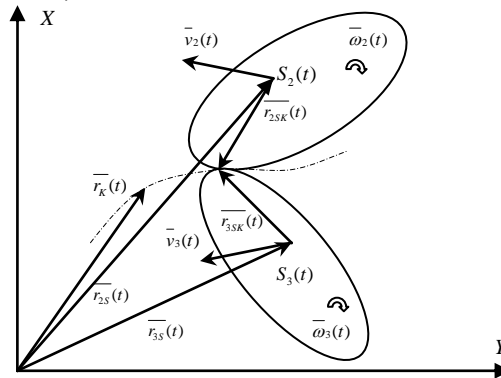
Figure 11.

- $\bar{r}_{2S}(t), \bar{r}_{3S}(t), \bar{v}_{2S}(t), \bar{v}_{3S}(t), \overline{\omega}_2(t), \overline{\omega}_3(t)$ vector-scalar functions, which sequentially determine the instantaneous position of the center of gravity, velocity and angular velocity of the 2nd and 3rd bodies (*Figure 12.*).
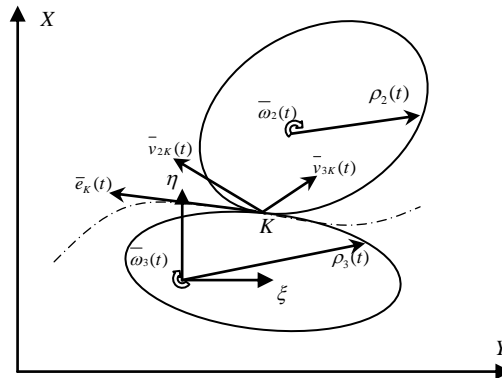
Figure 12.

In addition the following kinematic quantities can be directly estimated:

- Instantaneous values of F_f and F_N, which are the normal and frictional components of the connecting surfaces,

In order to examine the proportion of sliding and rolling, let us consider the following well-known formula from the results given by the MSC.ADAMS:

$$d\bar{r} = \bar{r}_{2SK}(t) = \bar{r}_K(t) - \bar{r}_{2S}(t) \tag{2}$$

Substituting the results of (1) equation into the (2) and (3):

$$\bar{v}_{2K} = \bar{v}_{2S} + \overline{\omega}_2 \times \bar{r}_{2SK}(t) \tag{3}$$

$$\bar{v}_{3K} = \bar{v}_{3S} + \overline{\omega}_3 \times \bar{r}_{3SK}(t) \tag{4}$$

Thus the instantaneous velocity of the connecting points of the bodies can be calculated in the $x-y$ coordinate system. If the instantaneous tangent unit vector of the connecting curvature can be determined:

$$\bar{e}_K(t) = \frac{\dot{\bar{r}}_K(t)}{\left|\dot{\bar{r}}_K(t)\right|} \tag{5}$$

Then by multiplying the velocity vectors with it, the sliding components of the velocities become quantifiable:

$$v_{2N} = \bar{v}_{2K} \cdot \bar{e}_K(t) \text{, and } v_{3N} = \bar{v}_{3K} \cdot \bar{e}_K(t) \tag{6}$$

By these results the sliding components can be calculated:

$$\Delta v_N = v_{3N} - v_{2N} \tag{7}$$

After the execution of the ADAMS program, the following numerical results were produced *(Figure 13.)*. The proportion of the Ff/Fn function *(Figure 14.)* can be directly plotted.
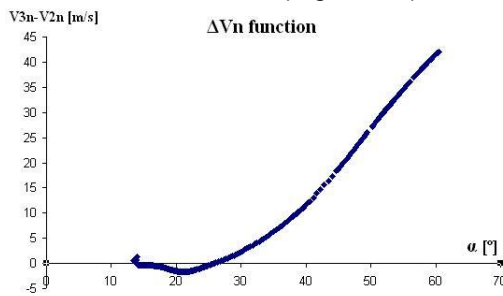
Figure 13.
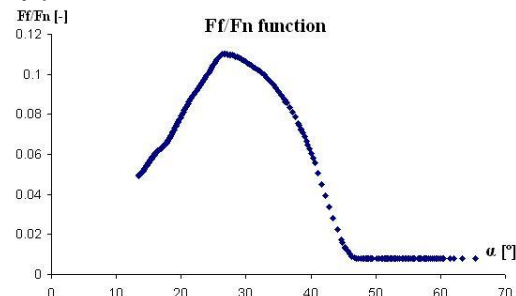
Figure 14.

Figure 13. correctly demonstrates that the sliding velocity components turn to be zero at approximately 26⁰, and by examining Figure 14. it shows the peak of the *Ff/Fn* function is also around 26⁰. That is the threshold where the first sliding occurs, and from that point until cca. 45⁰, the actions of sliding and rolling are combined. After 45⁰, the motion is characterized as pure sliding. Unfortunately, the integration of the sliding velocity component is not yet finished, but since the algorithm is already elaborated, the results will be soon presented.

5   FURTHER RESULTS AND APPLICATIONS

The above presented method provides a new way to investigate the phenomena of sliding and rolling in the case of planar motion. The method will be expanded to 3D investigations in the case of the sliding and rolling proportions of the condyles and prothesis. The goal with this method is partly to find the dominant part of the 3D surface, which takes on the majority portion during motion, and partly to investigate these quantities on several human subjects. In this way, by averaging the given results, hopefully a general conclusion will be drawn about the possible domains of the surface where the upcoming wear would be demolishing. In this part of the project, statistical methods will be applied on the set of data in order to determine the sliding-rolling proportions of the human knee. On the other hand, after creating a fairly accurate model, the idea is that according to the measured quantities of angles, the computational model would be adjusted to these statistical results. This can be carried out by an iterative modification of the geometry until the point where the numeric result correctly approximates the result measured by the POLARIS.

REFERENCES

[1] I. Bíró – B. M. Csizmadia – G. Katona: Determination of instantaneous axis of rotation of tibia and its role in the kinematical investigation of human knee joint, Proceedings of the Third Hungarian Conference on Biomechanics, Budapest, July 4-5, 2008, p. 55-62, ISBN 978 963 06 4307 8

[2] B. M. Csizmadia – G. Katona: Some result on the motion analysis executed on the experimental model of the human knee. 23rd Danubia Adria Symposium on Experimental Methods in Solid Mechanics – Extended abstracts, Podbanské – Zilina, Slovak Republic, 2006.11.26-27.

[3] G. Fekete: Numerical methods for determining local motions of human knee joint, Zilele Tehnice Studentesti - Editia a XII-A, Timisoara, 12-18 Mai (In press), 2008.

[4] B. M. Csizmadia – I. Bíró – G. Katona – Z. Szakál: A térdizület számítógépes megjelenítésén alapuló stereotaxisos navigációs műtéti eljárások (Stereo-taxis navigational methods of surgery, based on computational monitoring of human knee joint). NKFP/1B/0009/2002 pályázat keretében készült kutatási jelentés.

[5] Szentághotai János: Funkcionális Anatómia (Functional anatomy). Medicina Kiadó, Budapest – 1975.

[6] G. Fekete: Experimental methods for determining of mechanical model of human knee, Zilele Tehnice Studentesti - Editia a XI-A,Timisoara, 6-13 Mai, p. 1-8, ISSN 1843 - 1917, 2007.

[7] A. Marcus, Wimmer, T.P. Adriacchi: Tractive forces during rolling motion of the knee: Implications of wear in total knee replacement. Journal of Biomechanics 30 (1997), 131-137.

[8] N. Zheng, G.S. Fleisig, R.F. Escamilla, S.Barrentine: Analytical model of the knee for estimation of internal forces during exercise. Journal of Biomechanics 31 (1998), 963-967.

[9] J.Heegaard, P.F. Leyvraz, A. Curnier, L. Rakotomanana, R. Huiskes: The biomechanics of the human patella during passive knee flexion. Journal of Biomechanics 28 (1995), 1265-1279.

[10] W. Mesfar, A. Shirazi-Adl: Biomechanics of the knee joint in flexion under various quadriceps forces. The Knee 12 (2005), 424-434.

MACHINING THE ZIRCONIUM-DIOXIDE ENGINEERING CERAMICS

Gellért Fledrich

Institute for Mechanical Engineering Technology,
Faculty of Mechanical Engineering, Szent István University, Gödöllő, Hungary
www.geti.gek.szie.hu

Abstract In place of brittle ceramics used so far have appeared up-to-date so called tough ceramic materials resisting better against mechanical effects [2]. Such material is the zirconium-dioxide, too. The important advantage of hard-turning is the applicability of universal tool. Various outlines can be formed by a tool given. Machining ceramics in case of using traditional machining (turning, milling, drilling) requires special technological conditions (tools, machine-tools, technological parameters, etc.) which are developing presently. We would like extending our research work in this course, too.

Keywords polycrystal diamond, cubic boron nitride, two-way force measuring, thermocamera, heat ring, surface roughness

1.   INTRODUCTION

By industry development the demand is increasing for such materials to be applied at higher temperature beside at heavy physical and chemical load. The structural ceramics can have an important role exactly in this segment. The zirconium –dioxide is also such material [4]. At long-term it is predicted establishing the possibility of computer directed material structure starting from atomic level and of product manufacturing. However until the manufacturing technologies do not reach this level the role of ceramics hard-machining is increasing [5]. The zirconium-dioxide deriving from its lower hardness and from other characteristics is suitable to machine by tool having regular edge can become a potential material at piece or small- and medium series production. To ensure this it has to be known its cutting characteristics [6].

My research work focusing a part of this in keeping with the recommendation of the company producing and developing zirconium-dioxide semi-finished products.

2.   MATERIALS TESTED AND THEIR FORMS.

The common properties of engineering ceramics are that they have outstanding physical and chemical characteristics in very high temperature range [3]. The ceramics tested by us have got high hardness (1250-1800 HV), because of this it can be cut by polycrystal diamond and cubic boron nitride tools. The material tested is zirconium-dioxide ceramics. The specimens used at turning tests were cylindrical, their diameters were 16 and 20 mm (Figure 1.)

Figure 1. The zirconium-dioxide (Zn40)ceramics used at tests.

The ceramic properties tested [7].

	Dimension	
Material		ZN 40
Main component		ZrO_2-MgO
Density	g/cm^3	5,74
Bending strength	MPa	500
Compression strength	MPa	1600
Young modulus	GPa	210
Poisson - ratio		0,3
Vickers hardness HV0,5		1240
Thermal convectivity	W/mK	3
Linear coefficient of thermal expansion	$10^{-6}K^{-1}$	10,2

Cutting tests

During turning the work-piece rotating movement is the main movement, the auxiliary movements are the turning tool movement in feeding and depth of cut directions [1] (Figure 2.). I have set the cutting speed by the work-piece revolution number.
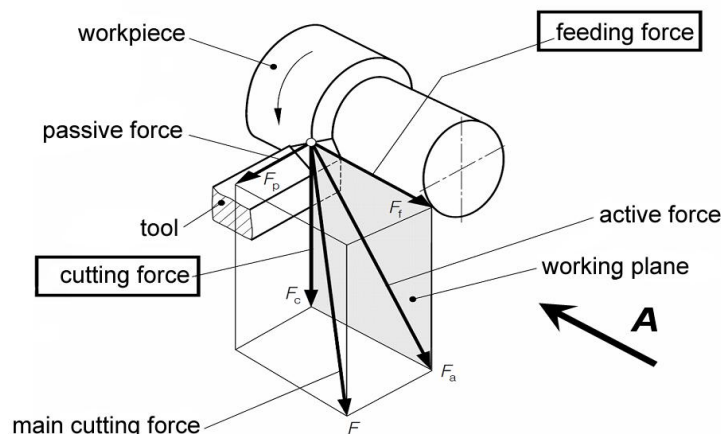
Figure 2. Cutting force components (ISO 3002/4, DIN 6584).

To measure the axial and tangential components of the cutting force I have used a measuring tool-head with strain gange developed and manufactured by me. The 3D –model of the measuring tool-head can be seen in Figure 3-4.
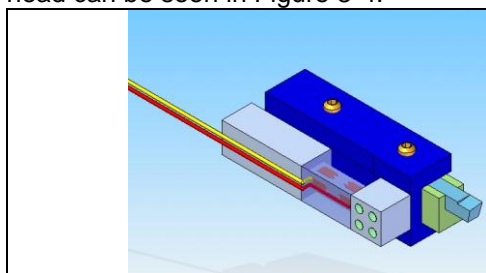
Figure 3. The model of the measure tool-head	Figure 4. The photograph of the measuring tool-head finished with the holder clamped.

I have used the Spider 8 measuring amplifier for the tests. I have connected four channels. I have coupled to the O-channel the revolution marker, I have measured the tangential and feeding-directional forces on the 1 and 2 channels. The 3. channel served to measure the tool displacement, here I have connected an inductive displacement tele-transmitter restored by spring.

Heat affected zone tests.

The heat arising during cutting influences considerably the removal of stock process as well as influences very much the tool durability. I have also made shots with thermo-camera during cutting to study the heat affected zone formed. Figure 5. shows the thermo-camera.

Figure 5. Thermocamera used for tests.

3. DISCUSSION

During cutting I have measured the main and feeding- directional forces affecting the tool. As a result of this I illustrate a diagram on Figure 6.
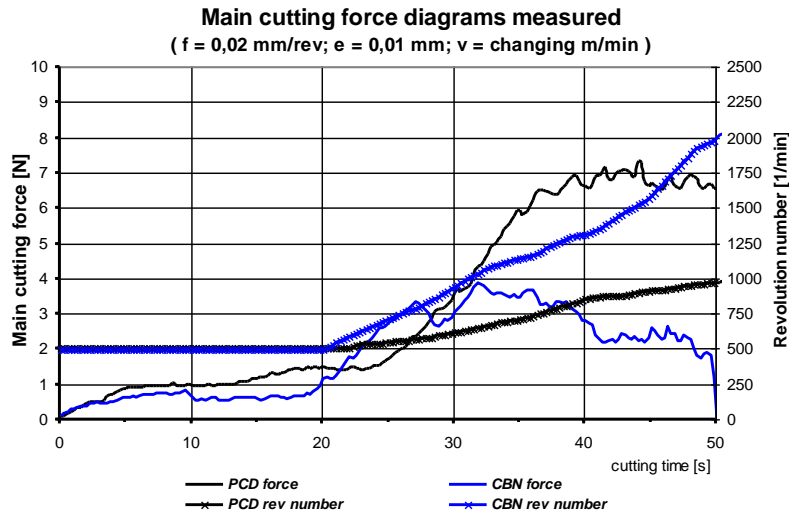
Figure 6. Main cutting force diagram.

I illustrate the main cutting force change with straight lines on the diagram in the function of alteration of cutting time and revolution number. The other thicker line shows the value of revolution number and it can be read from the right axis. It can be seen that the small forces at the beginning of cutting, they increase suddenly after some time in both cases of cutting tools. However the value of main cutting force has increased only for some time by increasing the revolution number at cubic boron nitride (CBN) tool. Approximately over 1000 r.p.m the force shows again decreasing tendency. In case of polycrystal diamond tool the force increase neither increased further. It is likely that it can be explain with chip removal as well as with the tool and ceramic heat conduction characteristics. Further evaluations are needed. The Figure 7. is similar to the previous Figure, however here I have presented the forces in feeding direction. The amount of arising forces approximately is half of the amount of main cutting forces in both cases of tool materials. It is interesting that the two forces show similar characteristics in tendency. However it can be likely that because of the wear of tool edge the two forces will show different change from one another.

Feeding-directional cutting force diagrams measured
(f = 0,02 mm/rev; a = 0,01 mm; v = changing m/min)
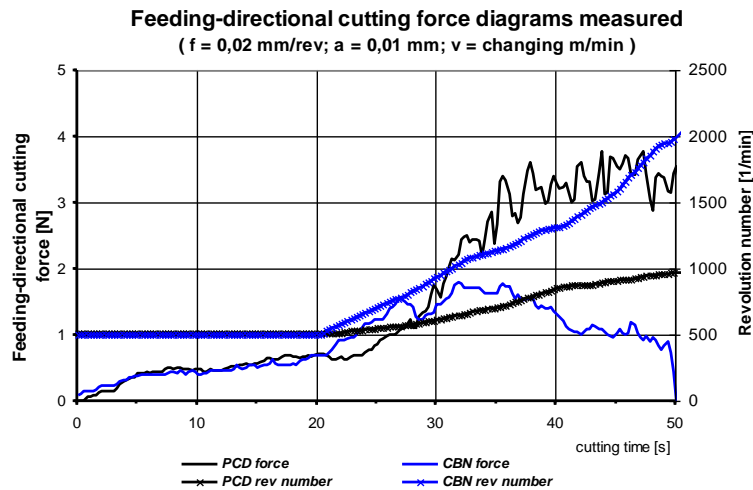
Figure 7. Diagram of cutting force in feeding direction.

I show again the change of main cutting force in the next diagram. However I have set the cutting speed to 50m/min. The feeding value was 0,02 mm/rev. The depth of cut values were: 0,02-0,03-0,04 mm.

By increasing the depth of cut the main cutting force also increases. Near straight proportion is between the two values.

However in case of 0,04 mm depth of cut the great degree of force fluctuation allows conclude to the damage of main cutting edge. This could be seen in microscopic pictures later. The force increase is significant in the beginning period. In the first spot of contact both the ceramic and the tool are at ambient temperature. During cutting substantial heat develops and the warming up starts. However this warming up increases the force value for some time then it sets in near constant value as in the diagram can be seen. (Figure 8.)

Main cutting force diagrams measured
(f = 0,02 mm/rev; e = 0,02 - 0,03 - 0,04 mm; v = 50 m/min)
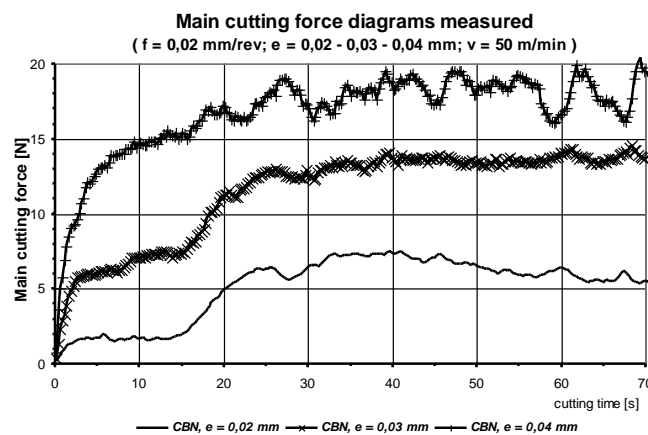
Figure 8. Main cutting force diagrams.

In the Figure 9. the change of force in feeding direction can be seen connected with the previous diagram. At 0,04 mm depth of cut it shows great fluctuation. This force change is less optimal at such parameters set.
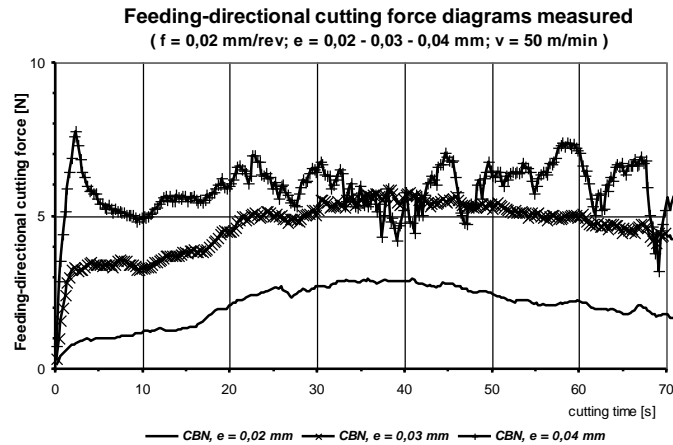
Figure 9. Diagrams of force in feeding direction.

Thermo-camera pictures from the heat affected zone formed during cutting can be seen in Figure 10. It can be unambiguously seen in the picture that because of the ceramic good heat insulation a heat ring formed on the work-piece at the tool edge which has increased significantly the tool edge thermal load. The first picture was made at the beginning of cutting here rather the tool point warmed up. By increasing the cutting length the tool and ceramic temperatures also increased significantly. The second picture shows this. The red colour shows the heat ring formed and the tool point namely the hottest points.
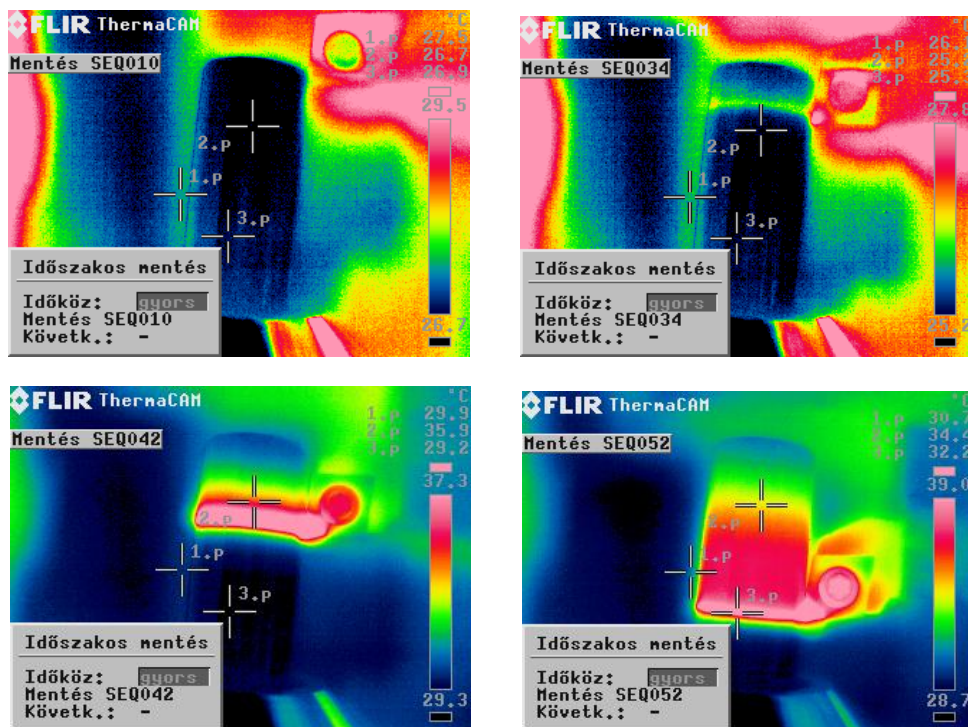
Figure 10. Thermo-camera picture, from the beginning to the end of cutting.

4.   SUMMARY

Trend characterizing steel turning appears at using CBN turning tool, local cutting force maximum can be identified.

Comparing the two cutting tools it can be stated that increasing the cutting speed the diamond turning tool has resulted significant cutting force increase, which has caused significant cutting heat evolution. Surface roughness at identical cutting parameters:

- CBN: 2,8-3,2 R_a
- PCD: 2,9-3,2 R_a
- Original surface grinded: 05, R_a.

It is possible turning zirconium-dioxide semi-finished product. The condition of the starting surface has got definite importance how is possible to turning the surface point of view. The raw-product surface grinded has damaged the PCD-tools in case of all cutting parameters tested.

The hardness recommendation accepted for tools in technical literature (3-4 times higher hardness difference in favour for the tool) can not be used at raw-products grinded in case of zirconium-dioxide ceramics, Softer, 2 times higher hardness can be used.

Testing the cutting speed and cutting force connection-zirconium-dioxide turning with CBN-tool-similar trend can be established as steels turning with carbide. A local maximum value can be measured which origin can be traced back to surface-tribological processes and to sudden change of thermal equilibrium. The phenomenon validity can be extended from the steel/carbide connection to the zirconium-dioxide/CBN friction, chip removal connection, too. The CBN and PCD-tools have resulted significantly different cutting forces. It can be stated that the cutting speed increase has resulted well measured increase in cutting force in case of diamond turning tool which has called forth significant heat evolution.

This is significantly unfavourable tribological connection.

The standard PCD and CBN –tools used did not result different surfaces regarding the surface roughness.

Based on measuring it can be stated that at surfacing the removing material as dust can be easily recompressed – verified by microscopic pictures – which results significant modification of power effects.

REFERENCES

1.   A. H. FRITZ, G. SCHULZE (Hrsg.) (2007):Fertigungstechnik. 8. Aufl *Springer Verlag, Berlin* 279. old.
2.   CURTIS, C.E. (1947): Development of zirconia resistant to thermal shock. *J. Am. Ceram. Soc. 30* 180-196.
3.   H. SALMANG, H. SCHOLZE (2007): Keramik, *Springer Verlag, Berlin*
4.   SWAIN, M.V.; ROSE, L.R.F. (1986): Strength Limitations of Transformation-Toughened Zirconia Alloys. J. *Am. Ceram. Soc.* 69 511-518
5.   MÉSZÁROS I., SZEPESI D. (2006): Edzett acélok nagypontosságú megmunkálása IV. *Gépgyártás* XLVI. évf. 4. sz. 29-33 old.
6.   SZÉPVÖLGYI J. (1994): Korszerű műszaki kerámiák, *Magyar Tudomány*, 4. sz. 7- 13 old.
7.   CeramTec AG Innovative Ceramic Engineering Medical Products Division: *Broschüre* 2008

ANALYSIS OF ELECTRO-RHEOLOGICAL FLUID
IN HYDRAULIC SYSTEM

Földi László, Jánosi László

Institute for Mechanical Engineering Technology,
Faculty of Mechanical Engineering, Szent István University, Gödöllő, Hungary
www.geti.gek.szie.hu

Abstract Use of intelligent materials has been a more widespread technology in the last ten years in the area of research and development of mechatronic equipments. It's main reason is that some problems of the utilization needed such a solution, which couldn't be solved only with new materials produced by material texture modification.

A claim has come up in the research of the mechatronical systems to develop materials that can get and understand an information from a computer and change their attribution accordingly. The connection, what we can establish between the computer and material, sets a limit to the quality characteristics that can be operated by the computer. This transposal can be ensured by effects that's induction and abolition rate can be compared or the control is bigger just as the velocity of the change of a material characteristic. From a control technology viewpoint using electric or magnetic field is the most obvious.

One group of these materials is electro-reologic (ER) liquids that change their shear strength according to the electric field. The flow qualities of the ER liquids can be continually changed inside certain borders, with orders of magnitude shorter interval from the previous hydraulic solutions. Making an opportunity by to create faster controlling and regulating systems from the present ones.

The main aim of this work is the modification of basic properties of this kind of liquids and specification of its utilization possibilities in mechatronic systems such as hydraulic control equipments. Mathematical model as well as its numerical solution of a flow control valve (ER valve) as an appropriate element of hydraulic systems has been prepared during this work. Function tests of this unit have been carried out by computer aided simulation of the above mentioned mathematical model.

Keywords *Electro-rheological, Flow control, Hydraulics, modeling*

1. INTRODUCTION

The ER phenomenon as a material model is described by the Bingham model related to ER liquids, which is based on the mathematical model describing the non-newton liquids [3]. The Bingham model is a complex viscoplastic rheological model [1]. As a material model it can be divided into an ideally ductile an ideally viscous member [7]. (Fig. 1)
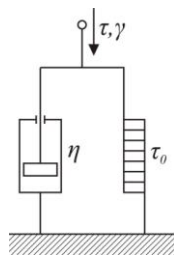
Fig. 1. The Bingham model
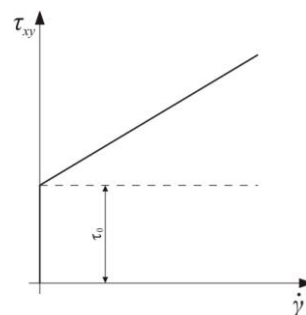
Fig. 2. The shearing tension in the function of shearing gradient

1.1 Research objectives

The aim of testing of the flow properties of the ER liquids is to establish a model, which can be generally applied of testing the behaviours of ER liquids made of different materials considering the phisycal data of the applied materials. By computer simulation the parameters of this mathematical model can be determined, which can be generated by minimum search. As the first step of the model identification the approximate search of the minimum of the established target fuction is accomplished by genetic algorithm, then the refinement of the result with the known numerical methods.

2. THE APPLICATION OF THE FLOW REGULATOR

During the further material and application tests it is practical to use a device which has application possibilities too. In this consideration for further investigations we need the design of a hydraulic ER valve, which can be operated built in hydraulic circuits.
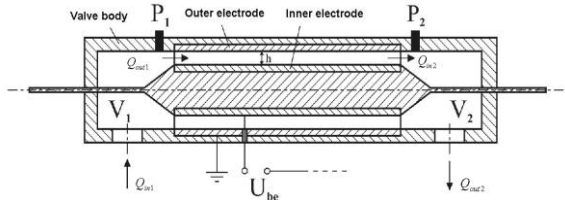
Fig. 3.: The ER valve
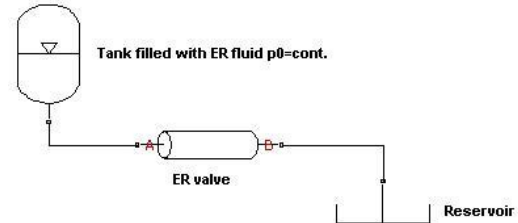
Fig. 4. The conceptual diagram of simulation

1.2 Applied Mathematical Model

The flow rates which go in and out the valve can be determined by the following equations:

$$Q_{in1} = \mu \cdot A_1 \cdot \sqrt{\frac{2 \cdot (p_0 - p_1)}{\rho_f}} \qquad (1) \qquad Q_{out2} = \mu \cdot A_2 \cdot \sqrt{\frac{2 \cdot (p_2 - p_3)}{\rho_f}} \qquad (2)$$

Where μ is the coefficient of flow loss, p is the pressure and ρf is the density of the liquid. On the basis of the incoming and leaving flow rates the balance (differential) equations are the followings:

$$Q_{in1} = \frac{V_1}{E_f} \cdot \frac{dp_1}{dt} + Q_{out1} \quad (3) \qquad\qquad Q_{in2} = \frac{V_2}{E_f} \cdot \frac{dp_2}{dt} + Q_{out2} \quad (4)$$

In equations (3) and (4) the Ef is the bulk modulus of the liquid. The flow rate between the electrodes is:

$$Q_{out1} = Q_{in2} = \frac{L \cdot \Delta p_N}{12 \cdot \eta \cdot b \cdot h^3} \quad (5)$$

In equation (5) L means the length of the electrodes, η is the ER liquid's dynamic viscosity, b is the inside circumference of the electrode, h is the size of the gap between the electrodes. The pressure drop of the liquid flowing through the ER valve is composed of two parts: the first part is resulted by the liquid's ideal viscid behavior (Δp_N); the second part comes from the electric field (Δp_{ER}). Hence by the right of Bingham-model the pressure drop is [5] [6]:

$$\Delta p_{12} = \frac{12 \cdot \eta \cdot L \cdot Q_{out1}}{b \cdot h^3} + \frac{2 \cdot L \cdot \tau_{ER}}{h} \quad (6)$$

The size of τER depends on the ER liquid's physical parameters and the electric field:

$$\tau_{ER}(t) = \alpha \cdot E^\beta \cdot \left(1 - e^{-\frac{t}{T}} \right) \quad (7)$$

In the equation (6) the α and the β are parameters, the T is the time constant. The value of the time constant depends on the applied electric field too. With the above equations the behavior of the ER valve can be described .

1.3 The Numerical Solution of the Applied Mathematical Model

The solution of the methetical model of the ER valve was accomplished by MATLAB with block–oriented method, using Kelvin-Thompson return-circuit principle [2] .
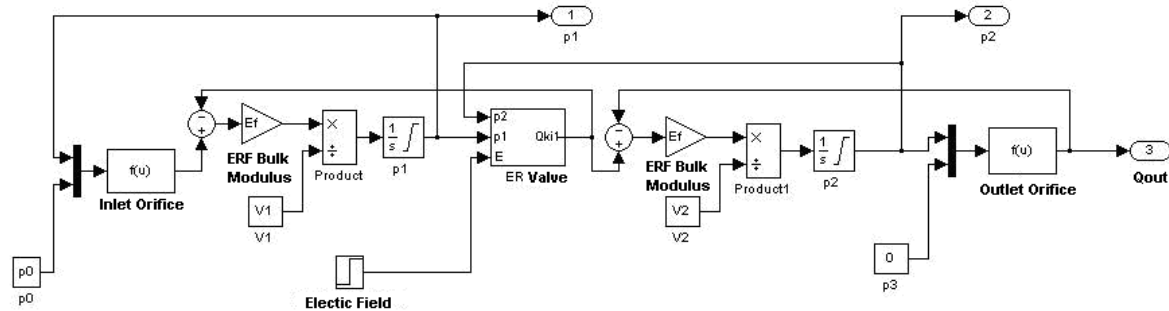
Fig. 5. The block diagram of simulation

With this method the volume, which was evolved by the constant pressure difference, put on the ER valve can be measured. In this layout the the liquid volume can be controlled by electric field strength. With this we can create a hydraulic valve, which without moving parts, can be controlled by the application of eletric field. It can be seen from the measurement data of the professional literature [4], that for the evolution of the effect it is enough (2-10) ms, which is a much smaller value, that the indication time of the proportional valves applied nowadays.

3. THE RESULTS OF OPERATION OF THE MODEL

In Chart 6 at making the simulation results we applied 6 bar inlet pressure.
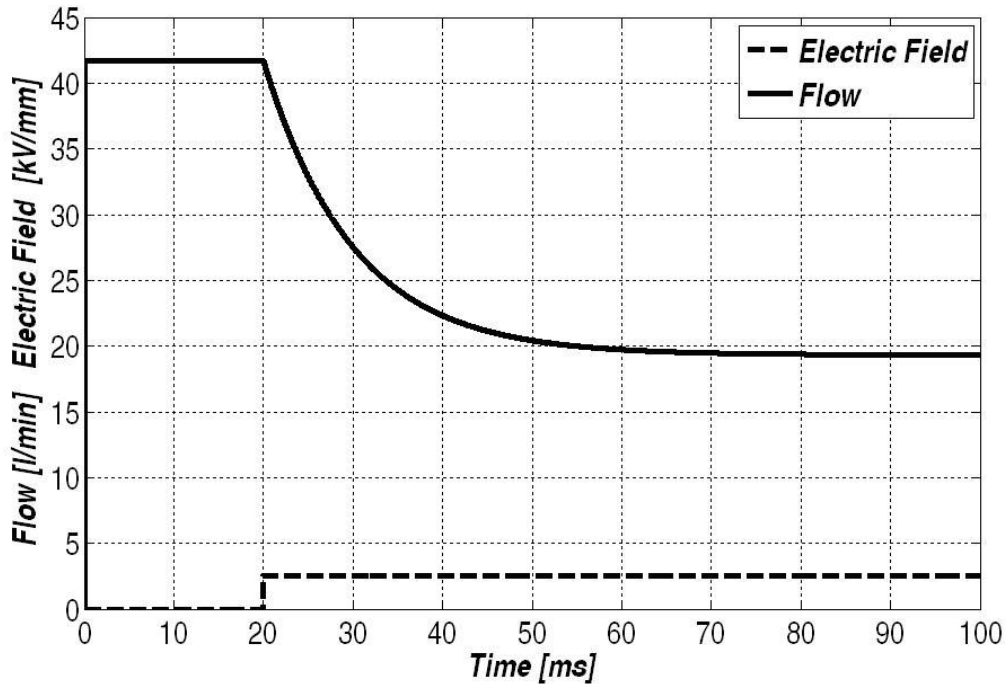
Fig. 6.

As it seems on the figure 6. the flow is 42 l/min up to 20 ms, then by switching 2 kV/mm electric field the streaming flow decreases to 18 l/min in 40 ms.
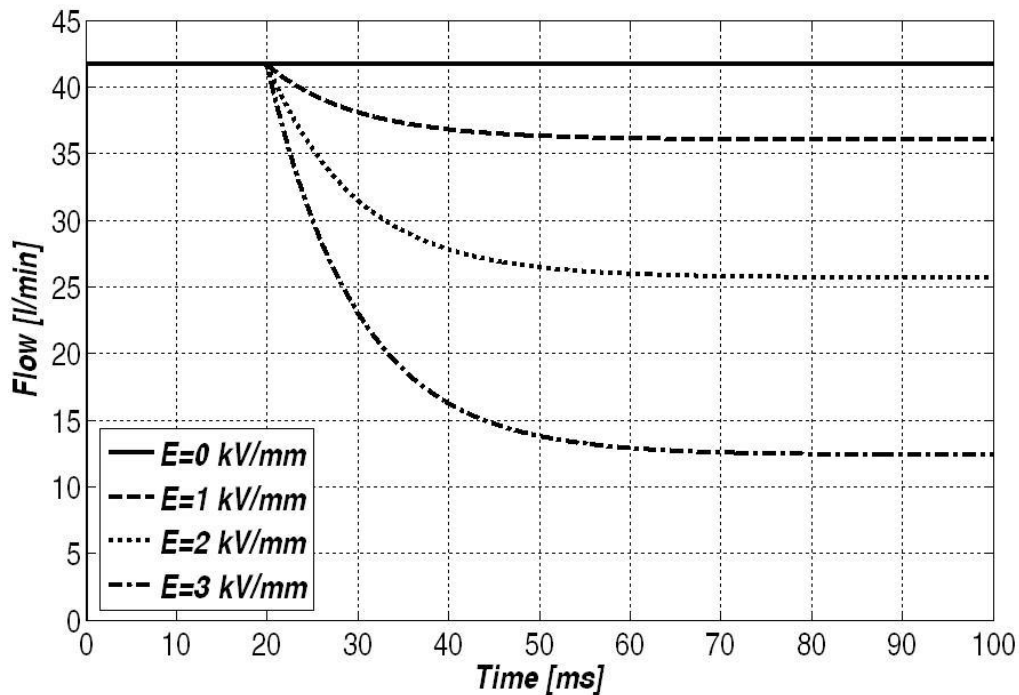
Fig. 7.

At the simulation in the figure 7. constant 6 bar inlet pressure (p0) was used. It is shown that how the flow changes at various size electric field.

4. EXPERIMENTAL SYSTEM AND RESULTS

The system consists of three main parts, like: the hydraulic power unit, ER circuit, data acquisition and control system. The hydraulic unit ensures the flow of ER fluid by a driving servo cylinder. The ER valve with flow meter and the pressure difference meter are fitted into the ER circuit.
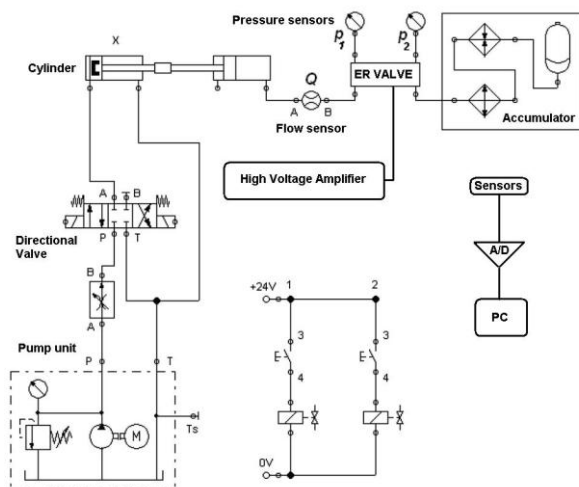
Fig. 8. Experimental setup

Fig. 9. Experimental setup (picture)

1.4 Results

The pressure difference required by the ER fluid to flow was ensured by a bladder-type accumulator had been pre-charged up to 6 bar before the experiment. The change of shearing stress of the fluid was determined by the equation of 6 from the pressure difference and the fluid flow rate after the electric field was switched on.
.
The Fig 10 shows the change of shearing stress of the ER fluid (line) influenced by the change of electric field of 8.2 kV/mm. The measure of orifice of applied ER valve is h = 0.5 mm, the length is l = 200 mm, the potential is U = 4.1 kV. The broken line shows the result of simulation made by the mathematic model introduced before.
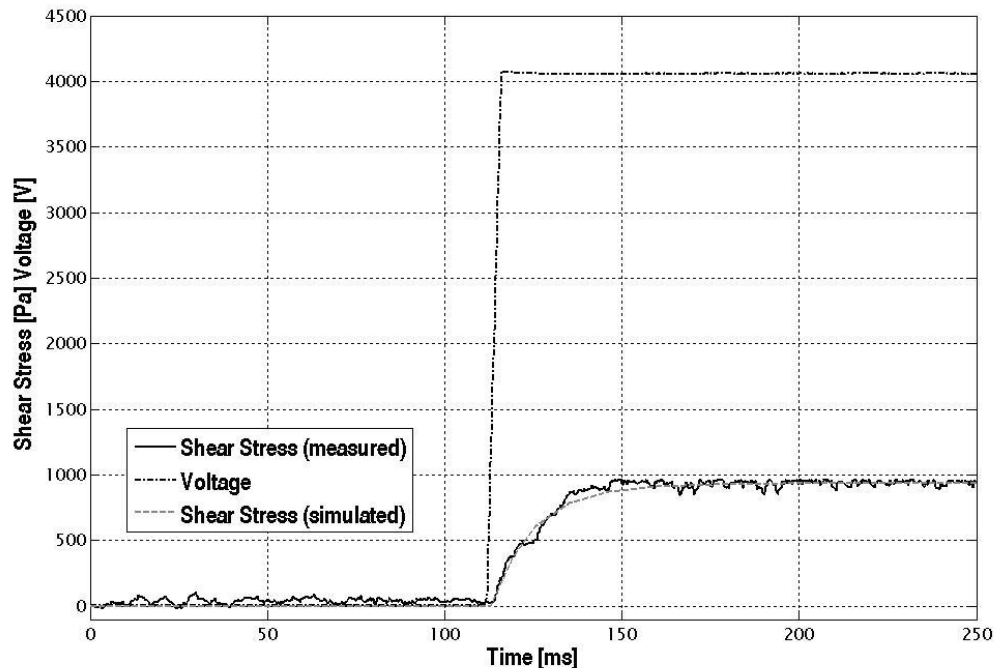
Fig. 10. The results of simulation and measurement

5. CONCLUSIONS

On the basis of simulation experiments we can assume that the above introduced ER valve can be applied in hydraulic systems. Certainly this concept has to be further tested in term of application technique, such as the wear-effect of the particles of the used ER fluid and the temperature dependency of the ER effect. Since the developed flow control valve doesn't containg moving parts and it can be controlled by external electrical field, thus, in theory, the probability of mechanical failures can also be decreased.

REFERENCES

1.   Csizmadia B. – Nándori E. (szerk.): Modellalkotás, Nemzeti Tankönyvkiadó, Budapest, 2003.

2.   Dr. Farkas I.: Számítógépes szimuláció. Gödöllő, 1999.

3.   H.-G. Lee – S.-B. Choi: Dynamic properties of an ER fluid shear and flow modes, In: Materials and Design, 2002., XXIII. évf.

4.   Valasek I. – Auer J. (szerk.): Kenőanyagok és vizsgálataik, Tribotechnik Kft., Budapest, 2003

5.   Seung-Bok Choi, Dong-Won Park, Myoung-Soo Cho : Position control of a parallel link manipulator using electro-rheological valve actuators. Mechatronics, Volume 11, Issue 2, 1 March 2001, Pages 157-181

6.   S. B. Choi, Y. T. Choi, E. G. Chang, S. J. Han, C. S. Kim: Control characteristics of a continuously variable ER damper. Mechatronics, Volume 8, Issue 2, March 1998, Pages 143-161

7.   Zrínyi M.: Intelligens anyagok, Magyar Tudomány, 1999., 6. sz., 682.

INHERENT POSSIBILITIES AND LIMITATIONS OF FINITE ELEMENT MODELLING OF DEFECTIVE GIRTH WELDS

S. Hertelé[1], W. De Waele[2], R. Denys[2], M. Abdel Wahab[2] and M. Verstraete[2]

[1] FWO Aspirant, Ghent University, Laboratory Soete, Belgium
[2] Ghent University, Laboratory Soete, Belgium

Abstract Welds unavoidably show defects, which can negatively affect the integrity of the entire structure and, worst case, result in a failure. Defects of a considerable size should therefore be detected, assessed and, if necessary, repaired. The assessment of a defect requires a procedure which allows a conservative estimation of the acceptability of the defect. To develop such procedure, both experimental and numerical research is performed. This paper describes the inherent possibilities and limitations of numerical research through finite element modelling, as compared to experimental research. Summarizing all arguments, it becomes clear that numerical research is a highly powerful tool, but a thorough experimental validation is of paramount importance. Moreover, some specific weld-related problems are highly difficult to address, namely the presence of stable crack growth and material heterogeneity. More research is needed to achieve a description of these phenomena, under a set of conservative assumptions.

Keywords

Finite element analysis, weld, defect

1   INTRODUCTION

Welding is a joining technique which, if appropriately performed, has a lot of advantages as opposed to other joining techniques. Noteworthy are the achievement of a light, stiff, fully sealed connection and the possibility for automation. Often, welding is the only economically and practically acceptable joining technique, e.g. in the case of large-diameter, high pressure transport pipelines.

Despite the advantages related to welding, a weld is often the most critical area of the structure, because of two reasons (Figure 1). Firstly, a weldment consists of a continuous transition between different microstructures, some of which show detrimental properties (reduced fracture toughness, reduced strength). Secondly, welds that are made in the field unavoidably contain defects, such as porosities, slag inclusions, lack of fusion.
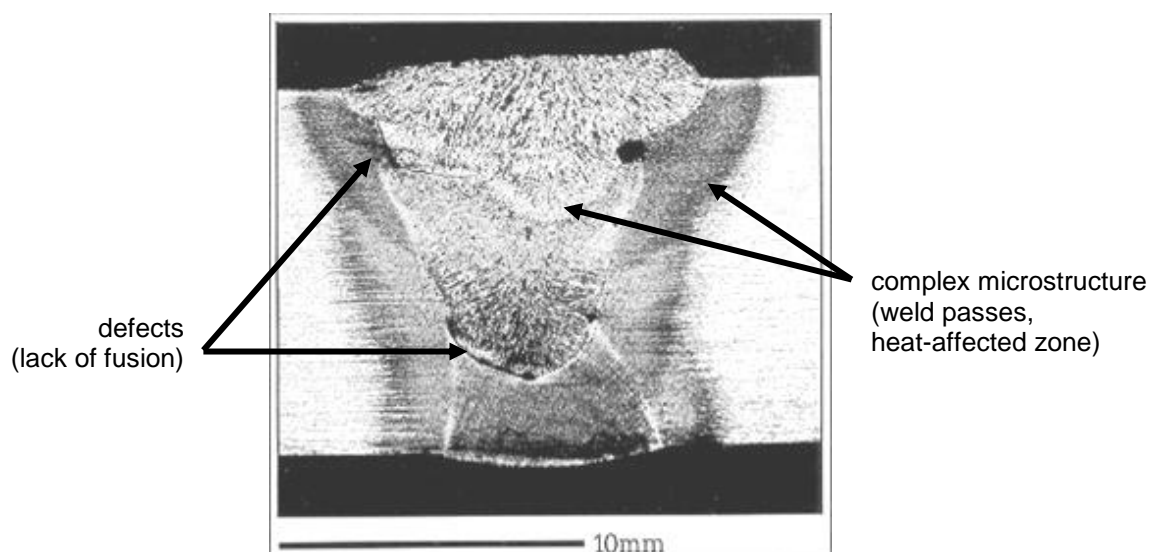
Figure 1: A weldment consists of complex microstructures and defects [1].

Weld defects give rise to stress concentrations, which can lead to crack initiation, followed by stable or unstable crack propagation. In the worst case, one single defect can result in a failure of the global structure, possibly causing casualties and ecological damage. A well-known example that illustrates the possible consequences of welding defects is the collapse of the Alexander Kielland oil platform (123 casualties) [1].

Since weld defects can have disastrous consequences, each structural weld should be non-destructively inspected and, if necessary, repaired. However, a 100% repair rate would be way too expensive. Therefore, defects should be assessed for their acceptability and, if allowable, not be act upon.

The assessment of defects requires an analytical procedure which allows to conservatively estimate their possible influence on the structural integrity. To develop such procedures, which are often application-specific, a lot of experiments have been and are still being performed.

Besides the analysis of experiments, however, there is a second possible approach: finite element analysis. For the specific case of pipeline welds, this approach has been widely applied for two general purposes. First, finite element analyses have been performed to investigate the qualitative effect of a limited set of parameters (descriptive). For instance, as regards the operational conditions, studies have been performed about the loading mode (bending or tensile) [2] and the presence of internal pressure [2,3,4]. Concerning the geometry, the structure's and the defect's size and geometry have been investigated [2-7]. Of particular importance in this category is the effect of weld misalignment [2;4;5]. Another important particular topic of investigation is the material behaviour, including strain hardening [3;6;7], weld strength mismatch [2;6-9], heat affected zone softening [4;9;10], resistance to crack growth [2;6;7;11-14], anisotropy [5] and toughness [5]. Second, finite element analyses have been used to describe an experiment as good as possible, including all important aforementioned aspects related to defective welds (predictive). This category is best represented by ongoing numerical research from ExxonMobil [15-19], and also includes some less extensive finalised projects [20,21].

Since the numerical alternative is fundamentally different to the experimental approach, it has some specific additional advantages, but also some drawbacks. This paper is concerned with the discussion of the positive and negative aspects of finite element analysis for the purpose of assessing pipeline girth weld defects, and how to achieve an optimal research programme. The article is structured as follows. Firstly, the possibilities of finite element modelling are discussed. Then, the limitations are investigated, along with a discussion on how to deal with them. Finally, conclusions are drawn.

2 POSSIBILITIES OF FINITE ELEMENT MODELLING OF PIPELINE GIRTH WELDS

As compared to experiments, finite element simulations provide advantages at three levels: analysis, flexibility and control. Each advantage is separately discussed in the sections below.

2.1 Degree of analysis

Unavoidably, the results of an experiment are confined to the extent and possibilities of the applied instrumentation. Mostly, this instrumentation gives information about a number of deliberately chosen, representative quantities, but not about the entire picture. In some specific cases, this can even give rise to unknown measurement errors [22]. Numerical simulations, on the other hand, can provide the complete space-time response of the investigated problem (Figure 2).

Apart from some basic quantities (stresses, strains, …), other related results can also be obtained. Given as an example is the J integral, which expresses the urge of a crack to initiate and propagate ('crack driving force'), and which can therefore be used to predict crack growth. This quantity is calculated as an integral over a random path around the crack tip, as first defined by Rice [23]. An analytical expression for J is known for only a limited number of standard experimental setups. In other setups, numerical solutions need to be addressed to obtain J.
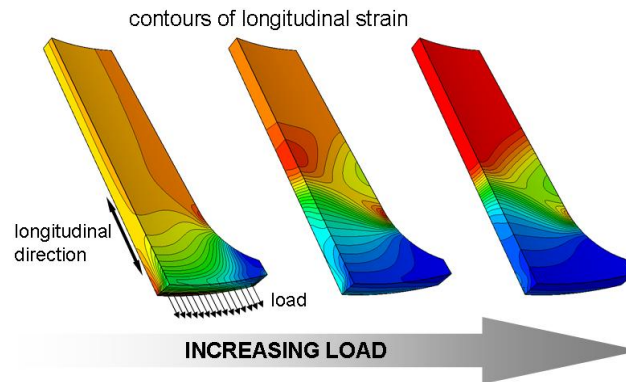
Figure 2: Finite element simulations provide full information in terms of space and time. This figure is an example result of an analysis of deformations in a curved wide plate specimen, performed at Laboratory Soete [22].

2.2   Degree of flexibility

Unavoidably, the amount of test material available in an experimental programme will be limited. Hence, it may be difficult to investigate the effect of variations of one specific geometrical or material parameter. Numerical simulations do not show this restriction, as every parameter can be freely adapted to the desires of the researcher. This paper elaborates two examples, which illustrate the flexibility of finite element simulations: firstly, the accurate description of a specific weld geometry, and secondly, the execution of a parametric study. Both studies have been performed at Laboratory Soete.

Firstly, it is possible to accurately describe any realistic weld geometry in an accurate way. To that purpose, a technique of node coordinate transformations has been developed. The principle is illustrated in Figure 3, where it is applied on an example of a weld (a). First, the paths of the fusion line and the weld cap are estimated (b). Next, these paths are described by mathematical equations (f_{bevel} and f_{cap}, respectively) (c). Using these equations, a coordinate transformation is then defined, starting from a perfectly regular rectangular grid (d). This transformation is finally applied on all nodes of a similar rectangular mesh (e). Using this technique, a good correspondence between the desired and the obtained mesh geometry is achieved (f). Moreover, the initially rectangular mesh is independent of weld geometry. Hence, a standard model can be built for all weld models, which is then transformed into the desired configuration. This allows for a high degree of automation.

Secondly, scripts that automate the entire process of performing finite element simulations, allow for an easy execution of parametric studies. In that way, the importance of, and the interaction between different parameters can be identified. An example of the procedure is illustrated in Figure 4. A series of parameter sets, each of which defines one model, is input to a Python script. This script communicates with the finite element software ABAQUS[®], which builds and executes each model. The requested results are written to text files, which are then post-processed using a Matlab[®] script. This script produces standardised Microsoft[®] Excel[®] spreadsheets and HTML files, which can be viewed in any browser.

To illustrate the possibilities of the above technique, Figure 5 shows the results of a parametric study. For an Y-shaped weld, with the weld metal stronger than the connected base metals, the bevel angle 2α was varied between 0° and 80°. Clearly, the opening of a present crack (CMOD – Crack Mouth Opening Displacement) is influenced by this bevel angle. Apparently, if stronger than the base metals, a wider weld shields the crack from any remotely applied deformations. The extent of this influence is highly significant, as it eventually determines the failure mode of the welded connection. Indeed, for narrow welds ($\alpha = 0°$ and $\alpha = 10°$) on the one hand, the crack causes the weld to collapse, resulting in a reduced deformation capacity. For wide welds ($\alpha = 20°$ and higher) on the other hand, the crack stabilizes. In the latter case, failure is no longer determined by the crack, but by the deformation capacity of the base metal. It should be remarked that possible stable crack extension has not been included in these analyses.
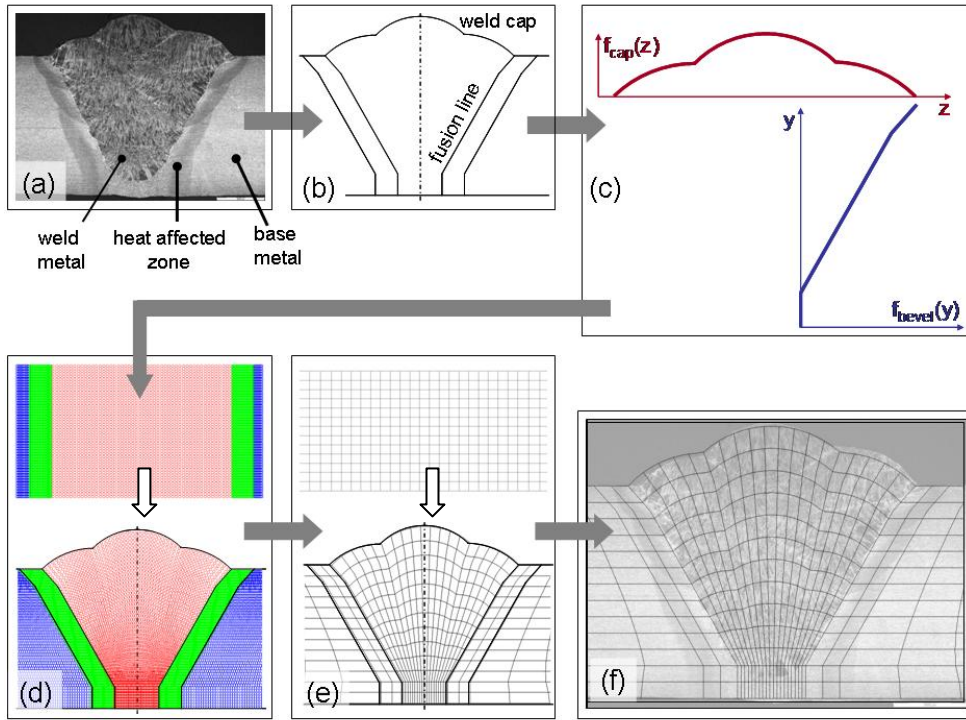
Figure 3: Coordinate transformations are used to create customized geometries.
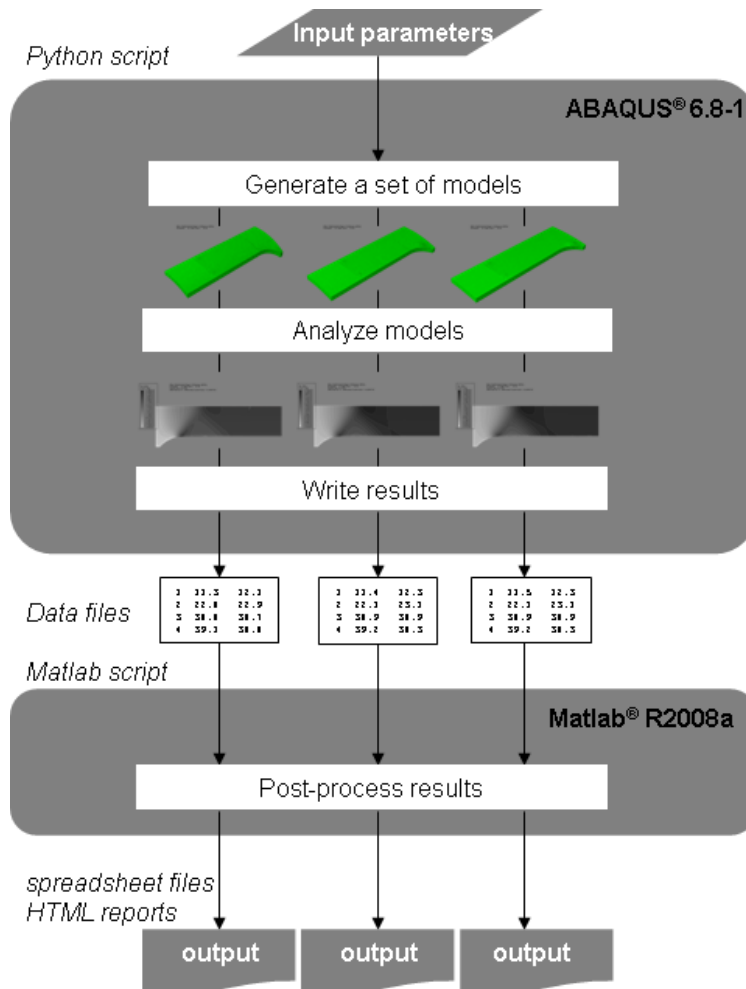
Figure 4: Structure of a parametric finite element study [22].
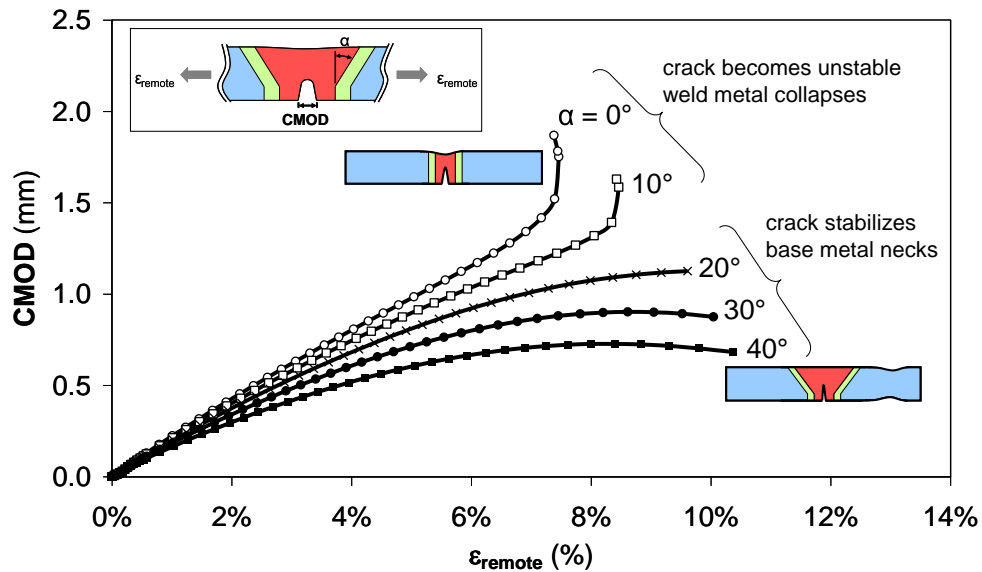
Figure 5: Example result of a parametric finite element study
(red: weld, green: heat-affected zone, blue: base metal).

2.3 Degree of control

Despite the fact that an experiment is performed in a controlled environment, there will always be a certain degree of uncertainty. This may affect the correct interpretation and repeatability of a test result.

For instance, Figure 6 shows a tensile test specimen, containing a weld, which was intended to measure deformations. To that purpose, pins were spot-welded on the specimen, in order to mount LVDTs and clip gauges. However, Figure 6 clearly shows that some of the pins' angular positions were affected by the deformation of the specimen, resulting in a hardly interpretable measurement after the onset of necking.
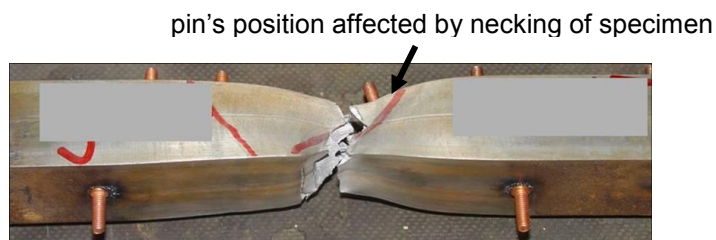
Figure 6: A tensile test specimen, on which spot-welded pins were welded to mount LVDTs and clip gauges.

Finite element simulations do not show the problem of uncertainty of circumstances. Indeed, they are created in a numerical environment, where every aspect of the situation (geometry, material, load, boundary conditions) is, in principle, under complete control. This eliminates possible sources of a bad outcome and facilitates the comparison between different results.

3 LIMITATIONS OF FINITE ELEMENT MODELLING OF PIPELINE GIRTH WELDS

Despite providing certain advantages as compared to experiments, finite element models show some inherent limitations that cannot be ignored. These limitations are situated in the inability of perfectly describing the required input parameters, and the unavoidable occurrence of numerical errors. Each limitation is separately discussed in the sections below.

3.1 Limitations with respect to a realistic description of material behaviour

A numerical simulation is merely the production of a series of 'zeros and ones', which, if carefully designed, provides an approximation of reality. Despite the large number of computational tools available, some physical phenomena are too complicated to perfectly represent in the field of finite element modelling. In

particular, two aspects are relevant for defected welds: heterogeneity of the materials, and crack initiation and growth.

Firstly, a weldment is a continous transition between different microstructures, all of which have resulted from a specific mechanical and thermal cycle during production and welding. Noteworthy are the occurrence of a heat-affected zone near the weld's fusion lines, the rich composition of coarse and fine-grained weld metal zones, due to subsequent weld passes (Figure 7; see also Figure 3(a)), but also the heterogeneity of the base metal (for instance, in the case of pipelines, due to pipeline forming).
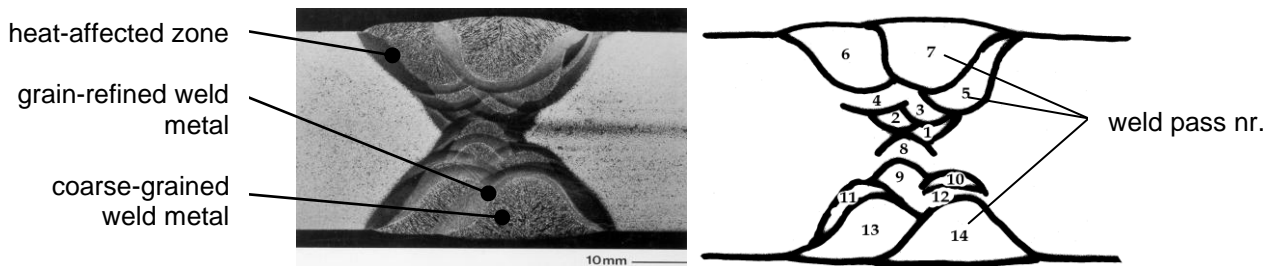
Figure 7: Heterogeneity in and around a weld metal, due to subsequent thermal cycles for each weld pass [1].

A heterogeneous material structure can be described in a finite element model. However, since it is extremely difficult or even impossible to accurately predict, or to experimentally retrieve the mechanical properties at every point in and around the weld, it is also impossible to describe the required input data for such heterogeneous structure in a numerical simulation. Approximations have to be made by using representative values, resulting from a number of characteristic tensile tests or simplified analytic predictions. Since the presence of heterogeneity has an unmistakable influence on the overall structural behaviour of the weldment [24-26], these approximations should be worst-case.

Secondly, the stress-strain concentration around a defect tip can give rise to the initiation and, subsequently, growth of a crack. The extent and direction of this crack growth depends on the applied loading, the degree of tri-axiality ('constraint') of the stress distribution at the crack tip, and the local microstructure. The first factor determines the crack driving force, whereas the last two factors define the so-called resistance curve. Expressed as a function of crack size, the amount of crack growth is determined by the intersection of the crack driving force curve with the resistance curve (Figure 8).
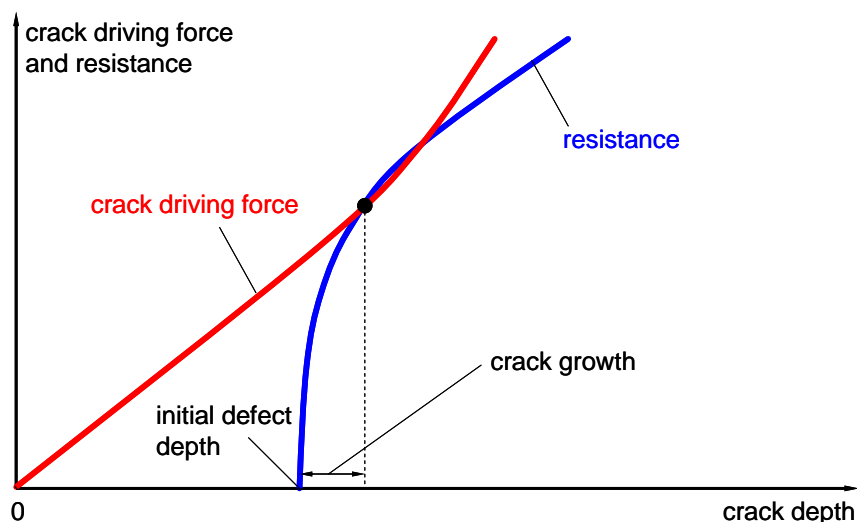
Figure 8: Crack growth is the result of a struggle between crack driving force and resistance.

Since the resistance curve depends on the local microstructure, which is highly heterogeneous, also the process of crack growth is characterized by a fair degree of scatter. To complicate matters even more, not only the extent, but also the direction of crack growth is determined by an interaction between applied

loading and local microstructure. This can give rise to fundamentally different failure mechanisms (Figure 9) [24;27].

Taking into account the abovementioned considerations and the fact that performing many simulations is time-consuming, finite element analyses should be restricted to the calculation of worst-case scenarios, under a set of conservative assumptions regarding material behaviour and crack growth properties. The results of these simulations then give a safe image of the qualitative influence of some parameters, more than an exact quantitative result. Alternatively, if the degree of scatter is known to some extent, numerical simulations can be used in the context of a probability-based design (stochastic finite element analysis). This, however, requires an extensive experimental characterization prior to simulating.

3.2 Numerical errors

Finite element modelling is a numerical technique, in which a continuous geometry is discretized into a finite set of elements. This discretization unavoidably involves the introduction of numerical errors. Choosing a larger set of smaller elements helps to reduce the order of magnitude of these errors, but requires more calculation time. Hence, choosing the mesh density is a trade-off between desired accuracy and available time. This trade-off should be chosen after a convergence study, taking into account the purpose of the analysis (Figure 10). If, on the one hand, the aim of the numerical model is to perform a parametric study based on a large amount of simulations, the calculation time should certainly be optimized. The corresponding reduction in result accuracy should, however, be kept limited. On the other hand, if the aim of the numerical model is a thorough, unique analysis of one specific situation, a highly accurate but time-consuming analysis may be chosen.

Figure 11 shows an example of a mesh convergence study, applied on the same model as in Figure 5. On the one hand, the coarsest mesh calculates very fast (147 seconds), but inaccurately. On the other hand, the finest mesh calculates very accurately, but is over ten times more time-consuming (1607 seconds). Given the fact that the model was intended for a large number of simulations, a trade-off was chosen to give a calculation time of about 10 minutes per simulation (600 seconds).

"Straight" path of fracture   "Slant" path of failure
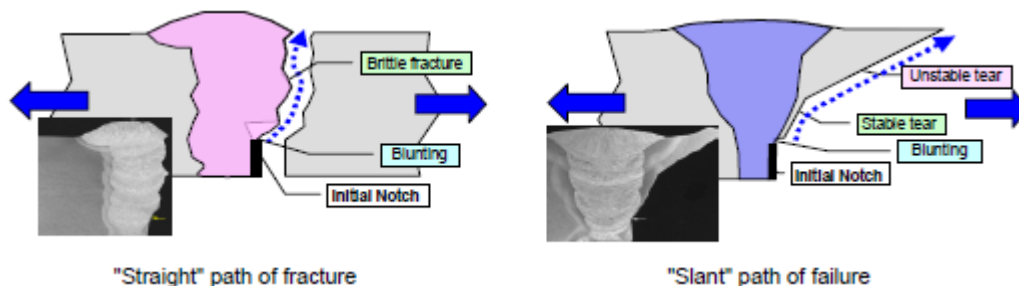
Figure 9: An initiated crack can grow in different directions, depending on the loading pattern and the local microstructures it encounters [24].
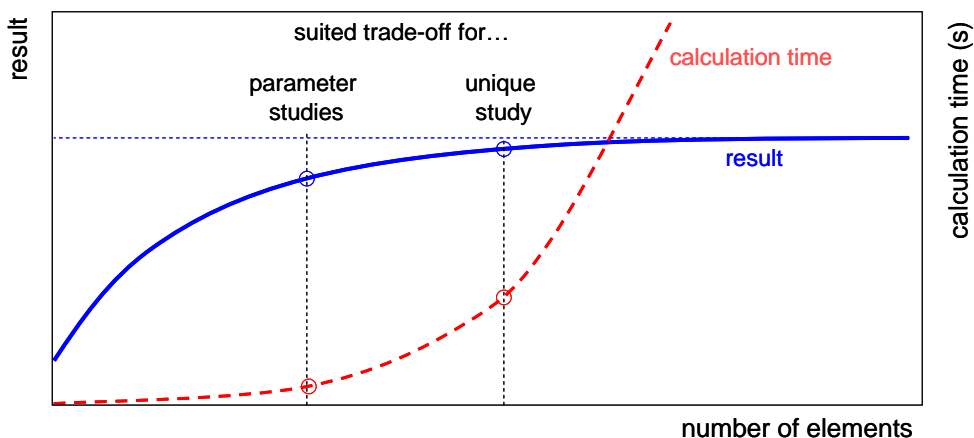
Figure 10: Philosophy behind a mesh convergence study.
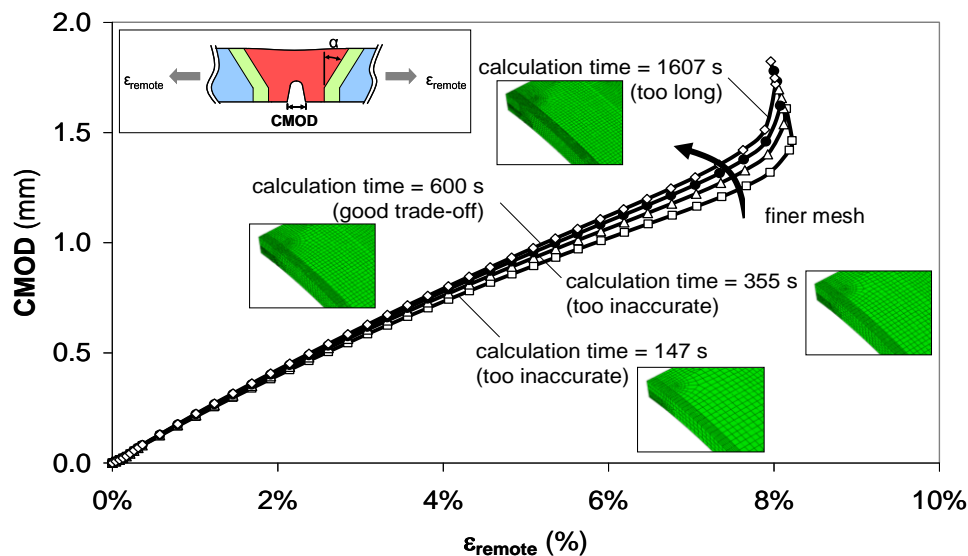
Figure 11: Example of a mesh convergence study.

4   CONCLUSIONS

Finite element simulations are powerful tools for the development of weld defect assessment procedures. They can provide an answer to the fact that not everything can be seen, changed, or avoided in an experiment. Indeed, a finite element simulation is under complete control of the user, and can be used to systematically investigate the influence of every single geometrical and material parameter.

However, the results of finite element simulations need to be interpreted with great care. A simulation is no more than a numerical attempt to describe the real situation through 'zeros and ones', and is therefore by definition an approximation. Moreover, every model should be consciously optimized in terms of accuracy and calculation time. The obtainable accuracy is highly dependent on the input parameters, which are not always deterministic. Hence, worst-case scenarios or probabilistic techniques should be considered.

Since approximations are unavoidable in a finite element simulation, the key to obtaining reliable results is a thorough experimental validation. Such validation can reveal the extent and acceptability of the idealizations made, and can allow for the postulation of conservative assumptions. That way, finite element simulations can be used to describe worst-case situations, resulting in a safe defect assessment.

5   ACKNOWLEDGEMENTS

6   REFERENCES

[1]   A. Dhooge, *Metaalconstructies - Constructietechnieken*, 2010.
[2]   E. Østby, E. Torselletti, E. Levold, *A strain-based approach to fracture assessment of pipelines*, Proceedings of FITNET, Amsterdam, The Netherlands, 2006.
[3]   K. R. Jayadevan, E. Østby, C. Thaulow, *Fracture response of pipelines subjected to large plastic deformation under tension*, International Journal of Pressure Vessels and Piping, 81(9), 2004, 771-783.
[4]   W. C. Mohr, *Pressure effects on strain concentration and constraint for strain-based design*, Proceedings of the 17th International Offshore and Polar Engineering Conference, 3121-3128, Lisbon, Portugal, July 2007.
[5]   Y. Y. Wang, M. Liu, *The role of anisotropy, toughness transferability, and weld misalignment in the strain based design of pipelines*, Proceedings of the 17th International Offshore and Polar Engineering Conference, 3164-3171, Lisbon, Portugal, July 2007.
[6]   E. Østby, C. Thaulow, Z. L. Zhang, *Numerical simulations of specimen size and mismatch effects in ductile crack growth - Part I: Tearing resistance and crack growth paths*, Engineering Fracture Mechanics, 74(11), 2007, 1770-1792.

[7] E. Østby, C. Thaulow, Z. L. Zhang, *Numerical simulations of specimen size and mismatch effects in ductile crack growth - Part II: Near-tip stress fields*, Engineering Fracture Mechanics, 74(11), 2007, 1793-1809.

[8] D. Horsley, Y. Y. Wang, *Weld mismatch effects on the strain behaviour of flaws in X100 (Grade 690) pipe and girth welds*, Proceedings of the 4th International Conference on Pipeline Technology, 267-277, Ostend, Belgium, May 2004.

[9] C. Thaulow, Ø. Ranestad, M. Hauge, Z. L. Zhang, M. Toyoda, F. Minami, *FE calculations of stress fields from cracks located at the fusion line of weldments*, Engineering Fracture Mechanics, 57(6), 1997, 637-651.

[10] M. Liu, Y. Y. Wang, D. Horsley, *Significance of HAZ softening on strain concentration and crack driving force in pipeline girth welds*, Proceedings of the 24th International Conference on Offshore Mechanics and Arctic Engineering, Halkidiki, Greece, June 2005.

[11] Y. Y. Wang, M. Liu, D. Horsley, *Application of constraint-sensitive fracture mechanics to the assessment of girth weld integrity*, Proceedings of the 5th International Pipeline Conference, Calgary, Alberta, Canada, October 2004.

[12] D. M. Duan, Y. Y. Wang, Y. Chen, J. Zhou, *Modeling and CMOD mapping of surface-cracked wide plates*, Proceedings of the 7th International Pipeline Conference, Calgary, Alberta, Canada, October 2008.

[13] K. R. Jayadevan, E. Berg, C. Thaulow, E. Østby, B. Skallerud, *Numerical investigation of ductile tearing in surface cracked pipes using line-springs*, International Journal of Solids and Structures, 43(7-8), 2006, 2378-2397.

[14] E. Berg, B. Skallerud, C. Thaulow, K. Holthe, *Ductile fracture of pipelines - effects of constraint correction and circumferential crack growth*, Proceedings of the 17th International Offshore and Polar Engineering Conference, 3224-3230, Lisbon, Portugal, July 2007.

[15] K. Minnaar, P. C. Gioielli, M. L. Macia, F. Bardi, N. E. Biery, W. C. Kan, *Predictive FEA modeling of pressurized full-scale tests*, Proceedings of the 17th International Offshore and Polar Engineering Conference, 3114-3120, Lisbon, Portugal, July 2007.

[16] S. A. Kibey, K. Minnaar, J. A. Issa, P. C. Gioielli, *Effect of misalignment on the tensile strain capacity of welded pipelines*, Proceedings of the 18th International Offshore and Polar Engineering Conference, 90-95, Vancouver, BC, Canada, July 2008.

[17] S. A. Kibey, J. A. Issa, X. Wang, K. Minnaar, *A simplified, parametric equation for prediction of tensile strain capacity of welded pipelines*, Proceedings of the 5th International Conference on Pipeline Technology, Ostend, Belgium, October 2009.

[18] S. A. Kibey, K. Minnaar, W. Cheng, X. Wang, *Development of a physics-based approach for the prediction of strain capacity of welded pipelines*, Proceedings of the 19th International Offshore and Polar Engineering Conference, 132-137, Osaka, Japan, June 2009.

[19] X. Wang, S. T. Barbas, S. A. Kibey, P. C. Gioielli, K. Minnaar, *Validation of strain capacity prediction method: comparison of full-scale test results to predictions from tearing analysis based on FEA*, Proceedings of the 5th International Conference on Pipeline Technology, Ostend, Belgium, October 2009.

[20] Y. Y. Wang, D. Rudland, R. Denys, D. Horsley, *A preliminary strain-based design criterion for pipeline girth welds*, Proceedings of the 4th International Pipeline Conference, Calgary, Alberta, Canada, September-October 2002.

[21] Y. Y. Wang, W. Cheng, M. McLamb, D. Horsley, J. Zhou, A. G. Glover, *Tensile strain limits of girth welds with surface-breaking defects - Part 1: An analytical framework*, Proceedings of the 4th International Conference on Pipeline Technology, 235-249, Ostend, Belgium, May 2004.

[22] S. Hertelé, W. De Waele, R. Denys, J. Van Wittenberghe, M. Verstraete, *Investigation of pipe strain measurements in a curved wide plate specimen*, Accepted for the 8th International Pipeline Conference, Calgary, Alberta, Canada, September-October 2010.

[23] J. R. Rice, *A path independent integral and the approximate analysis of strain concentration by notches and cracks*, Journal of Applied Mechanics, 35, 1968, 379-386.

[24] R. Denys, *Weld metal strength mismatch: past, present and future*, Proceedings of the International Symposium to Celebrate Prof. Masao Toyoda's Retirement from Osaka University, 115-148, Osaka, Japan, June 2008

[25] R. Denys, P. De Baets, A. Lefevre, W. De Waele, *Significance of the tension test in relation to plastic pipeline design*, Proceedings of the Pipe Dreamer's Conference, 173-182, Pacifico Yokohama, Japan, November 2002.

[26] R. Denys, W. De Waele, A. Lefevre, *Effect of pipe and weld metal post-yield characteristics on plastic straining capacity of axially loaded pipelines*, Proceedings of the 5th International Pipeline Conference, Calgary, Alberta, Canada, October 2004.

[27] R. Denys, P. De Baets, A. Lefevre, W. De Waele, *Material tensile properties in relation to the failure behavior of girth welds subject to plastic longitudinal strains*, Proceedings of the Pipe Dreamer's Conference, 159-172, Pacifico Yokohama, Japan, November 2002.

Research of machining forces and technological features of cast PA6, POM C and UHMW-PE HD 1000.

Róbert Keresztes, Gábor Kalácska
Institute for Mechanical Engineering Technology,
Faculty of Mechanical Engineering, Szent István University, Gödöllő, Hungary
www.geti.gek.szie.hu

Abstract Nowadays parts made of up-to-date engineering plastics are used more and more in mechanical engineering practice. These machine-elements are produced most frequently by injection molding or by one cutting process. The injection molding technology are used generally for great number of pieces, in case of serial production while cutting processes are preferred to piece (unit) or smaller number production.
We used lathe and measured the main- and feeding-directional cutting force at different engineering polymers (cast PA6, POM C and UHMW PE HD 1000). The analysis made can be well used in practice.

Keywords turning force components, lathe, force measuring, main cutting force

1. INTRODUCTION

Among cutting processes the turning takes place often. During turning engineering plastics many problems can arise. Among these one is the splint (continuous chip) forming which can cause accident and can cause failure maybe the total ruin, fracture of the cutting tool. Because of this it is important to set the proper cutting parameters by which it is possible forming elemental or transitional (easily fracture) chip, too.
It is also important to know during cutting the amount of the main cutting force. Knowing this the load of cutting tool can be made more constant as well as the remnant stress in the material chipped can be reduced to minimum in case of proper cutting parameters.

2. TESTING METHODS, INSTRUMENTS

The cutting is a machining method during which the required shape of the workpiece is formed by removing the surplus material layer in smaller – bigger particles (chip) with a suitable tool. Relative displacement is needed between the tool and workpiece for chip removal, for cutting movement. The following (Fig. 1) figure shows the relations of arising forces during turning.

Figure 1. Turning force components (ISO 3002/4, DIN 6584)

Equipment used for tests.

The CNC-lathe, type EMCO COMPACT 5, was used for tests. The equipment can be found in the laboratory of Institute for Mechanical Engineering Technology its programming takes place of G-codes. The photograph of the workpiece clamped as well as the shank with strain-gauges clamped into tool-box and the turning tool can be seen in Figure 2.
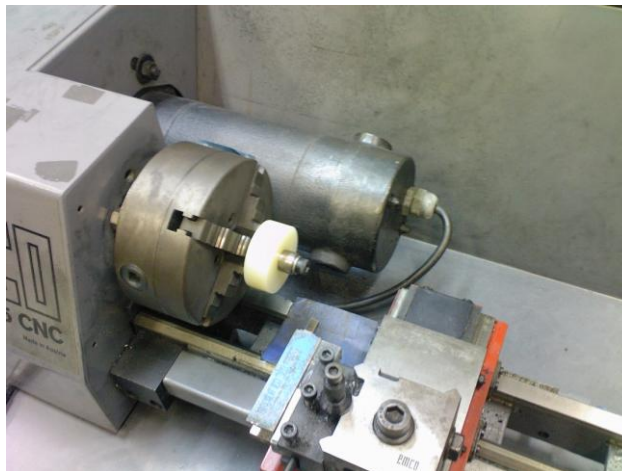
Figure 2. The lathe and the workpiece clamped

The tool clamping structure used for measuring the forces can be seen in Figure 3. The first section of the Figure shows the 3D-model.
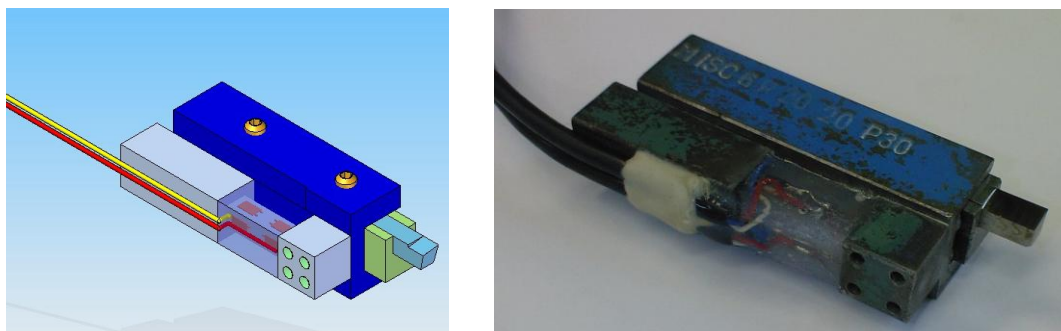
Figure 3. The force measuring shank model and its real picture

2-2 pcs. strain gauges are fixed at every side. Coupling the strain gauges into total (full) – bridge those is a possibility measuring the forces arising in two directions. To measure the main cutting force F_v (tangential) arising from the movement in vertical plane of the tool and F_f feeding (axial) force arising from the movement in horizontal plane. A second tool-box is fixed to 4 pcs. threaded holes on the measuring-shank into which the real cutting tool is fixed. The strain gauges measure the tangential (lower – upper) and the feeding (right side – left side) forces connect to a Spider-8 type measuring amplifier though wires, which amplifier convert the analogous signals into digital than transmits to the computer. With the help of Catman 3.1 program data measured can be seen. The frequency of measuring and data collecting is 25 Hz.

Materials tested.

The materials tested are those polymer basic types that are often used in engineering practice to manufacture machine-elements. Table 1 shows the name of product, the whole name and the marks accruing on lather diagrams. The specimens prepared for cutting are shown in Figure 4.

Table 1. Name and mark of plastics

Serial number	Product name [6]	Whole name	Own mark
1.	DOCAMID 6G H	Cast polyamide 6, (Magnesium)	PA 6G Mg
2.	DOCAMID 6G	Cast polyamide 6, (Natrium)	PA 6G Na
3.	DOCACETAL C	Polyoximethylene / Polyacetal	POM C
4.	DOCALENE	UHMW – Polyethylene	HD 1000
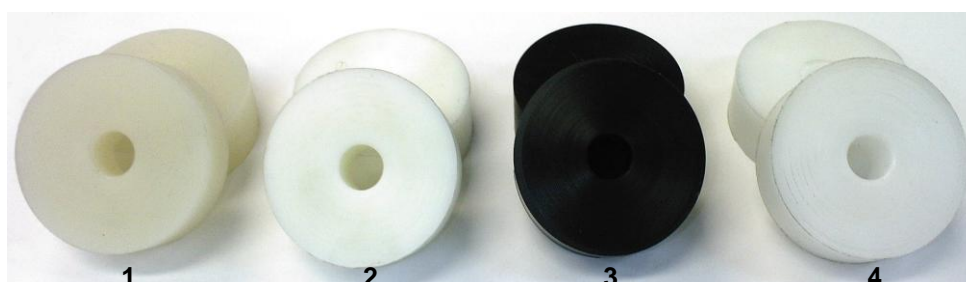
In the Table 2. the more important properties of polymers tested can be seen summarized.

Table 2. More important properties of plastics

Polymer	Strength [MPa]	Toughness (Charpy) [kJ/m^2]	Sliding characteristic (µ)	Thermo-duricity [°C]	Hardness	Density [kg/dm^3]
PA 6G Na	77 - 110	112	0,15 - 0,5	-40 - 140	Rockwell 85 – 98 HRC	1,15 – 1,6
PA 6G Mg	77 - 110	112	0,15 - 0,5	-40 - 140	Rockwell 85 – 98 HRC	1,15 – 1,6
POM C	70 – 80	8	0,25 – 0,45	5 – 120	Rockwell 86 – 90 HRC	1,4
HD 1000	20 – 24	no fracture	0,2 – 0,3	-80 – 110	Shore 60 – 65 D	0,96

Cutting parameters
Feeding/rev.: f = 0.025, 0.05, 0.1, 0.2 mm/rev.
Depth of cut: a = 0.1, 0.25, 0.5, 1, 2   mm
Cutting speed: v = 50, 100, 200   m/min

Table 3. contains the parameters summarized used at tets. Each cutting speed data registered means test carried out by one-one material to which belong one feeding and one depth of cut. This gives 60 measuring by each material.

Table 3. Cutting speeds in the function of feeding and depth of cut

a＼f	0,025 mm/rev.			0,05 mm/rev.			0,1 mm/rev.			0,2 mm/rev.		
0,1 mm	50 m/min	100 m/min	200 m/min	50 m/min	100 m/min	200 m/min	50 m/min	100 m/min	200 m/min	50 m/min	100 m/min	200 m/min
0,25 mm	50 m/min	100 m/min	200 m/min	50 m/min	100 m/min	200 m/min	50 m/min	100 m/min	200 m/min	50 m/min	100 m/min	200 m/min
0,5 mm	50 m/min	100 m/min	200 m/min	50 m/min	100 m/min	200 m/min	50 m/min	100 m/min	200 m/min	50 m/min	100 m/min	200 m/min
1 mm	50 m/min	100 m/min	200 m/min	50 m/min	100 m/min	200 m/min	50 m/min	100 m/min	200 m/min	50 m/min	100 m/min	200 m/min
2 mm	50 m/min	100 m/min	200 m/min	50 m/min	100 m/min	200 m/min	50 m/min	100 m/min	200 m/min	50 m/min	100 m/min	200 m/min

<u>Forming of the cutting tool.</u>

The cutting angles of high-speed steel (HSS Co5) turning tool have been determined on the basis of technical tables. The relief angle: $\alpha_0 = 10°$, the rake angle: $\gamma_0 = 5°$. The grinding of turning tool was carried out on profile-grinding machine using diamond grinding wheel. The ready made turning tool can be seen in Figure 5.
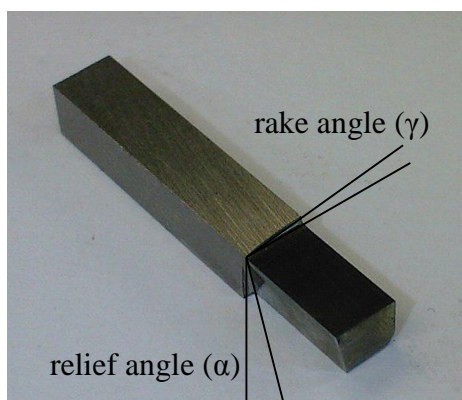
Figure 5. The bit of turning tool used.

3. TEST RESULTS AND THEIR EVALUATIONS

We have measured two-way forces during tests. The tangential-directional main cutting force and the axial feeding-directional force. We have grouped the materials by depth of cut, by feeding within on these by cutting speed. Unite these in one file we have got four series main cutting force and the same series feeding-directional cutting force diagrams. We have made one-one diagram by parameter from these. Figure 6. and 7. show one-one sample diagram. The cutting force given (main or feeding directional) as well as the feeding (f[mm/rev.]), depth of cut (a[mm]) and the cutting speed (v[m/min.]) appear in the diagram title. The force values [N] given appear on the vertical axis, the cutting time [s] appears on the horizontal axis. We have presented all four materials in one diagram, so it can be well comparing that at same cutting parameters how great force befalls onto the cutting tool at various materials. Each colour marks one material according to mark explanation under the diagram. Continuous line shows the test results. The dotted line shows the average during measuring time given. Its value can be seen beside the line.
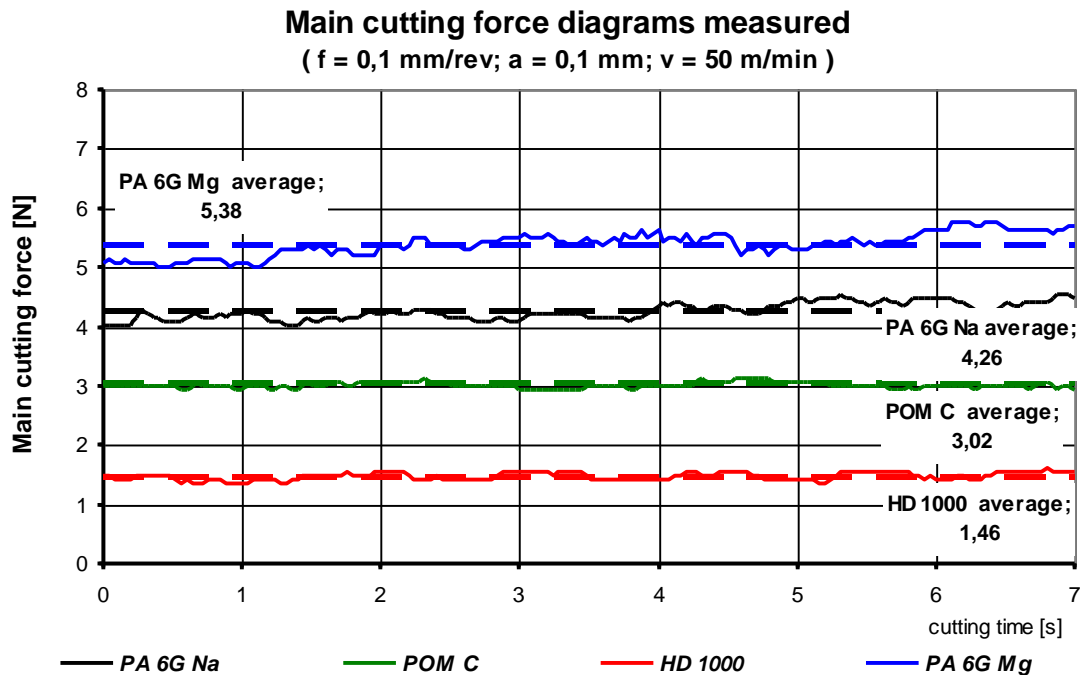
Figure 6. Main cutting force value at materials tested at cutting parameters given.
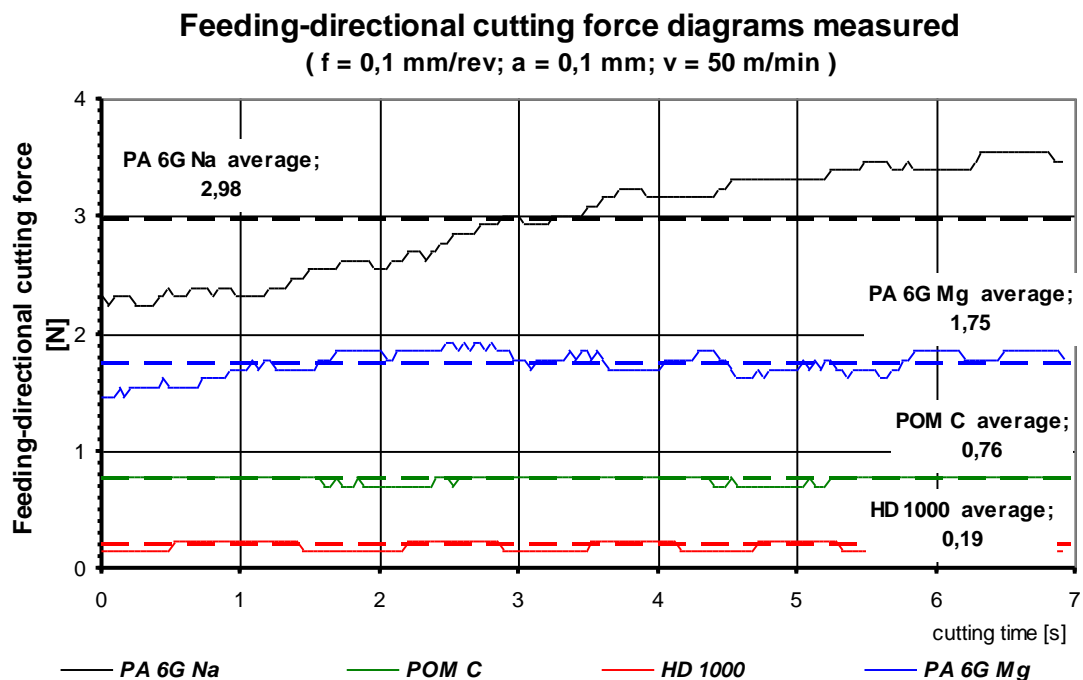
Figure 7. Feeding-directional cutting force at materials tested at parameters given.

As each workpiece tested had the same directions the measuring time period was continuously changing because of various feeding and cutting speed values. Therefore we have 7 s –time taken into account at most measuring. In case of certain cutting parameters this value could not be reached, therefore at these parameters the cutting time was reduced to 4 at one case 2 s respectively. After putting down into each diagram we have presented the main –and feeding- directional cutting forces in the function of depth of cut and of feeding from average values belonging to parameters given according to the following samples (Figure 8 – 11).
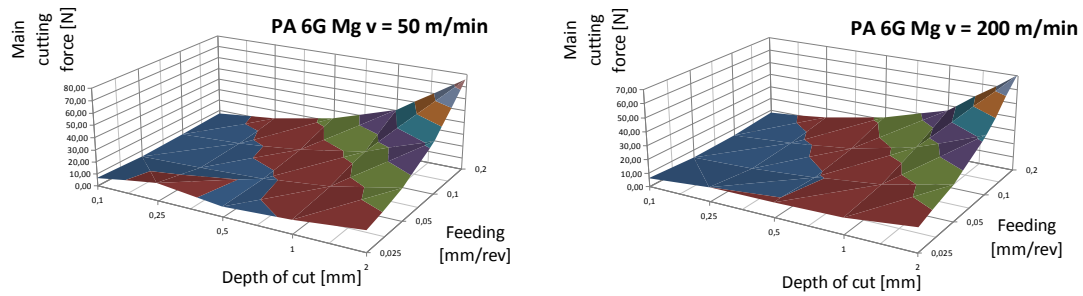
Figure 8. The value of main cutting force in the function of depth of cut and of feeding, PA 6G Mg
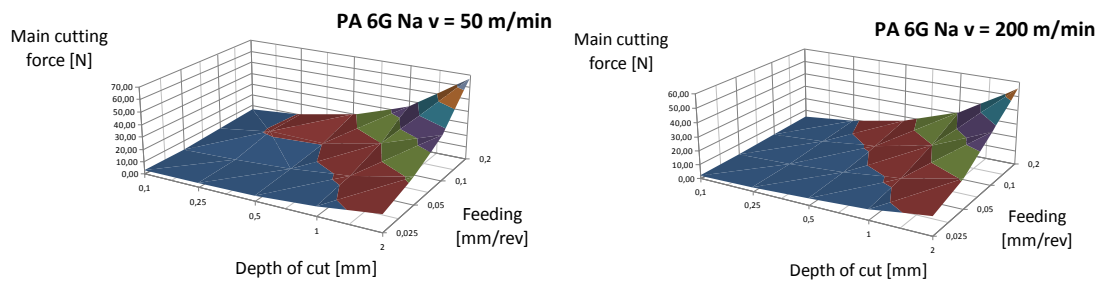
Figure 9. The value of main cutting force in the function of depth of cut and of feeding, PA 6G Na
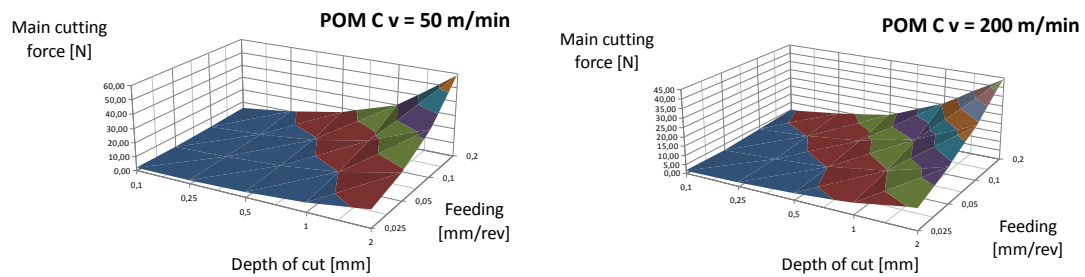
Figure 10. The value of main cutting force in the function of depth of cut and of feeding, POM C
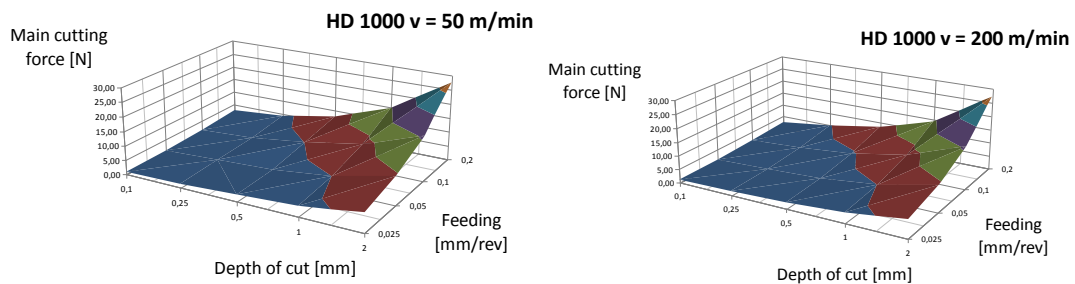
Figure 11. The value of main cutting force in the function of depth of cut and of feeding, HD 1000

Specific cutting resistance.

Cutting materials the specific cutting resistance (k_s) is an important factor. The following sample shows its change in the function of depth of cut and of feeding (Figure 12).
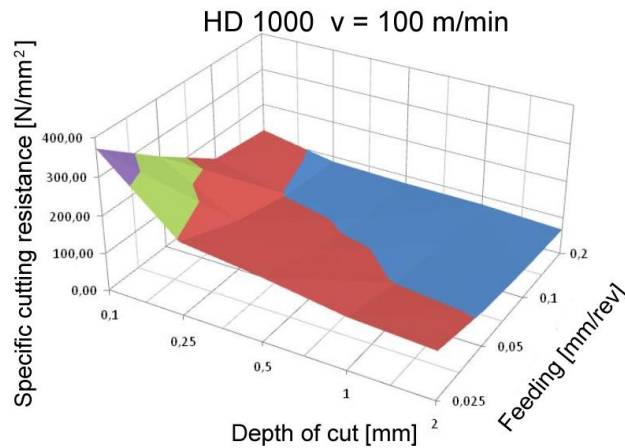
Figure 12. The value of specific cutting resistance in the function of depth of cut and of feeding, HD PE 1000

According to the relation to be found in the literature the main cutting force is the function of the specific cutting force (or resistance) and of the chip area. As during measuring we have also measured the main cutting force, the chip area was given because of parameters set, so the value of the specific cutting force can be got by transposing the original relation.

$$F_v = k_s \cdot A = k_s \cdot a \cdot s \Rightarrow k_s = \frac{F_v}{a \cdot s} \rightarrow \left[\frac{N}{mm^2} \right]$$

The material tested and the cutting speed used occur in the title of sample diagram. Beside the depth of cut and feeding the specific cutting resistance (y-axis) in N/mm^2 unit can be found on the datum lines.

Chip pictures (photographs)

The chip removed during machining have been collected and photographs have been made. Based on these the types of chips formed can be examined. Figure 13. shows the chip pictures (splint, continuous chip, transitional platelike, elemental) in the function of feeding and depth of cut at 50 m/min cutting speed at POM C material. It can be established those parameters at materials in case of which chip type meets well the practical requirements.
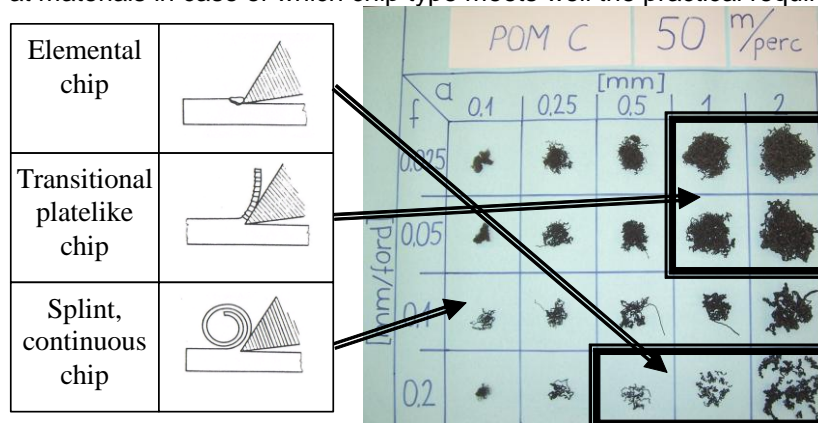
Figure 13. The forming of chip picture in the function of depth of cut and of feeding, POM C

4. SUMMARY

It can be established from the test results that PA 6G Mg –material proved to be the toughest from both the cutting force and the specific cutting resistance point of view. The specific cutting force decreases substantially by increasing the cutting parameters (feeding, depth of cut). Taking into account the chip type formed it can be said that it is a hardly machineable material. Using the lower feeding (0.025 mm/rev) is suggested.

The PA 6G Na polymer shows a little lower toughness from the cutting force point of view, on the other hand in case of the specific cutting force it shows already more important change, approximately it reduces into third. Its value with the increasing of feed and depth of cut does not decrease such amount as in case of Mg-containing material. At cutting the small feeding (0.025 mm/rev) and the greater depth of cut (1-2 mm) is suggested.

At POM C –material could be observed the further decrease of cutting – and specific cutting force. Both decreased into half approximately, but in case of latter, similarly finding PA 6G Na –material, neither here decreased such amount with increasing the feeding and depth of cut as at Mg –containing material. From the standpoint POM C had got the most favourable chip picture among the engineering plastics taking part in tests. Comparing to PA 6G –materials here is suggested the use of greater feeding with increasing depth of cut which results more favourable chip type forming, too.

The smallest cutting forces can be measured at HD 1000 –polymer. It can be well observed at the value of the specific cutting resistance that this material has got the lowest toughness. From the standpoint of turning this is not a favourable material as regarding the chip type formed is split (continuous chip) in great part of cases tested. The analysis made can be well used in practice. The favourable values of feeding, of depth of cut and of cutting speed, within the ranges tested, can be set for cutting materials tested and for the favourable chip picture.

REFERENCES

[1]   Antal – Fledrich – Kalácska – Kozma: Műszaki műanyagok gépészeti alapjai, Műszaki műanyagok gépészeti alapjai, Minerva-Sop Bt. Sopron, 1997

[2]   Angyal B., Dobor Lné., Palásti K. B., Sipos S. – A Forgácsolás és Szerszámai – Műszaki Könyvkiadó, Budapest, 1988

[3]   Frischerz, Dax, Gundelfinger, Häffher, Itschner, Kotsch, Staniczek – Fémtechnológiai Táblázatok – B+V Lap- és Könyvkiadó Kft., 1997

[4]   Dr. Kalácska Gábor - Műszaki Műanyag Féltermékek Forgácsolása - Quattroplast Kft., Gödöllő, 2005.

[5]   Nagy P. S. – Szerszámgépek, gyártórendszerek – BDMF jegyzet, Budapest, 1997

[6]   www.quattroplast.hu

HOW DESIGN QUIRKS AND CONDITIONS OF USE CONSPIRE TO STRUCTURAL FAILURE – A CASE STUDY

W. Ost[1], J. Van Wittenberghe[1] and P. De Baets[1]

[1] Ghent University, Laboratory Soete, Belgium

Abstract Sometimes designers introduce a number of quirks in their design, either due to a preference for certain technologies or practices or under the influence of the policies in the companies they work for. While most of the time these quirks are harmless, sometimes they can, either in themselves or in combination with the conditions in which the design is used lead to failure. In this paper a case is discussed in which a designer used a quirky solution of lengthening an existing design of a 40ft. freight container to 45ft.. While the design in itself was not fundamentally flawed, it proved to be incompatible to the handling equipment still in use at most seaports.

Keywords Failure, container, design, conditions of use

1   INTRODUCTION

Worldwide the most popular freight containers are either 20 feet long (hence the term TEU or twenty feet equivalent unit) or 40 feet long. For transport by road in the European Union however the preferred size for freight containers nowadays is 45ft. as this matches the maximum trailer length prescribed by the Highway Code. These 45ft. freight containers however are ill matched to the equipment use to handle freight containers at seaports (designed to handle either 20ft. or 40ft. freight containers). In this case study the failure of a certain type of 45ft. container is discussed. Failure of the freight container resulted from the combination of a design quirk with ill-matched handling equipment.

2   THE ACCIDENT

Figure 1. Overview of the failed freight container

During the handling of a 45ft. container loaded with about 20 tons of bottled mineral water the floor of the container gave way, spilling its contents on the quay floor (see figure 1). The container was not the standard type with corrugated sheet metal sides, but a so called "curtain sider" container in which both sides of the container were equipped with sliding curtains, enabling the easy loading and unloading of the container.

3   THE INVESTIGATION

3.1   Freight container design

The container was of recently introduced type, which design was based on the time proven design of a 40ft. curtain sider container. To lengthen the container to 45ft., sections of 2.5ft. were added to the front and the back of the existing 40ft. design. The curtains used at both sides of the container were kept at a length of 40ft. and two doors of 2.5ft. were added at both ends of the container. To ensure that the container could be handled using equipment designed for 40ft. freight containers the corner castings of the 40ft. design were retained and extra corner castings at both ends were added to ensure that the 45ft. container could be locked onto trailers designed for 45ft. freight containers.

This resulted in the design shown in figure 2 and 3. In these figures the freight container is shown on a 40ft. handling trailer called a "MAFI" after the company manufacturing these trailers;

Figure 2. View from the front of a container of the same type, on a 40ft. handling trailer.

3.2   Design quirks

When lengthening the design of the container from 40ft. to 45ft. the designer considered that the freight container would be handled mostly with the original castings interspersed by 40ft. (see figure 4). Consequently the extra 2.5ft. of container floor added at the front and the back were manufactured considerably weaker (and lighter) than the original 40ft. container floor in between. To make lifting the container at the 40ft. castings possible the steel doors were strengthened with a vertical girder and equipped with pins at the bottom and at the top of the door, which engaged with the 40ft. castings in the roof and the floor of the container, thus transferring the weight placed on the floor towards the 40ft. castings in the roof.

Due to this design strategy the weight of the container could be limited (the front and back 2.5 floor and roof additions were relatively light). However there was some danger inherent to this design – as the girders in the doors carried the load placed on the floor the doors should always be closed when lifting the container from the top. To notify handlers of this a warning sign to this effect was placed on all four doors.

Figure 3. View from the back of a container of the same type on a 40ft. handling trailer
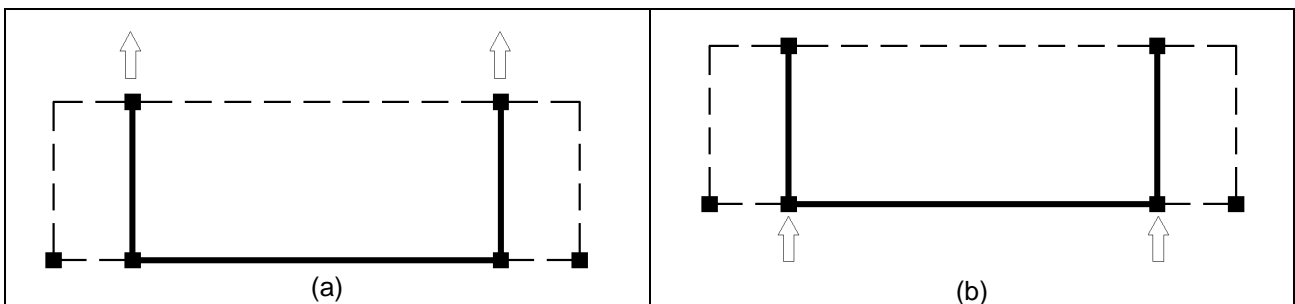
Figure 4. Loading situation considered in the design (a) lifting at the 40ft. castings (b) supported at 40ft. castings.

3.3   Conditions of use.

The accident occurred when the container was lifted from the top at the 40ft. castings (see figure 1). Initially some concerns were raised whether the side doors were closed and locked when the container was lifted from the top. The operator of the handling equipment was adamant that the side doors were closed. This was backed up by pictures taken immediately after the accident showing that the doors (which weren't wrenched open in the accident) were still closed and that the pins at the top of the door were still engaged with the castings (see for example figure 5).

Nevertheless the way in which the container floor failed at the back side of the container (see figure 6) clearly indicate the side doors failed before the floor dropped out of the container. The 2.5ft. floor addition is twisted upwards and the beams in the floor are halfway torn from the 40ft. and 45ft. castings.

Figure 5. Top of one of the side doors (view from inside container) showing the top pin still connected to the 40ft. casting.

Figure 6. View of the back of the floor.

The reason for this became evident when the doors were inspected. The pins connecting the bottom of the doors to the 40ft. castings in the floor of the container were badly bent. Something similar occurred to the pins of the side doors at the front of the container: the bottom pin of the right side door was missing and the bottom pin of the left side door was badly bent. Corrosion of the fracture faces indicated that the tears at the connection of the bottom pins to the doors shown in figure 6(b) had occurred sometime prior to the accident. Similar corrosion on the fracture surface of the missing pin shown in figure 7 proved that this pin had already gone missing before the accident, explaining the fact that this pin could not be retrieved at the site of the accident.

| (a) | (b) |

Figure 6. View of the bottom pins at the of the side doors at the back of the container: (a) bottom pin of right side door (b) bottom pin of left side door.

Figure 7. View of the front side of the container. Notice the bottom pin of the right hand side door is missing.

Copyright © 2010 by Labo Soete

Due to the failure of the bottom pins of the doors transferred the load from the doors to the 2.5ft. addition on both ends of the container. As these additions were never designed to withstand this load they failed and the floor dropped out of the container.
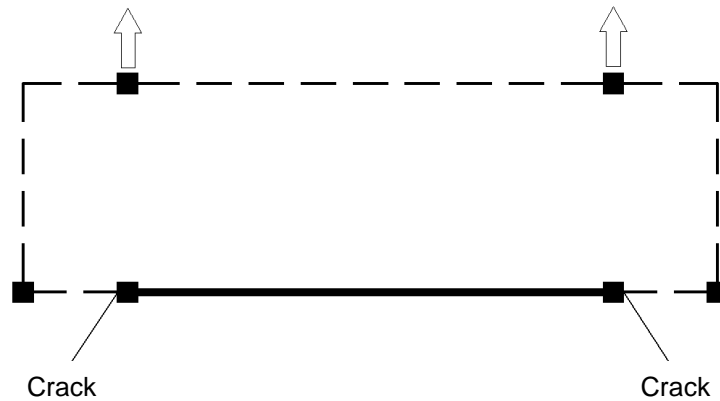
Figure 8. Schematic overview of the condition of the container at the time of the accident. Due to pin failure the doors did not carry any load.
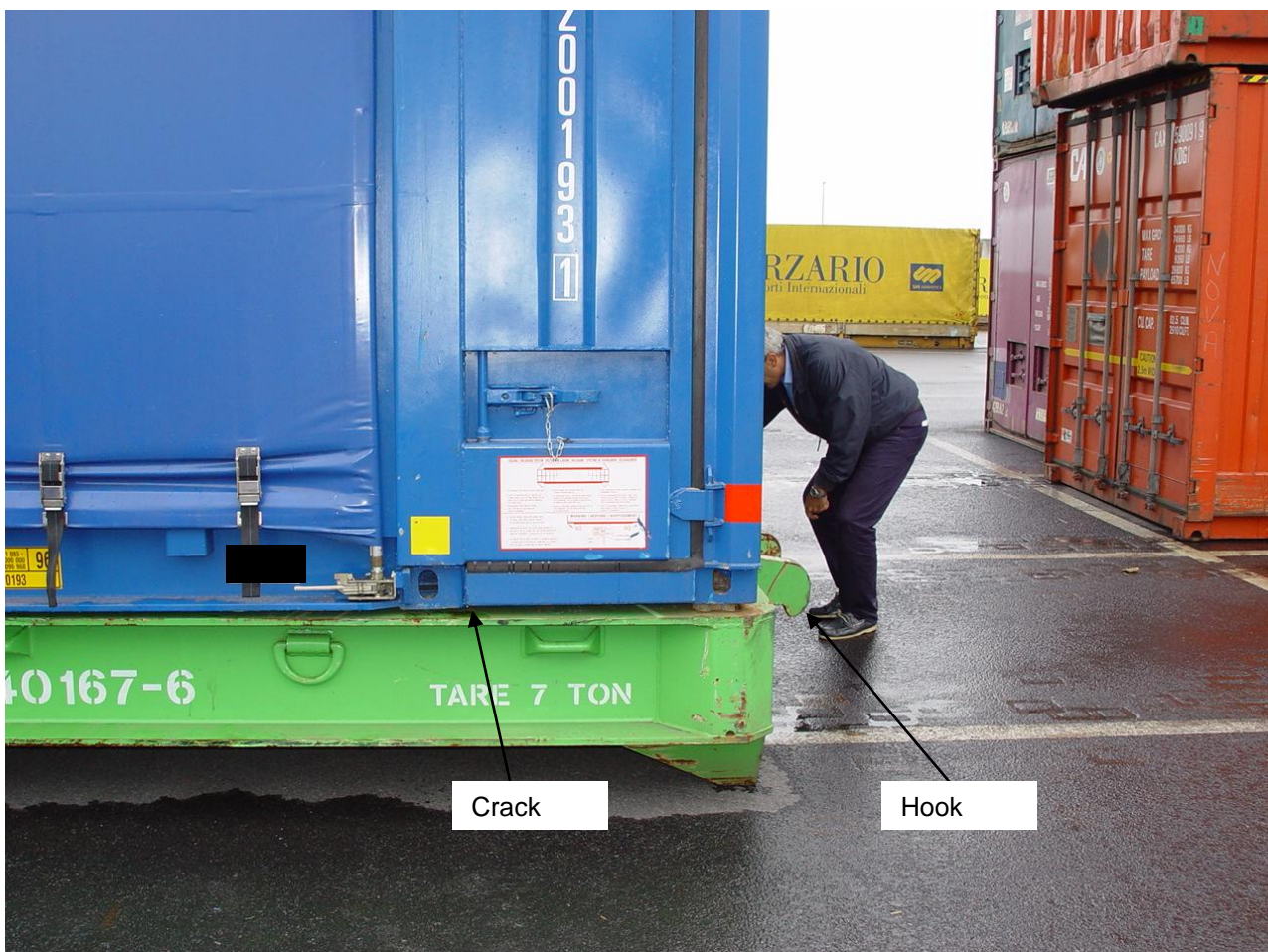
Figure 9. Side view of a similar container on a handling trailer – notice placement on the trailer so that hook is available.

3.4   Solution

So it is clear that the failure of the floor resulted from the failure of the pins. This resulted from a design error. At the time of the accident one of the bottom pins was already missing and the one other was half torn from the bottom of the door.

However this design flaw could be easily remedied by strengthening the connection of the pin to the door. But just locally strengthening the doors and the pins will not produce a good design. This is illustrated by the condition of another container which was in use on the quay. Figure 9 shows this container on a handling trailer. First notice that the floor of the 2.5ft. addition contains a large crack which will in a short

time frame lead to failure (see detail in figure 10). Secondly notice the placement of the container on the handling trailer. The hook at the front of the handling trailer needs to be available to lift this end of the trailer off the ground.

This means that the 2.5ft. floor additions at both ends of the container can be carrying the full weight of the freight in the container and that the design assumptions of figure 4 are erroneous. The load cases shown in figure 11 should have been considered in the design stage.

Figure 10. Detail of crack in floor beam of 2.5ft. addition just next to 40ft. casting.
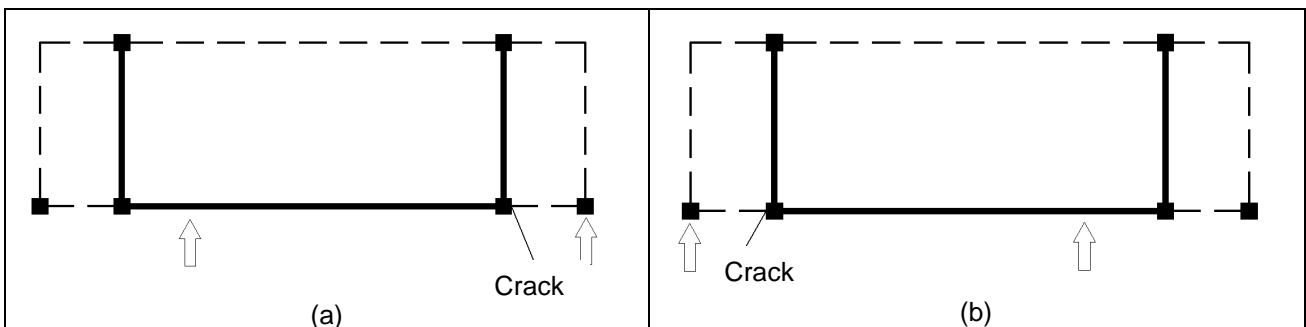
Figure 11. Load situation when the 45ft. freight container is placed on a 40ft. handling trailer. Container will overhang the trailer by 5ft. at one end.

4   CONCLUSIONS

Although the design of the freight container exhibited a number of flaws (too weak connections of locking pins to side doors) the failure of these containers was ultimately produced by a quirky design in combination with the conditions under which these containers were used. When a loaded 45ft. container was placed asymmetrically on a 40ft. handling trailer this introduced stresses in the 2.5ft. floor overhang which were not taken into account in the design of the freight container. A redesign of the container floor is necessary. The floor should be able to withstand the stresses introduced by the load when the container is only supported at both 45ft. corner castings.

FINITE ELEMENT SIMULATION OF SPRINGBACK IN TRIP 780 ADVANCED HIGH STRENGTH STEEL

M. Safaei, W. De Waele, M. Abdel Wahab, P. De Baets

Ghent University, Laboratory Soete, Belgium

Abstract This paper discusses the effects of mechanical anisotropy of TRIP 780 advanced high strength steel on the springback observed in sheet metal forming. A series of finite element analyses using the Hill's 48 transverse anisotropic yield model and a standard U-shape forming test based on the NUMISHEET'93 benchmark has been performed. A comparison of springback angles for different orientation of sheet strips relative to the rolling direction is presented. The results show that the amount of springback changes with respect to the orientation of the test samples.

Keywords Advanced High Strength Steel, Finite element model, Springback

1   INTRODUCTION

As new materials with higher strength are introduced to industry, the accurate simulation of springback in sheet forming becomes more essential. Springback has always been a focus of research in sheet metal forming. In spite of advances in finite element techniques, an accurate prediction of springback is still unsatisfactory. In this paper, the springback behavior of one type of advanced high strength steels, Transformation-Induced Plasticity (TRIP) steel, has been numerically investigated. Advanced high strength steels (AHSS) exhibit higher strength and formability, even when compared with conventional high strength steels. The only method of production of AHSS is through controlling the cooling rate from austenite or austenite plus ferrite phase; either on the runout table of the hot mill or in the cooling section of the continually annealing furnace [1]. As with all high-strength steels, springback is a concern with AHSS. Without appropriate compensation, the higher strength of the AHSS grades usually leads to more springback compared to conventional HSS.

Previous studies applied finite element technique on the evaluation of springback. For example, Azraq et al used finite elements for prediction of final shape and springback of TRIP 800 in stamping process [2]. Yuen noticed that different unloading schemes will affect the accuracy of the springback prediction [3]. Chen et al [4] applied finite elements and design of experiments to investigate the effects of variations in material, blank holder force and friction on the springback variation for an open-channel shaped part made of a dual phase (DP) steel. Panthi et al [5] carried out their simulation using a indigenous finite element code for prediction of springback in a typical sheet metal bending process. In the present work, finite element analysis of springback on the base of NUMISHEET'93 U-shape forming test [6] is presented.

2   FINITE ELEMENT MODEL

2.1   Geometric Model

The U-shaped cross-section introduced in NUMISHEET'93, shown Figure 1, was selected for this study [7]. The geometry used for springback measurement is shown in Figure 2. Springback assessment is performed by measuring the angles θ_1 , θ_2 and the radius ρ; Where θ_1 is the angle between the line "ab", (starting from point "a" in the workpiece, 15mm above the lowest part of the formed sheet metal, to point "b" , intersection of a circle of 35mm radius and a center coinciding with point "a" with the sidewall of the workpiece) and any horizontal line (ox). Other measurements were performed by measuring the angle between "ab" with the straight line "ef", and measuring the radius of a circle with an arc fitting the "acb" curve of the sheet strip, for θ_2 and ρ, respectively.

The die components have a width of 41 mm, the workpiece has a width of 39 mm and is centered with respect to the center line of the die.
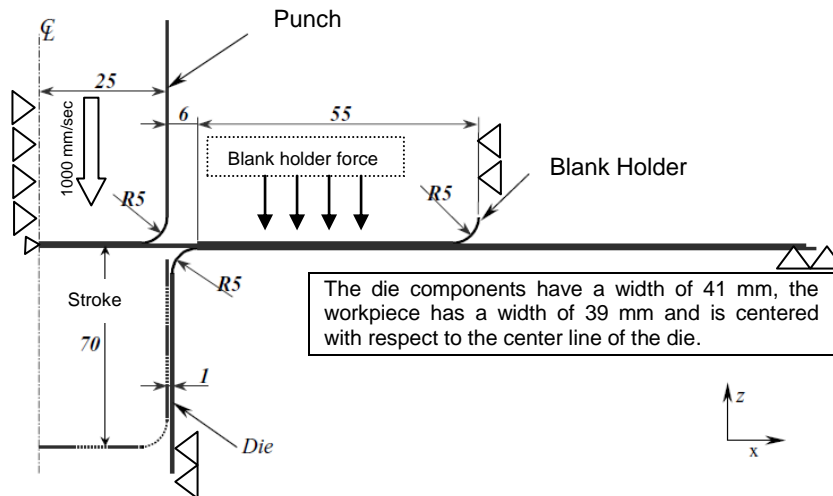
Figure 1. The NUMISHEET'93 benchmark geometry used for finite element springback analysis; Units: mm [7]
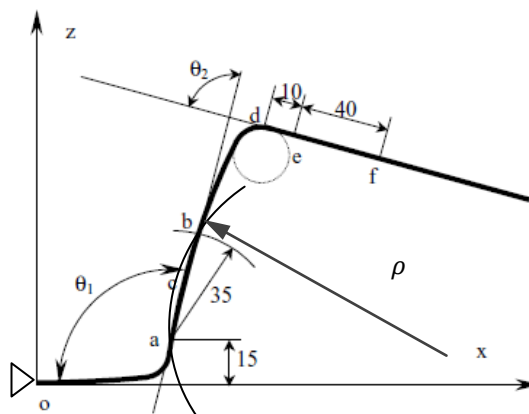
Figure 2. Variables used for springback measurement; Units: mm [7]

2.2 Material Model

The true stress versus true strain diagram of the sheet metal TRIP 780 for different orientations with respect to the rolling direction is shown in Figure 3 [8]. The change of orientation of polycrystalline grains due to the rolling process is the main reason of directional dependency of yield in the rolled sheet metals [9]. The flow stress equation of the TRIP 780 in the rolled direction and at a strain rate of $1.67E-3$, obtained according to the International Standard ASTM E 646-07, can be described as a Hollomon power law as presented in Equation 1.

$$\bar{\sigma} = 1444\bar{\varepsilon}^{0.208} \tag{1}$$

Various yield functions have been used in the literature [10-13]. In this study, the Hill's 48 transverse anisotropic yield model has been used to describe the material's anisotropic behavior. This equation assumes materials with three orthogonal axes of anisotropy, x, y, and z about which the properties have two-fold symmetry. The yz, zx, and xy planes are planes of mirror symmetry. In a rolled sheet it is usual to take the x-, y-, and z-axes as the rolling direction, the in-plane transverse direction, and the sheet-plane normal. The theory also assumes equality of the tensile and compressive yield strengths in every direction

[9]. Hill's 48 quadratic anisotropic yield function is expressed by equations 2 to 6 and its anisotropy ratios (width to thickness strain ratios) for the TRIP 780 material are presented in Table 1.
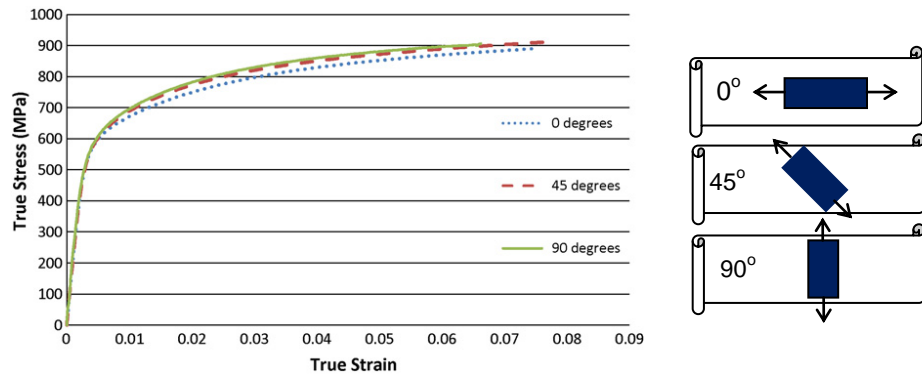
Figure 3. True stress- strain for TRIP 780 [8]

$$F\left(\sigma_{yy} - \sigma_{zz}\right)^2 + G(\sigma_{zz} - \sigma_{xx})^2 + H\left(\sigma_{xx} - \sigma_{yy}\right)^2 + 2L\tau_{xy}{}^2 + 2M\tau_{zx}{}^2 + 2N\tau_{xy}{}^2 = k^2 \tag{2}$$

$$F = \frac{R_0}{R_{90}(1 + R_{90})} \tag{3}$$

$$G = \frac{1}{1 + R_0} \tag{4}$$

$$H = \frac{R_0}{1 + R_0} \tag{5}$$

$$N = \frac{(R_0 + R_{90})(1 + 2 * R_{45})}{2R_{90}(1 + R_0)} \tag{6}$$

Where $\sigma_{xx}, \sigma_{yy}, \sigma_{zz}, \tau_{xy}, \tau_{zx}$ and τ_{xy} are the components of the Cauchy stress tensor defined in the orthotropic frame and F, G, H, L, M and N are the Hill coefficients that define the anisotropy and the R_0, R_{45} and R_{90} are the Lankford coefficients defined as the ratio of transverse to thickness strain in sheet strips with 0, 45 and 90 degree material orientation relative to the rolling direction, respectively.

Table 1. Anisotropy ratios for TRIP 780 [2]

R_0	R_{45}	R_{90}	$\bar{R}$	ΔR
0.498	0.872	0.583	0.70625	−0.3315

The coefficients of $\bar{R}$, normal plastic anisotropy, and ΔR ,planar plastic anisotropy, mentioned in Table 1 are:

$$\bar{R} = \frac{R_0 + 2R_{45} + R_{90}}{4} \tag{7}$$

$$\Delta R = \frac{R_0 - 2R_{45} + R_{90}}{2} \tag{8}$$

2.3 Finite Element Simulation

In the finite element code, elastic-plastic and rigid types of material were set for workpiece and dies (punch, blank holder and die), respectively
The geometries of dies and sheet strip were designed using SolidWorks® [14] and the CAD files used as the input geometries for the finite element code. Whereas the dimensions of the blank were $300 * 39 * 0.78 \ mm^3$, because of symmetric geometry of the blank only 150 mm of the sheet length was modeled. For more accurate results, a mesh with 40,000 tetrahedral elements was assigned to the workpiece (Figure 4).

For illustration purpose and a better understanding of position of the blank, whole geometry of the blank is shown in Figure 4. A blank holder force of 5kN was included and the displacement speed of the punch was simulated as 1000 mm/sec in the negative z- direction. Contact between workpiece and rigid dies was modeled using a 0.05 coulomb friction. The used coefficient of friction for specific sheet metal forming conditions, using lubrication and coated dies, produces reasonable results [15].
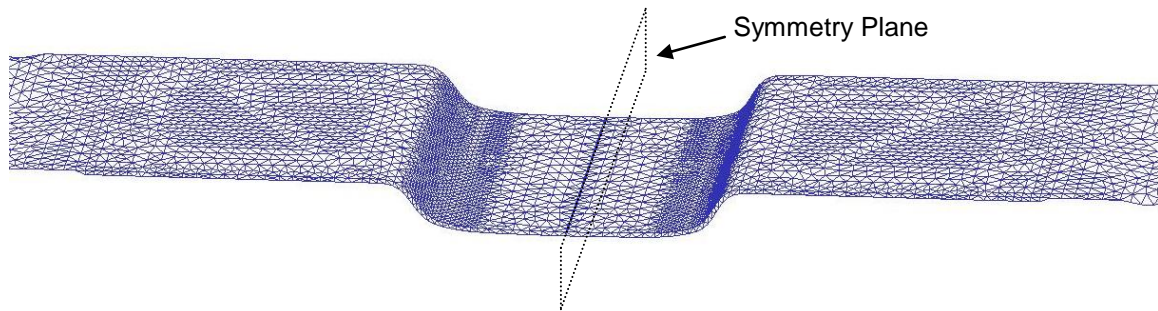
Figure 4. Tetrahedral mesh assigned to workpiece (due to symmetrical geometry of the part, just the left part of workpiece was used for simulation)

3   RESULTS

For an ideal sheet metal formed part, no springback is desired. The wall of the U-shape is expected to be flat ($\rho \rightarrow \infty$), and the angles θ_1 and θ_2 are desired to be 90°. Previous research [7, 16] concluded that as the yield stress increases, the elastic return increases. Figure 3 shows that the yield stress slightly increases with an increased angular deviation from the rolling direction. Therefore the amount of springback is expected to increase as the rolling direction increases (Figure 5). This conclusion can be observed in Table 2. This general result is supported by other research for different high strength steels [7]. The results show that with increase of springback, ρ decreases whereas θ_1 and θ_2 increase (Table 2).

Figure 5. Position of die, punch, blank holder and workpiece before and after load releasing, left to right respectively

To simulate the elastic recovery of the workpiece, after the final step of forming and achieving the desired punch movement, unloading steps were done. During these steps, the contact between the workpiece and rigid parts diminishes and finally all the internal stress components of the workpiece are equilibrated and the springback can be measured (Figure 6).

Table 2. Numerical results of springback

	θ_1	θ_2	ρ (mm)
0°	87	87	132
45°	88	88	128
90°	92	95	63
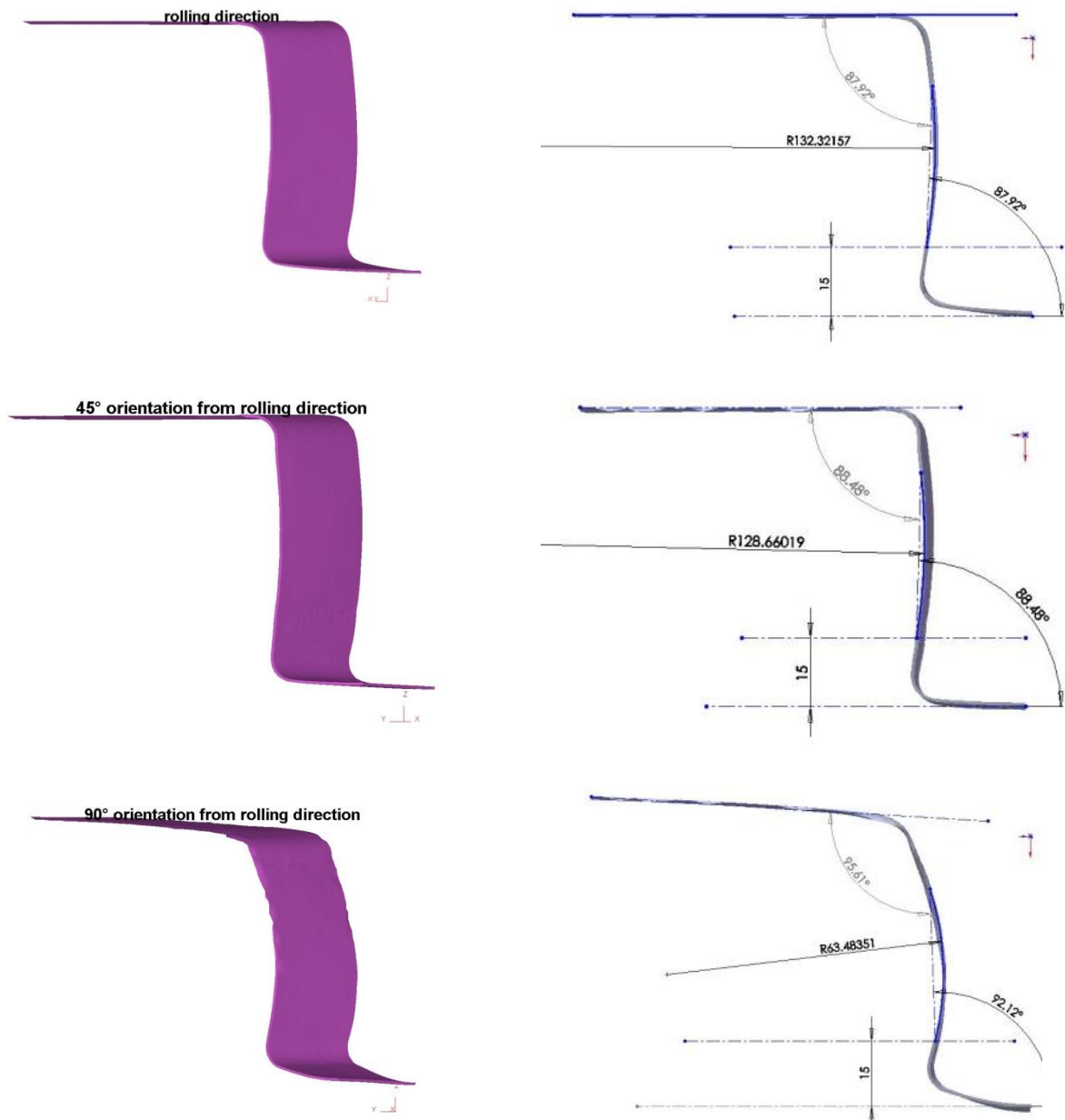
Figure 6. Finial shape after equilibration of internal stresses in blank strips with 0, 45 and 90 degree direction from rolling direction from top to down respectively

4   CONCLUSIONS

In the current study the effects of mechanical anisotropy of TRIP 780 on the springback was discussed. A series of finite element analyses using the Hill's 48 transverse anisotropic yield model and a standard U-shape forming test based on NUMISHEET'93 has been performed. The results show that as the yield stress increases with increased angular deviation from the rolling direction, the elastic return increases. The variations in springback from the 0° to 90° material orientations show considerable variation. These results clearly show how anisotropy contributes to springback and the possibility of observing these effects using finite element analysis. The next step of the current project will be the implementation of other advanced anisotropic yield functions and mixed isotropic-kinematic hardening rules into finite element code and comparison with experimental results.

5   NOMENCLATURE

θ_1 Angle between ox and ab (Figure 2).

θ_2 Angle between ab and ef (Figure 2).
ρ Radius of a circle through a, b and c (Figure 2).
a 15 mm from ox (Figure 2).
b 35 mm from point a (Figure 2).
c Middle point of the straight line ab (Figure 2).
d End of the Die's curvature (Figure 2)
e 10 mm from d (Figure 2).
f 40 mm from e (Figure 2).

6   ACKNOWLEDGEMENTS

7   REFERENCES

[1]   *Advanced high strength steel (AHSS) application guidelines.* www.worldautosteel.org,(Version 4.1), June 2009.
[2]   S.A. Azraq, et al., *Springback prediction with FEM analysis of advanced high strength steel stamping process*, in *Intelligent Production Machines and Systems*, Elsevier Science Ltd: Oxford. p. 264-269, 2006.
[3]   W.Y.D. Yuen, *Springback in the stretch-bending of sheet metal with non-uniform deformation.* Journal of Materials Processing Technology, 22(1): p. 1-20, 1990.
[4]   P. Chen and M. Koç, *Simulation of springback variation in forming of advanced high strength steels.* Journal of Materials Processing Technology, 190(1-3): p. 189-198, 2007.
[5]   S.K. Panthi, et al., *Finite Element Analysis of sheet metal bending process to predict the springback.* Materials & Design, 31(2): p. 657-662,
[6]   *NUMISHEET'93*, in *Proceedings of the second international conference of numerical simulation of 3-D sheet metal forming processes*, Isehara, Japan, 1993.
[7]   C. Gomes, O. Onipede, and M. Lovell, *Investigation of springback in high strength anisotropic steels.* Journal of Materials Processing Technology, 159(1): p. 91-98, 2005.
[8]   A. Nasser, et al., *Determination of the flow stress of five AHSS sheet materials (DP 600, DP 780, DP 780-CR, DP 780-HY and TRIP 780) using the uniaxial tensile and the biaxial Viscous Pressure Bulge (VPB) tests.* Journal of Materials Processing Technology, 210(3): p. 429-436,
[9]   W.F. Hosford and R.M. Caddell, *Metal forming : mechanics and metallurgy.* 2007, New York, NY: Cambridge University Press, 2007.
[10]   D. Banabic, et al., *An anisotropic yield criterion for sheet metals.* Journal of Materials Processing Technology, 157-158: p. 462-465, 2004.
[11]   F. Barlat, D.J. Lege, and J.C. Brem, *A six-component yield function for anisotropic materials.* International Journal of Plasticity, 7(7): p. 693-712, 1991.
[12]   R. Hill, *Constitutive modelling of orthotropic plasticity in sheet metals.* Journal of the Mechanics and Physics of Solids, 38(3): p. 405-417, 1990.
[13]   P. Van Houtte, *Application of plastic potentials to strain rate sensitive and insensitive anisotropic materials.* International Journal of Plasticity, 10(7): p. 719-748, 1994.
[14]   *SolidWorks*, Dassault Systems, SolidWorks Corp: Santa Monica,CA.
[15]   B.H. Lee, Y.T. Keum, and R.H. Wagoner, *Modeling of the friction caused by lubrication and surface roughness in sheet metal forming.* Journal of Materials Processing Technology, 130-131: p. 60-63, 2002.
[16]   J.J. Stien. *The effect of process variables on sheet metal springback*. in *Proceedings of the International Body Conference and Exposition.* Detroit, USA, 1998.

THE COMPARISON OF RAPESEEDS' OILS FROM HYBRID AND OPEN-POLLINATED VARIETIES BY THEIR HEATING VALUES IN THE ASPECT OF DIESEL UTILIZATION

Eszter Sárközi, László Jánosi
Institute for Mechanical Engineering Technology,
Faculty of Mechanical Engineering, Szent István University, Gödöllő, Hungary
www.geti.gek.szie.hu

Abstract The rape is one of the suitable plant species for biofuel feedstock in Hungary. Currently there are over 100 admitted rape sorts recorded in Hungary and their oils' application as biodiesel proposes new aspects of evaluation. From references it is noticeable that there are differences in the physical and chemical properties of the various rape sorts' oils and rapeseed-methyl-esters. Our aim is to analyze the differences in the quality of the various rape sorts' oils and to determine the most appropriate rape sort in the viewpoint of technical utilization. In the course of present research work we have measured the heating values of 21 various rapesorts' oils -12 from open-pollinated varieties and 9 from hybrids- and examined the differences between them. The outcome values dispersed in the range of the heating values found in the references, but the differences between them are less then the predicted, the variance and the coefficient of variation are reasonably slight, so the examined rape sorts' oils are similar in the viewpoint of the heating value. Furthermore, the energy content of the rapeseed oils is independent of the type (hybrid or open-pollinated variety) of the plant.
Keywords rapeseed oil, heating value, biofuel

1. INTRODUCTION

In the EU the energy sector for transport has two main challenges: the import dependency of energy sources and the environmental issues. Nearly all the energy used in the EU transport sector comes from oil and the import dependency of crude oil is extremely high, it was 83,7% for the EU-27 in 2006 [1]. Securing energy supplies for the future is not only a question of reducing import dependency, but including diversification of sources and technologies. The another important question is the environmental effects of the utilization of fossil fuels. In the EU transport is responsible for an estimated 21% of all greenhouse gas emissions that are contributing to global warming, and the percentage is rising. In order to meet sustainability goals, in particular the reduction of greenhouse gas emissions agreed under the Kyoto Protocol, it is essential to find ways of reducing emissions from transport [2].

Considering these issues the incremental utilization of renewable energy sources become a strategic aim of the European Union with the objectives of diversifying fuel supply sources, developing long-term replacements for fossil oil and reducing greenhouse gas emissions. Part of it the EU ordered that 5.75% (on energy content basis) of fossil fuels will be replaced by alternative fuels from renewable resources of the yearly consumption by 2010 [3].

One of the potential methods of the large scale biofuel production and utilization is the transesterification of the vegetable oils. Through the transesterification with glycerine secession the vegetable oil's triglycerid chains are decomposing and altering into vegetable oil-methyl-ester which is similar to the diesel oil in physical properties. In Europe one potential feedstock plant of biodiesel production is rape. Just in Hungary there are 104 sorts of rape in the National Sort Catalogue [4] and this number is increasing year by year. The differences of the various rape sorts were examined basically only by the aspect of agricultural utilization such as grain and oil yield; oil, glucosinolate and protein content [5]. New viewpoints of the evaluation have arisen with the industrial use of vegetable oils therefore our further object is to evaluate the different rape sorts's oil and determine the most appropriate rape sort for biodiesel stock in technical aspect.

The energy content is one of the most important parameters of the rapeseed oil in the viewpoint of use as biofuel feedstock. The energy content of the oil can be defined by the low heating value (LHV), which can be calculated from the measurable high heating value (HHV), the water content and the hydrogen content. In the references several data [6,7] can be found of the low heating value of the rapeseed oil from 36,87 MJ/kg [8] to 37,62MJ/kg [9]. In this work we examined the low heating value

of 21 rape sorts' oils in order to explore the differences between them and to rank the sorts by the oil's energy content.

2. EXPERIMENTAL METHODS

21 different rape sorts were chosen for this evaluation, all grown in Hungary. These are:

- open pollinated varieties (OPV): Bristol, Dante, Eleonora, GK Gabriella, GK Helena, GK Lilla, GK 704, GK 1103, Mohikán, Rasmus, Strauss, Viking
- hybrids: Artus, Baldur, Elektra, ES Saphir, Hybrid Star, Tenno, Titan, Trabant, Triangle.

The oilseeds were pressed separately by a small scale compactor. After the pressing the oils were filtered.

The high heating value (HHV) was measured by an IKA C2000 calorimeter by DIN 51900 standard. The water content was measured by a Mettler- Toledo HG73S Halogen Moisture Analyzer. The hydrogen content was measured by a WLD varioMacro CHNS elementar. The low heating value was counted from the following equation:

$$H_u = H_o - (wt\%_H * 9 + wt\%_{H2O}) * 0,2449 \tag{1.}$$

To compare the hybrid and open-pollinated group of rape sorts we have made a two sample t-test [10]. The null hypothesis of this test is that these two sample groups are similar. The assumptions of the application of the t-test are the following:

- the samples are independent,
- the groups has standard normal distribution,
- the deviation of the two groups are similar.

It can be stated that the samples of the two groups are independent as they are a parameter of different rapeseed oils. As the hybrid group has 9 and the open-pollinated group has 12 elements, a standard normal distribution test cannot be done, we can only presume that the distribution is normal.

The similarity of the deviations was verified by an F-test. In the course of the test we calculated an F_{calc} value by the (2.) formula which was compared with the corresponding critical value (F_{crit}) [10]. If F_{calc} is less than F_{crit}, then the deviations of the two groups are similar.

$$F_{calc} = s_{12} / s_{22} \tag{2.}$$

In the t-test a calculated t_{calc} value (3.) was compared with a critical t_{crit} value at a 5% rate of statistical significance. If t_{calc} is less then t_{crit} then the two groups are significantly different.

$$t_{calc} = \frac{x_{mean} - y_{mean}}{\sqrt{\frac{Q_x + Q_y}{n+m-2} * \frac{n+m}{n*m}}} \tag{3.}$$

3. RESULTS AND DISCUSSION

The results of the measurements of high heating value and hydrogen content are shown in Table 1 and Table 2 below, as well as the calculated low heating values. The water content is not shown as it was undetectable.

Table 1. Rapeseed oil properties

Rapesort	Hybrid (H) /Open-pollinated variety (OPV)	High heating value [MJ/kg]	Hydrogen content [wt%]	Low heating value [MJ/kg]
Artus	H	40,004	10,507	37,688
Baldur	H	40,024	10,832	37,636
Bristol	OPV	40,022	10,881	37,624
Dante	OPV	40,046	10,719	37,684
Elektra	H	40,114	10,705	37,754
Eleonóra	OPV	40,086	10,790	37,708
ES Saphir	H	40,004	10,638	37,659
GK 1103	OPV	40,049	10,803	37,668
GK 704	OPV	40,068	10,793	37,689
GK Gabriella	OPV	40,020	10,795	37,640
GK Helena	OPV	40,056	10,832	37,669
GK Lilla	OPV	40,034	10,661	37,685
Hybrid Star	H	40,007	10,659	37,658
Mohikán	OPV	40,129	10,888	37,729
Rasmus	OPV	40,094	10,833	37,706
Strauss	OPV	40,173	10,815	37,789
Tenno	H	39,967	10,886	37,567
Titán	H	40,114	10,956	37,699
Trabant	H	39,971	10,762	37,599
Triangle	H	39,929	10,724	37,565
Viking	OPV	40,013	10,947	37,600

Table 2. Rapeseed oil properties

	Minimum	Maximum	Mean	Variance	Coefficient of variation
High heating value [MJ/kg]	39,929	40,173	40,044	0,004	0,001
Hydrogen content [wt%]	10,507	10,956	10,782	0,012	0,010
Low heating value [MJ/kg]	37,565	37,789	37,667	0,003	0,002

The low heating value data are slightly greater than the values in the references, they stayed in the range between 37,56 and 37,78 MJ/kg with the mean of 37,67 MJ/kg.

We compared the heating value of the hybrid and open pollinated variety rapeseed sorts with t-test at 5% ratio of statistical significance. Firstly the adaptability of this method was checked by F-test. The result of the F-test can be found in the Table 3.

Table 3. The results of the F-test

	Variance of hybrid samples	Variance of OPV samples	F_{calc}	F_{crit} (p=5%)	Adaptability
Low heating value	0,00395	0,00246	1,602	2,95	**appropriate**

As the deviations of the two groups are the same due to the F-test, the t-test can be applied. The table 4. contains the results of the t-test.

Table 4. The results of the t-test

	Hybrid group			OPV group			t_{calc}	t_{crit} p=5%	Significant difference
	x_{mean}	m	Q_x	y_{mean}	n	Q_y			
Low heating value	37,647	9	0,032	37,682	12	0,0271	-1,43	2,093	NONE

On the basis of the results of t-test it can be stated that there is no significant difference in the low heating value between the hybrid and the open pollinated variety rapeseed oils.

4. CONCLUSIONS

From the results and discussion, the following conclusions can be declared:

1. The calculated low heating values of the 21 rape sorts stayed in the range which can be found in the references with the mean value of 37,67 MJ/kg. So the rapeseed oil has 12,3% less energy content then the diesel oil (with the high heating value 43MJ/kg), which means greater fuel consumption and less effective power using pure rapeseed oil or rapeseed-methyl ester than diesel engine fuel compared with fossil diesel oil.

2. As the variance and the coefficient of variation are very slight of the low heating value data, it can be declared that these rapeseed oils are similar in the viewpoint of hydrogen and energy content. Even so these slight differences are worth considering as the fuel consumption of the internal combustion engine is very important.

3. The hybrid rape sorts and the open-pollinated rape sorts are not different in their oils' heating values, so in the viewpoint of the energy content of the oils, it is indifferent that the rapeseed oil comes from hybrid or open-pollinated variety.

NOMENCLATURE

H_u	low heating value	MJ/kg
H_o	high heating value	MJ/kg
$wt\%_H$	hydrogen content	%
$wt\%_{H2O}$	water content	%
s_{12}	the variance of the first group (the higher value)	-
s_{22}	the variance of the second group (the lower value)	-
x_{mean}	the mean of the first group	-
y_{mean}	the mean of the second group	-
n	the number of the element of the first group	-
m	the number of the element of the second group	-
Q_x	the sum of squares of the first group	-
Q_y	the sum of squares of the second group	-

REFERENCES

1. European Commission, D.-G. f. E. a. T. (2009), EU energy and transport in figures, Statistical pocketbook 2009
2. COM(2006)34 (2006), An EU Strategy for Biofuels
3. Directive 2003/30/EC (2003), Directive of the European Parliament and Council on the promotion of the use of biofuels or other renewable fuels for transport

4. MgSzH- Hungarian Central Agricultural Office (2009), Szántóföldi növények nemzeti fajtajegyzék 2009. http://www.ommi.hu
5. MgSzH- Hungarian Central Agricultural Office (2005), Államilag elismert káposztarepce fajták eredményei 2005. http://www.ommi.hu
6. Vaitilingom, G., C. Perilhon, et al. (1998), "Development of rape seed oil burners for drying and heating." Industrial Crops and Products 7(2-3): 273-279
7. Hancsók, J. (2004), Korszerű motor- és sugárhajtómű üzemanyagok III. Alternatív motorhajtóanyagok. Veszprém, Veszprémi Egyetemi Kiadó
8. Labeckas, G. and S. Slavinskas (2006), "Performance of direct-injection off-road diesel engine on rapeseed oil." Renewable Energy 31(6): 849-863
9. AltIn, R., S. Çetinkaya, et al. (2001), "The potential of using vegetable oil fuels as fuel for diesel engines." Energy Conversion and Management 42(5): 529-538
10. Hajtman B. (1968), Bevezetés a matematikai statisztikába, Akadémiai Kiadó, Budapest

AERODYNAMICS OF FLUE ORGAN PIPE VOICING

D. Steenbrugge[1], P. De Baets[2]

[1]Hogeschool Gent, Belgium
[2]Ghent University, Laboratory Soete, Belgium

Abstract The objective of this paper is to investigate the possibility of giving useful interpretations of flue organ pipe voicing practices in terms of the aerodynamical and aeroacoustical behaviour of the pipes. An overview is first given of the current state of the knowledge on sound generation in flue instruments. After an introduction into the limited literature on voicing an scheme is presented as a possible framework to classify and characterize various voicing approaches. Use is made of dimensionless analysis to quantify the specific properties of voicing methods in terms of aerodynamic parameters rather than geometric data. It is concluded that such an analysis might be a useful tool to be able to better document and understand historic instruments and their genesis in order to better conserve them.

Keywords musical acoustics, aeroacoustics, aerodynamics, resonators, flue organ pipes, pipe organs, pipe voicing, organ building, conservation,

1   INTRODUCTION

Associating the term aerodynamics with an activity which always has been considered as the culprit of craftsmanship and artistry in organ building may seem a little respectless at first, yet it is a fact that organ pipes above all are aerodynamical systems. Particularly in flue organ pipes, and just like in all other flute instruments, essentially only the air inside is vibrating and the solid geometry 'merely' serves to exploit the instabilities inherent in the fluid so as to cause it to perform more or less periodic movements. As will be stressed in this paper however, the acoustic radiation, which is what the pipe is made for, turns out to be only a small side effect of these movements. This, together with the elusiveness of the vibrating medium, has obliged the instrument builders to develop empirical and highly individual approaches towards sound design typical and indispensable for the creation of true art. Interfering in this process by means of modern science is not going to make even better art, but opens other possibilities. Different kinds of art arise under the influence of modern science, for instance in sound design using current technologies, and it can benefit from results obtained by viewing traditional sound production using more recently obtained knowledge. Such is the case in sound synthesis based on physical models of traditional (acoustic) instruments. This paper however is intended to bring a contribution to another important application of modern knowledge, namely the conservation of art. Knowing how a work of art has been conceived and realised is an extremely important, although difficult to grasp aspect of art conservation. This is the very point where the individualistic nature of art has to face its ephemerality.

So the main argument in this paper will be that physics can be used as a tool in the analysis of the original instruments, with the goal to effectively describe and organize how their came into being, yet admittedly leaving the most subtle aspects to the expert. From a conservation point of view, this evolution is inevitable and throughout history evidence shows this kind of codification to be a necessary step in order to conserve at least some part of the original works. Books and music scores represent only a part of what the creator of their contents wanted to express, but they are a way of codification without which nothing at all would be left of his message after some time. Similarly, masterworks of all kinds deteriorate but if one can grasp and codify part of their genesis then at least part of them can survive.

The sciences of aerodynamics and aeroacoustics are relatively young, most of their fundaments having been developed from not much more than a century ago onwards. Accordingly it's not surprising that the art and craft of flue organ pipe voicing doesn't show any connection with them, not even in the great XIXth and XXth century 'theoretical' works on organ building [Töpfer 1888, Audsley 1905, Ellerhorst 1936]. The first contacts date from the 1960's were a number of physicists became interested in developing a scientific view on the drive mechanism of flue instruments. Since then a few research groups in the world have established themselves as leading the progress, but the main motivation has usually been the intention to build better physical models capable of reproducing naturally (mechanically) generated sound. Very little attention has been given to the potential applications in the field of conservation of musical instruments.

This paper will first give a very brief overview of current mainstream knowledge on the aerodynamics (and some acoustics) of flue instruments, thereby giving an idea of the basic operating principles. Next the stage is completely changed in order to give an idea of what has been published on the subject of flue organ pipe voicing. In the next part a scheme will be proposed as a possible framework within which to characterize

voicing techniques. This framework is based on aerodynamic rather than on geometric parameters. Finally some proposals and examples are given on how traditional voicing rules can be expressed and organized in terms of this framework and its associated aerodynamic parameters.

As this text is meant, by its interdisciplinary character, to be readable by a relatively broad audience, attention is given more to a qualitative presentation of concepts rather than a mathematical treatment. Various experimental results reproduced here as illustrations have been obtained from an experimental flue pipe with precision controllable geometry, the complete description and preliminary measurements obtained with it are reported elsewhere [Steenbrugge 2009].

2   AN OVERVIEW OF CURRENT KNOWLEDGE ON THE AERODYNAMICS OF FLUE INSTRUMENTS

2.1.   General principles

The mechanical operation of musical instruments is generally subdivided into a linear 'acoustic' part, essentially a resonator, and a non-linear part, which transforms a steady input flow of energy into more or less regular flow bursts [McIntyre, Schumacher & Woodhouse 1983]. These parts are interconnected and feedback loops can be identified which, under appropriate conditions, allow the system to perform periodic self-sustained oscillations. Based on this scheme the flue instrument is modelled on the one hand as a one-dimensional air column subject to specific boundaries allowing certain, more or less harmonic, passive resonances to develop, and on the other hand as an air jet flow interacting with the acoustic field of the resonator. The air jet exits through a long straight flue and is therefore considered to be more or less two-dimensional. This flue is generally positioned near one of the open ends of the air column. Consequently the air jet can exchange energy with the acoustic field and vice versa: the latter can strongly influence the behaviour of the inherently unstable air jet. In order for the air jet to produce flow bursts it needs a separating edge, the upper labium, placed downstream which will cause the air jet flow to be alternately directed inwards and outwards once the feedback loop enters a stable regime.

The energy exchange process within the pipe, which includes volume injection as well as turbulent mixing of air flows, is of the order of only a few percent and the remaining energy is further dissipated mostly through friction and thermal losses at the walls, so that finally little is left over as acoustic radiation energy [Fletcher & Rossing 2005]. Despite this dissipation the mutual interaction between air jet and acoustic flow is strong enough to drive a positive feedback loop which can, under favourable circumstances, generate self-sustained oscillations. Furthermore, because of the relatively sharp impedance minima of the strongly coupled resonator, at which frequencies the pipe air flows can be particularly strong, the periodicity of the oscillations will be essentially determined by these air column resonances.

2.2.   The resonator

The acoustic behaviour of wind-instrument bores, including various nearly-cylindrical profiles, has been fairly well understood since many decades. The acoustic properties of these bores, including their strong dependence on their cross-section, can be found in many classic acoustics texts [Pierce 1990] and will not be repeated here. In recorders the bore diameter is frequently adjusted in the voicing stage in order to optimize individual notes. In organ building however the bore diameter is normally kept the way it is made, except maybe at the (open or half-open) end, because considerable modifications are still possible at the mouth region knowing that the organ pipe must be optimized for only one frequency.

Because voicing the organ pipe mostly deals with making adjustments influencing the mouth end correction, which is much larger than a normal open end correction, this aspect of resonators will be looked at somewhat closer here.

For an unflanged pipe end it was calculated [Levine & Schwinger 1948] at low frequencies the end correction is about 0.61a, where a is the pipe radius, approximately varies as $0.6a - 0.1ka^2$, where k is the wavenumber, as long as ka < 4, and essentially 0 when ka > 4. The end correction of the mouth region cannot be exactly calculated but approximate formulae exist, such as the well-known low-frequency formula [Ingerslev and Frobenius 1047] for a rectangular mouth cut in a cylindrical tube:

$$L_m = \frac{2.3a^2}{\sqrt{HW}}$$

(1)

where H is the cut-up and W the width of the mouth. These formulae no longer apply if tuning slots, sleeves or ears are applied.

The effect of the end corrections can be seen in the following measurement of the passive resonances of an open organ pipe, obtained by measuring the open end sound pressure while injecting white noise into the mouth:
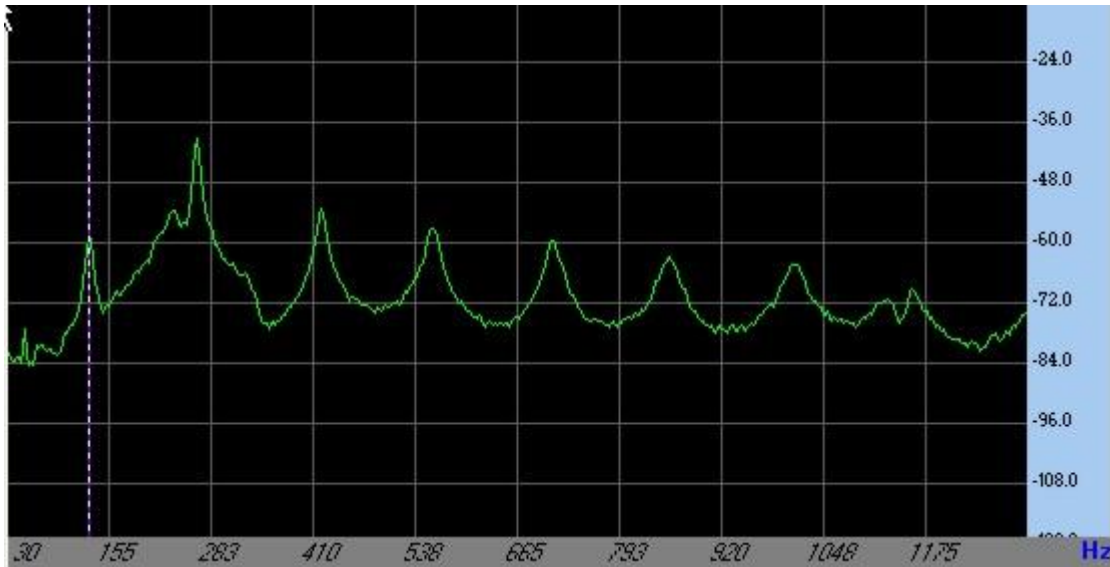
The cursor indicates the first passive resonance of 130Hz. Higher resonances are successively stretched and thus inharmonic.

The next measurement shows the open end spectrum of the same pipe blowing at 130Hz:
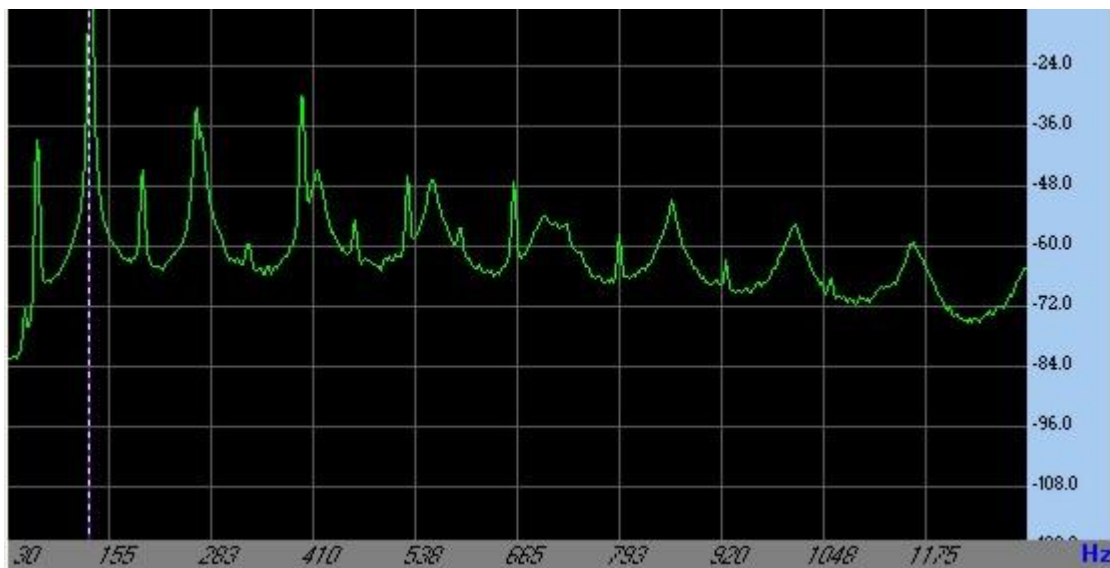
Two additional series of peaks are visible:

- Sharp peaks at the exact harmonic locations of the fundamental 130Hz

- Some sharp peaks as uneven harmonics of half the fundamental caused by reflection against the measuring microphone.

Those harmonics that coincide best with any of the passive resonances (in this case the first few) will sound stronger. The higher ones only coincide now and then.

The way the end correction voicing, especially of the mouth, influences the pipe resonances can be characterized by a dimensionless parameter L_m/L. For narrow-scaled pipes this value will be, considering (1) and typical proportions of the mouth, of order 0.05, corresponding to the soft violinlike sound of this so-

called string family. The other extreme two orders of magnitude larger is reached with the broad-scaled dull sounding flute pipes, where everything contributes to maximum inharmonicity.

2.3.   The air jet driven by the resonator

Fluid jets have been extensively studied, including the particular case of the two-dimensional air jet subjected to an air cross-flow. Their behaviour is governed by the strong shear layers between the two flows and this behaviour turns out to be very difficult to treat analytically from the basic fluid dynamics laws. Therefore many approximate physical models have been developed applicable within the range of certain assumptions made.

A basic feature of the air jet in flue instruments is its intrinsic instability, which has as a consequence that a small disturbance imposed on the jet by the external flow (for instance the flow of an acoustic field) is not only propagated on the jet but also amplified. Both effects contribute much to the positive feedback loop mentioned before. A complete theory on exactly how the cross-flow influences the air jet remains to be developed [Fletcher 2001].   The most recent studies on this subject [Nolle 1998, Verge 1995, Fabre 2000] seem to favour, by the lack more physically consistent theories, a semi-empirical model describing the jet trajectory which assumes an exponential amplitude growth of any disturbances propagated along the jet, combined with a simple convection with the cross-flow, and satisfying the basic boundary condition that the jet exits a stationary flue. When the cross-flow velocity is assumed to be v.cos(ωt), where t is the time, ω the radial frequency and v the velocity amplitude, the displacement y along the jet trajectory as a function of the distance x from the flue along the direction towards the upper labium is:

$$y(x) = v\left[cos\omega t - cosh\mu x \cdot cos(\omega(t - \tfrac{x}{u}))\right]$$

(2)

where additionally:

    u   the phase velocity of the disturbances propagating on the jet

    μ   the exponential growing coefficient

The meaning of most of these parameters is clarified in the next figure, showing in profile the air jet issuing from the flue exit and heading towards the upper labium of the flue instrument, with the coupled resonator on the lower side.
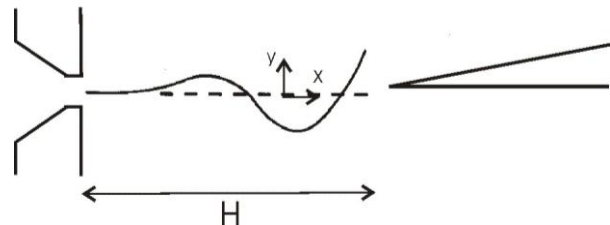
u depends in a complex way on the air jet flow velocity V, which in turn depends on the air supply pressure P. As a first approximation it can be stated:

$$u \approx \tfrac{1}{2}V$$

(3)

$$V \approx \sqrt{\tfrac{2P}{\rho}} \quad \text{or} \quad V \approx 13\sqrt{P} \qquad \text{if P is expressed in cm } H_2O$$

(4)

where:

        ρ is the air density

From (2) the disturbance displacement at the flue is seen to lead the acoustic velocity by ¼ of a period, and the disturbance travels the distance H over the jet from the flue to the upper labium, the cut-up, during the fraction fH/u of a period.

The velocity profile of the jet depends on the windchannel. If there is a long windchannel like in recorders the the velocity profile will be that of a fully developed flow, in the other extreme, more likely in organ pipes, it will be more like a top-hat at the flue, but will rapidly develop into a lateral profile described by a $sech^2$ in case of laminar flow, the so-called Bickley profile. Turbulent jets have a velocity behaviour that is even

more complex, much more details on air jets in flue instruments can be found among others in [Nolle 1998, Segoufin 2001, Yoshikawa 1999].

2.4. The resonator drive by the air jet

As the air jet is driven by the acoustic flow from the resonator it is best placed at an admittance maximum. However, in order to drive the air in the resonator and deliver energy, the air jet needs a pressure to work against. An open end is an admittance maximum looking into the pipe, which is favourable for the first condition, and a real acoustic open end always presents a non-zero impedance to the acoustic flow, the end correction, so the pressure at the open end is not perfectly zero. Accordingly an open end is thus a suitable location for an air jet to interact with the resonator and this is found in all flue instruments.

The interaction of the jet with the air column in the pipe is a complex fluid dynamical phenomenon the details of which are not yet completely clear. The air jet flow injects volume but also contributes momentum, both contributions have a different dependency on V and imply different phase shifts. It turns out that in practice the volume contribution dominates [Fletcher&Rossing 2005] and very roughly the jet drive can be seen, in a linear approach, as a 'current' source driving the resonator, with impedance Z_p, and the mouth, with impedance Z_m, in parallel, so that:

$$v = \frac{Z_p}{Z_p + Z_m} \cdot \frac{V \cdot S_j}{S_m}$$

(5)

where:

S_j is the (periodically varying) cross-section of the part of the air jet flowing into the resonator:

$$S_j = \quad V(y+b) \text{ if } y < b, \text{ where } b \text{ is the jet half width at the upper labium}$$

(6)

$$V2b \text{ if } y > b$$

S_m is the surface of the mouth.

As an electrical network equivalent this can be represented as:
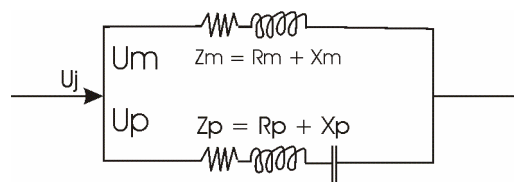
2.5. Closing the feedback loop

Clearly in (5) the acoustic field velocity v leads the air jet flow VS_j in phase by ¼ of a period, so that in order for the complete feedback loop to be closed the disturbance transit time fH/u must be ½ of a period. Moreover, in an open end pipe the transit time for a pressure disturbance to travel from the mouth to the open end and back is of course also equal to this period, so that the, in reality double, feedback loop is closed. With a closed end pipe the pressure disturbance simply performs 4 transits through the pipe, being reflected once in the middle of the period at the open end. In practice the loop tolerates considerable deviations from these values because in normal operation the frequency is near a point of low Z_p, where the phase of Z_p rapidly switches from $-\pi/2$ to $\pi/2$, and thus can considerable adjust the phase shift implied in (5). This explains why the frequency very slightly rises when the blowing pressure rises and vice versa.

The amplitudes reached in the steady loop is determined by the balance of energy supply and losses. Both increase with increasing amplitudes, but at a certain point the energy supply saturates as the air jet is fully blowing into the pipe.

2.6. Harmonic generation:

The complete feedback loop is mainly driven by the fundamental frequency of the sound, higher harmonics do not much intervene, rather they are generated at different places by various non-linearities. The air jet flow constitutes the main nonlinearity of the feedback loop [Fletcher & Douglas 1980], due to the velocity profile and to flow saturation when the jet displacement at the upper labium becomes so large that it completely flows into one side for an extended time. When the air jet flow is perfectly symmetric around the upper labium the spectrum of the flow into the resonator will be mainly driven by uneven harmonics of the fundamental. Other values of asymmetry, which can be obtained by giving the air jet a different orientation

or displacing the upper labium position with respect to the air jet mid-plane, will suppress various other multiples. A simulation of this phenomenon [Fletcher & Douglas 1980] shows regular minima and maxima for the various harmonics, the even harmonics having a minimum at the symmetry axis.

The next figure shows this behaviour as it was observed in the experimental flue pipe when laterally displacing the upper labium:
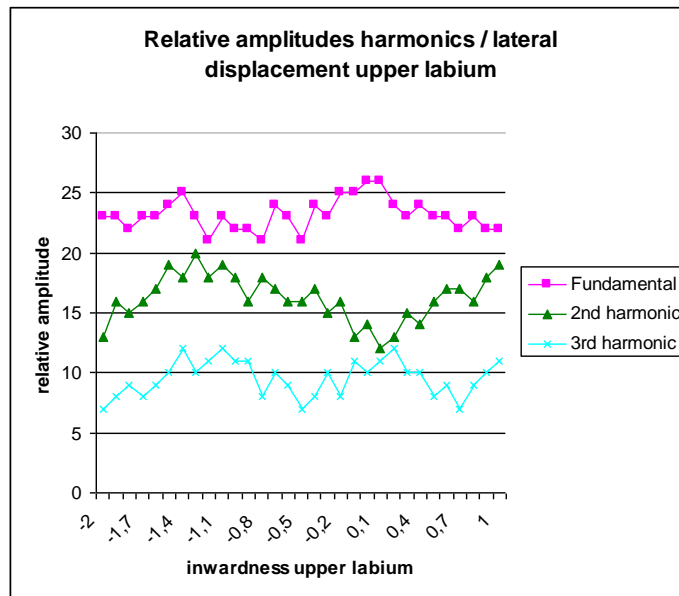
The second harmonic has a minimum near 0,3mm, while the third harmonic is minimum at two points around the symmetry axis.

3   VOICING RULES

Relatively little has been written on the subject of organ pipe voicing [Dom Bedos 1766, Goebel 1975, Monette 1992, Ellerhorst 1936, Bruder 1829, Pento 1995, Toepfer 1888, Cavaille-Coll 1840], and studying this material is not a good start into learning to voice. Most of these texts seem to have been copied from a notebook in the workshop on which the progress of the voicing process was logged. Even today the craft is transmitted on a one-to-one exchange basis from master to pupil (the artistic part is, for some obviously, not transmitted).

Some reports simply refrain to a simple list of causes and effects, such the following extract [Janke 2005]

156. **Niedriger Winddruck, weiter Fuß, weite Spalte lockere, schluchzende Ansprache** voller Ton, klar
157. **Hoher Winddruck, enger Fuß, enge Spalte zähe , fauchende Ansprache** magerer Ton, matt
158. **Sehr dicker Kern, 85° Fase, weite Spalte voller Ton mit gambigen Strich** dumpfes Rauschen

Most authors use literary quite sophisticated phrases to express their ideas, such as "The windsheet either gets in its own way or gives out" [Monette 1992], when describing the air jet in action.

The only formula on voicing that ever seems to have been published is the 'Voicing Number' [Ising 1971]:

$$I = \frac{V \cdot \sqrt{W}}{f \cdot H \cdot \sqrt{H}}$$
(7)

where:

      I = the voicing number

V = the maximum jet velocity

W = the flue width

H = the cut-up

When I=2 the pipe is supposed to operate with maximum power. When I lies between 2 and 3 the pipe becomes gradually more principallike. Above I=3 the pipe overblows.

Its derivation using dimensionless analysis is obscure and it shows some anomalies. When I=2, for a pipe sounding optimally, one can expect V/(fH) to be 4 as shown before. This would imply a W/H ratio of ¼ which corresponds to the geometry of a recorder but not of an organ pipe. The tendencies predicted for rising I are reasonable but, all other thing being equal, V can not produce the same effects as √W. The number never seems to have been used very much anyway.

An exhaustive review of writings on voicing will be the subject of a future paper. The question will be raised whether to what degree these explanations correspond to real voicing practice and whether the results of it can be traced in organs still in existence.

4   AN AERODYNAMIC APPROACH TO VOICING METHODS

As the sound of flue instruments usually is quite distinctive from other wind instruments, it is clear that the air jet and its interaction with the air column plays a major role. They are mainly characterized by:

jet velocity profile, depending on flue channel geometry and varying along the jet. This parameter can be roughly characterized by a jet width and a maximum velocity. Practically, for a given flue geometry, it is mainly controlled by toe hole diameter and flue width. Roughly, since these parameters determine the amount of air supplied into the pipe and thus with the energy delivered to the pipe, they tend to be the main parameters, but certainly not only or the only ones, to determine the loudness.

upper labium location, which strongly influences the way the jet interacts with the acoustic flow. This parameter is usually divided into distance from the flue along the jet centreline ('cut-up') and lateral displacement with respect to this centreline. Practically, both of these parameters can be adjusted, languid lowering or heightening having a rather similar effect as the latter. These parameters, since they influence the air jet flow modulation, will tend to have more effect on the spectrum of the oscillating flows.

4.1.   Air jet velocity

The air jet velocity is of major importance to the loudness and the stability regime of the pipe, it mainly depends on the toe hole cross section. The toe hole is not part of the oscillating system, it merely feeds a small stagnation chamber in the foot of each pipe which in turn supplies air to the flue. The shape of the toe hole can lead to turbulences in the flow which could propagate well into the air jet. Used as a flow constriction it can reduce the pressure in the wind chamber and thus the air jet velocity. This leads to a first family of voicing practices traditionally based on toe hole regulation, and practiced mainly in the XVIIIth and XIXth century but known to and used by organ builders long before and after this period.

By keeping the flue width at a constant large value in these methods the air flow injected by the air jet is thus mainly determined by its velocity. Accordingly a bright and full sound can be obtained through a relatively low cut-up, but strongly increasing the loudness by opening the toe hole also requires increasing the cut-up, thus making the sound less bright.

Looking for a dimensionless parameter to characterize this voicing family, a natural choice seems to be:

$$Str_H = fH/V \tag{8}$$

It expresses the fraction of jet transit time through the mouth to the oscillation period, the parameter is given this specific name because formally it belongs to the socalled Strouhal numbers, which in general relate the time en space scales of a process to some characteristic velocity. Voicing with Str_H lower than the standard value ¼ gives overblown regimes which are very stable, and vice versa. How it can characterize loudness will be the object of further analysis and measurements.

4.2.   Jet width

While the maximum velocity of the air jet is mainly determined by the pressure in the wind chamber below the flue, the air jet width depends entirely on the flue width and the geometry of the wind channel leading to

the flue. This leads to a second family of voicing methods where the air jet flow is determined by the latter parameter, the pressure being kept constant by making the toe hole wide. Consequently the cut-up tends to be rather high and the slender high aspect ratio air jet turns out to stimulate well the higher harmonics. This voicing method seems to have been preferred in the XVIIth century during the heydays of Baroque organ building, when builders tried to obtain as much loudness as possible with as little wind consumption as possible. Using a low wind pressure it is possible to reduce the cut-up and thus delicate and transparent sounds ideally suited for polyphonic music are obtained. Increasing loudness by opening the flue will slightly brighten the timbre [Monette 1992, Janke 2005].

A good candidate to characterize this family is the air jet aspect ratio W/H, which strongly determines how the jet develops and thus interacts with the cross-flow. The linear model for the jet displacement breaks down for large aspect ratio values [Dequand 2001], in which a vortex model, consisting of vortices developing alternatively on both sides [Holger et al 1977] becomes more realistic. Further measurements are needed to determine the applicability limits and corresponding aspect ratio value for the case of open toe voicing.

4.3. Mouth end correction

The air jet transit time largely determines the self-sustained oscillation regime, in that it determines what the operating frequency will be with respect to the first passive pipe resonance. As seen before the mouth end correction has a considerable influence on the resonator: it can strongly influence the relative position of the operating frequency harmonics to the passive resonances. Accordingly, it can give rise to a specific voicing family where the characteristics of the mouth combine to give an aerodynamic control parameter. The geometry of the mouth is mainly defined by the cut-up, the mouth width, the presence of ears and other provisions to stabilize the air jet. Cut-up is the primary regulation parameter. A high cut-up can accommodate larger phase delays on the air jet and thus the operating frequency will be lower than the first pipe resonance, which will bring the higher harmonics further out of tune with the higher pipe resonances. The result is a decrease in harmonic content, the sound becomes duller. According to this behaviour some voicing methods start with pre-determined cut-up values and adjust the air jet parameters in order to obtain an appropriate loudness-brightness balance. Low cut-up is invariably associated with a thin and bright spectrum with a weak fundamental, whereas high cut-up brings about a broad, not necessarily very interesting, sound [Pento 1995].

The way the end correction voicing, especially of the mouth, influences the pipe resonances can be characterized by a dimensionless parameter L_m/L. For narrow-scaled pipes this value will be, considering (1) and typical proportions of the mouth, of order 0.05, corresponding to the soft violinlike sound of this so-called string family. The other extreme two orders of magnitude larger is reached with the broad-scaled dull sounding flute pipes, where everything contributes to maximum inharmonicity.

4.4. Air jet lateral displacement relative to upper labium

This regulation has a major impact on the sound spectrum of the speaking pipe, yet is almost completely out of direct observation: minute alterations of the languid height with respect to the lower labium can cause strong displacements of the air jet with respect to the upper labium. Moreover the non-linearity introduced by the air jet flow dividing effect of the upper labium is the main source of harmonic generation in the pipe, but apparently the elusive character of this parameter has precluded it from becoming a basic regulation parameter of some voicing method. Rather it is actively used as a welcome additional degree of freedom capable of strongly influencing harmonic development and transient behaviour.

As a characteristic parameter the ratio y_0/H , where y_0 is the lateral displacement of the jet axis with respect to the upper labium, could be useful. Further study is needed to determine the strength of this.

4.5. The optimal operating point

Several authors mention the existence of regions of voicing parameter values which allow 'optimal' operation of the pipe or part of it.

4.5.1. The air jet

Numerical studies of jet instability [Drazin&Howard 1966] show that the growth coefficient μ is not constant along the developing jet but shows a maximum where the jet thickness equals one fifth of the disturbance wavelength. Roughly assuming the air jet to spread with 12º so that the jet thickness is about 2/5 of the distance covered, this will take place at a distance of half a disturbance wavelength. This is precisely the condition of a phase delay on the jet corresponding to the pipe sounding at her first passive resonance frequency of the air column and thus a lucky coincidence.

Moreover the acoustic field around the pipe mouth turns out to have a non-uniform velocity distribution across the mouth. The next figure shows a simulation of the acoustic (potential) flow field in the pipe mouth, using some geometric simplifications [Verge 1995]:

Velocities much higher than average are found near the labium, in the region of large μ. The result is that the air jet suddenly becomes strong lateral displacements as it approaches the upper labium, as shown in the following Schlieren visualisation, showing different phases of one period of steady oscillation (left to right, right is inside the pipe):
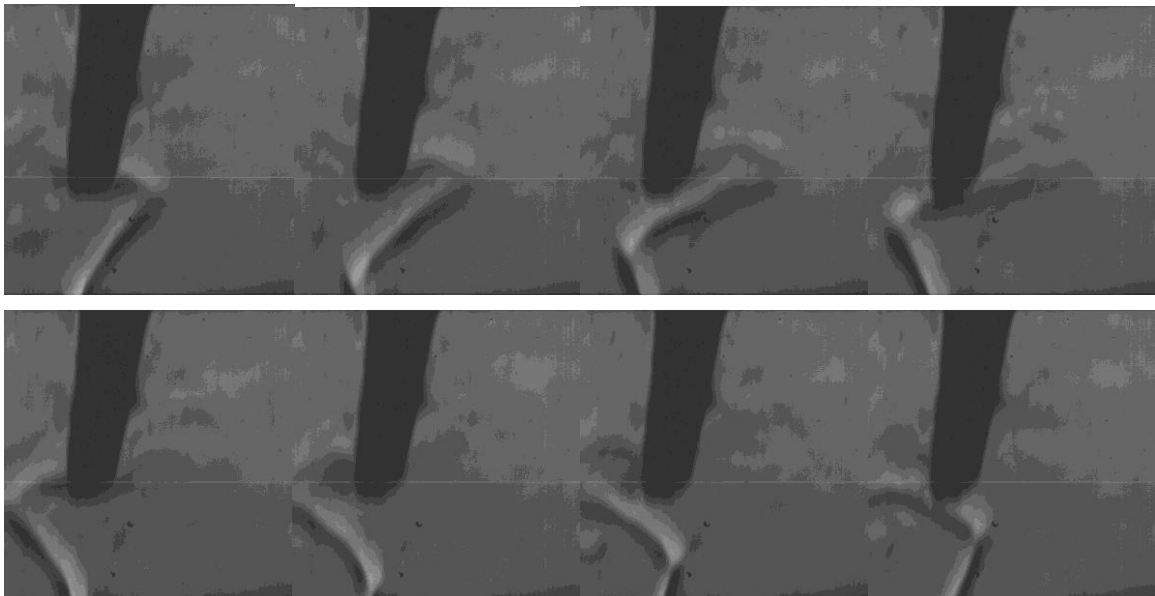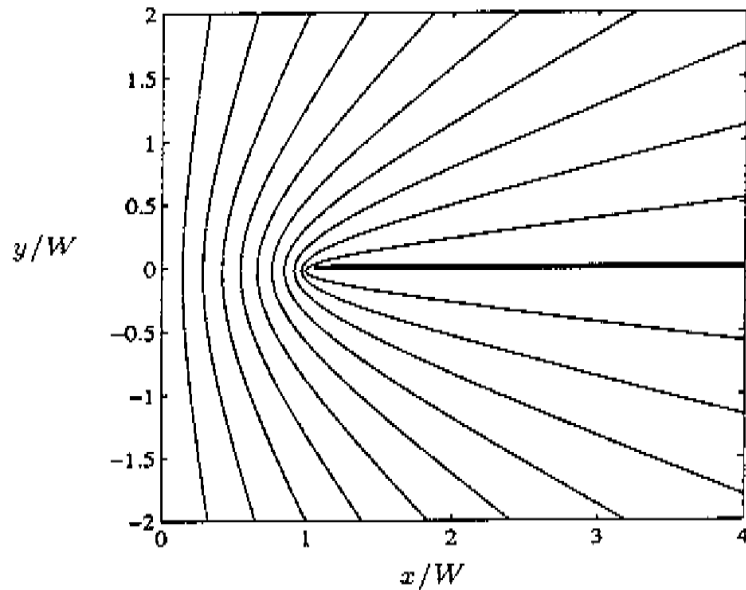
It is clearly visible that in the first half of the period the upper part of the jet is convecting into the pipe and this all the faster the more the upper labium is approached because of the larger acoustic velocity field, As a result the upper part of the jet is more and more tilted. At the end of the first half of the period the acoustic field velocity changes direction and process now repeats in the other direction. Details on the operating conditions for these images are found in [Steenbrugge 2009].

From these qualitative data it can also be seen that the air jet flow starts to enter the pipe when the acoustic flow into the mouth is maximum, thus confirming the phase delay of around ¼ of a period previously mentioned for a pipe sounding at its passive resonance frequency.

It can be hypothesized that the perfectly periodic oscillations which flue instruments are able to generate, despite the fundamentally unstable nature of the source medium, is essentially due to the presence and cooperation at the same location of these three fluid dynamical phenomena: acoustic flow concentration, excessive air jet instability and optimal disturbance phase conditions on the jet.

4.5.2. Toe hole and flue width voicing

A short experimental analysis [Nolle 1979] concluded that toe hole and flue width voicing can be interchanged within a certain range of parameters. Accordingly the acoustic pressure was found to be proportional to the product of wind pressure and flue width and harmonic content was constant as far as the first 3 or 4 harmonics were concerned. This suggests that toe hole voicing and flue width voicing are extreme cases that evolve toward each other when the respective basic parameters are being mixed. These observations and their relationship to the other optima discussed in this paper will be the subject of further study and measurement.

5   PHYSICAL MODELLING AND VOICING

The number of applications of physical modelling of systems not developed from physics first principles, such as natural phenomena or art objects, has greatly increased with the introduction of more and more powerful data processing capabilities. Accordingly virtual representations of musical instruments has become a wide research topic, but the field has always faced a formidable challenge: acoustical instruments, and especially wind instruments, usually and necessarily have an internal life which is very different from their external appearance. By the laws of acoustics the low frequency end of the oscillations is almost unable to escape from it, whereas the high frequency part is quite freely liberated. This means that the instrument essentially operates through the lowest frequency components, which, taking into account their sequestration, must be very strong, and the high frequencies, the ones evolution has brought living beings to be most interested in, are in fact nothing more than weak superfluous byproducts. Internally the high frequency part of the instrument's operation is thus a higher order effect whereas most current physical models are limited to lower order behaviour.

Practical applications of physical modelling, for instance in sound synthesis, therefore usually require the use of fine tuning parameters, the effect of which is not explicitly built into the model but is controlled by an external and adequately sensible agent. This is the situation in the mainstream application of musical instruments modelling which consists in creating virtual instruments.

As suggested above, physical modelling of organ pipes not only allows to disentangle voicing practices and gain a better understanding of efficient voicing methods, it can be a useful toolbox with which the most important aspects of a specific organ builder's voicing practices can be characterized. As a small demonstration, the late organ builder Charles Fisk, who introduced neo-baroque organs in the USA during the 1960's, writes:

"If you first agree that the windway must be kept open (almost the width of the material of the lower lip) …, then classical voicing is a matter of balancing the toe hole opening and the cutup (i.e., the height of the mouth opening). If we choose a wide open toe hole, then underblowing will be achieved if we raise the cutup *just beyond* the point at which the pipe appears to be giving out its maximum volume of sound. Thus the classically voiced organ pipe is one in which the cutup is "a little too high." With the cutup on the high side, the tone becomes fuller and gentler; more important, the pipe is not quite as stable as it would be with a lower cutup, and this makes it *much* more easily influenced by pulses or irregularities in the flow of air coming through its toe hole." [Fisk 1976]

This recipe, which essentially belongs to the toe hole regulation family, can be readily understood and memorized if one is reminded of the 'optimal' cut-up distance where ½ of a disturbance wavelength is on the air jet. This is Fisk's point of 'maximum volume of sound'. Raising the cut-up while leaving the toe hole and thus pressure the same underblows the pipe, and the jet velocity profile near the upper labium has become smoother whence less harmonic drive. On the other hand, increasing the mouth surface increases mode competition because the higher passive resonances become more harmonic: the pipe looses some of its stability. Explaining Fisk's voicing rule has required no other knowledge than what was presented above in the short overview of flue instrument models.

Arrived at this point however the biggest problem remains, which is the determination of voicing techniques used in extant organs, especially if little or no information is available from or about the builder/voicer. As the voicing parameters are not mutually independent in their effect it is usually difficult to conclude about a specific voicing method used on the basis of these parameters alone, except in extreme cases. What is needed is what the taxonomist used to do when a new species was discovered, a comparison is made between the specimen and similar ones in a collection. As the history of voicing methods and their inheritance has not yet been written this identification task is very difficult. Moreover the question arises which data such data bases need to contain in order to seriously allow this comparison. It is well known that even the most complete inventories of organ pipes do not contain all necessary values needed to be able to faithfully reproduce a given pipe with a given sound. For instance the angle of attack of the air jet, so important for the acoustic properties, is never included because it's not part of the geometry. Toe hole dimensions are often given but their cross-section is often so irregular that a simple description is

inaccurate because a small variation can cause large pressure differences in the pipe foot. A first step towards a better documentation would certainly be a quantitative description of the all-important velocity profile along the jet: its amplitude, its lateral and longitudinal velocity distribution, its direction, its width, etc…

6   CONCLUSION

Based on the aerodynamic properties of the self-sustained oscillations in the flue organ pipe, different voicing categories were identified and briefly characterized. Because they are not directly based on geometrical parameters it's easier to describe cause and effects in each of them in terms of mutually independent dimensionless quantities. The relevancy of the chosen quantities, which have been chosen largely on the basis of good guesswork, has to be further established by measurements on more different cases.

From the presented short overview of the aerodynamics in flue instruments it became clear that the air jet is the essential operator in the system: it is the active element allowing positive feedback, it accommodates in a rather flexible way necessary phase delays, and together with the upper labium it constitutes the main source of inharmonicity which is of the highest relevance from a musical point of view. The air jet behaviour is very sensitive to small geometric variations in the mouth and therefore analyzing the voicing of flue pipes could benefit from taking into consideration the aerodynamics in the mouth region.

Further work in this direction will include trying to more exhaustively and quantitatively characterize different voicing styles by means of the aerodynamic parameters presented in this paper.

7   ACKNOWLEDGMENTS

8   REFERENCES

[1]   Audsley G. A.., The Art of Organ Building 2Vol. Dover Publications 1905/1965.
[2]   Cavaillé-Coll, A. (1840). Études Expérimentales sur les Tuyaux d'Orgues. In Complete Theoretical Works of A. Cavaillé-Coll. Buren (GLD.), The Netherlands: Frits Knuf 1979
[3]   Bédos de Celles (Dom), F. (1766-78). *L'art du facteur d'orgues - 4 vols.*; facsimile edition, Paris: Bärenreiter-Kassel, 1958.
[4]   Bruder I., Orgel- und Spieluhrenbau, Aufzeichnungen des Orgel- und Musikwerkmachers Ignaz Bruder aus Waldkirch von 1829 und die Entwicklung der Walzenorgel Vierunddreissigste Veröffentlichung der GdO 1968 by Sanssouci Verlag AG Zürich,
[5]   Dequand, S., Luo, X., Willems, J. F. H., and Hirschberg, A. ~2001!. "Self- Sustained Oscillations in a Helmholtz-like Resonator. Part 1: Acoustical Measurements and Analytical Models," in *7th AIAA/CEAS Aeroacoustics*
[6]   *Conference* ~Maastricht, Nl!, submitted to the AIAA Journal
[7]   Drazin P.G. & Howard L.N. Hydrodynamic stability of parallel flow of inviscid fluid , Adv. Appl. Mech. 9:1-89, 1966.
[8]   Ellerhorst W.: *Handbuch der Orgelkunde.* Einsiedeln 1936, Frits Knuf, Buren 1986 (3. Repr.), ISBN 90-6027-519-5
[9]   Fabre, B., and Hirschberg, A. ~2000!. "Physical Modelling of Flue Instruments: a Review of Lumped Models," Acust. Acta Acust. 86, 599–610.
[10]   Fisk C., Articulateness and the Organ: A problem for the Organ Builder Lecture given at the dedication of the Flentrop Organ, Duke University, November 1976
[11]   Fletcher, N. H. & Rossing, T. D. (2005). *The Physics of Musical Instruments*. New York: Springer-Verlag
[12]   Fletcher N.H.(2001), Recent progress in the acoustics of wind instruments, Acoust. Sci. & Tech. 22, 3.
[13]   Goebel, J. (1975). Theorie und Praxis des Orgelpfeiffenklanges. Frankfurt am Main.
[14]   Holger, D. K., Wilson, T. A., and Beavers, G. S. ~1977!. "Fluid mechanics of the edge-tone," J. Acoust. Soc. Am. 62, 1116–1128.
[15]   Ingerslev F. & Frobenius W.(1974), Some measurements of the end-correction and acoustic spectra of cylindricalopen flue organ pipes. Tran. Dan. Acad. Tech. Sci. 1, 1-44.
[16]   Ising, H. (1971). "Erforschung und Planung des Orgelklanges." *Walcker Hausmitteilung, 42*, 38-57.
[17]   Janke R, (2005) Intonationsvorschriften,

[18]   Levine H. & Schwinger, J. (1948), *On the radiation of sound from un unflanged circular pipe,* Phys. Rev. 74, 383-406.
[19]   M. E. McIntyre, R. T. Schumacher and J. Woodhouse. (1983), On the oscillations of musical instruments. *J. Acoustical Society of America* 74 1325-1345.
[20]   Monette, L. G. (1992). *The Art of Organ Voicing.* Kalamazoo, MI: Western Michigan University
[21]   Nolle A., Sinuous instability of a planar air jet: Propagation parameters and acoustic excitation, J. Acoust. Soc. Am. 103(6), 3690-3705.
[22]   Pelto, P. (1995). "Four Voicing Techniques," *The Organ Yearbook* (Vol. XXV).
[23]   Pierce A.D., Acoustics. McGraw-Hill, NY, Acoustical Society of America 1990.
[24]   Sato H. ,The Stability and Transition of a two-dimensional Jet, J.Fluid.Mech.7, 53-80. 1937
[25]   Ségoufin, C., Fabre, B., Verge, M. P., Hischberg, A., and Wijnands, A. P. J. (2000). "Experimental Study of the Influence of the Mouth Geometry on Sound Production in a Recorder-like Instrument: Windway Length and Chamfers." *Acustica, 86*(4), 649-661.
[26]   Steenbrugge (2009) "A flue organ pipe with micro-adjustable mouth geometry : design and measurement procedures". Hogeschool Gent.
[27]   Töpfer J.G., „Die Theorie und Praxis des Orgelbaues" [Buren] : Knuf. 1888/1972
[28]   Verge, M.-P. (1995). Aeroacoustics of Confined Jets with Applications to the Physical Modeling of Recorder-Like Instruments. Techische Universiteit, Eindhoven

ABRASIVE TRIBOLOGICAL TESTING OF DIFFERENT HOT-DIP GALVANIZED MULTILAYERS

László Szabadi

Institute for Mechanical Engineering Technology, Faculty of Mechanical Engineering,
Szent István University, Gödöllő,

Abstract One method for steel structures corrosion resistance is using hot-dip galvanizing process. Nowdays it is widely used in Europe considering its favourable characteristics. Lately beside the corrosion resistance demand of hot-dip galvanized coatings as a new requirement is wear resistance. The cause of this is more and more steel constructions are provided with zinc coatings as durable protection against corrosion. The industrial floor boards, agricultural walking grids get heavy abrasion effect. The abrasive wear resistance is a less tested, less known domain.

Keywords diffusion, abrasive wear, gradient material structure.

1. INTRODUCTION, APPLICATION FIELDS OF COATING HOT-DIP GALVANIZED, THEIR PRODUCING AND THE COATING CHARACTERISTICS.

The hot-dip galvanizing technology is used for durable resistance against of surfaces of iron- and steel constructions and of goods sold by the piece, its protection effect depends decisively on the thickness of a layer. Its main application fields suggested is the surface protection against atmospheric load in all corrosity grades as well as to protect the metal structures of indoor ventilated spaces. Its application expands continuously because of its reliable protective effect, the process industrial-scale applicability, its comparatively high productivity and low need for human labor demand. Continually increasing proportion of steel constructions manufactured in Europe-yearly more than 6 million ton-are covered by coatings hot-dip galvanized. Nowdays the products get also mechanical loads beside corrosion effects at industrial filters, industrial, agricultural, public square pavement grids hot-dip galvanized meaning new and at the same time expanding application fields. At surfaces hot-dip galvanized exposed to abrasive wear, sand and breakstone spreading there is an application demand for today wear- and friction resistant coatings. Comparing test data regulated relating to wear resistance there are not available neither in technical literature nor in the data-base of companies producing and developing coatings. These data are indispensable to develop technology improving wear resistance.

Two basic groups developed hot-dip galvanizing (1). The most characteristic phase of individual processes are the dip into the metal bath exists at each group, however there are significant differences between individual solutions considering the preceding surface preparation and subsequent treatments. There is no difference between the two process groups considering the zinc-layer forming which takes place by the same physical-chemical processes. They so called continuous technologies belong to the first group, during which the product to be galvanized "as spliced" continuously with suitable speed passes through on the technological system.

The continuous broad strip-, narrow strip- and wire galvanizing processes have similar methods essentially. The strip surfaces are oxide relieved in a closed technological system, their materials are heated up then are guided into zinc-bath where the coat develops.

The so called periodic technologies belong to the second group. At there the products get treatment by individually or in groups. The surface is here also pre-treated then this is followed with hot-dip galvanizing. Covering steel constructions belong to this group, too.

The pure zinc is readily-formed and soft metal. The Zn hardness- 55-70HBS (2) is far below of the mild steel hardness -120HBS-, thus its wear resistance is also significantly smaller. In case of alloyed steels this difference can be still significantly greater. The structure of zinc-layer is determined decisively by the chemical composition and texture of steel base-metal, the zinc-bath temperature, the dip duration, the zinc-bath alloying elements, the surface condition and thickness of the workpiece as well drawing out speed and the lifting method of the workpiece to be coated (3). During dip-hot galvanizing an intermetallic, multi phase zinc layer develops on the products surfaces. The last step of technological treatment is the galvanizing when at about 450^0C temperature the zinc atoms diffuse into the clean metal surface and produce atomic (cohesion) bond infiltrating into the metal-crystalline, namely they form an alloy with iron, on the zinc-iron boundary surface zinc rich Fe-crystallines

develop. This forms essentially the "adhesive-bridge" between the zinc coating and the iron plate. The further alloy layers are based on this which iron content decreases progressively to the outer layer and in case of optimal steel quality also cease to exist. The coating thickness is about 80-100 µm. Figure 1. shows the zinc layer structure.
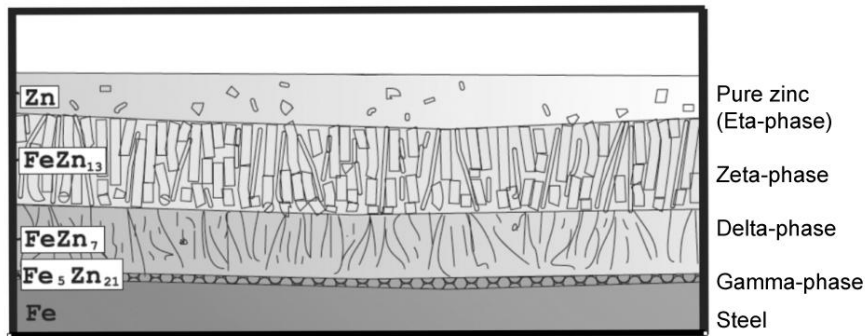
Figure 1. The zinc layer structure and the individual phases.

The gradient material structure developed during diffusion is not homogeneous, its composition changes in the function of thickness.

2.   METHOD AND RESULTS

2.1.   Specimens tested.

We have chosen S235JRG2 steel as specimen material used for abrasive tests, which is the most definite base metal for example of pavement grid. As this material is desoxidized with aluminium- and not with silicium – and the mechanism of layer developing is determined first of all by the amount of silicium to be in steel, therefore it can be hot-dip galvanizing outstandingly. We have taken into account at deciding the specimens dimension the tool form of the abrasion tester, as well as those positions and the geometrical dimension of the container containing the abrasive medium ensuring abrasion. Figure 2 shows the dimension of specimen galvanized.
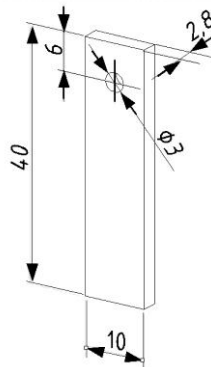
Figure 2. Specimen dimension.

Two types of coating were tested in the function of friction length, speed and pressure of abrasive medium.

- Technigalva: The determining components are the zinc (Zn), aluminium (Al), lead (Pb) and nickel (Ni) of the zinc-bath. The coating was made by dry periodic technology.
- Technigalva heat treated: Some part of the specimens were heat treated in order to the coating should have zinc-iron alloy phases in the total cross-section.

Figure 3. and 4. show the SEM-pictures made from coatings. Certain layers, phases can be separated very good in the thousand-fold magnification. We have also carried out EDS (Electron Detector System) tests.

The abrasion resistance of coatings depends on its hardness, therefore it is needed to measure the micro-hardness. The micro-hardness tests showed that the Techigalva coatings had 48HVM in average, while the heat treated coating had 106 HVM in average.
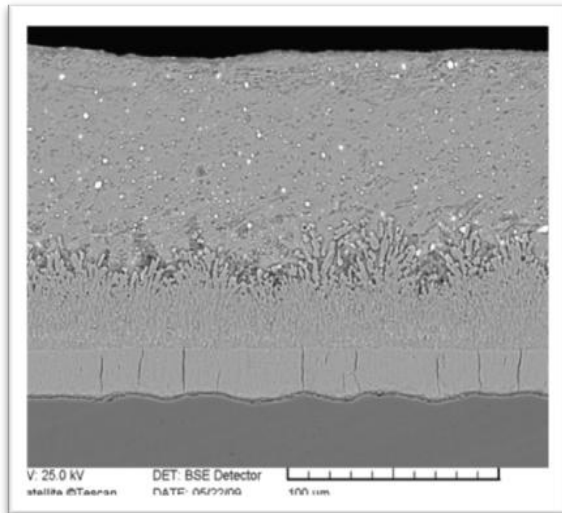
Figure 3. 1000X-magnification of Technigalva specimen zinc coating
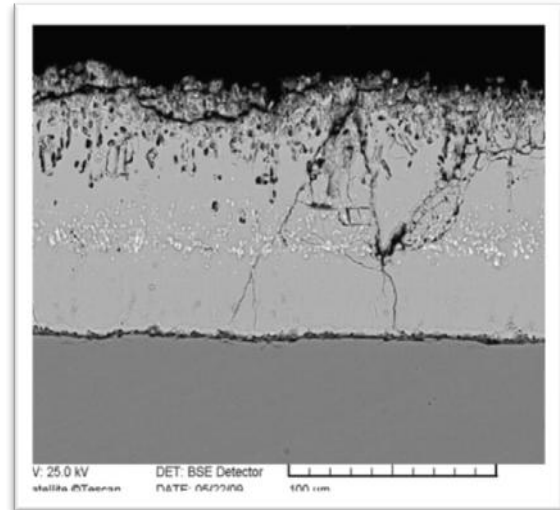
Figure 4. 1000X magnification of specimen heat treated zinc coating

2.2. Abrasion test with "sand-slurry" equipment

The "sand-slurry" principle is well known in the VI. test category of tribological modeling. Several versions are wide-spread but they agree that for example in a sand with grain composition given - as in abrasive medium – a specimen moves in circular orbit generally with speed given. Great number of specimens can be measured at the same time in abrasive medium given as well as it can be well define but beside in different conditions with the abrasion tester developed in the Institute for Mechanical Engineering Technology. The results got made possible the evaluation according to various standpoints, too. Figure 5. shows the abrasion tester developed.
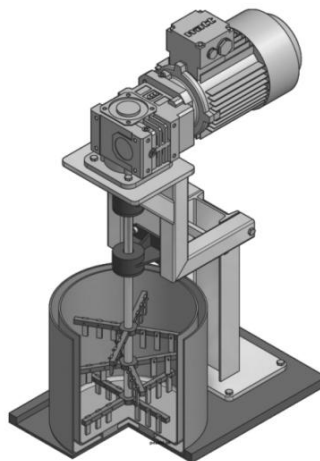
Figure 5. The abrasion with specimens mounted.

The electric motor shaft connects to a worm-gear which gear transmission in 22,58. The working shaft can be found at the exit side of the worm-gear on which 3 pcs. arm cross-clamps can be found – in different heights related to the base plate (Figure 6.)
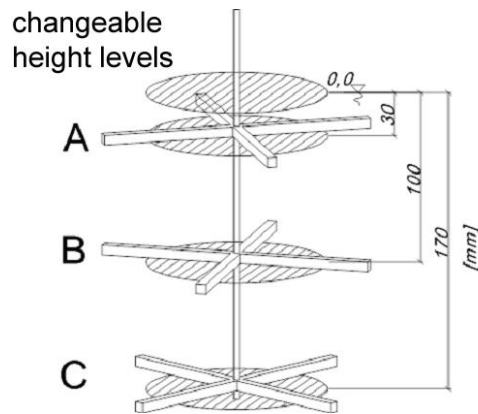
Figure 6. Specimens placed on three levels.

The specimens to be abraded can be fixed in suitable position on this. To one tool, to each arm 3 pcs. altogether 6-6 pcs. specimens can be fixed.

Important characteristic of the cross-clamps is that the specimens can be fixed with each other in 90^0 included position, at their sides in pairs altogether 6 various positions related to the centre of gyration. The tools are set turned away to one another on the working shaft in top view the circle is divided to 30^0 sectors. The container containing the abrasive medium can be put into an outer container in case of demand, which can be filled with cooling-heating water to the thermal dynamics of measuring procedure can be regulated.

The abrasive medium was 0/8 OK – type ballast stone. Its average aggregation density in dry condition is 1,7 ton/m^3. There is no practically clay-sludge content as it is produced from washed, granulated gravels by knapping. The grain fraction is between 2 and 8 mm.

The specimens to be in different radiuses move with various different peripheral speed in the abrasive medium and the height position results different surface pressure rations (Figure 7.) The abrasion tester makes possible exceptional complex evaluation in the function of these variables.
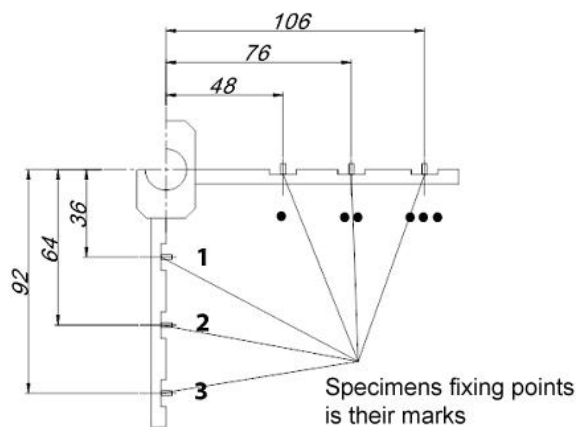
Figure 7. Position of specimens on different radiuses.

2.3. The abrasion and speed connection.

We have measured the abrasion of the 6 pcs. heat treated and 6 pcs. not heat treated specimens placed in all three levels (A,B,C) after seven various abrasion time.

The specimens covered different length with different peripheral speed moving on various radiuses. After averaging the abrasion results measured at each specimen, repeating three times the measuring series the same incline could be seen at the lines to be adapteable to the plot at heat treated and not heat treated specimens, too. Based on these the speed independence supposed were proved by mathematical – statistical methods, by covariance analyses at all three levels at heat treated and not heat treated specimens, too. The abrasion values of all specimens to be in the different levels can be presented with a single regression straight line.

This means that the abrasion values do not depend on the abrasive speed in the speed domain tested (Figure 8. and 9.). There is no significant difference between the specimens moved with various speeds but placed at the same level.
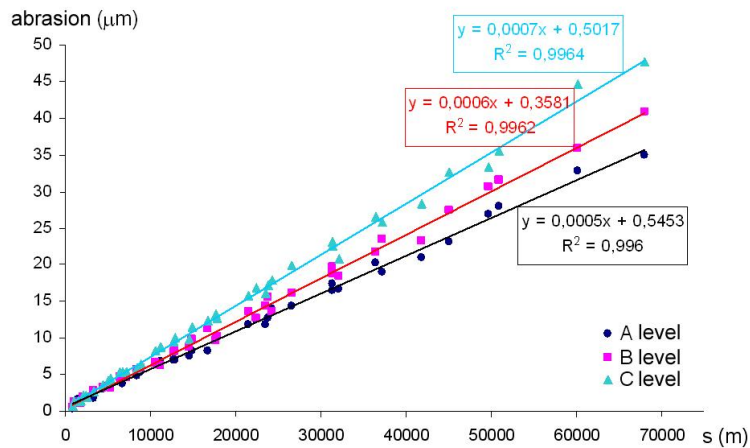
Figure 8. Abrasion values of heat treated specimens on "A", "B" and "C" level
(h_1, h_2 and h_3 depth)
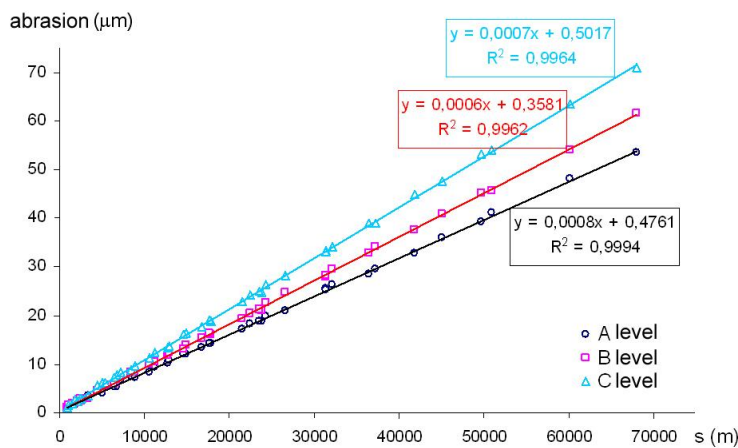
Figure 9. Not heat treated specimens abrasion values on "A", "B" and "C" levels.

2.4. Connection between surface load and abrasion

The specimens placed on the "A", "B" and "C" level get different surface loads because of this the abrasion values measured on "A", "B" and "C" levels has to be compared. According to the hypothesis the abrasion values depend on the load. It can be approximated with linear trend-line the appropriate data to different levels on the diagrams, the matching is close in each case. The data appropriate to different levels can be separated visibly however if there is significant difference between them it has to be examined by regression analysis. The worst case is where there is the smallest difference: this is the "A" and "B" level data of the specimens heat treated. The calculations carried out proved that there is significant difference between the abrasion values of specimens fixed on "A" and "B" level. This means that the amount of surface load has significant effect on the abrasion values in the system tested. In case of higher load the specimens have got higher abrasion.

2.5. Comparing the layer structure of coating and abrasion values.

The abrasion measured as a resulting effect on the surface of specimens means the continuous decreasing of coatings with layer structure. In Figure 10. can be seen how changes the percentage rate of decesive chemical elements in certain layers of heat treated specimens. The chemical composition' changing does not influence the abrasion intensity. According to data tested by EDS spectroscopy the percentage rate of chemical elements in the layers of not heat treated specimens is formed otherwise, but this compound does not influence the abrasion intensity of certain layers.
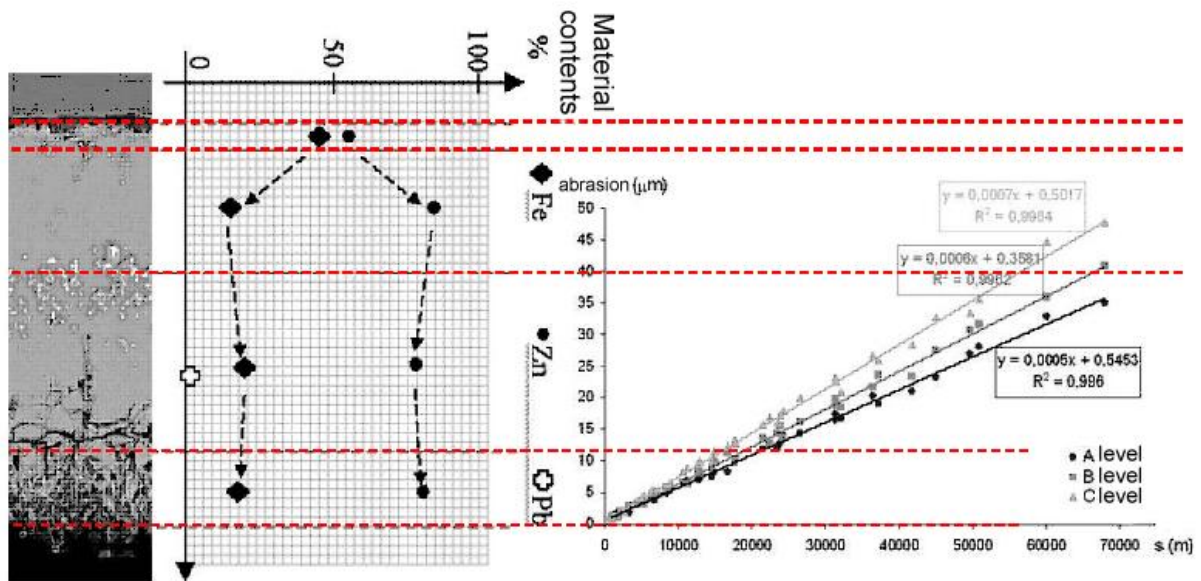
Figure 10. Heat treated specimens abrasion and the connection of layer structure.

3. CONCLUSION

- The multilayer coatings of hot-dip galvanized abrasion intensity in the test-system does not depend on the fiction speed neither at heat treated nor at not heat treated specimens, but it depends on the medium pressure and on the resistance of medium deriving from that.
- The heat treatment improves the abrasive resistance. The higher hardness results higher abrasive resistance improvement.
- SEM-pictures and EDS spectroscopy proved that heat treatment results different gradient layer structure and composition.
- The linear abrasion dynamics of hot-dip galvanized layers tested does not depend on that, which layer comes to friction connection with abrasive medium. The inner gradient friction character did not effect the abrasion intensity measured, but the resultant of different gradient structure has different abrasive resistance.

REFERENCES
1. Magyar Tűzihorganyzók szövetsége: Szakmai Ismeretek, Dunaújváros, Dunatáj Kiadó Kft., Dunaújváros, 1997
2. Dr. Zorkóczi Béla: Metallográfia és anyagvizsgálat, Tankönyvkiadó Budapest, 1975
3. Magyar Tűzihorganyzók szövetsége, Tűzihorganyzás, CD-kiadvány, 2008

MICROWELDING TECHNOLOGY PLATFORM

N. Van Caenegem

[1] Belgian Welding Institute, Belgium

Abstract The BWI (Belgian Welding Institute) works in collaboration with CEWAC (Centre d'études wallon de l'assemblage et du contrôle des matériaux) and MULTITEL, 2 other approved research centers on a project concerning micro welding and associated quality controls. A platform that groups different micro welding processes and adapted, advanced quality controls has to be build up. The technologies are: micro friction stir welding, micro-plasma, micro-TIG, micro-resistance welding, micro-laser welding, micro-electron beam welding, digital micro-radiography and micro-control via adapted penetrant inspection. Some of these technologies are already available at CEWAC, others are new. The installation of all the equipment, the existing and the new machines, is foreseen by July 2010. This platform will be accessible for all companies, to know the technology, to compare different techniques, to ask for the best solution, the best parameter set-up for their application, to make small pre-series, etc…

Keywords micro welding, non destructive testing

1   INTRODUCTION

The BWI (Belgian Welding Institute) works in collaboration with CEWAC (Centre d'études wallon de l'assemblage et du contrôle des matériaux) and MULTITEL, 2 other approved research centers on a huge project concerning micro welding and associated quality controls. The application of this project is done within the frame work of the first call of the FEDER project 2007-2013. It has started on July 2008. To start with, a platform that groups different micro welding processes and adapted, advanced quality controls has to be build up at CEWAC. The technologies are: micro friction stir welding, micro-plasma, micro-TIG, micro-resistance welding, micro-laser welding, micro-electron beam welding, digital micro-radiography and micro-control via adapted penetrant inspection.

This platform is open for all companies that are interested in it. By participation in this research project, companies get an insight in the possibilities of micro-welding and associated quality controls. They will be able to assess if these processes are usable for their specific applications, taking into account the joint properties, the necessary investments, the profit increase in comparison with the current applied technique, the reliability of the processes, and so on…

The different projects are described more in detail

2   DESCRIPTION OF THE PROJECT

2.1   Project « MICROSOUD »

This project, with the collaboration of Cewac and BWI, is about the investment in high-technological equipment and in complementary infrastructure in order to realize collective research projects. The technological platform about 'micro welding and adapted, advanced controls' will be developed under strong accreditations (for aerospace, aircraft, medical world...). This platform gives service and knowledge of the modern technology of micro welding and associated quality control to the companies, and more specific to the SME's. This will allow them to use these technologies in the creation and realization of innovative products/services (taylor-made pre-series) and/or to adapt their existing, less competitive product.

The goal is to introduce these technologies more easily in the companies by sensitization and collecting practice technological expertise. Training, application specific to the company will be possible and also they will be capable to realize small series at CEWAC, following the strong standards and accreditations. So, companies should easily get introduced in the new market and have insight in the technology, accreditation, profitability, environment and training of their human resources.

The project is focused on the advanced technologies such as: micro friction stir welding*, micro-plasma, micro-TIG, micro-resistance welding, micro-laser welding*, micro-electron beam welding*. The technologies indicated with * has been bought within this project and will be operational by July 2010; the others were already available at CEWAC.

Also the associated quality controls such as digital micro-radiography and micro-control with adapted penetrant inspection will be available. These are very cost-effective techniques, which are at the same time difficult to access and which mean an investment as well for purchase as for the training of the people as for the knowledge of the accreditation and standards in the domains of micro mechanics, aircraft, aerospace, medical, electromechanics, transport, security,…

This project fits completely in the further development of the research centers CEWAC and BWI, who work closely together since the signature of a scientific collaboration in 2005.

Figure 1. Examples of micro-assemblies

2.2 Project Laser NDT

This project 'laser NDT', a collaboration between Cewac and Multitel, wants to introduce and develop the technology of micro laser welding in the companies and at the same time, wants to miniaturize existing components. This project is focused on the development of specific control methods for micro laser welding (so it can be seen as a more in-depth study of the previous project).

The industrial development of the laser technology requires a qualitative non-destructive control usable in the production line. This can reduce the cost and avoids also the production of wasted products. Taking into account the small joints and the small thicknesses, the classical non-destructive tests are not appropriate, with the exception of radiography. The radiography is at the moment less profitable for a continuous industrial project, due to his cost, the difficulty of interpretation, the application after the welding and so on.

The goal of this project is to study and validate an innovative method for quality control which can be used in a continuous process of micro welding, in other words, an automatic system of in-line quality control. The system will exist of signal acquisition, filtering and analysis which will be compared to reference signals and as result will send an alarm in case of inacceptable failure.

2.3 Project Introtech PME

This project consists of the offer of technological services (information, dissipation, technological transfer) which give an answer to the needs concerning establishing, development and/or reinforcement of the companies, and more specific the Walloons SME's and SE's. This has to allow to introduce innovative technologies of welding and quality control in the production, mainly of metals. This makes the company able to improve the competitively, productivity and/or the quality of the production.

The micro-assembly technologies such as laser, electron beam welding, friction stir welding, micro-TIG, micro-plasma, radiography, … will be valorized.

3 CONCLUSIONS

This platform MICROSOUD will support the build-up of a network of competitive SME's in the domain of micro-assemblies and micro-controls. They will have access to similar technologies which will improve and accelerate the dissipation and the transfer of technology, in the direction of the SME's, as well as in the direction of technology centers and training centers.

4 ACKNOWLEDGEMENTS

FATIGUE INVESTIGATION OF THREADED PIPE CONNECTIONS

J. Van Wittenberghe[1], J. De Pauw[1], P. De Baets[1], W. De Waele[1], M. Abdel Wahab[1], W. Ost[1], G. De Roeck[2] and T.T. Bui[2]

[1] Ghent University, Laboratory Soete, Belgium
[2] K.U.Leuven, Department of Civil Engineering, Belgium

Abstract Threaded pipe connections are used to connect well casing, well tubing, drill pipes and risers. For many of these applications fatigue resistance plays an important role. In this study the fatigue properties of threaded connections are studied using a combination of finite element modelling and experimental testing. Using 2D axisymmetric FE analysis several connections are compared. It is shown that the load distribution over the engaged threads is an important feature. Experimental tests are carried out on three setups. A small scale four-point bending setup is used to develop S-N curves. An S-N curve for a standard API Line Pipe connection is compared to an S-N curve for a connection that showed an improved load distribution over the engaged threads in the FE analysis. On a medium scale four-point bending setup, strains together with crack opening are measured. The strain measurements are compared with the strains obtained by the numerical model. Finally a full scale resonant bending fatigue setup is presented, which will be used in future testing of pipe connections ranging from 168 mm (6") to 508 mm (20") in diameter.

Keywords threaded connection, threaded and coupled, premium connection, pipe, finite element model, experiment, fatigue, four-point bending, resonant bending

1   THREADED CONNECTIONS: AN OVERVIEW

Fossil fuels such as oil and natural gas are finite resources. However, they will continue to be significant energy providers during the foreseeable future. Increased demand presents several engineering challenges since exploration of new sources moves further to greater depths, deeper ocean water and into harsher environments. This results in extreme requirements for the equipment used during exploration and exploitation of the wells.
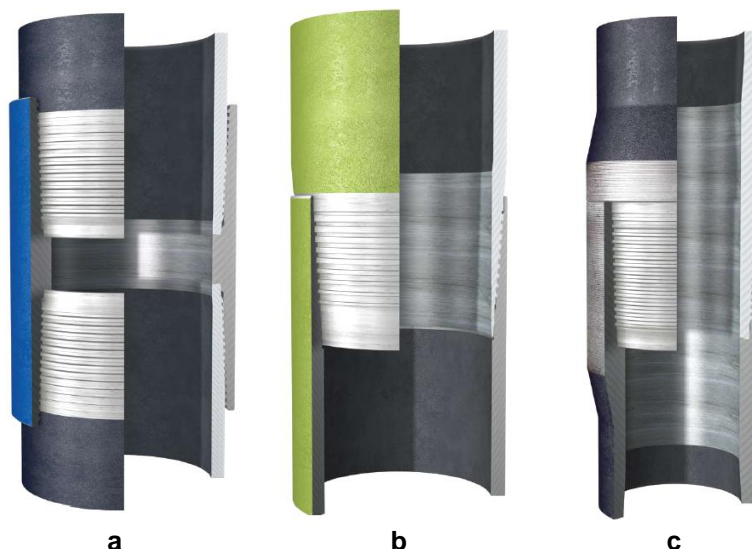
Figure 1. a) Threaded and Coupled, b) Integral Flush, c) Integral Upset Connection [1]

During well construction, a hole is drilled using a drilling tool connected to a long string of subsequent drill pipes. To avoid the well from collapsing, casing pipes are placed inside the well. After well completion, a tubing string is inserted by which the oil and gas flows to the surface. In case of offshore wells, an additional riser pipeline connects the wellhead at the bottom of the sea to a production platform. The drill pipes, the casing and tubing and in many cases also the riser pipes are connected using threaded connections. The threaded pipes of casing and tubing are regularly called *Oil Country Tubular Goods* (OCTG). Generally, threaded pipe connections can be divided in three different types, as can be seen in

Figure 1 [1]. For the first type, the pipes carry male threads at both ends and a separate coupling part is used to connect them. These connections are called *Threaded and Coupled* (T&C, see Figure 1.a) and are commonly used in OCTG and riser applications. The other types are called *Integral* types, since the pipes have a male and female part of the connection at either end. Hence no separate coupling part is used for these connections. When the connection is produced in the pipe material without any local increase in inside or outside diameter, it is called a *flush* connection (see Figure 1.b). However, when the connection is produced in a part with a thicker wall than the rest of the pipe, it is called an *upset* connection (see Figure 1.c). Integral flush connections are used in casing pipes while integral upset connections are more common for tubing and drill pipes. The male and female part of a threaded connection are called respectively *pin* and *box*.

A number of casing, tubing and drill pipe connections are standardized by the American Petroleum Institute (API) [2, 3]. Most OCTG connections are T&C types, and the drill pipes have integral connections. However, as can be seen from Table 1, the applicability of those connections is restricted to oil wells and onshore gas wells with limited depth and bottom hole pressure. Once connections are needed that require better characteristics, so-called *premium connections* should be used, which are connections developed by private companies. Theses connections exhibit better performance than the standard API connections.

Gas Wells	Offshore	Premium Connections	
	Onshore	API	
Oil Wells			
Well Depths [km]		3.0	6.0
Bottom Hole Pressure [bar]		275	550

Table 1. Applicability of API and premium connections

Typically standard OCTG connections were designed for static load cases, such as tension or compression, bending and internal or external pressure, that either alone or combined affect the string. The main design concern for these connections was leak-tightness. Riser connections are additionally subjected to high dynamic loads caused by waves and currents. And with drill strings dynamic loads are introduced by bending during drilling and torque vibrations. This introduces additional requirements for the fatigue resistance of these premium connections. Additionally, when moving to deeper wells and offshore gas wells, the bottom hole pressure increases and additional sealing measures have to be provided.

Although there exists a wide variety of premium drill connections, during the last years there is a tendency to use casing pipes for drilling particular wells [4-6]. This is more cost-effective since no drill pipes are necessary and the casing can stay in the well after drilling. However, this practice demands better fatigue properties for OCTG connections since they are subjected to additional dynamic loads due to the drilling operation. Hence with changing applications and environmental conditions, threaded connections of all kinds need continuous improvement and fatigue resistance is one of the important features that has to be considered.

In this study the fatigue resistance of threaded pipe connections is studied using numerical modelling and experimental testing. With the numerical model, a wide variety of connections can be assessed in a relatively fast and structured way, which can reveal general trends and underlying mechanisms. However experimental testing remains a necessity since the model output depends highly on prior assumptions, simplifications and boundary conditions. Hence experimental data serves as validation of the results generated by the simulations. In the following paragraphs an overview will be given of the obtained results of this study.

2   NUMERICAL MODELLING

2.1   Axisymmetric model

Threaded pipe connections are commonly modelled using 2D axisymmetric finite element models with elastic-plastic material behaviour and contact interaction of the threads [6-10]. Full 3D models of threaded couplings still require very long calculation times due to the high number of nodes in the contact analysis. The disadvantage of the 2D simulations is that they neglect the helical shape of the threads and the runout region. However, it was recently validated by the authors and earlier by Zhong [12] that the results of 2D axisymmetric models are in good agreement with the results of accurate time-consuming full 3D models.

The connection modelled in this study is a API Line Pipe threaded and coupled connection. The modelled connection is shown in Figure 2 and has a size of 4.5" with dimensions according to the API 5B

specifications [2]. For the numerical model, only the section in the dashed rectangle is used. The resulting model is shown in Figure 3. The model geometry is generated by the parametrical program *ThreadGen*[©] developed at the Laboratory Soete [13]. This allows easy variation of the connection's geometrical parameters such as pin and box diameter and wall thickness, number of engaged threads and thread dimensions. This is particularly useful to compare different geometrical modifications, since numerous premium connections exist, which claim to provide better fatigue properties by changing the box geometry. However, no quantifiable results have been published to prove such claims.

2.2   Analysis results

To ensure adequate sealing and a robust connection while being subjected to external loads, the connections are preloaded. To introduce this preload, the API Line Pipe connection has a conical shape (see Figure 2). Premium connections frequently use rotary shouldered connections with one or more metal-to-metal sealing surfaces. The connection is then assembled by giving it a number of rotations, which results in a certain *make-up torque*, which has a specific value for every connection type and size. The make-up is modelled in the 2D axisymmetric models by giving the pin and box a certain radial overlap corresponding to the specified number of make-up turns. Due to the combination of the make-up turns and external loads, together with the thread geometry, a complex multiaxial stress distribution develops over the connection. In Figure 4, the von Mises equivalent stress is shown for make-up only (Figure 4.a) and for the combination of make-up and an external axial tensile stress of 150 MPa (Figure 4.b). Note that the location with the highest stress is the last engaged thread (LET) of the pin (as indicated by the arrow in Figure 4.b), which will be the region where fatigue cracks will tend to initiate. The high stress intensity at the LET of the pin is a result of the non-uniform load distribution over the different engaged threads of the connection (see Figure 5). For this reason and the fact that improved fatigue resistance is aimed for, one should try to get a more uniform load distribution over the connection.
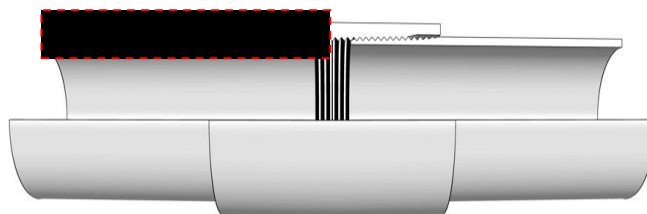

Figure 2. API Line Pipe T&C connection: section view
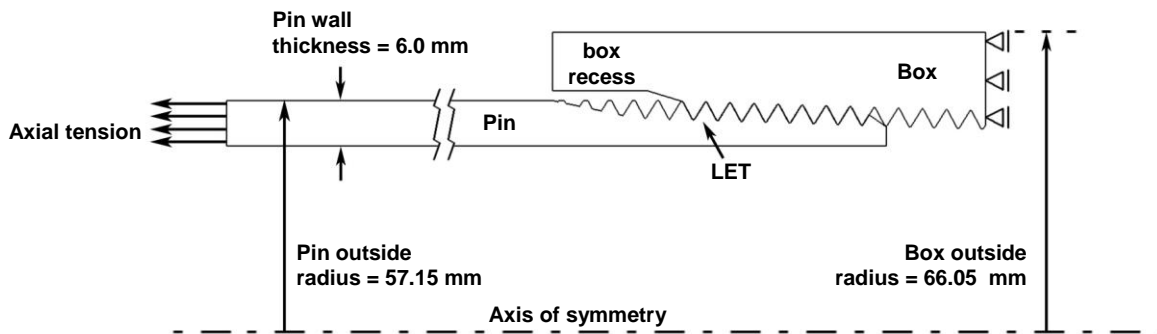
Figure 3. 2D axisymmetric model of the API Line Pipe connection
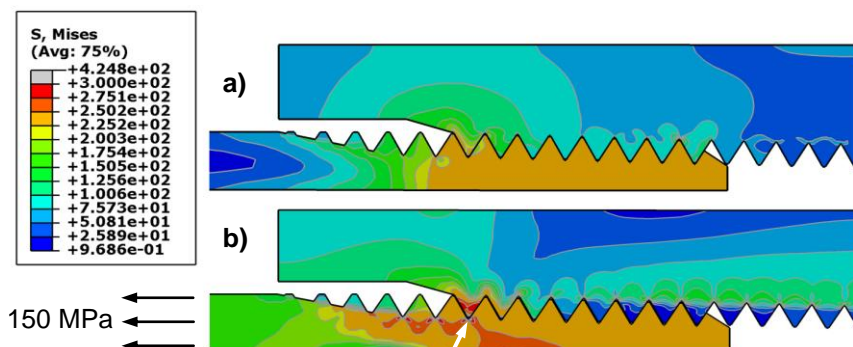
Figure 4.Von Mises stress distribution a) at make-up, b) with additional external axial tensile stress of 150 MPa
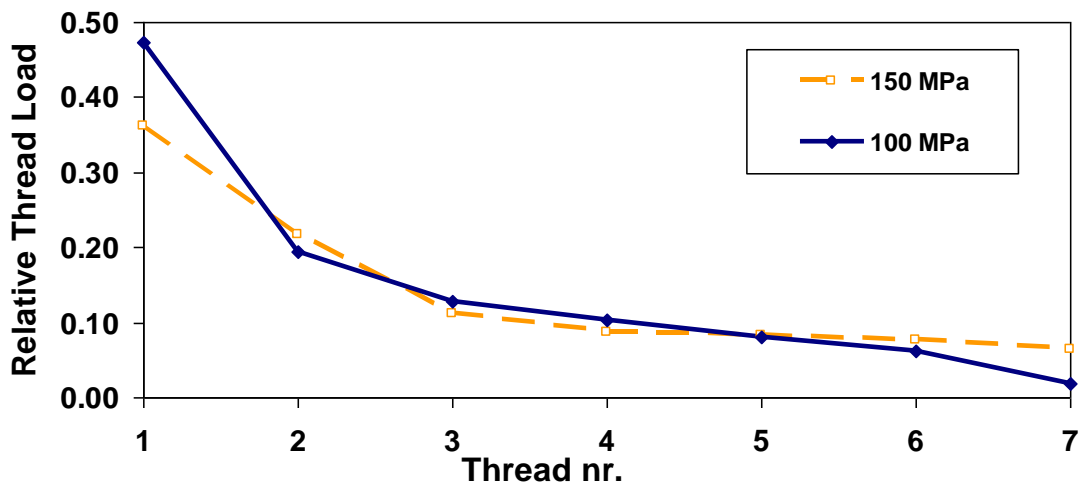
Figure 5. Load distribution over the engaged threads of the connection (LET = thread nr. 1)

3   EXPERIMENTAL FATIGUE TEST SETUPS

To obtain experimental results over a wide pipe diameter range and to be able to assess size effects, three different experimental fatigue setups are used. In the following paragraphs all three setups are discussed.

3.1   Small scale four-point bending setup

Tests were carried out on standard 1" (pipe diameter = 33.4 mm) API Line Pipe connections on the small scale four-point bending setup to develop S-N curves. This setup, shown in Figure 6, is built on an ESH 100 kN universal test machine. The test sample consists of a central box (1a) with two made-up threaded pipes (1b) and is supported by the two outer load points (indicated by the blue arrows in the figure). A dynamic load is applied by the hydraulic actuator (2) and transferred through the loadcell (3) to a transverse beam that carries the two inner load points. To avoid a bending moment in the loadcell, the loadcell is connected to the transverse beam through a hinge (4).

Tests were carried out under load control with a load ratio $R = F_{min} / F_{max} = 0.1$ and at a testing frequency of 15 Hz. To detect through thickness cracks, the tube samples were pneumatically pressurized at a pressure between 1 and 2 bar. When a crack grows through the wall thickness of a pipe, pressure drops below a threshold and the test is stopped. The number of elapsed load cycles before the stop, is considered the fatigue life of the connection. To create two separate pressure chambers, a plug is inserted inside the box, between the two threaded pipe samples. This way a crack in either pipe sample could be distinguished from each other. The internal pressure in the two samples was continuously monitored using the pressure transducers (5) at both ends of the test sample. After a pressure drop, the connection was disassembled and the exact crack location was found using die penetrant. The failed pipe was then replaced by a dummy sample and the test continued until failure of the second pipe occurred.

In Figure 7.a the obtained S-N curve of the standard 1" API Line Pipe connection is compared to the results of an optimized connection for which the box wall thickness was reduced with 1 mm. It can be seen that the latter has a fatigue limit that is about 20% higher. This better fatigue performance can be explained by the improved (i.e. more uniform) load distribution over the connection as shown in Figure 7.b. The stress amplitude σ_a is given as a percentage of the material's yield stress σ_y (356 MPa).
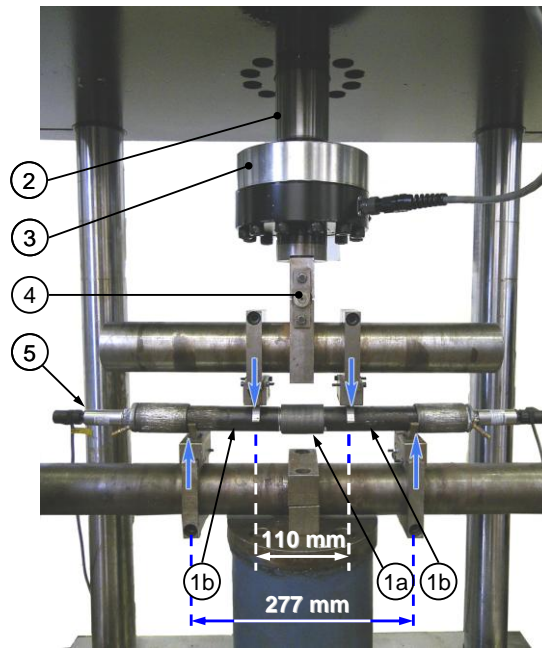
Figure 6. Small scale four-point bending test setup
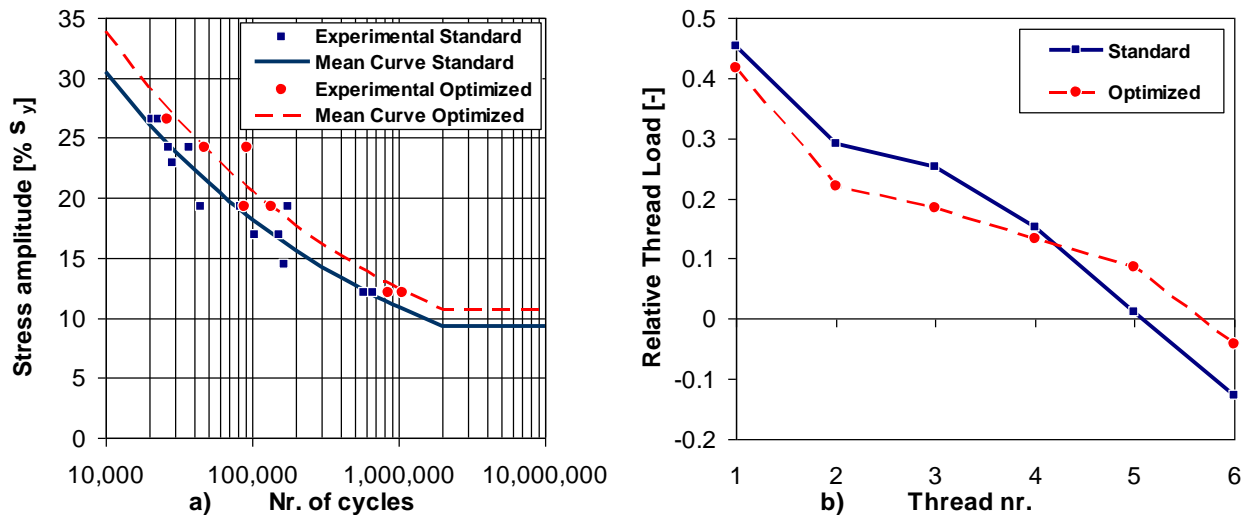
Figure 7. a) S-N curves for the standard 1" API Line Pipe connection and for a modified connection with changed wall thickness, b) thread load distribution for the standard and modified connection

3.2 Medium scale four-point bending setup

To test 4.5" (pipe diameter = 114.3 mm) API Line Pipe Connections, the medium scale four-point bending test setup, schematically shown in Figure 8, is used. The test specimen, consisting of two threaded pipe segments (1b) connected by a 4.5" API Line Pipe coupling (1a), is carried by two supports that are positioned 3 m apart on a central beam. A vertical force is applied by a hydraulic cylinder (2) that is connected to a transverse beam by a ball joint (4), with a loadcell (3) in between. The beam transmits the load to two points on the test specimen symmetric to the coupling. Strains are measured by strain gauges (5) on both pin and box. Since fatigue cracks are expected to initiate from the last engaged thread of the pin, two clip gauges (6) are mounted at either side of the box, to measure the axial distance between the edge of the box and a point on the pipe body of the pin. This way when a crack starts to grow, the crack opening displacement is detected by the clip gauges. Tests are carried out at a load frequency of 1 Hz.

In Figure 9.a a comparison is given between the strains calculated by the finite element model as described in section 2 and the strains measured by the strain gauges. In Figure 9.b the crack opening displacement is shown as measured by the clip gauge over the side that cracked. It can be seen that the crack started to grow rapidly after about 18600 cycles. The test was stopped after 20350 cycles.
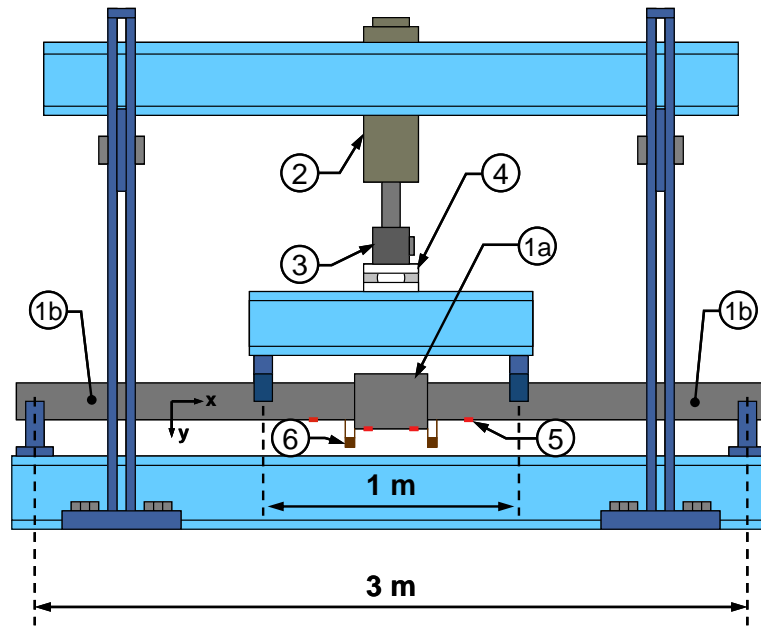
Figure 8. Medium scale four-point bending test setup
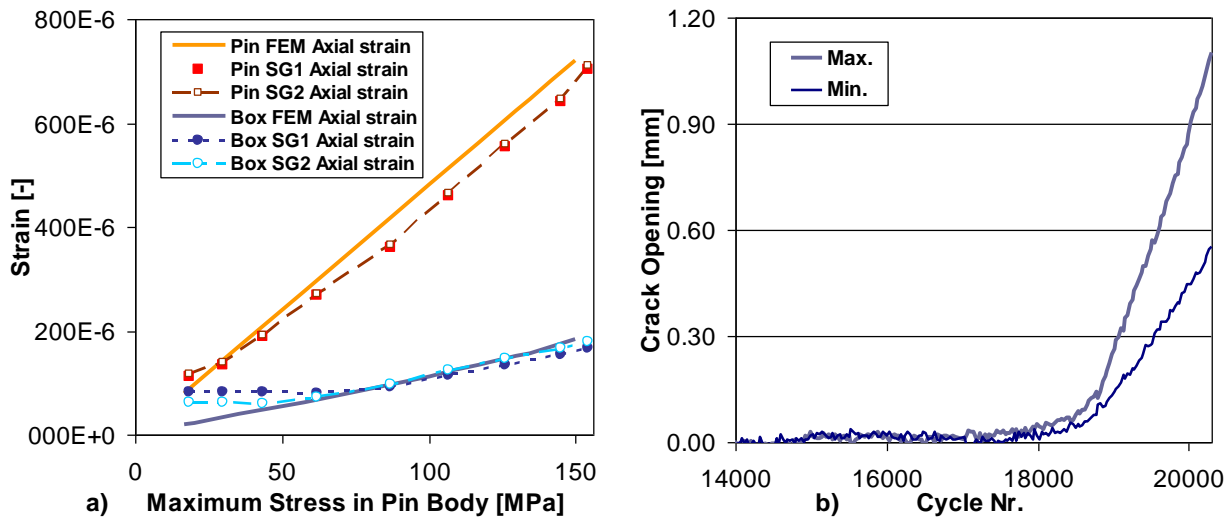
Figure 9. a) Comparison between modelled and measured strains, b) crack opening

3.3 Full scale resonant bending fatigue setup

To test couplings with a diameter up to 20", a new full scale resonant bending fatigue test setup was developed at the Laboratory Soete. A representation of the setup is shown in Figure 10. In this setup the test pipe (1) with a central threaded connection is excited by a drive unit (2) with eccentric masses. This unit is powered via a cardan shaft (3) by an electrical motor (4) of 7.5 kW. The excitation frequency is close to the natural frequency of the system. At the other pipe end a compensating mass (5) is attached to obtain a symmetric deformation of the pipe. The pipe is supported by the two supports (6) which are placed in the nodes of the first eigenmode of the system. The position of these supports can be changed by hydraulic cylinders. The total setup is placed on a heavy framework (7) and an additional safety frame (8) is placed over the central section of the pipe. This central section will be subjected to the highest cyclic loads during the fatigue test.

Pipe Diameter	Pipe Wall Thickness	Pipe Length	Pipe Deflection	Frequency	Motor Power
168 mm to 508 mm (6" to 20")	5 mm to 40 mm	4 m to 6 m	13 mm to 38 mm	20 Hz to 40 Hz	7.5 kW

Table 2. Resonant bending setup properties

The main properties of the setup are summarized in Table 2. Based on the size of pipe diameter and wall thickness, the pipe length is chosen to obtain a natural frequency within the range of the electrical motor (from 20 to 40 Hz). To lower the natural frequency of the pipe, it is filled with water which will be slightly pressurized for the purpose of leak-detection. The deflection of the pipe depends on the desired stress level and will be about 13 to 38 mm. Test results obtained with this new setup will be published in the future.
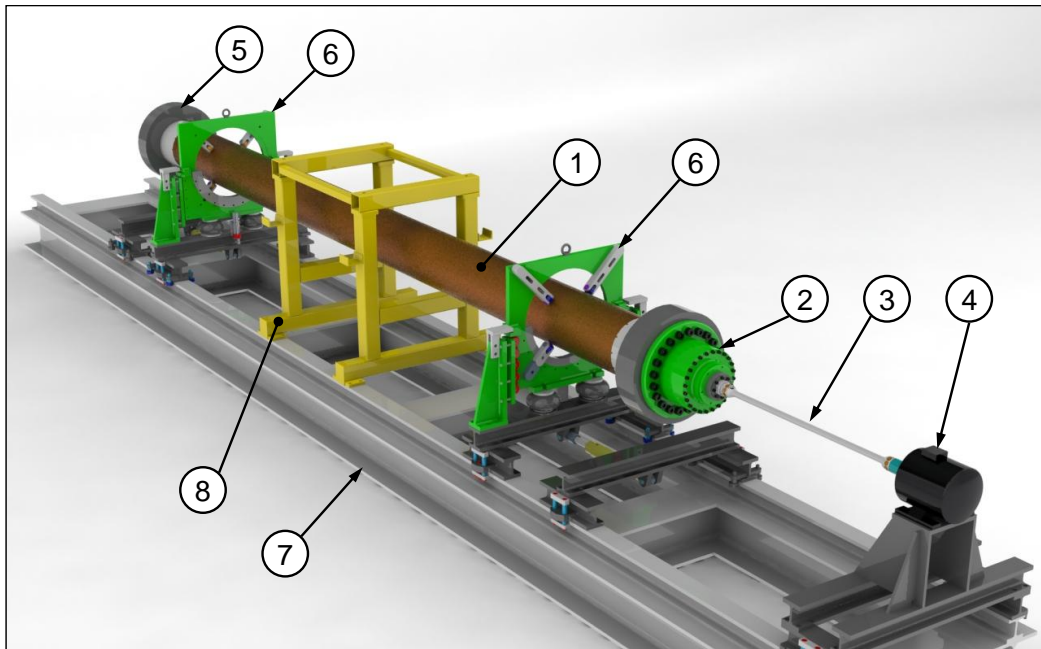
Figure 10. Full scale resonant bending fatigue setup

4   CONCLUSIONS

Fatigue resistance is an important feature for a wide range of threaded pipe connections. In this paper the fatigue properties of threaded connections are studied using a combination of numerical modelling and experimental testing. From the developed 2D axisymmetric finite element model it is known that the high stress concentration at the LET of the pin is caused by a highly non-uniform load distribution over the different engaged threads of the connection. Three different experimental fatigue setups for testing pipes from small to full scale are discussed. Results of strain measurements and S-N curves correspond well with trends observed in the numerical model. Future work will include full scale tests on a resonant bending fatigue setup.

5   ACKNOWLEDGEMENTS

6   REFERENCES

[1] TenarisHydril, *Premium Connections Catalogue*, http://www.tenaris.com/tenarishydril/, Version 01, March 2009.
[2] API Specification 5B, *Specification for Threading, Gauging and Thread Inspection of Casing, Tubing and Line Pipe Threads (U.S. Customary Units)*, American Petroleum Institute, fourteenth edition, 1996.
[3] API Specification 7, *Specification for Rotary Drill Stem Elements,* American Petroleum Institute.
[4] Santi, N. J., Carcagno, G. E., Toscano, R., *Premium & Semi-premium Connections Design Optimization for Varied Drilling-with-Casing Applications*, Offshore Technology Conference, OTC17221, 2005.
[5] Strickler, R.D., Wadsworth, T.M., *Drilling with casing: Are you damaging your casing?*, World Oil, 3, 51–53, 2005.
[6] Carcagno, G.E., Bufalini, A., Conde, L., Toscano, R., *Low SCF Integral Premium Connections for Use in Highly Demanding Casing and Tubing Drilling Operations*, Offshore Technology Conference, OTC16566, 2004.

[7] Dvorkin, E.N. and Toscano, R.G., *Finite element models in the steel industry, Part II: Analyses of tubular products performance*, Computers and Structures, 81(8-11), 575–594, 2003.

[8] Kristensen, A.S., Toor, K., Solem, S.I., *Finite Element analysis of jar connections: modeling considerations*, Journal of Structural Mechanics: Special issue for the 18th Nordic Seminar on Computational Mechanics, 1-4, Helsinki, Finland, 2005.

[9] Guangjie, Y., Zhenqiang, Y., Qinghua, W., Zhentong, T., *Numerical and experimental distribution of temperature and stress fields in API round threaded connection*, Engineering Failure Analysis, 13(8), 1275–1284, 2006.

[10] Bertini, L., Beghini, M., Santus, C. and Baryshnikov A., *Fatigue on drill string conical threaded connections, test results and simulations*, 9th Int. Fatigue Congress, Atlanta, USA, 2006.

[11] Santus, C., Bertini, L., Beghini, M., Merlo, A., Baryshnikov, A., *Torsional strength comparison between two assembling techniques for aluminium drill pipe to steel tool joint connection*, International Journal of Pressure Vessels and Piping, 86(2-3), 177-186, 2009.

[12] Zhong, A., *Thread Connection Response to Critical Pressures*, Abaqus Users' Conference, pp. 690–706, Paris, France, May 2007.

[13] Van Wittenberghe, J., De Baets, P., De Waele W., *Modeling of preloaded threaded pipe connections*, 8th National Congres on Theoretical and Applied Mechanics, 149–156, Brussels, Belgium, 2009.

EVALUATION OF PIPE BENDING REFERENCE STRESS EQUATIONS

M. Verstraete[1], W. De Waele[1], S. Hertelé[1], R. Denys[1]

[1] Ghent University, Laboratory Soete, Belgium

Abstract The use of a Failure Assessment Diagram (FAD) is widespread in the assessment of weld defects. To determine whether a defect is acceptable or not, this requires the calculation of a load ratio and a fracture ratio for the defect under consideration. Nowadays, many formulae are available to calculate these two quantities and no clear guidance is given on which equation(s) should (not) be used. A partial clarification of this problem is achieved by comparing different reference stress equations. This article is concerned with such comparison, for the specific case of welded pipes subjected to a bending load. A large set of historical experimental data has been investigated in which defected pipes were subjected to an increasing bending force until failure occurred. Two kinds of reference stress equations are considered, full pipes subjected to a bending load and flat plates subjected to a uniform tension load. From the equations under consideration, the flat plate solution of Goodall & Webster and the empirical full pipe equations of Willoughby and Wilkowski & Eiber describe the pipe failure in the most accurate way.

Keywords Failure Assessment Diagram, Reference stress, Pipe bending, Defects

1 INTRODUCTION

Girth welds of pipelines unavoidably contain defects. Whether these defects are acceptable or not is, in codes and standards, often determined by using a Failure Assessment Diagram (FAD) [1, 2]. This paper focuses on the assessment prescribed in the general European FITNET procedure [3].

Using a FAD, two values have to be calculated in order to determine the severity of a defect. The first value is the fracture ratio (K_r), which is determined as the ratio of a stress intensity factor to the material's fracture toughness. The stress intensity factor can be calculated by different available formulae [3, 4]. In this paper, only the Newman and Raju equation (see Appendix B) will be used. The second value is the load ratio (L_r), determined as the ratio of a reference stress to the material's yield strength. The reference stress can be calculated according to many formulae, each of them applicable to a specified load condition and geometry. If the calculated failure assessment point (L_r, K_r) is located underneath the failure assessment curve, the defect is considered to be acceptable (see Figure 1).

$$K_r = \frac{Stress\ intensity\ factor}{Material's\ toughness}$$

$$L_r = \frac{Reference\ stress}{Material's\ yield\ stress}$$
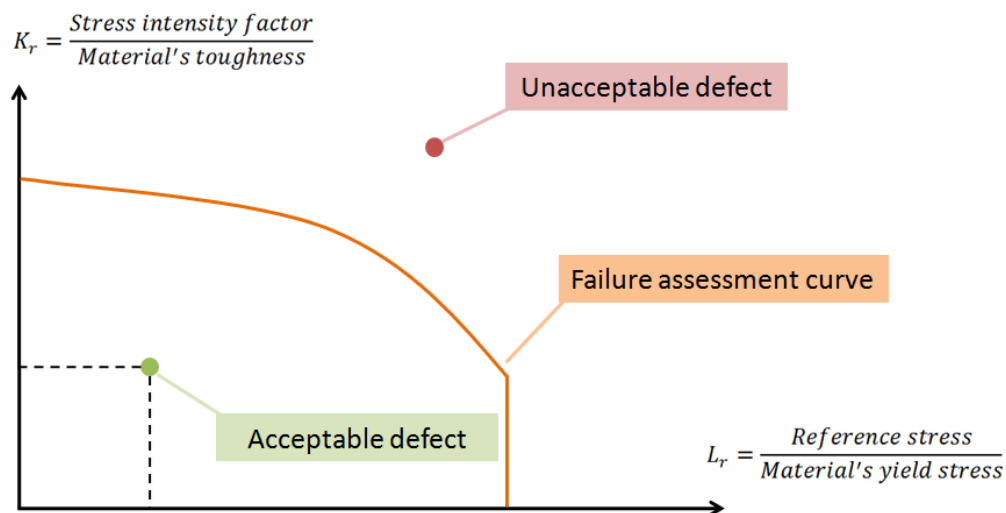
Figure 1. The Failure Assessment Diagram (FAD) can be used to determine the acceptability of a defect

In the open literature, many equations are available to calculate the reference stress, which makes it complicated to decide which equation should be used. Therefore a comparison of reference stress equations was made for pipes subjected to a bending moment, based on a large amount of full scale test data [5, 6]. The equations under investigation were derived either for full pipes subjected to a bending load or for flat plates subjected to a uniform tension load. This paper briefly describes the used reference stress

equations and then compares them based on the historical experimental data. Final conclusions provide advice on which equation should be used for the considered case.

2   REFERENCE STRESS EQUATIONS

Following a literature review, several reference stress equations have been selected. The following paragraphs give a brief description of these equations together with their limitations. The defect dimensions are defined according to Figure 2.
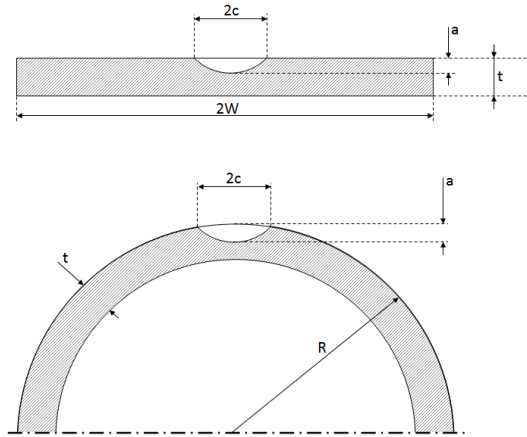
Figure 2. Pipe, plate and defect dimensions used in limit load equations

The pipes are loaded as illustrated in Figure 3. From the applied bending moment, the bending stress can be calculated in two ways, elastically ($\sigma_{b,e}$) and plastically ($\sigma_{b,p}$):

$$\sigma_{b,e} = \frac{M}{\pi \cdot R^2 \cdot t} \tag{1}$$

$$\sigma_{b,p} = \frac{M}{4 \cdot R^2 \cdot t} \tag{2}$$
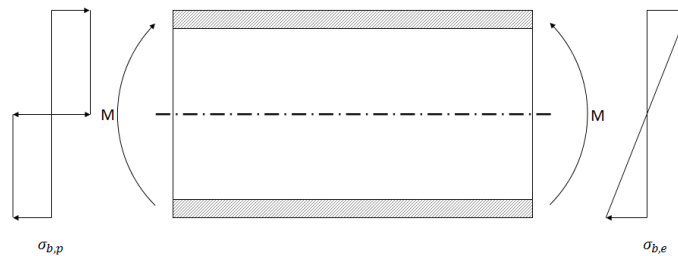
Figure 3. Applied load

The reference stress equations can be divided into two subgroups. On the one hand reference stress can be calculated using equations for entire pipes subjected to bending. On the other hand reference stress equations obtained from flat plates subjected to a uniform tensile stress are discussed. This second category makes sense since the pipe section containing the defect is in the tension loaded region of the pipe. Besides for large D/t-ratios this section is subjected to a (nearly) constant stress and the curvature of the plate is limited.

2.1   Full pipe bending reference stress solutions

The applied stress (elastically or plastically) used in these equations differs, depending on the way the equations were developed.

2.1.1   Wilkowski and Eiber equation [7]

The Wilkowski and Eiber equation is empirical. The reference stress (σ_{ref}) can be calculated using the following equations:

$$\frac{\sigma_{b,e}}{\sigma_{ref}} = \frac{\eta}{1 - \frac{(1-\eta)}{M_0}} \tag{3}$$

$$M_0 = \sqrt{1 + 0.26\, z + 47\, z^2 - 59\, z^3} \tag{4}$$

191   Copyright © 2010 by Labo Soete

With:

$$\eta = 1 - a/t$$
$$z = {}^{c}/_{\pi R}$$

The dimensionless parameter η represents the size of the uncracked ligament (*t-a*) relative to the wall thickness (*t*), whilst the parameter *z* represents the relative length of the crack (*2c*) to the circumference of the pipe (*2\pi R*). The Wilkowski and Eiber equation has been validated based on tests for *z*-values up to 0.15.

2.1.2   Willoughby equation [7]

Another empirical equation is the Willoughby equation which has been experimentally validated for η-values up to 0.2. The Willoughby reference stress is calculated using the next equation:

$$\frac{\sigma_{b,e}}{\sigma_{ref}} = 1 - 1.6\,(1 - \eta)\beta$$

With:

$$\beta = {}^{c}/_{R}$$

The dimensionless parameter β represents the semi-angle of the circumferential crack in a cylinder.

2.1.3   Miller equation [7]

This analytical equation was derived by Miller and is advised by the FITNET procedure. The net section collapse formula contains two different equations depending on the position of the neutral axis:

$$\frac{\sigma_{b,p}}{\sigma_{ref}} = \cos\frac{(1-\eta)\,\beta}{2} - \frac{(1-\eta)\sin\beta}{2} \qquad if\ \beta \le \frac{\pi}{1+\eta} \tag{5}$$

$$\frac{\sigma_{b,p}}{\sigma_{ref}} = \eta\,\sin\frac{\pi - \beta\,(1-\eta)}{2\,\eta} + \frac{(1-\eta)\sin\beta}{2} \qquad if\ \beta > \frac{\pi}{1+\eta} \tag{6}$$

No limitations have been found for this equation.

2.2   Plate tension reference stress solutions

The applied stress used to calculate the reference stress, is the plastic bending stress ($\sigma_{b,p}$) as defined in equation 2. From a comparison of different plate widths, it was seen that a plate-half width (*W*) of 300mm resulted in the most accurate predictions for the equations described below. Therefore plate half-width (*W*) is assumed to be 300 mm except for these two cases which define the plate width. Firstly the FITNET plate equation, which prescribes a plate width equal to the sum of the crack length (*2c*) and two times the wall thickness (*2t*). Secondly, the net section yielding equation is based on a reference stress calculation using a fixed plate width of 300mm.

2.2.1   Goodall & Webster equation[8]

An analytical reference stress equation for plates subjected to bending and tensile loading was presented by Goodall & Webster. This equation is applicable to *a/t*-ratios below 0.5. Reducing this equation to pure tension results in the following reference stress equation:

$$\frac{\sigma_{ref}}{\sigma_{b,p}} = \frac{\gamma + \left\{\gamma^2 + \left[(1-\gamma)^2 + 2\,\gamma\,(\alpha-\gamma)\right]\right\}^{1/2}}{(1-\gamma)^2 + 2\,\gamma\,(\alpha-\gamma)} \tag{7}$$

With:

$$\alpha = a/t$$
$$\gamma = (a\,c)/(Wt)$$

2.2.2 Lei equation [9]

The Lei equation is based on a large number of finite element simulations. The crack geometries used to derive the reference stress equation have a/t-ratios from 0.2 to 0.8 and a/c-ratios from 0.2 to 1.0. The reference stress, in case of pure tension, can be calculated from the following equations:

$$\frac{\sigma_{b,p}}{\sigma_{ref}} = \frac{d_1}{\gamma + \sqrt{\gamma^2 + d_1}} \qquad\qquad \psi \leq 1 \qquad\qquad (8)$$

$$\frac{\sigma_{b,p}}{\sigma_{ref}} = \frac{d_2}{\gamma \frac{1-\psi}{\psi-\gamma} + \sqrt{\left(\gamma \frac{1-\psi}{\psi-\gamma}\right)^2 + \frac{\psi}{\psi-\gamma} d_2}} \qquad\qquad \psi > 1 \qquad\qquad (9)$$

With:

$$d_1 \;\; = (1-\gamma)^2 + 2\,\gamma\,(\psi - \gamma)$$

$$d_2 \;\; = (1-\gamma)\left[2 - \psi\,\frac{1-\gamma}{\psi-\gamma}\right] + 2\,\gamma\,(\psi - \gamma)$$

$$\psi \;\; = \frac{a}{t}$$

$$\beta_p \;\; = \frac{c}{W}$$

$$\gamma \;\; = \psi\,\beta_p$$

2.2.3 FITNET plate equation [3]

The FITNET plate solution is based on the Lei equation, but prescribes the plate width to be used. The plate width ($2W$) recommended by the FITNET standard is given by:

$$2\,W = 2\,c + 2\,t \qquad\qquad (10)$$

2.2.4 Net section yielding equation [10, 11]

This reference stress equation is basically a flat plate solution, which has been extensively used for the analysis of wide plate test results (with $2W$ = 300mm). The reference stress can be calculated using the following equation:

$$\frac{\sigma_{b,p}}{\sigma_{ref}} = 1 - \frac{a\,c}{W\,t} \qquad\qquad (11)$$

When the defect under consideration has a length exceeding 300 mm, the equation is assumed to be invalid.

2.2.5 Sattari-Far equation [12]

This equation has been determined by using finite-element analysis. The analysis was carried out on configurations containing defects with η-values ranging from 0.2 to 1.0 and c/a ranging from 1 to 5. The reference stress can be calculated solving the following equation:

$$\frac{\sigma_{b,p}}{\sigma_{ref}} = (1 - \zeta)^{0.87} \qquad\qquad (12)$$

With:

$$\zeta = \begin{cases} \dfrac{a\,c}{W\,t} & W < c + t \\[2ex] \dfrac{a\,c}{t\,(c + t)} & W > c + t \end{cases}$$

3 EXPERIMENTAL TEST DATA

The evaluation and comparison of the different equations is based on 59 full scale bend tests on (welded) pipes [5, 6]. The D/t-ratio of the tested pipes ranges from 28 to 90 and c/R is between 0.01 and 0.78. A summary of these test data, including the material's yield strength (σ_{YS}), the bending moment at failure (M_{fail}) and fracture toughness (K_{mat}) is presented in appendix A.

4 ASSESSMENT PROCEDURE

The assessment of each defect requires the calculation of the specific load ratio (L_r) and fracture ratio (K_r) [13]. Because this paper focuses on the comparison of reference stress equations, K_r is always calculated using the widely accepted plate solution derived by Newman and Raju (see Appendix B - [4]). This formula is also used in the BS7910 and the FITNET code [2, 3]. The different reference stress equations discussed in section 2 are used to calculate L_r for every pipe failure.

The failure assessment curve used for this comparison is the curve prescribed in the FITNET code in case of an Option 1 assessment. It should be stated that the FITNET Option 1 does not account for ductile tearing although this was reported for some failures. This can lead to a certain degree of over conservatism resulting from the fact that too much defects are assessed as unsafe. This might be prevented by using a higher assessment level, which unfortunately requires input data that is not available (p.e. the CTOD R-curve and the amount of tearing). Nevertheless, assuming a round-house post-yield behavior, the failure assessment curve for an Option 1 assessment is described by:

$$K_r = f(L_r) = (1 + 0.5\,L_r^2)^{-1/2} \cdot [0.3 + 0.7 \cdot exp(-\mu\,L_r^6)] \qquad L_r \le 1 \qquad (13)$$

$$K_r = f(L_r) = f(1)\,L_r^{(N-1)/(2\,N)} \qquad\qquad 1 < L_r \le L_{r,max} \qquad (14)$$

With:

$$N = 0.3\left(1 - {\sigma_{YS}}/{\sigma_{UTS}}\right) \text{ [-]}$$
$$L_{r,max} = 0.5\left(1 + {\sigma_{UTS}}/{\sigma_{YS}}\right) \text{ [-]}$$

Combining the calculated failure assessment curve and the failure assessment point (L_r, K_r) enables a plot in the FAD. The FADs for all reference stress equations can be seen in Figure 4 and 5. The assessment points located on the vertical axis represent invalid predictions because η or z was beyond the limitations discussed in section 2.1. For one case, the Newman and Raju equation could not be used because its limitations were exceeded. This assessment point is not presented in the FADs.
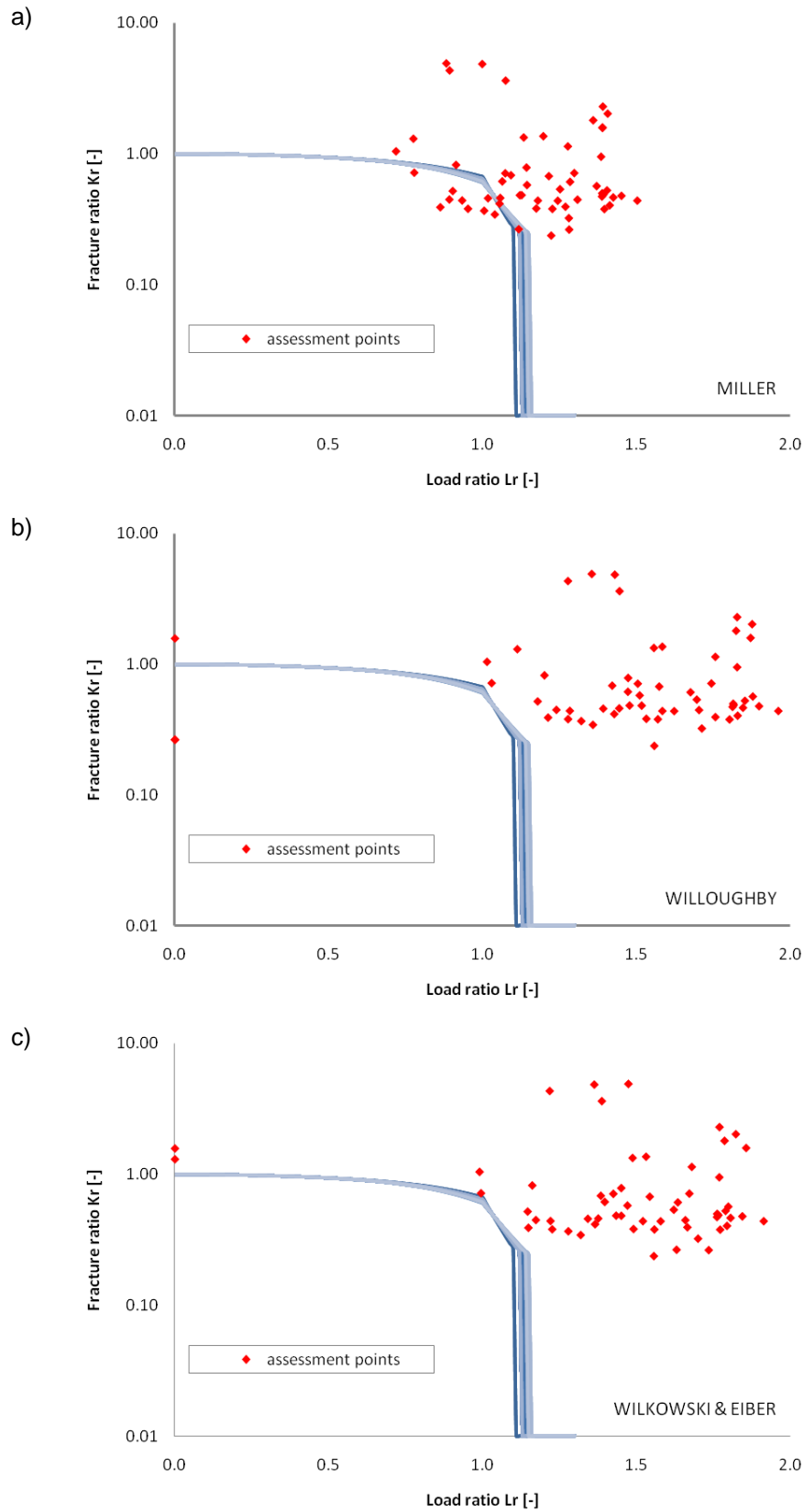
Figure 4. Failure assessment points using the Miller equation (a),
the Willoughby equation (b) and the Wilkowski and Eiber equation (c).
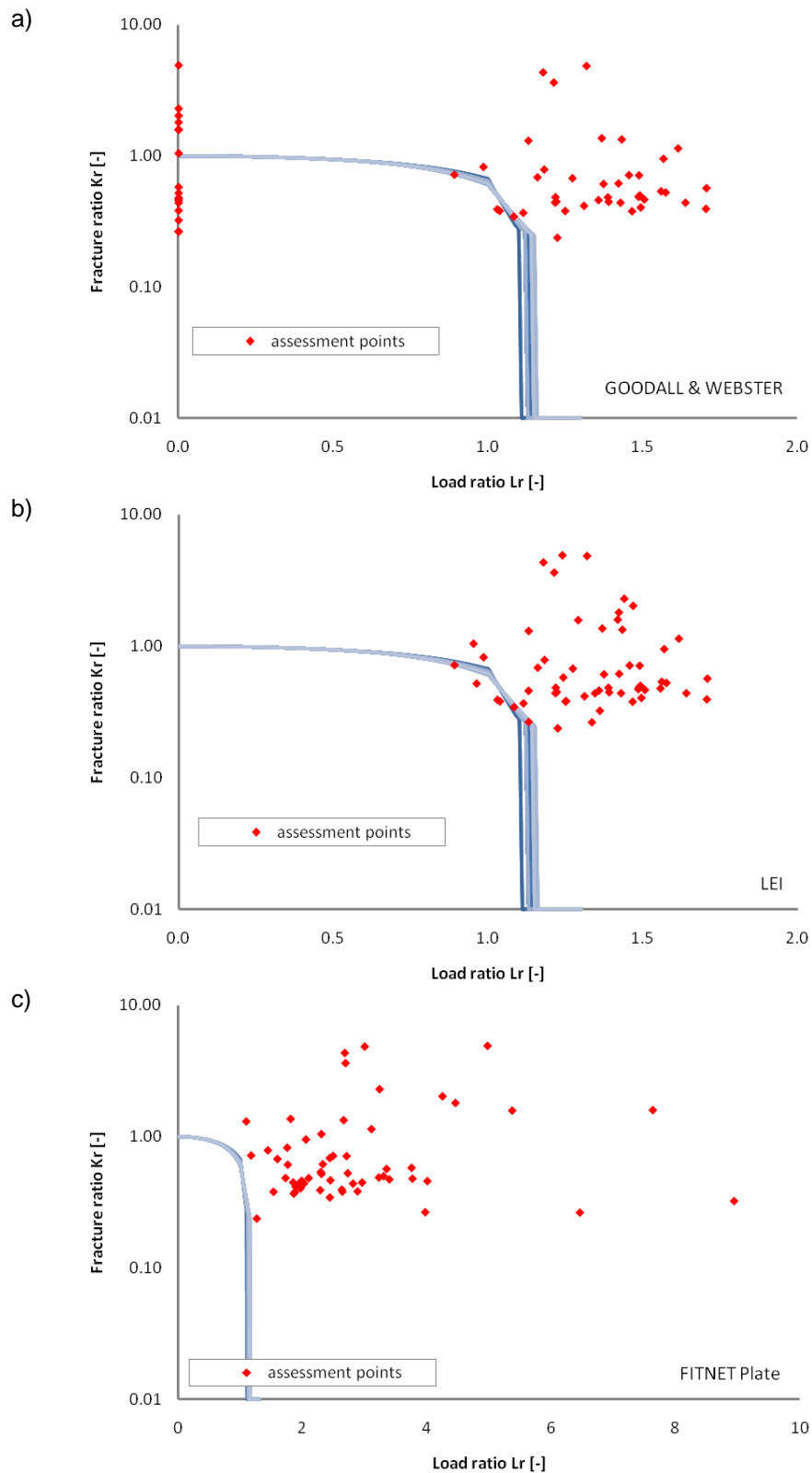
Figure 5. Failure assessment points using the Goodall & Webster equation (a),
the Lei equation (b) and the FITNET Plate equation (c).

d)

d)
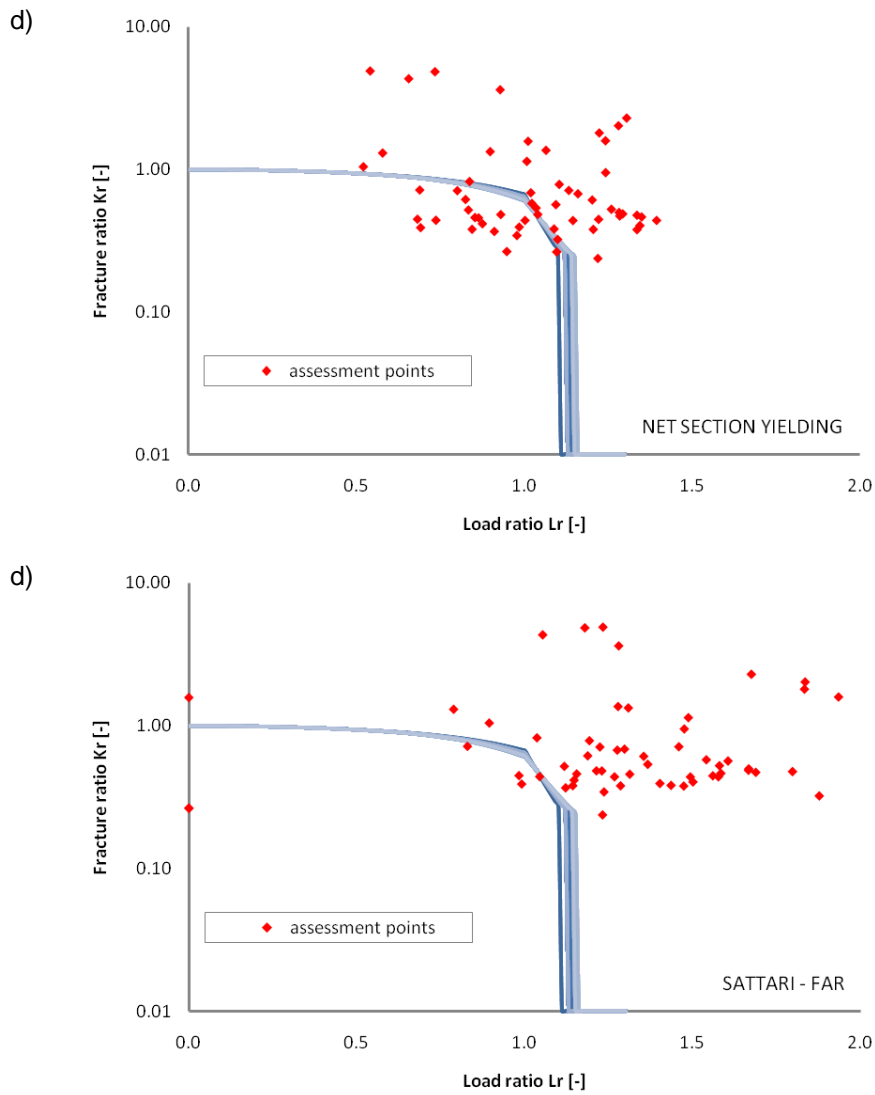
Figure 5. Failure assessment points using the Net Section
Yielding equation (d) and the Sattari-Far equation (e).
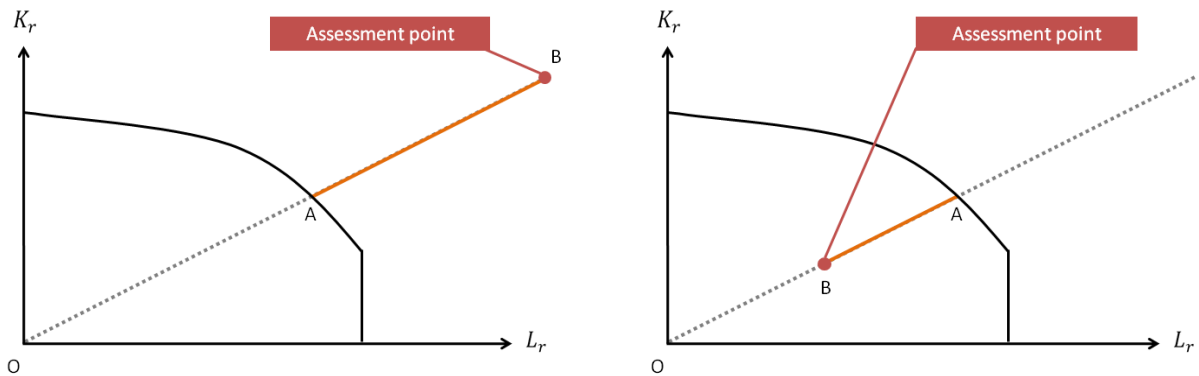
Figure 6. a) Degree of safety of the predicted failures (left) and b) Degree of unsafety of the predicted
failures (right)

197

5   COMPARISON & DISCUSSION

To judge which of the above reference stress equations predicts failure in the most accurate way, the different FADs have been compared according to different criteria. It should again be mentioned that the fracture ratio has been calculated using the Newman & Raju equation only.

5.1   Number of (un)safe predictions

A first comparison of the different equations is based on the number of unsafe predictions made by each equation (see Figure 7). A prediction is judged unsafe when the assessment point is located under the failure assessment curve because in that case the assessment procedure would have accepted the defect although failure actually occurred.

When it comes to unsafe predictions, the Net Section Yielding equation and the Miller equation show a high number of unsafe predictions. Willing to predict the failure as accurate as possible, this is not preferred. On the other hand, some equations show no unsafe predictions. From this point of view, the use of the Willoughby, Wilkowski & Eiber and the FITNET plate equation is recommended. The fact that the first two equations do not show any unconservative predictions is in good agreement with the empirical way in which they were derived. Noteworthy is also the high number of invalid predictions in case of the Goodall & Webster equation, which appear from deep cracks (deeper than half wall thickness).

5.2   Degree of safety

Besides the number of safe predictions, it is also useful to compare the degree of safety. When the failure is safely predicted, the degree of safety is defined corresponding Figure 6a as:

$$degree\ of\ safety = \ |AB| \tag{15}$$

The higher this number is, the more conservative the assessment is. From Figure 8 it can be concluded that the FITNET plate reference stress equation should not be recommended although no unconservative predictions were made. The predictions based on this equation incorporate too much conservatism, which does not enable an economical efficient design.

The difference between the other equations is limited, although it can be seen that the Goodall & Webster equation shows the best performance. The difference between this equation and for instance the Wilkowski & Eiber equation is still 18%.

5.3   Degree of unsafety

On the other hand, in case of an unsafe prediction, the degree of unsafety is also important. A small degree of unsafety might be acceptable because other safety factors are included in the assessment procedure. Analogue to the degree of safety, the degree of unsafety is defined as illustrated in Figure 6b:

$$degree\ of\ unsafety = \ |AB| \tag{16}$$

The degree of unsafety is compared for all reference stress equations in Figure 9. Hereby, the reference stress equations, which showed a large number of unsafe predictions or a large degree of safety are marked in grey and the focus is on the equations left. Taking into account the absence of unsafe predictions in some cases, a degree of unsafety equal to zero can be understood. Focusing on the equations which made unsafe predictions, the Sattari-Far equation and the Lei equation show a larger degree of unsafety than the Goodall & Webster equation.
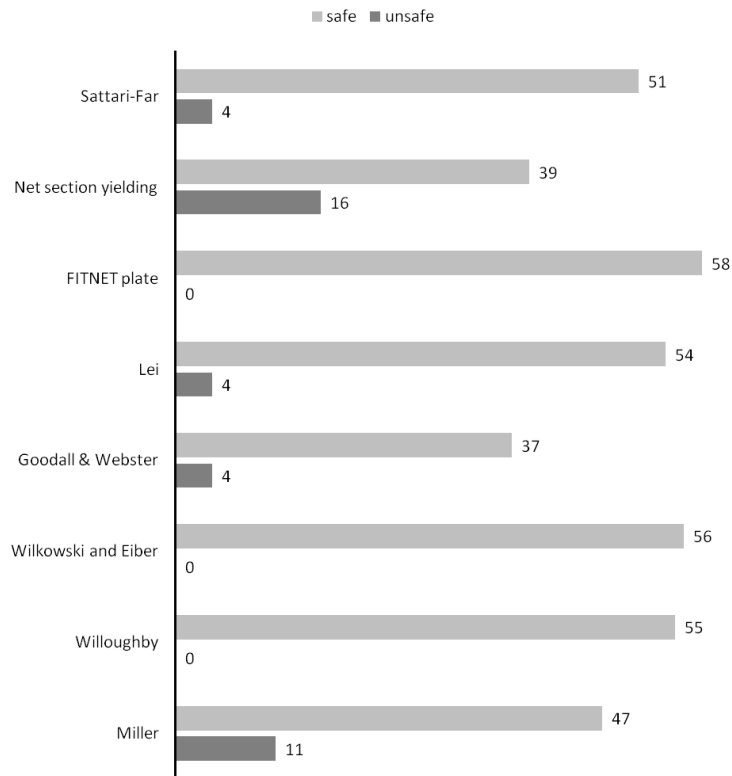
Figure 7. Comparison of the number of (un)safe predictions
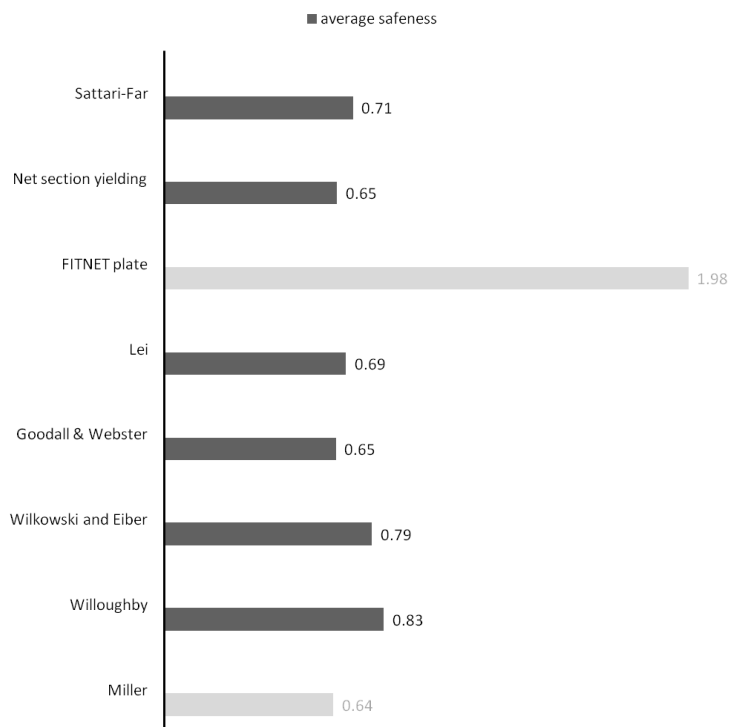
Figure 8. Comparison of the average and maximum safeness
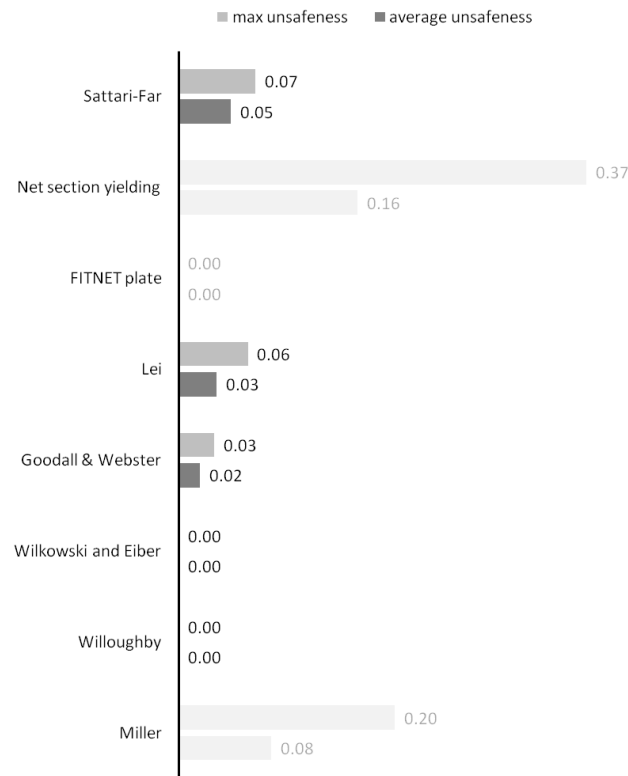
Figure 9. Comparison of the average and maximum unsafeness

6 CONCLUSIONS

Tree criteria have been used to compare and evaluate different reference stress equations. The flat plate solution of Newman & Raju is always used for calculating the fracture ratio. A historical database of full-scale bending experiments on (welded) pipes with circumferential defects has been assessed using the FAD approach. A number of different pipe and plate solutions have been used to calculate the reference stress and load ratio. From this comparison it can be concluded that the use of a flat plate solution, the Goodall & Webster equation, shows a comparable performance to the full pipe solutions by Wilkowski & Eiber and Willoughby. The strength of these three equations, compared to the other equations used in this comparison, is the limited degree of safety and unsafety in combination with a small number of unsafe predictions.

The two empirical equations, namely the Wilkowski & Eiber and the Willoughby equation, have the advantage over the Goodall & Webster equation that no unsafe predictions were made. On the other hand, the degree of safety is larger (+18%) for these empirical equations which might result in a more economical efficient design in case the Goodall & Webster equation is used. The most restrictive condition for using the Goodall & Webster equation is the fact that it is only applicable to shallow defects ($a/t < 0.5$).

Therefore, we advise to use the Goodall & Webster reference stress equation when an engineering critical assessment has to be performed for circumferential defects in pipes subjected to a bending load. If this equation is not valid, when the defect is too deep, the Wilkowski & Eiber or Willoughby equation should be used.

7   NOMENCLATURE

σ_{YS}	Yield stress	MPa
σ_{UTS}	Ultimate tensile stress	MPa
σ_{ref}	Reference stress	MPa
L_r	Load ratio	-
K_r	Fracture ratio	-
K_{mat}	Charpy V-notch toughness	MPa√m
ε_f	Strain at failure	-

8   ACKNOWLEDGEMENTS

9 APPENDIX A: EXPERIMENTAL TEST DATA [5, 6]

D [mm]	t [mm]	2c [mm]	a [mm]	K_{mat} [MPa√m]	σ_{YS} [Mpa]	M_{fail} [kNm]	ε_f [%]
914	11.1	63.5	5.9	136	531	6704	0.5
914	11.1	69.8	5.5	136	531	6704	0.5
914	11.1	68.6	7.8	74	531	5480	0.3
914	11.1	61.0	5.4	74	531	5286	0.3
914	11.1	76.5	10.1	74	531	2504	0.1
914	11.1	81.8	8.8	136	531	6074	0.5
914	11.1	59.3	6.4	74	531	4358	0.2
914	11.1	79.0	9.3	136	531	6074	0.5
914	11.1	63.5	6.3	136	531	7001	0.5
914	11.1	59.6	6.1	136	531	5675	0.4
914	11.1	64.8	5.5	136	531	6732	0.5
914	11.1	60.3	5.5	136	531	6333	0.5
914	10.3	300.0	4.1	154	689	5926	0.8
914	10.3	300.0	3.6	154	689	5926	0.7
914	11.1	265.0	3.3	136	531	5276	0.3
914	11.1	278.0	3.2	136	531	5888	0.4
914	11.1	279.0	3.9	127	466	3811	0.2
914	11.1	331.0	3.7	127	466	3616	0.2
914	11.1	75.0	3.5	127	466	6074	0.5
1067	15.0	14.0	0.9	131	496	10349	0.7
1067	15.0	38.0	3.0	131	496	10349	0.8
1067	15.0	70.0	8.0	131	496	10349	0.6
914	11.1	315.0	3.7	187	441	4887	0.3
914	11.1	282.0	3.1	127	466	4358	0.3
914	11.7	280.0	2.9	128	470	5219	0.4
914	11.7	134.0	3.7	128	470	4514	0.3
914	11.7	116.0	2.2	128	470	6423	0.7
610	6.8	100.0	3.1	121	532	1225	0.2
610	6.8	199.0	2.8	121	532	1074	0.2
610	6.8	51.0	3.1	121	532	1363	0.3
610	6.8	107.0	3.9	120	532	1290	0.2
508	8.7	108.0	8.7	20	469	1306	-
508	8.7	42.6	4.8	20	469	1437	-
508	8.7	44.9	8.7	20	469	1396	-
508	8.7	52.4	6.4	20	469	1383	-
508	8.7	52.4	6.8	20	469	1410	-
508	8.7	50.0	5.9	20	469	1437	-
762	15.8	239.0	11.9	20	573	4064	-
762	15.8	239.0	7.9	20	573	4312	-
762	15.8	119.0	7.9	20	573	5422	-
762	15.8	239.0	7.9	20	573	4826	-
914	11.7	112.0	2.0	126	460	6207	0.8
914	11.7	141.0	3.9	126	460	6148	0.4
914	11.7	300.0	3.5	126	460	4516	0.3
762	19.0	105.0	3.5	81	472	6244	0.4
762	19.0	139.0	3.7	99	472	6564	0.5
762	19.0	125.0	5.0	121	472	5737	0.5
711	25.4	127.0	10.9	114	470	7524	0.6
762	15.9	89.0	6.4	58	487	4007	0.2
762	15.9	597.0	3.1	58	487	3231	0.2
762	15.9	89.0	2.5	58	487	5087	0.9
914	25.0	178.0	4.6	188	486	14974	1.1
914	25.0	199.0	5.9	93	499	14056	0.6
914	25.0	212.0	6.1	73	514	8103	0.2
914	25.0	207.0	6.1	60	526	12782	0.5
914	25.0	191.0	12.3	188	486	13178	0.6
914	25.0	205.0	12.0	93	499	12573	0.5
914	25.0	210.0	11.5	73	514	11508	0.3
914	25.0	210.0	15.4	60	526	7310	0.2

10   APPENDIX B: NEWMAN AND RAJU EQUATION

$$K_I = (S_t + H\, S_b)\sqrt{\pi\, \frac{a}{Q}}\; F$$

With:

$$Q \quad = 1 + 1.464\left(\frac{a}{c}\right)^{1.65}$$

$$F \quad = \left[M_1 + M_2\left(\frac{a}{t}\right)^2 + M_3\left(\frac{a}{t}\right)^4\right] f_\phi\; g\; f_w$$

$$M_1 \quad = 1.13 - 0.09\,\frac{a}{c}$$

$$M_2 \quad = -0.54 + \frac{0.89}{0.2 + a/c}$$

$$M_3 \quad = 0.5 - \frac{1.0}{0.65 + a/c} + 14\left(1.0 - \frac{a}{c}\right)^{24}$$

$$g \quad = 1 + \left[0.1 + 0.35\left(\frac{a}{t}\right)^2\right](1 - \sin\phi)^2$$

$$f_\phi \quad = \left[\left(\frac{a}{c}\right)^2 \cos^2\phi + \sin^2\phi\right]^{1/4}$$

$$f_w \quad = \left[\sec\frac{\pi c}{2\,W}\sqrt{\frac{a}{t}}\right]^{1/2}$$

$$H \quad = H_1 + (H_2 - H_1)\sin^p\phi$$

$$p \quad = 0.2 + \frac{a}{c} + 0.6\,\frac{a}{t}$$

$$H_1 \quad = 1 - 0.34\,\frac{a}{t} - 0.11\frac{a}{c}\frac{a}{t}$$

$$H_2 \quad = 1 + G_1\,\frac{a}{t} + G_2\left(\frac{a}{t}\right)^2$$

$$G_1 \quad = -1.22 - 0.12\,\frac{a}{c}$$

$$G_2 \quad = 0.55 - 1.05\left(\frac{a}{c}\right)^{0.75} + 0.47\left(\frac{a}{c}\right)^{1.5}$$

With:

> h Half-length of cracked plate [mm]
>
> M Applied bending moment [Nm]
>
> S_b Remote bending stress on outer fiber [Pa]
>
> $$= \frac{3\,M}{W\,t^2}$$
>
> S_t Remote uniform tension stress [Pa]
>
> t Plate thickness [mm]
>
> ϕ Parametric angle of the ellipse [deg]

Boundary condition:

> $$0 < \frac{a}{c} \leq 1$$
> $$0 \leq a/t < 1$$
>
> $$c/W < 0,5$$
>
> $$0 \leq \phi \leq \pi$$

11   REFERENCES

1.   *API 1104: Welding of pipelines and related facilities.* 2007, American Petroleum Institute.

2.   *BS 7910: Guide to methods for assessing the acceptability of flaws in metallic structures*. 2005, British Standards Institution.

3.   *FITNET: Fitness-for-Service Procedure.* 2006, European Fitness-for-Service network.

4.   Newman, J.C. and I.S. Raju, *Analyses of surface cracks in finite plates under tension or bending loads.* NASA Technical paper 1578, 1979.

5.   Pistone, V., *Fitness-for-Purpose assessment of defects in pipeline girth welds.* EPRG.

6.   Coote, R.I., et al., *Alternative girth weld acceptance standards in the Canadian gas pipeline code.* 1986.

7.   Miller, A.G., *Review of Limit loads of structures containing defects.* Int. J. Pres. Ves. & Piping, 1988. **32**: p. 197-327.

8.   Goodall, I.W. and G.A. Webster, *Theoritical determination of reference stress for partially penetrating flaws in plates.* Int. J. Pres. Ves. & Piping, 2001. **78**: p. 687-695.

9.   Lei, Y., *J-integral and limit load analysis of semi-elliptical surface cracks in plates under combined tension and bending.* Int. J. Pres. Ves. & Piping, 2004. **81**: p. 43-56.

10.   Denys, R.M., et al., *Effects of stable ductile crack growth on plastic collapse defect assessments.* Pipeline technology: Proceedings of the third international pipeline technology conference, 2000. **1**: p. 169-189.

11.   Denys, R.M., et al., *Failure characteristics and defect tolerance levels of girth welds in large diameter X65/X70 steel pipelines: experimental verification through wide plate testing and comparison with ECA prediction models.* Pipeline technology: Proceedings of the third international pipeline technology conference, 2000. **1**: p. 151-167.

12.   Sattari-Far, I. and P. Dillström, *Local limit load solutions for surface cracks in plates and cylinders using finite element analysis.* Int. J. Pres. Ves. & Piping, 2004. **81**: p. 57-66.

13.   Zerbst, U., R.A. Ainsworth, and K.H. Schwalbe, *Basic principles of analytical flaw assessment methods.* Int. J. Pres. Ves. & Piping, 2000. **77**: p. 855-867.

DEVELOPMENT OF THE VIERENDEEL:

CALCULATION, AESTHETICS, WELDING, CONCRETE

K. Verswijver[1], R. De Meyer[1], R. Denys[2], E. De Kooning[1] and J. Belis[3]

[1] Ghent University, Department of Architecture and Urban Planning, Belgium
[2] Ghent University, Department of Mechanical Construction and Production, Belgium
[3] Ghent University, Department of Structural Engineering, Belgium

Abstract   The Vierendeel is a frame with rigid joints patented in 1896 by Belgian engineer Arthur Vierendeel (1852-1940). His invention came about after he noticed that experiments and calculation methods on iron and steel frameworks didn't agree, making his invention a response in the then discussion on secondary stresses. After designing a church tower and testing a full-scale bridge model during the 1897 Brussels World Fair, many bridges 'système Vierendeel' were erected the following decades in his homeland, as well as a few dozens around the globe. At times the discussion on the Vierendeel got heated in trade journals and amongst people, mainly due to a lack of 'visual' safety and theoretical uncertainties concerning calculation, safety factors and welding techniques. Nowadays the Vierendeel principle is still topical and many (structural) designers apply his formal ideas. This led to a broader meaning of the word Vierendeel varying from aesthetic to strictly structural.

Keywords Vierendeel, structural mechanics, construction history, Belgium, 19th and 20th century, iron, steel, welding, concrete

1   INTRODUCTION

Historically, a Vierendeel is a series of rectangular frames "in which the diagonals are removed and the vertical members rigidly connected to the booms by rounded pieces in such manner that the booms and vertical members form practically one piece." (Vierendeel [26]) It is named after its inventor, Belgian engineer Arthur Vierendeel, who patented it for the first time in 1896. Contrary to the typical pin-jointed truss in which theoretically only axial stresses occur, the Vierendeel transfers shear from the chords by bending moments in the vertical webs.

On reflection it is not easy to determine the characteristic traits of a Vierendeel. The meaning may be obvious to all those engaged in civil engineering, the actual denotation has meandered between different senses up until today. Moreover, even before Vierendeel's patents, engineers were looking for a better grasp of the distinctions between pin-jointed and rigid connections.

This paper will examine the origin of Vierendeel's rigid framework within the scope of the general history of iron and steel frameworks, a history that covers more than 150 years of contemplation for all the metalworkers, engineers and architects involved. Their discourses had various assumptions, from purely architectural to purely structural. As a result the Vierendeel tells a history of many disciplines: initially starting out as a solely engineer's invention, it gradually became a tool to solve aesthetic, technical and structural issues in architecture.

2   ARTHUR VIERENDEEL AND 19TH CENTURY FRAMEWORK CONSTRUCTION

2.1   Life and work of Arthur Vierendeel

In 1874 Belgian Jules Arthur Vierendeel (1852-1940) obtained with great distinction the degree of *ingénieur des arts, des manufactures, du génie civil et des mines* at the Ecoles Spéciales of the Catholic University of Leuven. Two years later he started his career in the building industry as a commissioner of the Ateliers Nicaise et Delcuve in La Louvière where he worked until 1885 - in 1913 the Ateliers merged with La Brugeoise and they constructed many Vierendeel bridges in Belgium. In La Louvière, Vierendeel took charge for the construction of the Royal Circus in Brussels, one of the first large iron frameworks in Belgium. This building did not arise without a struggle though. The owners and the press were convinced that the light structure would never be sufficiently supportive. Only after an ultimate test with a regiment of grenadiers ordered by the minister, animadversion came to an end.

In 1885 Vierendeel was named head-engineer-director of the technical services of the province of West-Flanders, making him among other things responsible for 2271 km of road construction. After the First

World War, which had been extremely destructive for the coastal province, he played an important role in the reconstruction of the heavily devastated front.

Four years after Vierendeel started working in West-Flanders, Louis Cousin asked him to be his successor for the course on structural mechanics at the Catholic University of Leuven. When Vierendeel began teaching, his architectural work that had included the covering of the railway station of Kortrijk and the tower of the church of Dadizele came to a standstill. From then on he would only construct bridges, pylons and other civil works. As a jack-of-all-trades Vierendeel also wrote on soil mechanics, electromagnetism and aircraft building (never published) and he derived a general formula to explain buckling failure.

2.2 Theories on pin-jointed and rigid frames at the end of the 19th century

The year 1851 marked a turning point in the use of iron and steel in construction, materials that Vierendeel would defend vividly from the moment he became a professor and his writings started to flourish. A milestone was the Crystal Palace, a cast-iron and glass structure erected in Hyde Park, London, to house the Great Exhibition (the first World Fair). Another event in 1851 - one that heralded the beginning of the discussion on pin-jointed and rigid frames - was the introduction of the term 'trussed framework' by German structural engineer Karl Culmann (1821-1881), a pioneer of graphical methods in engineering. He introduced this word in the first of his 2 travelogues - he had made a study tour to the United Kingdom and the United States from 1849 to 1851 - and it marks a new era where the timber framework and by extension the carpenter were replaced by the iron framework and the metalworker. (Kurrer [5])

Also in 1851 Berlin engineer Johann Wilhelm Schwedler (1823-1894) noted that the individual framework components can be assumed to be capable of rotation. When later riveted joints were preferred over bolted ones, this theory was less applicable and German engineer Emil Winkler (1835-1888) noted that the pin-jointed model contradicted with the as-built reality with riveted joints. This led to the theory of secondary stresses, as they were called at the time. Secondary stresses were due to the bending moments and shear forces that existed in the truss members, next to axial forces of tension and compression. Because of the statically indeterminacy of rigid-jointed structures, calculations were much more complex. The second half of the 19th century was a breeding ground for this discussion on pin-jointed and rigid-jointed frames, a discussion that Vierendeel joined in the beginning of the 1890s when he designed the supporting structure for the tower of the Dadizele church.
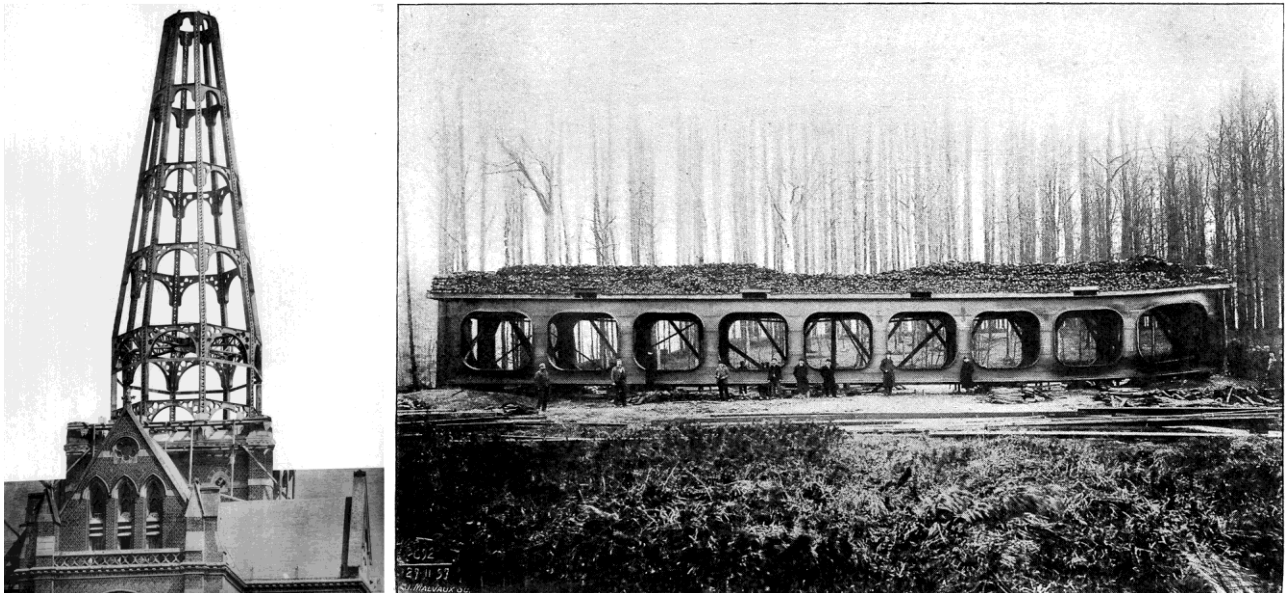
Figure 1. Framework of the crossing tower of the Dadizele church (Vierendeel [27], pl. 94) and Vierendeel's experiment of Tervuren in 1897 (Lambin, Christophe [6]).

3 THE 'POUTRE À ARCADES' OR VIERENDEEL

3.1 The iron tower of the Our Lady church in Dadizele

The Our Lady church in Dadizele, 50 km south of Vierendeel's hometown Bruges, Belgium, illustrated his first use of rigid joints. The church, designed by Edward Welby Pugin (1834-1875), was erected between 1859 and 1880.

Nevertheless there was no crossing tower by the time of the inauguration in 1880 and Vierendeel and architect Van Assche came up with a brand-new structural design: an iron construction that respected Pugin's formal design. This tower wasn't erected until 1893. Vierendeel described the structural design as particularly interesting since the dead weight of the tower, which was to be supported by four slender brick columns, could hardly be increased.

The reason for using gussets composed of sheet iron instead of diagonal braces was only described very vaguely and didn't seem to be inspired by the aforementioned problems: "Nous avons remplacé ces éléments multiples et compliqués par une seule espèce de membrures (des arcatures) jouant simultanément le rôle d'enrayures horizontales et de treillis verticaux, c'est l'emploi et le calcul de ces arcatures qui constituent la nouveauté de notre système de construction; elles ont pour avantage de donner une construction plus simple et plus claire, en un mot, plus architecturale." (Vierendeel [27]) Furthermore, there seemed to be no technical nor formal grounds to avoid braces, as there were no windows or other openings. Vierendeel clearly designated the novelty of *his* construction system.

3.2 Testing and patenting his invention during the 1890s

A few years later, in April 1897, Vierendeel published the structural theory of his 'poutre à arcades' as he used to call his invention, initially in his book *Longerons en Treillis et Longerons à Arcades*. Examples of structures with fully rigid joints were very uncommon at the time. He could only refer to the Dadizele church tower.

Vierendeel mentions his system for the first time in public at the *Congrès International des Architectes* in August 1897 in Brussels. There he also revealed his upcoming test on a 31,5 m span bridge he was going to build at his own expense within the scope of the Brussels World Fair in Tervuren. It would be loaded to failure to verify the agreement between calculations and measurement. "Et maintenant le treillis: grande sujétion dans l'emploi artistique du fer, car le treillis avec ses formes raides, droites, sans variété, sans elasticité, est un dispositif constructif qui n'est rien moins qu'esthétique; mais, heureusement, du treillis nous sommes delivrés; voici, un pont dont les fermes en fer sont realisées sans intervention d'aucune diagonale, d'aucun treillis, et cette réalisation est obtenue en faisant une économie de matière et sans rien sacrifier de la solidité, ainsi que le prouvent les expériences, actuellement en cours, à Tervueren, sur un pont analogue de 32 mètres de portée." (Vierendeel [24])

While Vierendeel's patents describe vaguely the calculations without explaining the trailing theories, his book goes into detail on how to calculate the particular case of a symmetric bridge with parallel flanges and the general case of an asymmetric bridge with non-parallel flanges.

Vierendeel's main criticism on contemporary calculation was a discrepancy between analytical structural theory and actual building practice. Calculation assumed pin-jointed connections whereas the execution with rivets tended to be more rigid. After Schwedler and Winkler, German scientific assistant Heinrich Manderla (1853-1889) had described a calculation method in 1880 to determine the additional secondary stresses. He assumed that angular rotations were not possible in a framework. However Vierendeel still thought this method to be incorrect, primarily because the rigid joint was also far from perfect: the truth balanced between a rigid joint and a pin-joint. (Vierendeel [24])

Dutch engineer J. Schroeder van der Kolk summarized in the *Tijdschrift van het Koninklijk Instituut van Ingenieurs* (edition 1889-1890) the results of an experiment that listed the secondary stresses of a truss bridge in relation to the primary stresses. It was striking that those secondary stresses could not be ignored, as they amounted up to 60 % of the primary stresses. Secondly, Vierendeel indicated that in the diagonals the secondary stresses were limited (ranging from 6 to 16 % of the primary stresses). In other experiments he had noted that deformations in the diagonals were nearly negligible.

Vierendeel also referred to Winkler who tried to lower these stresses by using St. Andreas crosses, i.e. doubling the diagonals. It had already been applied in the Netherlands on some railway bridges between Rotterdam and Amsterdam. German civil engineer Otto Mohr's method was used to calculate the basic structure, along with Manderla's equations. However according to Vierendeel it didn't reduce the secondary stresses. After tests in France in 1893 ordered by the state, engineers tried to turn truss bridges into girder bridges by using a lattice-work. Though Vierendeel acknowledged some of the advantages, he still argued that "la vraie solution se trouvera, non pas en compliquant le treillis, mais en la simplifiant encore, c'est-à-dire en supprimant la diagonale dans le canevas triangulaire." (Vierendeel [24])

At first there seemed to be no advantages by eliminating the diagonals, since then all members were combined stress members and greater dimensions were required, not saving on material nor cost. At the time however, when steel trusses were riveted, large gussets were necessary, not providing isostaticity either. The exacter calculation Vierendeel provided, could enhance the safety, and thus indeed save material. His theory, embedded in the discussion on secondary stresses, was new, so his articles and projects were not instantly reliable, but all the more interesting to his contemporary colleagues. These

discussions were held in trade journals like *Annales des Travaux Publics de Belgique* and *Ossature Métallique* in Belgium and *Der Eisenbau* in Germany.

3.3 The Vierendeel as an aesthetic concept

Though Vierendeel focused mainly on the structural aspect of his invention, other publications of his pointed out that the Vierendeel was more than just a part of a technical or structural development, as it was an important part of his own aesthetic discourse described in his opus magnum *L'Architecture en fonte, fer et acier*. He criticized the Eiffel Tower and the Galérie des Machines, since they relied on superseded architectural theories and 19th century neo-styles. He stated that, due to the slender form of its composing elements (mainly in the lattice-work), light can easily deform them, creating a structure with an awkward look. In the end Vierendeel tried to refute the argument of iron being a massless material by building up structures using as few slender lines as possible.
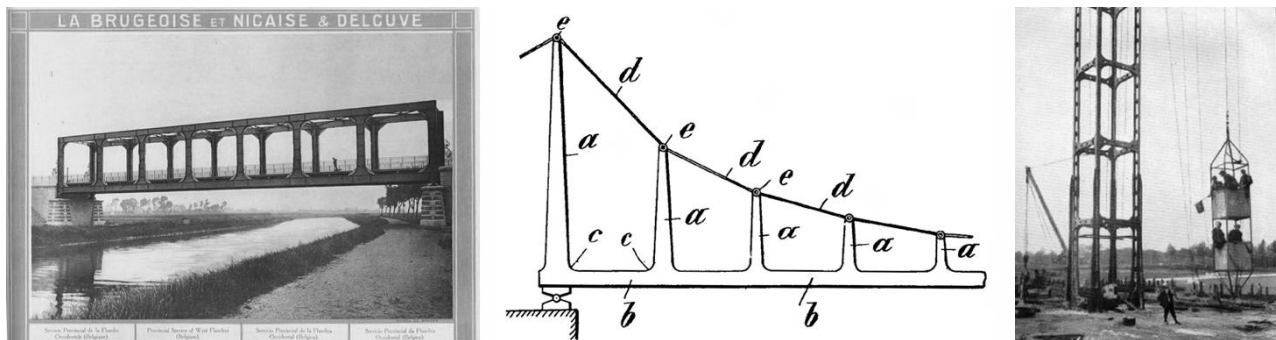

Figure 2. Vierendeel's first large bridge in Avelgem built in 1904 (contractor's catalogue); A concrete suspension bridge (Vierendeel [29]); A 287 m high radio pylon in Ruiselede (Jadot [4]).

3.4 Rise and fall of the Vierendeel in bridge construction

It comes as no surprise that the first large Vierendeel bridge was erected in the province where Vierendeel was head-engineer-director. In 1904 he could prove in Avelgem that his poutre à arcades could provide enough strength and stability (Fig. 2a). Even after the Tervuren experiment the dogma of the triangle was not yet overcome and his opponents outnumbered his followers, with e.g. quite a number of his workmen being suspicious - a flashback to the problems he had to deal with during the construction of the Brussels Royal Circus. And so during a final structural test the worker who had to drive the fully-loaded coach to measure the deformation demanded that Vierendeel would be standing in the middle of the bridge during this trial.

After this first bridge many more Vierendeel bridges were erected. The railway bridge in Grammene, 30 km southwest of Ghent, was ordered by the Belgian State Railways and was to be compared with a typical truss bridge.

The Vierendeel's popularity increased after two events in 1929. The creation of the 130 km long Albert Canal connecting Antwerp and Liège, and the spread of welding. The canal required 65 bridges and almost half took the Vierendeel form. By 1930 there were over 30 Vierendeel bridges in Belgium and 23 in the Belgian Congo.

As electric arc welding was a new technique during the interwar period, it did provide opportunities, but there was a downside when insufficient knowledge of welding techniques led to a series of serious bridge collapses. Though he was not to be blamed, they got often attributed to the notion of the Vierendeel.

After Second World War, the role of the Vierendeel in bridge (re)construction was minimal. The landscape was now redefined with slender arches, as well as unpretentious girder bridges. Larger spans, as required in other countries, were handled by suspension bridges, whereas France was preoccupied with its own invention, prestressed concrete. (Wickersheimer [32]).

3.5 Less-known Vierendeels: pylons and concrete suspension bridges

Vierendeel applied his construction not only to spans, but also to erect masts, like the 8 radio pylons of 287 m high for the Télégraphie Sans Fil in Ruiselede, close to Dadizele, in 1927 (Fig. 2c). These masts were meant to provide communication with the Belgian Congo, but due to atmospheric interferences this was impossible. Until 1940 they were used to communicate with ships crossing the Atlantic. A few years earlier Vierendeel had patented another unlike Vierendeel application: a concrete suspension bridge of which the

lower part was a Vierendeel, and the upper part were steel cables (Fig. 2b). Applications of concrete Vierendeel bridges still exist in Belgium and abroad, though the suspended version has not been known to exist.

4   THE POST-VIERENDEEL ERA

4.1   Semantics of the notion Vierendeel

The Vierendeel is a structural element still in use. It is moreover the abundant occurrence of the man's name in patents, books, research papers, architectural monographs and articles that prove that the name - or the word, since the link with the person is sometimes lost - has considerably adopted the idea of a rigid frame. At the same time 'Vierendeel' is not a narrow definition. It has a cloud of meanings around it. The word Vierendeel obviously refers to the engineer; to a (simplified) calculation method for rigid frames - the true original meaning; a structure with rigid connections instead of pin-joints; a global step in the process of determining (secondary) stresses in metal frameworks at the end of the 19th century; or any structure using rigid connections, not necessarily in the form of a rectangular frame. It is mainly this latter definition that is suitable for most of the current Vierendeels.

5   CONCLUSIONS

Challenging the dogma of the triangle was one of his objectives, Vierendeel said. Nevertheless this dogma was merely a rhetorical cover. Vierendeel was an engineer who believed in the prospects of iron and steel in architecture and who had thoroughly examined frameworks and its structural and mechanical behaviour.

Blindly following the tradition of trusses with improper calculation would not drive mankind to progress. So when Vierendeel delved into the 19th century issue on secondary stresses, he seized his chance to solve this, by working out approximate methods to determine stresses in frameworks without diagonals. He had seen that during experimental loading, the diagonals were hardly charged and their secondary stresses were limited. He found an analytical theory that matched the as-built reality.

After his first experiments and overcoming some resistance, Vierendeel convinced state principals to order dozens of Vierendeel bridges in Belgium and its African colony during the next decades. The 'poutre à arcades' as he had called it initially, was also applied in some other structures as pylons and concrete spans.

The Vierendeel is a crossbreed, a structural compromise. It is not as rational as a truss when it comes to loadbearing capacities, but it remains superior when it comes to spatial qualities. In retrospect we can say that the concept of the Vierendeel has shifted. Vierendeel's definition as described in his 1899 USA patent is a beam in "which the diagonals are removed and the vertical members rigidly connected to the booms by rounded pieces in such manner that the booms and vertical members form practically one piece." Nowadays calculation uses different methods and since the breakthrough of digital calculation more complex algorithms are possible. His name is however still connected to the concept of rigid frames that gain stiffness through these rigid corners. The connotation with the inventor is sometimes lost, but the multifunctional aspects to obtain aesthetic, formal, mechanical or structural plus-points will remain its ace of trumps.

6   ACKNOWLEDGEMENTS

The authors would like to acknowledge the support of prof. Patricia Radelet-De Grave from UCL University for her help and research on Arthur Vierendeel.

7   REFERENCES

[1] A. Becchi, M. Corradi, F. Foce, O. Pedemonte (eds), *Essays on the history of mechanics: In memory of Clifford Ambrose Truesdell and Edoardo Benvenuto*, *Between mechanics and architecture*. Basel: Birkhaüser, 2003.
[2] F. Escrig, J. Sánchez, A New Roof Grid to Cover a Large Area: The Vierendeel Solution. *International Journal of Space Structures* 19(4), 177-194, 2004.
[3] S. Giedion, *Bauen in Frankreich: Eisen, Eisenbeton*. Leipzig: Klinkhardt & Biermann, 1928.
[4] O. Jadot, *Manifestation en l'honneur de Monsieur Arthur Vierendeel, ingénieur, professeur à l'Université de Louvain*, 25 octobre 1924. Leuven, 1924.
[5] K.-E. Kurrer, *The History of the Theory of Structures, From Arch Analysis to Computational Mechanics*. Berlin: Ernst & Sohn, 2008.

[6] A. Lambin, P. Christophe, *Le pont Vierendeel. Rapport sur les essais jusqu'à la rupture effectués, au parc de Tervuren, par M. Vierendeel, sur un pont métallique de 31m.50 de portée, avec des poutres à arcades de son système*. Annales des Travaux Publics de Belgique 55(1), 53-139, 1898.

[7] A. G. Meyer, *Eisenbauten, ihre Geschichte und Æsthetik*. Esslingen am Neckar: Paul Neff Verlag, 1907.

[8] T. F. Peters, *Transitions in engineering: Guillaume Henri Dufour and the early 19th century cable suspension bridges*. Basel: Birkhäuser Verlag, 1987.

[9] A. Picon (ed.), *L'art de l'ingénieur: constructeur, entrepreneur, inventeur*. Paris: Centre Georges Pompidou, 1997.

[10] P. Radelet-de Grave, *Arthur Vierendeel (1852-1940), Pour une architecture du fer*. In: A. Becchi et al. (eds), *Towards a History of Construction*: 417-435. Basel/Boston: Birkhäuser, 2002.

[11] P. Radelet-de Grave, *The surprising posteriority of Arthur Vierendeel (1852-1940)*. Lecture at First International Congress on Construction History, Madrid, 20-24 January 2003.

[12] P. Radelet-de Grave, *Ingenieurporträt (Jules) Arthur Vierendeel, Erfinder des Trägers ohne Diagonalen*. DB Deutsche Bauzeitung 137(8), 84-87, 2003.

[13] A. Saint, *Architect and engineer: a study in sibling rivalry*. New Haven (Connecticut): Yale University Press, 2007.

[14] J. Timmerman, *Arthur Vierendeel (1852-1940), Hoofdingenieur-Directeur Provinciale Technische Dienst West-Vlaanderen, Hoogleraar Katholieke Universiteit Leuven*. Bruges: Provinciebestuur van West-Vlaanderen/K.U. Leuven, 1989.

[15] A. Van Loo (ed.), *Repertorium van de architectuur in België, van 1830 tot heden*. Antwerp: Mercatorfonds, 2003.

[16] K. Verswijver, R. De Meyer, R. Denys, E. De Kooning, *The writings of Belgian engineer Arthur Vierendeel (1852-1940), homo universalis or contemporary propagandist?* In Karl-Eugen Kurrer et al. (eds), Proceedings of the Third International Congress on Construction History, Cottbus, 20-24 May 2009, 1463-1470. Cottbus: BTU Cottbus, Institut für Bau- und Kunstgeschichte, 2009.

[17] A. Vierendeel, *Cours de Stabilité des Constructions*. Leuven: Uystpruyst, 1889.

[18] A. Vierendeel, *L'architecture métallique au XIXe siècle et l'Exposition de 1889, à Paris*. Brussels: Ramlot, 1890.

[19] A. Vierendeel, *Le Pont de mille mètres*. Leuven: Uystpruyst, 1896.

[20] A. Vierendeel, *Les Ponts architecturaux en métal*. Leuven: Uystpruyst, 1896.

[21] A. Vierendeel, *Brevet d'invention*. Belgian Patent #122,018, 1896.

[22] A. Vierendeel, *Brevet d'invention*. Belgian Patent #128,573, 1896.

[23] A. Vierendeel, *L'architecture du fer et de l'acier, Conférence donnée au Congrès international des Architectes réuni en août 1897, à Bruxelles*. Brussels: Ed. Lyon-Claesen, 1897.

[24] A. Vierendeel, Improvement in the Construction of Trellis Girders or Beams. UK Patent #20,214, 1897.

[25] A. Vierendeel, Longerons en Treillis et Longerons à Arcades. Leuven: Uystpruyst, 1897.

[26] A. Vierendeel, *Girder or Beam for Bridges*. USA Patent #639,320, 1899.

[27] A. Vierendeel, *La construction architecturale en fonte, fer et acier*. Leuven: Uystpruyst, 1902.

[28] A. Vierendeel, *Pont sur la Lys, Route Ousselghem-Zulte*. Brussels: L'Imprimerie Nationale, 1911.

[29] A. Vierendeel, *Pont suspendu rigide à ossature en béton armé ou en métal*. French Patent #504,066, 1920.

[30] A. Vierendeel, *Esquisse d'une histoire de la technique*. Brussels: Vromant, 1921.

[31] A. Vierendeel, *Poutres en béton armé*. French Patent #543,702, 1922.

[32] D. J. Wickersheimer, *The Vierendeel*. The Journal of the Society of Architectural Historians 35(1), 54-60, 1976.

TRIBOLOGICAL BEHAVIOR AND SURFACE QUALITY OF POLYMERIC INDUSTRIAL SEALING MATERIALS

László Zsidai, Róbert Keresztes

Institute for Mechanical Engineering Technology,
Faculty of Mechanical Engineering, Szent István University, Gödöllő, Hungary
www.geti.gek.szie.hu

Abstract Tests presented in our research work as an example give look into the wear and friction behaviour of some typical polymer sealing compound (POM, PEEK, PA). The measurements examine above all the effect of surface roughness onto the wear and friction behaviour wear in case of optimal loading relations. We have carried out the test in pin-on –disc system. Based on the test results we have classified the polymers on the basis of wear and friction factors.
Keywords *polymer tribology, sliding seals, surface roughnes, pin on disc*

1.   INTRODUCTION

The practical choosing of moving (sliding) seals used in industry takes place in many cases by „ad hoc" manner keeping in view first of all load characteristics (pressure-tighness, mechanical properties). Less attention is given to the tribological factors (wear resistance, friction coefficient) and less data are available, too. It would be important in particular to carry out tribological tests connected with optimal operational parameters (sliding speed, load) which could help the practical selection. These tests also could be generally accepted (standardized) laboratory tests. These use small-scale specimens, which advantage are:

-    Simple test set, small loading force, small-scale specimens,
-    Environmental characteristics easily set and the costs are low.

The most important tribological questions of the sealing systems belong the material combining (seal-metal surface) and the morphology of sliding surfaces (roughness, geometry).

The technical literature of tribological characteristics of sealing compound is extensive [1-5], but within these few number of sources give account from sliding and wear characteristics of new generation polymer sealing compounds. The main aim of present tests is to give look into wear and sliding friction characteristics between small scale polymer specimens and steels having different surface roughness. We have carried out the laboratory tests by standard pin-on-disc continuously sliding system, the changes to be ensued we have observed with optical method. The results got can contribute to optimizing and widening the possibilities using sealing compounds, too.

2.   METHOD

1.1   Materials tested

We have aspired at choosing the material to be tested to be widely used at such places where the wear is significant in sealing technique (for example centering or supporting rings of actuating cylinders). Based on the formers and industrial demand respectively we decided on Polyamid (PA)-types, one modified polyetheretherketone (PEEK) and one polyoxymethylene co-polymer (POM C).
Table 1. contains the materials tested and their important characteristics.

Table 1.

	Polyamide 6.6 (PA 66)	*Polyetheretherketon e modified (PEEK mod)*	*Copolymer Polyoxymethyle n (POM C)*	*Polyamide 66+teflon (PA 66 TF)*
Density g/cm³	1,15	1,44	1,41	1,15
Yield stress N/mm²	85	-	30	60-90
Modulus in tension N/mm²	3300	-	3000	1600-3500
Application temp. continuous °C	-30 bis 80	250	-50 bis 100	80-100

Shortly on te role of sealing technique of materials tested [6].

- The polyamid 66 is widely used for bearings and in actuating cylinders as supporting-guiding ring, because it's good abrasive wear resistance remains in dry condition, too. Its use is limited by its heat resistance and its bad dimensional stability.
- The POM C belongs to the acetal groups, it is used as bearing, as guide bush and hydraulic cylinder seal because of it's good, mineral oil and fuel stability.
- PEEK is an engineering plastic with high pressure heat resistance and it has got suitable resistance against oil and gas. It is used as „U" and „V"-sealing element for piston and valve ring.

Further information can be found on tribological tests with different parameters of the polymers or their versions tested [7-9].

1.2 The test set

The measuring of dry sliding coefficient of polymer/steel sliding pair was carried out on standardized pin-on-disk (ASTM 699-95a) test set. The sketch of the model tested, the cylindrical plymer specimen and metal counter disk with its dimensions can be seen in Fig 1.
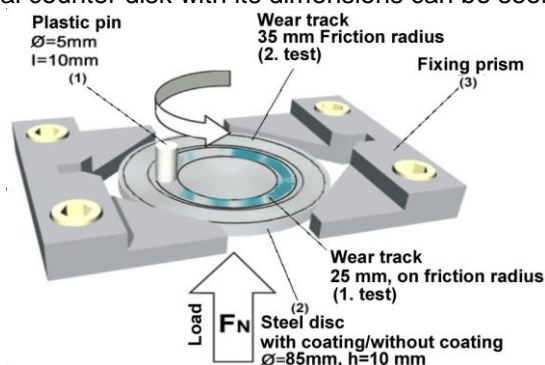
Figure 1. The position and dimension of specimens at pin-on-disk testing system.

The Dynamic Tribotester was the concrete test set developed in our institute, which is also suitable for traditional pin-on-disk tests (Fig 2). To set the revolution an electric motor rotation (5) is used controlled by computer and having encoder, which revolution can be changed infinitely from zero. More information from the test set can be found in technical literature [10-11].
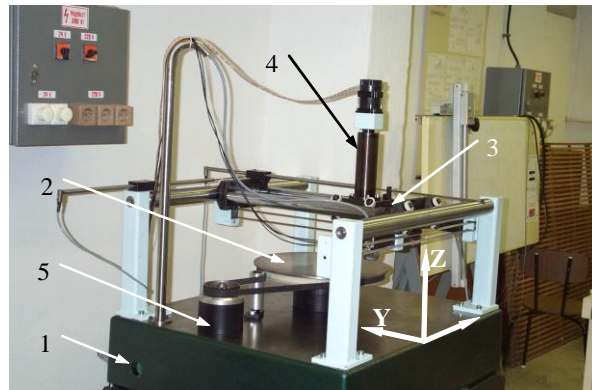
Figure 2. The dynamic tribological test set

Further measuring instruments used at tests:
- surface roughness tester: MITUTOYO Surftest SJ-201 P
- laboratory scale: WA-33 TYP PRL T A13

Cleaning appliances, materials used at tests:
- denaturated alcohol
- hand-drill with rotating plastic cleaning brush

1.3 Test parameters

Decesive standpoints were the followings determining test parameters:
- to indicate wear values first of all, to be estimated according to, comparatively short time measuring (surface roughed properly)
- the deformation of polymers does not influence the wear and friction (small load)
- to keep the heat developing during friction at low value that it can not cause melting from the polymer surface (small sliding speed)

Based on the concrete test parameters, we have set up three measuring grades, which characteristics can be seen in Fig 2. We decided the test time that the friction could reach into the stabile section at all types of material and appreciable material transfer processes could be developed.

Table 2.

TEST PARAMETERS	I. grade (rough)	II. grade (middle)	III. grade (smooth)
Plate/disc R_z surface roughness, [μm]	50-80	-	20-60
Test time, t [h]	1,5		
Load, P [MPa]	0,4-0,6		
Sliding speed, v [m/s]	0,05		
Relatíve humidity, RH [%]	50		
Ambient temperature, T [°C]	25		
Frictional radius, r [mm]	33, 40		

We have carried out the tests on two frictional radiuses at every disc from economicalness consideration. The parameters can be seen in Table 2. in the „Rough" the „Middle" and the „Smooth" test category names referring to the condition of surfaces roughness peaks. The following remarks belong to these:
- The surface of steel disc used as frictional reverse counterpart was machined by shaping in order to reach the proper roughness, we have marked surface with „rough" name referring to the sharp roughness peaks.
- The wear tests were carried out on different frictional radiuses (25 and 35 mm) of the steel disk in three groups successively with four different types of polymer in each group

- At the tests of third group already the wear of roughness peaks belong to the "smooth" category
- The second category means the "middle" surface in reference to the "rough" and "smooth" surfaces

Determining the surface roughness was carried out with needle surface roughness tester (MITUTOYO).

3. DISCUSSION

The figures 4, 5, 6 and 7 show the column diagrams summarizing the test results. The materials tested (PA 66, PA66 TF, POM C, PEEK mod) can be seen in all figures in the same sequence. Three columns can be seen at each material also in similar sequence; the first with "rough" then with "middle", finally with "smooth" category results.

3.1 The categories tested and the comparison of polymers from wear viewpoint

We have determined the specimens wear during tests equally with weight measuring and also continuous dimensional change (length reduction) measuring during measuring. The two methods independent from one another in well visible manner, establish identical wear sequences beside suitable correlation among materials tested.
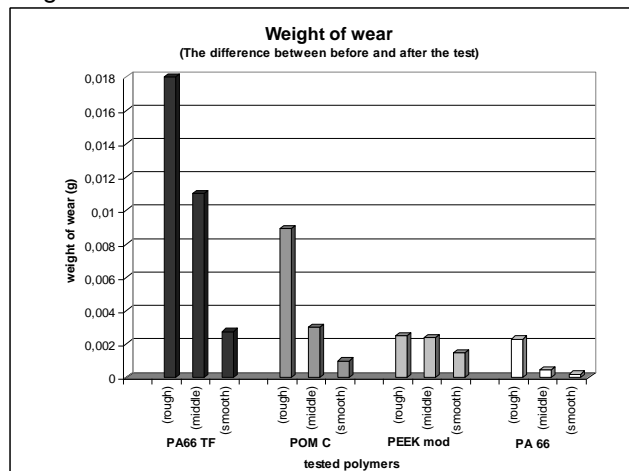

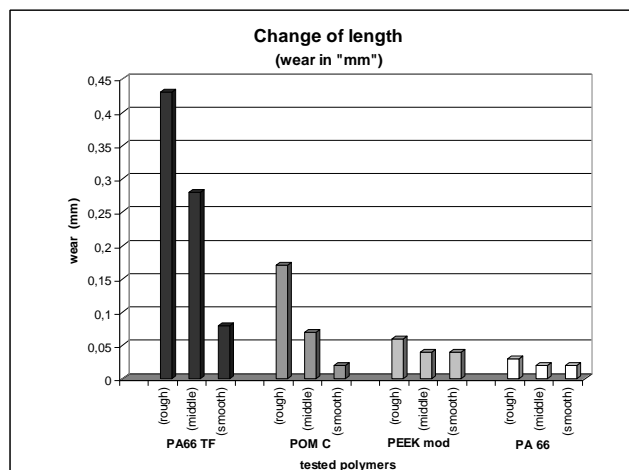*Figure 3. Summed up results of different weight of worn material results*

Figure 4. Summed up results of different specimens change of length results

Considerable wear at „PA66 TF" and „POM C"-polymers can be established because of strong cutting effect at test group having „rough" surface roughness peaks. The „PA 66" (See Fig.5) and „PEEK mod" polymer showed substantially lower wear.
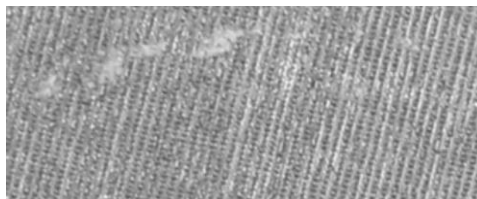

Figure 5. PA 6.6-polymer insignificant wear track on „rough" surface.

We have got essentially more favourable wear values at test group having „middle" surface roughness peaks compared with „rough" category group. It can be probable that the cutting effect reduced to a large extent of the slightly worn (middle) roughness peaks caused this favourable wear value. Among the other polymers the „PA 66" and the „PEEK mod" are the most favourable.
In case of test group of „smooth" surface roughness peaks also the PA 66 polymer showed the smallest wear, but here the POM C-polymer is already in the second place.

3.2 Comparing the categories tested and polymers considering the friction coefficient and friction temperature

Determining the friction coefficient takes place through the measuring of the friction force with the help of specimen holder installed with strain gauges (fig. 2.) The friction coefficient results got can be seen in Fig.6. The column heights mark the dynamic, the stars over them mark the values of static friction coefficient.
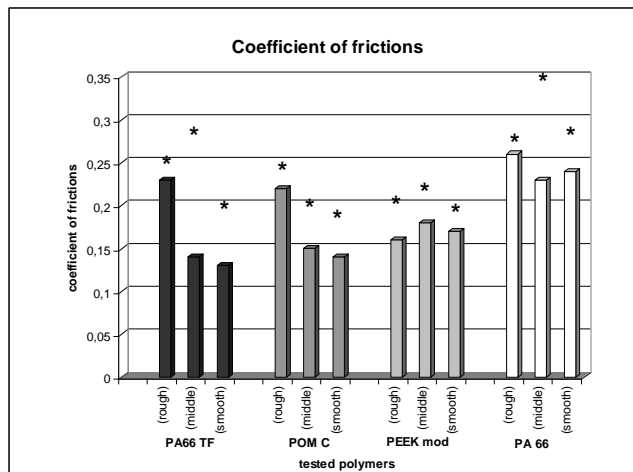
Fig. 6. Values of friction coefficient of polymers tested at different roughnesses

The friction results show constracted order of rank with the wear results. The PA66-polymer shows the largest but almost the same friction on all three surfaces. The PEEK-polymer changes its friction only slightly in the function of surface roughness similarly to the previous polymer however the values are lower contrary to that.
In case of PA66 TF and POM C polymers the friction coefficient changes essentially as a results of surface roughness and the extensive wear results in lower friction.
During tests we have also measured continuously the developed heat in the friction zone. We couldn't indicate significant temperature rise and significant differences because of the small loads and relative large masses and dimensions. Therefore it can be follow up that rougher surface qualities produces a little higher temperature at all materials tested. This results from the values of higher friction coefficient belong to rougher surface.

4. CONCLUSIONS

The following conclusions can be drawn up based on tests carried out:
- The PA66 polymer had the most favourable wear resistance in all three categories and beside this the POM-C polymer already on wearing-in surfaces.
- The PA66 TF polymer suffered the largest wear in all three categories.
- The effect of different roughness-peaks influenced only slightly the "PEEK mod" polymer wear.
- The effect of different roughness-peaks influenced in a great extent the POM C and the PA66 TF polymers wear, at the same time in case of PEEK mod. polymer did not cause significant changes.
- The wear characteristics do not mean definitely the favourable values of friction coefficients. It can be probable that to the value of lower friction coefficient of materials with larger wear (PA 66 TF, POMC) the replenisher effect of surface roughness of the worn material also contributed. (Figure 7.)
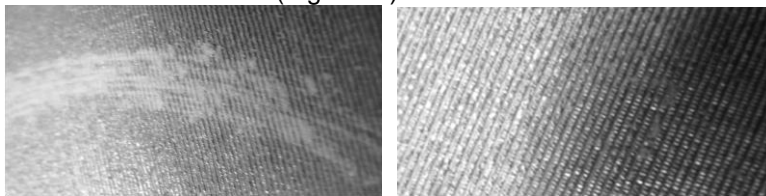
a.) Rough   b.) Smooth
Figure 7. The POMC-polymer wear tracks on rough and smooth surfaces.

- The greater surface roughness helps to get the solid lubricant to the surface, which in case of PA66 TF-polymer brings about PTFE-film development which significantly reduces friction and stick-slip effect. (Fig. 8.)
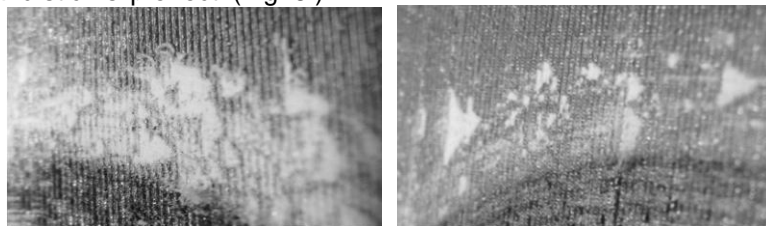
a.) Rough   b.) Smooth
Figure 8. The PA66 TF-polymer wear tracks on rough and smooth surfaces

The results of tribological tests are system-dependent so they do not provide generalization and absolute designing data. They convey useful information on purpose to relative comparison.

REFERENCES
1. R.K. Flitney, I. Hansford and B.S. Nau, 'The effect of surface texture on reciprocating seal performance', BHR Group Report CR 3069, 1989.
2. N.A. Peppiatt, 'The influence of the cylinder tube surface finish on reciprocating seal performance', 13th Int. Sealing Conference, VDMA, 2004.
3. Y. Tatseishi, 'Tribological issues in reducing piston ring friction issues', *Tribology International*, 1994.
4. J.K. Lancaster, 'Accelerated wear testing of PTFE composite bearing materials', *Journal of Lubrication Tribology*, April 1979.
5. 15. J.K. Lancaster, 'Abrasive wear of polymers', *Wear*, October 1969.
6. Robert Flitney, Seals and Sealing Handbook, Fifth Edition, Elsevier Ltd. 2007. ISBN: 978 1 85617 461 9
7. ODI-OWEI S., SCHIPPER D .J. (1991): Tribological behaviour of unfilled and composite polyoximethylene. *Wear,* Vol. 148 363-376. p.

8.   KUROKAWA M., UCHIYAMA Y., NAGAI S. (2000): Tribological properties and gear performance of polyoxymethylene composites, *Journal of Tribology, Transactions of the ASME,* Vol. 122. (4) 809-815. p.

9.   UETZ H., WIEDEMEYER J. (1985): Tribologie der Polymere. München, Wien: Carl Hanser Verlag. 378 p.

10.   Keresztes R, Zsidai L. Kalácska G.; Műszaki Műanyagok dinamikus tribológiai vizsgálata. Műanyag és Gumi, 2002. 39.évf. 11-12szám P 427-432.,ISSN 0027-2914

11.   G. Kalácska- L. Zsidai- M. Kozma- P. De Baets: Development of tribological test-rig for dynamic examination of plastic composites. Hungarian Agricultural Engineering. N.12/1999. Hungarian Academy of Sciences. P 78-79. HU ISSN 0864-7410

HET ORGANO DI LEGNO, EEN BASSO CONTINUO INSTRUMENT VOOR DE STILE MODERNO EN DE SECUNDO PRATICA ROND DE EEUWWENDE 1600 IN ITALIË

Jan Boon[1], Patrick De Baets[2]

[1]Hogeschool Gent, Departement Conservatorium België
[2]Universiteit Gent, Laboratorium Soete, België

Abstract Tijdens de laatste decennia van de 16de eeuw ontstaat in Italië een nieuwe muziekstijl die een veranderend gebruik en een spectaculaire ontwikkeling van de muziekinstrumenten met zich meebrengt. Vele van deze instrumenten hadden specifieke kenmerken en kenden een geëigend gebruik. Eén van deze instrumenten was het *Organo di legno.* Na een schets van de culturele context wordt er aan de hand van primaire en secundaire bronnen, van het enige overgeleverde *Organo di legno* in de Silberne Kapelle in Innsbrück, en niet het minst van het onderzoek van Prof. Dr. Pier Paolo Donati (Firenze), in dit artikel naar gestreefd een beeld te schetsen van het wezen en het gebruik van het *Organo di legno*.

1   INLEIDING

Het mentale scheppingsproces en de materialisatie van een kunstwerk zijn in alle kunstvormen onlosmakelijk met elkaar verweven. Bij de muziek is dit niet anders : zo maakt het aangewende instrumentarium integraal deel uit van de conceptie en van de uitvoering van een muziekstuk. De specifieke eigenheden van het muziekinstrument, zoals bereik, stemrecept, speelaard, klankidioom, en evenzeer de ruimtelijke opstelling, hebben onmiskenbaar impact gehad op de muzikale schepping en zijn bijgevolg wezenlijk mee bepalend geweest bij de totstandkoming van de compositie. Tegelijkertijd hebben de aspiraties van de musici, zowel componisten als uitvoerders, ongetwijfeld de inspiratie en innovatiedrang van de instrumenten-bouwers gestimuleerd.

Wanneer we de muziek willen uitvoeren, beluisteren en begrijpen zoals ze door componisten in vroegere tijden was bedoeld, kunnen we niet naast de resultaten van de artistieke kruisbestuiving en het spanningsveld tussen de musici en de instrumentenbouwers.

Van de veelheid en variëteit aan muziekinstrumenten die vroeger waren gekend zijn er een groot aantal in onbruik geraakt. Zoals bij veel andere cultuuruitingen heeft zich bij de instrumentenbouw doorheen de tijden een uniformisering doorgezet. Deze heeft geleid tot het ingeburgerde concept van duidelijk onderscheiden instrumentenfamilies. In het besef dat zich in de loop van de voorbije eeuwen een verarming heeft voorgedaan aan soorten en varianten van muziekinstrumenten, wordt duidelijk dat vandaag vaak een vertekend beeld bestaat over het wezen van de toenmalige muziek en uitvoeringspraktijk. Bovendien blijkt dat in onze tijd het muziekinstrument vaak onderworpen is aan eenzijdige, dikwijls tot vervlakking leidende visies : zij het in de huidige uitvoeringspraktijk waar prestatiedrang dikwijls tot twijfelachtige compromissen leidt, in de bouwpraktijk waar hoge productiviteit meermaals waarachtigheid, diepgang en zeggingskracht in de weg staat, in het opzetten van collecties in musea - veelal kort na de Franse revolutie - waar vooropgestelde criteria veelal de antiekwaarde, het anekdotische of het extravagante zijn, of in de hedendaagse museumpraktijk waar de ontsluiting van het patrimonium in conflict treedt met de primaire opdracht, namelijk de conservatie van de historische substantie, of tenslotte in de muziekwetenschap waar het instrument vaak erg simplistisch wordt geclassificeerd. Het grondig herbestuderen, het doordacht herbouwen of reconstrueren en het gefundeerd hergebruiken van in onbruik geraakte instrumenten kan slechts leiden tot een beter begrip van de overgeleverde muziek, en aan een verfrissende esthetische herbeleving ervan. Dit artikel kadert in een onderzoeksproject in de ontwikkeling van de kunsten met als onderwerp het concipiëren en realiseren van een *'Organo di legno'* in de vorm van een transporteerbaar orgelpositief met verticaal opgesteld pijpwerk, naar de principes van de Italiaanse orgelbouw uit het Cinque- en Seicento, in functie en ten behoeve van het stijlbewust uitvoeren van Italiaanse en van Italiaansgeoriënteerde muziek uit deze periode in het algemeen en van het verzorgen van 'basso continuo' - partijen binnen het repertoire van de seconda pratica in het bijzonder.

2   DE STILE MODERNO EN DIENS INVLOED HET INSTRUMENTARIUM.

Gedurende de laatste decennia van het Cinquecento, tijdens de hoogdagen van het maniërisme, wordt door de *Camerata Fiorentina*, een aantal humanistische wetenschappers en kunstenaars (waaronder Emilio de' Cavalieri, Cristofano Malvezzi, Luca Marenzio, Giulio Caccini, Jacopo Peri, Vincenzo Galilei, e.a.…) gegroepeerd rond Giovanni de' Bardi een nieuwe muziekstijl leven ingeblazen, in een streven naar uitvoeringen volgens, naar wat zij geloofden, de principes van de klassieke Griekse muzikale declamatie.

In tegenstelling tot architecten, beeldende kunstenaars en schrijvers, die konden terugvallen op tastbare voorbeelden uit de Klassieke Oudheid, moesten de musici inspiratie putten uit en voortbouwen op de artistieke ontwikkelingen van hun tijd. Het Platonische principe dat de muziek gestuurd dient te worden door het woord was ongeveer hun enige houvast in hun betrachtingen de muziek uit de oudheid opnieuw tot leven te wekken.... Vanuit dit beginsel wordt dan ook het grootste belang gehecht aan de gevoelsuitdrukking en een affectieve tekstexpressie.

De composities krijgen grosso modo de vorm van een door akkoordinstrumenten quasi improviserend begeleide monodie, waarbij de zanglijn en de baslijn domineren, en zetten zich in feite af tegen de harmonieuze, uitgebalanceerde en vaak complexe werken van de meesters uit de hoge Renaissance, bij wie de traditionele polyfonie een helder verstaanbare en expressieve uitdrukking van de tekst in de weg staat. De nieuwe muziek wordt gekenmerkt door veelvuldig gebruik van chromatiek, stijlvolle delicate diminuties en een virtuoze techniek. De componisten streven naar affect, verfijning, raffinement en schoonheid en zoeken naar symbolen voor emotie.

Deze *Stile Moderno,* ook *Nuove Musiche* is tevens de grondslag van de *Basso continuo*-praktijk en de *Seconda Pratica* en gaat gepaard met het ontluiken van het muziektheater.

Terwijl voordien muziekinstrumenten vooral werden ingezet om vocale stemmen te begeleiden, te verdubbelen of te vervangen, en de zuiver instrumentale muziek vaak werd gemodelleerd naar vocale vormen en genres, waarbij gestreefd werd naar een homogeen klankidioom, ondermeer door het spelen op 'instrumentenfamilies' die werden gebouwd in diverse groottes, van bas naar discant, krijgt het instrumentarium nu een nieuwe rol toebedeeld.

De componisten van de nieuwe stijl verbeelden zich een grote diversiteit aan klankkleur, en maken hierbij gretig gebruik van de veelheid aan soorten instrumenten die in deze door panache en uitvindervreugde gekenmerkte tijden een spectaculaire ontwikkeling kennen. Enerzijds worden nieuwe instrumenten gecreëerd of heruitgevonden, waarbij dikwijls het concept en de inspiratie rechtstreeks uit de oudheid wordt gepuurd (bijvoorbeeld de *chitaronne*, die een grote *kitara* verbeeld of de *Lirone,* een pastiche van de antieke *Lyra,* gebouwd als basinstrument). Bestaande instrumenten worden verder uitgewerkt (bijvoorbeeld de *arpa doppia,* de *arpa a tre ordini*). Anderzijds worden instrumenten die hun oorsprong en gebruik kenden in verschillende muzikale en sociale contexten (zoals de *cornetto, tromba* en *trombone,* eigen aan de *alta cappella*, en de *arpa, leuto, clavicembalo, viola da gamba* uit de *bassa cappella*) gecombineerd in het *Concerto,* samen met instrumenten van lagere klasse, die worden 'opgewaardeerd' wanneer een antieke oorsprong wordt vermoed en toegeschreven, zoals bijvoorbeeld bij de *viola da braccio*, die volgens Severo Bonini zou afstammen van de *Lyra* [1].

Het gebruik van de instrumenten in het samenspel is gevarieerd edoch functioneel. Zo maakt bijvoorbeeld Agostino Agazzari een onderscheid tussen enerzijds instrumenten die deel uitmaken van het *fondamento*, (zoals *Organo, Gravecimbalo,* of indien er weinig stemmen of solostemmen zijn, *Leuto, Tiorba, Arpa*) ter begeleiding van de baslijn en ter ondersteuning van het geheel van alle stemmen in het *Concerto* en anderzijds instrumenten die behoren tot het *ornamento* (*Leuto, Tiorba, Arpa, Lirone, Cetera, Spinetto, Chitarrina, Violino, Pandora, et altri simili)*, die dienen om de muziek te versieren en die geschikt zijn van het contrapunt [2].

Aan diverse Italiaanse hoven, stadsstaten en republieken werden instrumenten-collecties uitgebouwd, waarin opvallend veel orgels aanwezig zijn.

Zo schrijft Ercole Bottigare in 1594 dat in dat in Ferrara Alfonso II d'Este beschikte over twee "*camere de' Musici"* die naast talloze muziekboeken een indrukwekkende verzameling speelklare muziekinstrumenten bevatten. Deze laatste werden voortreffelijk onderhouden en gestemd door ervaren meesters die hiervoor door de Hertog gepast vergoed werden : *"et sono cosi tenuti da mastri valenti che li sanno et accordare, et fabricare eccelentissimamente et sono da Sua Altezza Serenissima percio' del continovo trettenuti et provvisionati"* [3] Wanneer de inboedel van het Castello Estenze na de uitzetting door de paus werd verhuisd naar het Palazzo dei Diamanti, werd in 1600 een inventaris opgemaakt van deze in totaal meer dan vijftig muziekinstrumenten waaronder een tiental orgels van uiteenlopende grootte [4]. Het hof van de Medici in Firenze bezat een vergelijkbaar assortiment instrumenten, bewaard in de "*guardaroba per il Servizzio della Musica"*, gelokaliseerd in het Palazzo Pitti. Documenten bewaard in het Archivo di Stato in Firenze d.d.

1640, 1652, 1654 en 1669, betreffende het onderhouden, het inventariseren en het uitlenen van instrumenten aan hofmusici vermelden eveneens een groot aantal orgels [5] en ook in het Palazzo Ducale in Mantua verwijzen tientallen geschriften naar het aankopen van muziekinstrumenten, waaronder meerdere orgels [6].

3   HET "KLASSIEKE" ITALIAANS ORGEL EN HET ORGANO DI LEGNO.

Uit een aantal van voorgenoemde bronnen kan informatie gepuurd worden over de hoedanigheid van deze orgels, maar vooreerst volgt hieronder een korte uiteenzetting over het Italiaanse orgel zoals dit zich manifesteerde in de kerken tijdens het Cinquecento. Zonder te willen veralgemenen kunnen aan deze instrumenten een aantal karakteristieken toegekend worden, die hun oorsprong vinden in de eeuwen daarvoor en die in grote lijnen gehandhaafd zullen blijven tot in de negentiende en zelfs twintigste eeuw.
De orgels zijn éénmanualig, soms voorzien van een beperkt aangehangen pedaal. Het pijpwerk - in de regel gemaakt uit lood of loodlegering voor de binnenpijpen en tin voor de frontpijpen - is opgesteld op één windlade (oorspronkelijk sleeplade, later springlade voor grotere instrumenten, terwijl de sleeplade blijft gehandhaafd voor kleinere instrumenten en positieven). De winddruk, steeds geproduceerd door twee of meer meervouwige spaanbalgen is doorgaans laag, wat lage opsneden van de pijpmond impliceert. In combinatie met eerder smalle mondbreedten resulteert dit in een vrij zachte maar boventoonrijke en dragende klank. De speeltractuur is licht, compact en efficiënt.
De dispositie van de orgels, die kan gezien worden als de opsplitsing van een blokwerk in afzonderlijke rangen, is gebaseerd op de *Principale*. Dit register, letterlijk en niet mis te verstaan 'de belangrijkste', wordt in het prospect geplaatst, en is het fundament van de *Ripieno*. Deze is samengesteld uit een aantal individuele rangen, alle in prestantmensuur en qua toonhoogte bepaald door de opeenvolging van de natuurlijke boventonen, en genoemd naar de numerieke situering van de eerste toon van het register ten opzichte van de eerste toon van de *Principale*.

Hieronder ter illustratie een stereotiep voorbeeld van een Ripieno gebaseerd op een 8-voet Principale, in dit geval bestaande uit vijf rangen :

(I) Principale   (8-voet)   C
VIII (Ottava)   (4-voet)   c
XV (Quintadecima)   (2-voet)   c'
XIX (Decimanona)   (1 1/3-voet)   g'
XXII (Vigessima seconda)   (1 voet)   c''

De grootte van het orgel wordt, eerder dan door het aantal rangen, bepaald door de toonhoogte van de grootste pijp - dus de grondtoon - van de Principale (bijvoorbeeld 24-voet, 12-voet, 8-voet, …), deze is in de regel op zijn beurt in verhouding met de omvang van de ruimte waarvoor het orgel wordt geconcipieerd. Niet zelden worden in grotere ruimtes de laagste registers in de discant meerkorig gebouwd *(raddoppi)*. Belangrijke voorbeelden hiervan zijn het orgel Van Lorenzo da Prato in de San Petronio in Bologna (ca. 1475) en het orgel van Onofrio Zefferinni in de Badia Fiorentina (ca. 1558).
De *Ripieno*, waarvan de registers *registri d'Organo* worden genoemd, wordt vanaf circa de tweede helft van het Cinquecento (ondermeer door de inbreng van transalpijnse bouwers) frequent uitgebreid met *registri da concerto* zoals - in de eerste plaats - "*flauto in ottava*" en "*flauto in quintadecima»,* maar ook *" tromboni, fagotti, cornetti, voci umane, ed altre galanterie"* [7]. Het betreft hier registers in fluitmensuur, tongwerken en samengestelde registers, die bedoeld zijn als imitaties van muziekinstrumenten of van de menselijke stem, en die zowel solistisch, als in combinatie met de laagste *Ripieno*-stemmen als in samenspel met andere instrumenten worden gebruikt.
Naast het gebruik van tin en lood voor het pijpwerk werd ook geëxperimenteerd met andere materialen : zo schrijft ondermeer Adriano Banchieri over orgels opgetrokken met pijpen uit papier, hout en ook buxus, glas en albast :*" …l'Organo...è stato eretto con canne di piombo, stagno, cartone, e legno, ma parimente con canne d'oro, argento, e bosso, vetro, e allabastro..."* [8] en ook Antonio Barcotto verwijst naar het gebruik van uiteenlopende grondstoffen *:* hout en papier, messing en doek :*"Di diverse sorti di materia s'usano formare canne per organi, come di stagno, piombo, legno e carta, ed anche di ottone e banda..."* Erg belangrijk zijn de specificaties die Barcotto verder over orgels met houten pijpen geeft : *"Sono usate le canne di legno, e la maggiore ragione è per formare istrumenti dolci da camere, e sale, o vero d'Accademia, acciocche per la vicinanza delle orecchie d'ascoltanti non siano fastidite dall'altezza del suono, poiché in luoghi piccoli, comme camere o sale non si ricerca gran quantità di suono e gli strumenti in tali luoghi quanto più son dolci, tanto maggiore (armonia e) soavità formano. E che cio sia vero, si vede, che tal sorte d'Organi vieni fabricata di due soli registri, lasciando fuori tutti li ripieni..."* [9].

Samengevat : deze orgels met houten pijpen, dixit Barcotto, hadden een zachte klank en werden gebouwd voor het gebruik in kleinere ruimtes met een matige akoestiek. Zij werden geconcipieerd met twee registers terwijl de Ripieno achterwege werd gelaten. De "zachte" klank van het orgels met houten pijpen wordt in meerdere bronnen vermeld en zelfs benadrukt :

" …organo di canne de legno perfettissimo di dolcezza e soavità ..." [10]

" TUTTE LE CANNE SONO FATTE DI LEGNO, (…) E RENDA DOLCE INTONAZIONE (…) DI VOCE GRAVE E DOLCISSIMA… " [11]

"IN LUCCA NELL'ACCADEMIA DEL SIG. TOMASO RAFAELLI UN ORGANO SOAVE DI CANNE LIGNEE, FATTO DA ANDREA LUCHESE, …" [12]

" CON TAL BELLA OCCASIONE FARO SONNARE LE CHITARONI ALLI CASALANTI NEL ORGANO DI LEGNO IL QUAL'È SOAVISSIMO… " [13]

"Sono usate le canne di legno, e la maggiore ragione è per formare istrumenti dolci ..." [14]

Een bezoek aan de Palazzi in Firenze en Mantua en het Castello Estenze in Ferrara leert ons dat de grootste Salone, waar de orgels mogelijk werden opgesteld, hooguit enkele tientallen meters lang, een achttal meter breed en een zestal meter hoog zijn.

Tussen de orgels waarvan sprake in het bronnenmateriaal te Ferrara, Firenze en Mantua kunnen er een aantal worden geïdentificeerd als "*Organo di legno"* , en in enkele gevallen wordt de dispositie weergegeven :
In de inventaris in Ferrara bevindt zich *"Un Organo di Cipreso",* op de lijsten in Firenze is ondermeer sprake van *"Due Organi di Legno, uno con Principale, e ottava, e l'altra all'unisono con un'principale, un Organno grosso di legno di quatordici piedi, Un'Organino di legno di cinque piedi con un' registro solo, Un organino di legno con un' flauto, e regale"* (1640); "*Un'Organo di Cipresso di 45 tasti à uno registro solo..."* (1654); *"Un Organo di cipresso di tre registri di 41 tasti..."*. [15]. In 1607 wordt in Mantua, in opdracht van Francesco Gonzaga *"L'Orfeo, favola in Musici"* van Claudio Monteverdi opgevoerd. In de druk van 1609 vraagt Monteverdi voor de uitvoering twee *Organi di legno* [16] en in 1611 schrijft Monteverdi in een brief aan Kardinaal Ferdinando Gonzaga over een gepland concert met madrigalen in de *Sala degli spechhi* dat hij "bij zulk een gelegenheid de *chitarroni* wil laten samenspelen met het *Organo di legno,* hetwelk zéér zacht klinkt" (*"Con tal bella occasione faro sonnare le chitaroni alli casalanti nel organo di legno …"* [17].

Het gebruik van het Organo di legno door Monteverdi in het licht van de *Stilo Moderne* is allicht het meest bekende, maar zeker geen alleenstaand voorbeeld. In Firenze gaf Emilio dei Cavallieri aan de orgel- en klavecimbelbouwer Francesco di Niccolo Palmieri opdracht tot het bouwen van meerdere *Organi di legno*, die ondermeer gebruikt werden tijdens de intermedii die in 1589 georganiseerd werden ter gelegenheid van het huwelijk tussen Groothertog Ferdinando de' Medici en Prinses Christine van Lorraine met muziek van *Malvezzi, Bardi, Cavalieri,* e.a… Deze orgels zijn overigens terug te vinden in de bovengenoemde inventarissen van de *Guardaroba* in Palazzo Pitti. Verder zijn *'Rappresentazione di Anima e di Corpo'* (Cavalieri, Rome*,* 1600) en '*La liberazione di Ruggiero dall' Isola d'Alcina'* (Francesca Caccini, Firenze 1625) gekende muziektheatercreaties waarbij het *Organo di legno* wordt vermeld.
In de gedrukte versie van *L'Orfeo* van Claudio Monteverdi wordt de instrumentatie meermaals weergegeven in de partituur. Opvallend is dat het *Organo di legno,* samen met een *chitarrone* (deze combinatie bleek gewaardeerd, want ook gebruikt door Cavalieri in de *Rappresentazione*) wordt ingezet voor de begeleiding van de recitatieven waar het verlies van de geliefde het thema is. Hier wordt het *Organo di legno* duidelijk gekoppeld aan het affect, en gezien het gebruik van muziekinstrumenten in functie van de symboliek legio was rijst het vermoeden dat het *Organo di legno* hier verwijst naar de Panfluit. In het tweede bedrijf zingt een herder : *"Qui Pan, dio de' pastori s'udi talor dolenter imembrar dolcemente suoi sventurati amore"* (*Hier hoorde men Pan, de god van de herders soms zacht klagen terwijl hij zijn ongelukkige liefdes zacht in herinnering bracht…*). Een bijkomend argument is hier dat Severo Bonini in zijn *Discorso e Regole*, wanneer de oorsprong van het orgel ter sprake komt alludeert naar de Panfluit.

Dat het *Organo di legno* ook in de liturgie werd gebruikt kan ondermeer afgeleid worden uit een brief van Emilio de' Cavalieri uit 1591 aan de Florentijnse ambassadeur in Rome waarin sprake is van een instrument bedoeld voor de kapel waar de vespers worden gezongen : *" Madamma manda a presentare al Papa un organo di legno, per metterlo nella cappella dove si canta il vespro"* en uit het feit dat Palmieri in 1590 en in 1591 opdracht krijgt om voor de heilige week drie *Organi di legno* héén en terug te verhuizen van het Palazzo Pitti naar Pisa [18]

4   TECHNISCHE KENMERKEN VAN HET ORGANO DI LEGNO.

Slechts één anoniem en ongedateerd *Organo di legno* van Italiaanse oorsprong uit de besproken periode werd bewaard en bevindt zich in de Silberne Kapelle in Innsbrück.
In tegenstelling tot de voorbeelden die terug te vinden zijn in de historische bronnen gaat het hier om een vrij groot instrument, met een uitgebouwde *Ripieno*; dit is mogelijk een reden waarom het instrument de tijd overleefde. Het orgel werd in 1990-1992 gerestaureerd door het Gabinetto Restauro Organi, toen werkzaam in het Palazzo Pitti in Firenze, onder leiding van Prof. Dr. Pier Paolo Donati.
In functie van dit onderzoeksproject werd het instrument ter plaatse en aan de hand van het restauratierapport [19] bestudeerd.

Met uitzondering van de bouw van het pijpwerk in cipressenhout hebben de (soms slechts fragmentarisch) bewaarde originele onderdelen van dit instrument alle kenmerken, constructiemethoden en materiaaltoepassingen van het Italiaanse orgel uit het Cinque- en Seicento. De sleeplade werd gebouwd als een massieve planksleeplade in notelaar, met uitgehaalde cancellen, typisch voor kleinere instrumenten uit deze periode. De pijpstokken, slepen, loze slepen en pijproosters, gingen verloren maar de boringen in de windlade geven een goed beeld van de oorspronkelijke, grotendeels geschrankte pijpopstelling, waarbij het binnenpijpwerk de frontopstelling in drie velden weerspiegelt. Ook de originele ventielen en pulpeten zijn verdwenen. Van de speel- en registertractuur bleven een aantal typische gesmede wellen en hefbomen bewaard. Van het klavier is enkel het beleg en de frontons oorspronkelijk. De spanen van de schepbalgen zijn mogelijk origineel.

Belangwekkend is uiteraard het houten pijpwerk en de constructie ervan. Hieronder enkele waarnemingen.
Na het uittekenen van de pijpdiameters in een mensuurtabel blijkt dat bij het pijpwerk van de Principale de verhouding van de diameter van het octaaf tot de diameter van de grondtoon dicht bij de gulden snede ligt. Het mensuurverloop is regelmatig, met één knik : de eerste drie pijpen zijn enger gemensureerd. Dit zou een spoor kunnen zijn van de praktijk waarbij de bas van orgels oorspronkelijk tot F, werd uitgebreid met Mi, Re, Ut, zoals vermeld wordt in historische diverse bronnen. Het mensuurverloop van de hogere Ripieno-registers loopt vrij gelijk met het mensuurverloop van de Principale.
Het pijpcorpus uit cipressenhout is samengesteld uit een voorwand met een met het kruishout afgeschreven en in fase uitgebeiteld bovenlabium, twee zijwanden en een rugwand, die een notelaren kernblok in langshout omsluiten. De voor- en achterwand meesteren over de zijwanden. Het kernblok met windkanaal wordt vooraan afgesloten met een opgelijmde voorslag in cipres, die dienst doet als onderlabium. De hout van de corpuswanden is gezaagd van kwartiers over vals kwartiers naar dosse. De ervaring leert ons dat cipressenhout, zelfs wanneer dun gezaagd in dosse, buitengewoon stabiel is. Zo werd bijvoorbeeld bij cipressen zangbodems van Italiaanse klavecimbels ook geen rekening gehouden met de zaagrichting. De doorsnede van het pijpcorpus is quasi vierkant; in het algemeen zijn de pijpen, vooral in de bas, een weinig minder diep dan breed, waarschijnlijk is dit een gevolg van een werkwijze waarbij na het lijmen van de (bij aanvang een weinig bredere) zijwanden tegen het in oorsprong vierkante kernblok; de wanden werden dan gelijk geschaafd met het kernblok - waarbij bijna onvermijdelijk fracties van het blok werden afgehaald - alvorens voor en achterwand werden opgelijmd. Tot zover is er, op de gebruikte houtsoorten na, geen onderscheid met de " traditionele" constructiemethode van houten pijpwerk zoals wij die kennen in andere gebieden.
Uitzonderlijk echter is vooreerst het feit dat de breedte van het bovenlabium smaller is dan de binnenbreedte van het pijpcorpus, en gelijk aan de breedte van de kernspleet. Dit impliceert een ongewone constructie van het windkanaal in het kernblok. Het windkanaal is langgerekt, bovenaan even breed als de kernspleet en het bovenlabium en het heeft zowel in de breedte als in de diepte een wigvormig verloop, in de breedte versmallend en in de diepte vergrotend naar de pijpvoet toe. Een ander opmerkelijke vaststelling is dat het windkanaal zowel in het blok àls in de voorslag (zij het in mindere mate, maar tot aan de kernspleet toe) wordt uitgespaard. Een dergelijke constructie moet grote voordelen opleveren bij de intonatiepraktijk : zo kan bijvoorbeeld de kernspleetdikte vergroot worden door het windkanaal dieper uit te halen in de voorslag, of kan de richting van de windstrook veranderd worden door een minimale fase aan te brengen aan de kernspleetrand van de voorslag, terwijl het onnodig is de pijp van de windlade te nemen. Een dergelijk werkwijze laat niet alleen toe om sneller en dus efficiënter klankresultaat zoals aanspraak en volume te beoordelen en te vergelijken tussen de pijpen onderling, maar deze methode vergroot ook de marge om te experimenteren en te corrigeren in die zin dat het pijpblok behoed wordt; wanneer zou blijken dat de kernspleetdikte bij de intonatiewerkzaamheden te groot is geworden, kan de voorslag aan de binnenkant afgeschaafd worden, of desnoods vervangen, wat een gering verlies aan materiaal betekent.

Tijdens een prospectie van het orgel in Innsbrück werd het orgel bespeeld, zowel solistisch als in een begeleidende functie met blokfluit. De registratie werd beperkt tot Principale of Principale en Ottava. Een audio-opname werd gerealiseerd.

Opvallend is dat, wanneer het orgel solistisch wordt gespeeld, de klank in eerste instantie wordt ervaren als die van een Italiaans orgel met metalen pijpwerk; wanneer het orgel echter een begeleidende functie krijgt valt pas op dat het orgel een relatief matige geluidssterkte heeft, waardoor de solistisch gespeelde blokfluit als het ware op de voorgrond treedt. Deze ervaring werd onderschreven door personen die de opnames nadien beluisterden.

Dit fenomeen doet onvermijdelijk denken aan de historische bronnen waar de klank van het *Organo di legno* wordt omschreven als *dolce, perfettissimo di dolcezza e soavità, di voce grave e dolcissima, soave, soavissimo…*

5   HET REALISEREN VAN EEN ORGANO DI LEGNO MET BEPERKTE DISPOSITIE.

In functie van de reconstructie van een Organo di legno werden grondstoffen (cipres, notelaar, populieren, …)aangekocht en primair verwerkt. Op basis van de mensuren van het orgel te Innsbrück, van orgelpositieven met metalen pijpwerk uit het Cinque- en Seicento en van technische kenmerken zoals deze beschreven worden in historische bronnen, werd in functie van de realisatie van een *Organo di legno* met beperkte dispositie een ontwerp gemaakt van windlade, prospect en tractuur. Dit ontwerp zal, samen met de historische bronnen, worden besproken in een vervolg op dit artikel.

ACKNOWLEDGEMENTS

REFERENTIELIJST
[1] BONINI Severo, *"Discorso e regole sopra la Musica et il contrapunto"*, Firenze, 1649/1650, p.

[2] AGAZZARI Agostino, *"Del sonare sopra 'l basso"* , Siena, Flacini, 1607.

[3] BOTTIGARI Ercole, "*Il Desiderio, 1594",* in *"Un decennio di spese msuicale alla Corta di Ferrara",* E.Durante/A.Martellotti Fasona, 1982.

[4] in : DURANTE Elio en MARTELLOTTI Anna, *"Cronistoria del concerto delle Dame Principalissime di Margherita Gonzage d'Este"*, Firenze 1989.

[5] HAMMOND F., *'Musical Instruments at the Medici Court in the Mid-Seventeenth Century"*, in "Analecta Musicologica", Studien X, 1975.

[6] BESUTTI Paola, *"La galleria musicale dei Gonzaga: intermediari, luoghi, musiche e strumenti in corte a Mantova"*, in *"Gonzaga, la Celeste Galeria"*, Milano, 2002.

[7] BARCOTTO Antonio, *"Regola e breve raccordo per far rendere aguistati, e regolati ogni sorte di Istrumenti da vento, cioè Organi, Claviorgani, Regali e simili",* Padova 1652.

[8] BANCHIERI Adriano, "*Conclusioni nel suono dell'organo"*, Bologna 1609.

[9] Cf. 7

[10] CORADONI F. *La cappella musicale del Duomo di Arezzo*, in : "*Note d'archivio per la storia musicale*", XIV (1937), XV (1938), XVIII (1941), in "*Arte nell'Aretino, la tutela e il Restauro degli Organi Storaci*" (Firenze 1980), P.P.Donati e.a..,

[11] VICENTINO, Nicolo, "*Circolare descrittiva l'Arciorgano",* gedrukt door Nicola Bevilacqua, Venetia 1561.

[12] Cf. 8

[13] STEVENS, Denis, *The letters of Claudio Monteverdi*, Cambridge 1980.

[14] CF. 7

[15] CF. 5

[16] MONTEVERDI CLAUDIO, *L'ORFE FAVOLA IN MUSICA,* GEDRUKT DOOR RICCIARDO AMADINO,VENETIA, 1609.

[17] STEVENS Denis, *The letters of Claudio Monteverdi*, Cambridge 1980.

[18] KIRKENDALE Warron, *Emilio de' Cavalieri "Gentiluomo romano"*, Firenze 2001.

[19] DONATI Pier Paolo, *"L'Organo della Silberene Kapelle di Innsbrück, Realizione de restauro",* Informazione Organistica, Anno XVIII n° 1, Aprile 2006